Control of Wall-Bounded Turbulence Through Closed-Loop Wall Transpiration

Thesis by
Simon Silvio Toedtli

In Partial Fulfillment of the Requirements for the
Degree of
Doctor of Philosophy in Aeronautics

CALIFORNIA INSTITUTE OF TECHNOLOGY
Pasadena, California

2021
Defended May 7, 2021

Simon Silvio Toedtli
ORCID: 0000-0001-9371-9572

ACKNOWLEDGEMENTS

First and foremost, I would like to thank my advisor, Beverley McKeon. Thank you, Beverley, for your guidance and support throughout the years and for helping me grow not only as a researcher, but also as a person. I admire your ability to master a broad range of skills in many different settings: As a researcher, you build bridges between seemingly disconnected subfields. As a human, you combine technical and soft skills with ease. And as a leader, you bring together people from different backgrounds and build meaningful communities. Thank you for being a great role model and for encouraging everyone in the group to develop a broad skill set as well. I very much appreciate your help and encouragement in research, your caring about my personal well-being, and your support for my time-consuming side projects that were often not directly related to my research.

I also thank my other mentors who have been influential along the way. Thank you, Tony Leonard, for your help, friendship, and the many interesting discussions. I very much enjoyed our weekly lunches, and your enthusiasm and kindness have always been a great source of inspiration. Thank you, Petros Koumoutsakos, for sparking my interest in computational fluid dynamics, for hosting me in your group as an undergraduate, and for opening so many doors for me. Even though we have not yet managed to resurrect your original control scheme, it has informed the work in this thesis and I think there is hope that we will eventually come full circle. Thank you, Dan Meiron, for your input to my research along the way, during the Tuesday talks and my candidacy exam. I am also very grateful for all your support and work for the GALCIT student initiatives I was involved in, particularly the Caltech Space Challenge and the GGSC. Thank you, Nick Hutchins, for the insightful discussions during your sabbatical at Caltech and for your interest in our control work. Your input came at just the right time and has played an important role in shaping this thesis. I would also like to thank Tony, Dan, and Nick for serving on my thesis committee.

Next, I would like to thank all the past and present members of the McKeon group (roughly in order of how we overlapped): Rashad Moarref, Mitul Luhar, Reeve Dunne, Subrahmanyam Duvvuri, Esteban Hufstedler, Tess Saxton-Fox, Scott Dawson, Sean Symon, Kevin Rosenberg, Jonathan Morgan, David Huynh, Angeliki Laskari, Arslan Ahmed, Ryan McMullen, Maysam Shamai, Ben Barthel, Morgan Hooper, Jane Bae, Salvador Gomez, Jacque Tawney, Yuting Huang, Anagha Mad-

husudanan, Tanner Harms, Greg Stroot, and Miles Chan. You all made the time in our wall-bounded office fun. I am grateful for all the good conversations we had on scientific and not-so-scientific topics, for the beer evenings at the Rath, and for the supper club outings in the greater LA area. A special thank you to Mitul, who helped me with the resolvent-based flow control design work and provided important input during discussions throughout my PhD. A big thank you also to my summer students Christine Yu, Dory Castillo, and Sarah Barrett. I enjoyed working with you all, and I thank you for helping me grow as a mentor.

I am also indebted to the many people who have ensured that all administrative aspects are taken care of. Thank you to our group admins, Jennifer Stevenson, Jamie Meighen-Sei, Denise Ruiz, and Liza Bradulina, for supporting the research group so well and for taking care of administrative issues before we even knew they existed. Thank you to Christine Ramirez for helping with all GALCIT-specific aspects and for supporting the activities of the GGSC. And a big thank you to Laura Flower Kim and Daniel Yoder from ISP for helping with all visa-related questions and for organizing community building events throughout the years. One of the aspects I really enjoyed about Caltech is its global village vibe and all of your work for the international community is crucial.

I would also like to thank the funding sources that enabled this research. Thank you to the Resnick Sustainability Institute for providing a fellowship for my first year at Caltech. In particular, I would like to thank Neil Fromer for the stimulating chats during our quarterly check-ins and for organizing numerous interesting fellow events. A special thank you to Peter and Melanie Cross, whose donation to the Resnick Institute established the fellowship that I was part of. My subsequent years at Caltech were funded through the U.S. Air Force Office of Scientific Research (Grant No FA 9550-16-1-0361) and the Office of Naval Research (Grant No N 00014-17-1-3022), and I very much appreciate their financial support. I would also like to thank Petros Koumoutsakos for providing the computational resources for this study.

The coolest side project during my PhD was the 2019 Caltech Space Challenge, and I would like to thank all the helpers, sponsors, and participants. I would especially like to thank Fabien Royer, who co-organized the event with me, and Michele Judd from the Keck Institute for Space Studies, who was the super hero and took care of all the issues we encountered along the way. I would also like to thank Michele for making me part of the KISS family, and for organizing so many interesting events for

the fellows. A big thank you also to the GALCIT admin staff, in particular Denise Ruiz, Peggy Blue, and Jamie Meighen-Sei, and all the volunteers from GALCIT and JPL, without whom the event would not have been possible.

During my six years at Caltech I have also been extremely fortunate to have become friends with people from all over the world, and I hope we can stay in touch as we now spread across the globe. I would certainly forget a lot of people if I tried to make an exhaustive list of everyone who filled the past six years with life and joy, therefore I limit myself to a few special mentions. Thank you Daniel Pastor Moreno, Gautam Venugopalan, and Johan Melis for your continued friendship since day one of grad school, for the many epic trips all over the US (and maybe one day Ethiopia?), for the Smash Bros and beer nights, and for the self-inflicted suffering on trail runs in the San Gabriel Mountains. Thank you to Erika Figueroa-Schibber, Fabien Royer, Thibault Guillet, Abbas Tutcuoglu, and Ke Yu for the many library sessions during first year, for joining forces for quals preparation, and for the continued friendship. Danke to the Swiss connection – Andrea Zürcher, Florian Kehl, Martina Troesch, and Giacomo Castiglioni – for the many fun evenings and for the impromptu trip to Burning Man. Thank you, Soledad Altrudi and Agustin Fernandez Lado, for treating me to many delicious home-made meals (including dearly missed Fondues!), great evenings, and good Netflix suggestions. A big thank you also to Subrahmanyam Duvvuri and Sivani Vempati, for many great get-togethers, and for hosting me in Princeton and Bangalore. And thank you to all my roommates in the past six years for the good company in the Cats: Johan Melis, Alexandr Kapshuk, Stephen Grant, Andrea Coladangelo, Florian Schaefer, Fabien Royer, and Victor Zhang.

Finally, a big thank you to the people with a special place in my heart. Thank you, Christine Do, for your love and support, and for keeping me sane during the thesis writing process. I love you very much, and I am looking forward to many more adventures together. And thank you to my family, my parents Luzia and Walo Tödtli, my sister Maria Fuchs and brother-in-law Roman Fuchs, and my grandmother Ruth Gees, for all your love and support throughout my life. Thank you for giving me roots when I was little, and wings once I was grown up, so that I could fly and explore the world. Thank you also for supporting my decision to move across continents, for the close emotional connection despite the physical distance, and for the weekly Skype calls which I always enjoy. I love you all very much.

ABSTRACT

Many wall-bounded flows of practical relevance are turbulent, including the flows past airplanes and ships. The turbulent motions enhance momentum mixing and, as a result, the drag force on the engineering surface increases, for transportation vessels typically by at least a factor of two compared to laminar flow. Turbulent flow control aimed at drag reduction therefore has the potential to deliver enormous energetic and economic savings, but many challenges remain despite active research for well over a century. The present thesis aims to contribute towards two open questions of the field: first, what are suitable controller design tools for high Reynolds number flows? And second, how does actuation through closed-loop wall transpiration change the flow physics? We investigate aspects of these questions through direct numerical simulation (DNS) and modal analyses of an example control scheme, which is applied to a low Reynolds number turbulent channel flow. The controller is a generalization of the opposition control scheme, and introduces a phase shift between the Fourier transformed sensor measurement and actuator response.

The first part of the thesis demonstrates that a low-order model based on the resolvent framework is able to approximate the drag reduction results of DNS over the entire parameter space considered. The model is about two orders of magnitude cheaper to evaluate than DNS at low Reynolds numbers, and we present a strategy based on subsampling of the wave number space and analytical scaling laws that enables model-based flow control design at technologically relevant Reynolds numbers. The second part of the thesis shows that the physics of the controlled flow can be understood from two distinct families of spatial scales, termed streamwise-elongated and spanwise-elongated scales, respectively. Wall transpiration with streamwise-elongated scales attenuates or amplifies the near-wall cycle and therefore leads to drag reduction or increase, depending on the phase shift. In contrast, wall transpiration with spanwise-elongated scales only leads to drag increase, which occurs at positive phase shifts and is due to the appearance of spanwise rollers which largely enhance momentum mixing. Both patterns are robust features of flows with closed-loop wall transpiration, and the present study offers a simple explanation of their origin in terms of phase relations at distinct spatial scales. The findings of this study may set the stage for a unifying framework for various forms of wall transpiration, and implications for future flow control design are discussed.

PUBLISHED CONTENT AND CONTRIBUTIONS

Toedtli, S., Yu, C., and McKeon, B. (2020). "On the origin of drag increase in varying-phase opposition control". In: *International Journal of Heat and Fluid Flow* 85, p. 108651. DOI: 10.1016/j.ijheatfluidflow.2020.108651.
S.T. ran the simulations and linear analyses, processed the data, created the figures, and was the primary author of the paper.

Toedtli, S., Luhar, M., and McKeon, B. (2019). "Predicting the response of turbulent channel flow to varying-phase opposition control: Resolvent analysis as a tool for flow control design". In: *Physical Review Fluids* 4 (7), p. 073905. DOI: 10.1103/PhysRevFluids.4.073905.
S.T. ran the simulations and linear analyses, processed the data, created the figures, and was the primary author of the paper.

Toedtli, S., Yu, C., and McKeon, B. (2019). "Structural and spectral analysis of varying-phase opposition control in turbulent channel flow". In: *Proceedings of TSFP 11*.
S.T. ran the simulations, processed the data, created the figures, and was the primary author of the paper.

CONTENTS

LIST OF FIGURES

LIST OF TABLES

Chapter 1

INTRODUCTION

The present study concerns fluid flow in one of the simplest configurations possible: an incompressible, isothermal flow of a Newtonian fluid with constant properties (density ρ and kinematic viscosity ν) past a solid bounding surface. The qualitative behavior of such flows depends on a single dimensionless group of problem-specific parameters $\mathrm{Re} = UL/\nu$, where U and L are characteristic velocity and length scales of the problem at hand. The dimensionless number Re is called the Reynolds number, after Osborne Reynolds, who observed in a series of dye experiments in a glass pipe that the nature of the flow undergoes a fundamental change as Re increases. In his own words (Reynolds, 1883):

> The internal motion of water assumes one or other of two broadly distinguishable forms - either the elements of the fluid follow one another along lines of motion which lead in the most direct manner to their destination, or they eddy about in sinuous paths the most indirect possible.

A modern analogue to Reynolds' famous sketches of the streamlined and sinuous flow pattern (figs. 3 to 5 in Reynolds (1883)) is shown in figs. 1.1a and 1.1b. These display the cross-section of a channel flow, where fluid flows from left to right between two parallel plates located at the top and bottom. The color represents the instantaneous fluid velocity in the mean flow direction (we will refer to this velocity component as the streamwise velocity u hereafter), and warmer colors indicate higher velocity. The flow field at low Re is shown in fig. 1.1a and corresponds to what Reynolds described as streamlined flow pattern. The velocity is independent of the wall-parallel coordinate and varies smoothly in the wall-normal direction. One could think of it as layers of constant velocity stacked upon each other, which is why this flow state is called "laminar flow" in modern terminology (from Latin *lamina* "plate, layer"). At sufficiently large values of Re, the flow pattern changes fundamentally, and the layered structure of the flow is lost, as can be seen from fig. 1.1b. This is what Reynolds described as sinuous motion: a disordered velocity field, marked by strong spatial and temporal fluctuations. In modern terminology,

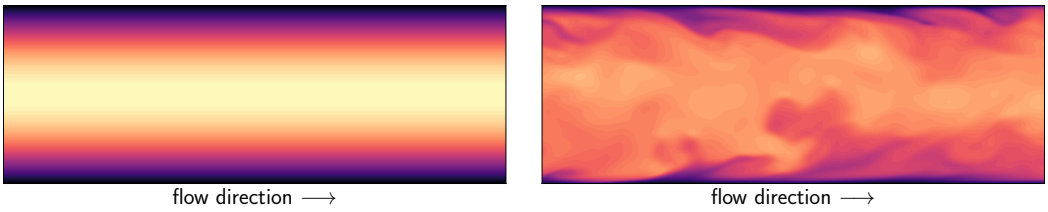

(a) laminar (b) turbulent

Figure 1.1: Example streamwise velocity fields of a channel flow.

this flow state is called "turbulent," from Latin *turbulentus* "agitated, tempestuous," but also "making trouble" (which accurately describes the effect these flows have had on generations of scientists). Laminar flows can only be realized under very specific conditions, and almost all flows of practical importance are therefore turbulent.

The presence of a solid surface has profound implications for a turbulent flow. The first one is that the boundary imposes a length scale on the flow, which limits the maximum size of the turbulent flow structures. In the example of fig. 1.1b, the channel height (i.e. the distance between the two plates) limits the size of the largest flow structures. If we denote the channel half-height by h, we can therefore say that the largest turbulent motions scale with h. The second implication is that the boundary imposes constraints on the motion of fluid elements adjacent to it. For a solid surface, the velocity normal to it must be continuous across the fluid interface. This is a purely kinematical constraint and results in the "no-through" or "no-penetration" boundary condition for the vertical velocity. To a good approximation, the tangential velocity components are also continuous across the interface (see e.g. Batchelor, 2000, chapter 1.9 for an in-depth discussion of this topic). This is a molecular effect and the resulting boundary condition is known as "no-slip" condition in the literature. Due to the no-slip condition, the fluid velocity has to decrease from a finite value in say the core of the channel to zero at the wall, which results in a monotonic velocity gradient or shear, at least in an average sense. The mean shear acts as an energy source for the turbulent velocity fluctuations, so that they self-sustain in wall-bounded flows despite the ever-present dissipation by molecular viscosity.

The turbulent fluctuations themselves feed back on the mean velocity profile, which can be seen from comparing figs. 1.1a and 1.1b. The laminar and turbulent flow are constructed such that they transport the same amount of mass, and equal colors imply equal velocity in both plots. The visual comparison of the instantaneous flow fields

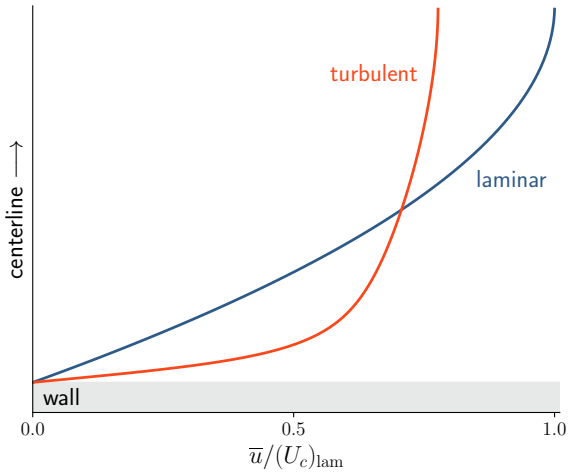

Figure 1.2: Example streamwise mean velocity profiles $\overline{u}$ normalized by the laminar centerline velocity $(U_c)_{\mathrm{lam}}$.

suggests that the laminar flow moves slower than its turbulent counterpart close to the wall, but flows faster in the channel center. These observations also hold in a statistical sense, which can be seen from the averaged velocity profiles in fig. 1.2, and are a consequence of turbulent mixing. Turbulent motions greatly enhance molecular mixing of transported quantities, such as momentum, and therefore lead to a more uniform velocity profile across the channel. The flow still has to satisfy the no-slip condition, and the velocity gradient of the turbulent flow is therefore much larger in the near-wall region. This has far-reaching consequences for engineering applications, because the mean wall-shear stress $\overline{\tau}_w$ (drag force per unit area) is proportional to the mean velocity gradient at the wall. The transition from a laminar to a turbulent flow goes therefore hand in hand with a significant increase in drag on the surface, which may be a ship hull, pipeline, or airplane fuselage. For example, Marusic, Mathis, and Hutchins (2010) estimate that 50% of the total drag force exerted on an airplane is due to turbulence (i.e. due to the steeper velocity gradient at the wall), and that fraction is even bigger for large oil tankers. The environmental and economic implications of better understanding and ultimately reducing turbulent fluctuations near solid surfaces can therefore not be overstated.

Finally, the turbulent flow state is also marked by a wide range of active spatial and temporal flow scales. We have already encountered one of them, the channel half-height, which is an example for a so-called outer flow scale that limits the largest flow motions. Another set of scales, so-called inner or viscous scales, can be defined from the flow in the near-wall region, where viscosity is most important.

The friction velocity is defined in terms of the wall shear stress $u_\tau = (\overline{\tau}_w/\rho)^{1/2}$, and can further be used to construct a viscous length scale $l_v = \nu/u_\tau$. Flow quantities normalized with u_τ and l_v are usually denoted with a superscript +. The viscous length characterizes the smallest dynamically relevant flow structures, and we can therefore say that they scale with ν/u_τ. The ratio between outer (largest) and inner (smallest) scales defines a Reynolds number $\mathrm{Re}_\tau = u_\tau h/\nu$, which is commonly referred to as friction Reynolds number. Many industrial applications operate in the regime $10^3 \leq \mathrm{Re}_\tau \leq 10^6$ (see e.g. Smits and Marusic, 2013), and scientific endeavors should therefore focus on turbulent flows at high Reynolds numbers. However, this regime is extremely challenging, if not impossible, to study experimentally or numerically with current capabilities. This can be best understood from the channel example, where the largest scale h is fixed by the geometry. Therefore, as Re_τ increases, the viscous scale decreases and becomes increasingly difficult to measure experimentally or resolve numerically. Even for the simplest geometries, accurate numerical simulations lag about two orders of magnitude in Re_τ behind experimental capabilities, which in turn lag behind industrial applications.

The present thesis concerns a particular aspect of wall-bounded turbulent flows, namely control for drag reduction, and will study this problem by means of direct numerical simulation (DNS) and low-order models. Control is applied by replacing the no-through condition at the wall with a nonzero wall-normal vertical velocity, a configuration also known as wall transpiration. The controller operates in closed-loop, which means that the vertical wall velocity is a function of the flow state. In order to provide the necessary background for our study, we summarize the most relevant literature results in the following sections. Section 1.1 gives an overview of the statistical and structural features of wall-bounded flows, which have motivated many of the previous flow control approaches summarized in section 1.2. We then review low-order modeling techniques for both canonical and controlled wall-bounded flows (section 1.3) and close this chapter with an outline of the specific thesis objectives and organization (section 1.4). The review generally subsumes the canonical wall-bounded flows channel, pipe, and zero-pressure-gradient boundary layer. There is broad consensus that all three flows behave qualitatively similarly, but it is important to keep in mind that quantitative differences between internal (channel, pipe) and external (boundary layer) flows exist, in particular at large scales (see Monty et al., 2009, for more details). We will therefore differentiate between geometries where necessary.

1.1 Structure of Wall-Bounded Turbulent Flows

Even though instantaneous snapshots of wall-bounded turbulent flows are much more disordered than their laminar counterparts, these flows are not devoid of structure. In a statistical sense, the structure manifests itself in robust averages, and we have already encountered an example statistical flow quantity in fig. 1.2, where we discussed the turbulent mean velocity profile. For internal flows (and boundary layers under the parallel flow assumption), statistical flow quantities only depend on the wall-normal coordinate (denoted by y) and typically scale with different characteristic lengths in different wall-normal regions. The location-dependent scaling reflects the overall structure of the flow, which is typically divided into distinct wall-normal layers derived from the properties of the mean velocity profile.

One important conclusion from the earlier discussion of boundary conditions and turbulent mixing is that the effect of viscosity is largest in the near-wall flow region. As the Reynolds number increases, the flow region dominated by viscosity becomes ever smaller, but remains finite since the no-slip condition has to be enforced even in the limit of very large Re_τ. These observations suggest that at sufficiently large Reynolds numbers, the mean velocity profile should exhibit a viscosity-dominated region that scales with l_v (which in an internal flow decreases with increasing Re_τ), and a turbulent fluctuation dominated core/outer region that scales with h. In-between there is a region where both scalings apply and it can be shown in various ways that the scaling overlap implies a logarithmic dependence of the mean velocity profile on the distance from the wall (see e.g. Tennekes and Lumley, 1972, for a detailed discussion). The structure of the mean profile implies a layer structure for the flow itself, which consists of three different regions that are parametrized by their distance from the wall: an inner region, which extends from the wall to about $y^+ \leq 30$, where viscosity dominates and flow quantities typically scale with inner scales, a core or outer region located at $y/h > 0.2$, where viscosity is negligible and flow quantities scale with outer scales, and an inertial or overlap region in-between, where both scalings apply. There is some scatter in the literature regarding the approximate bounds for each region, and the values above are taken from Klewicki et al. (2007). The classical segmentation of the flow outlined above is deemed sufficient for the purpose of the present study, but we note that recent work proposed an alternative layer structure based on the mean force balance, with implications for the layer localization and velocity scaling (Klewicki et al., 2007).

Wall-bounded turbulent flows also exhibit structure in a spatial and temporal sense. The seminal work of Kline et al. (1967) revealed the persistent presence of well-organized low-speed streaks very close to the wall, and subsequent research efforts over the past decades have shown that so-called coherent structures (i.e. fluid motions that have coherence over a spatial region and last for a reasonable period of time) exist throughout the flow. The coherent structures near the wall (say $y^+ < 70$, which includes the inner and parts of the overlap region) are usually referred to as near-wall cycle and consist of the aforementioned streaks and quasi-streamwise vortices. Not surprisingly, these structures scale in viscous units, and it is generally accepted that the streaks are about $100l_v$ wide and $1000l_v$ long. The streamwise vortices are somewhat shorter and their typical length is around $100l_v$ (see e.g. the review by Panton, 2001). The term cycle is appropriate because the vortices and streaks are connected by a self-replicating dynamical process: the streamwise vortices redistribute streamwise momentum, which leads to spanwise fluctuations in the streamwise velocity, i.e. the streaks. A linear instability of the streaky base flow leads to perturbation growth and eventually streak breakdown. Nonlinear interactions of the post-breakdown flow regenerate streamwise vortices, and the cycle begins anew (see e.g. Waleffe, 1997; Schoppa and Hussain, 2002). The near-wall cycle is autonomous, in the sense that it sustains itself even if the core flow is artificially removed (Jiménez and Pinelli, 1999), and it is the most energetic flow feature at low Re_τ. The near-wall cycle persists with increasing Reynolds number, but its overall energetic contribution to the flow decreases (Hutchins and Marusic, 2007a).

The consensus in the community about flow structures in the logarithmic and core region is less firm. This is at least partially owed to the fact that the investigation of these regions require sufficiently high Reynolds numbers, which makes experiments and simulations challenging. A thorough review of all the flow features observed in the logarithmic and outer region over the past decades is beyond the scope of this introduction, and we instead focus on the structures which have an imprint in the streamwise energy spectra. At large enough Reynolds numbers, long meandering velocity streaks appear in the logarithmic region, which are denoted very large scale motions (VLSMs) in internal flows and superstructures in external flows. The prefix super indicates that these structures are longer than the outer length h, and their spectral signature depends on the wall-normal location and flow geometry. In internal flows, the VLSM length increases with distance from the wall and can reach up to $14 \leq \lambda_x/h \leq 20$ in the core flow, where λ_x is the streamwise

wavelength (Guala, Hommema, and Adrian, 2006; Del Álamo et al., 2004; Monty et al., 2009). On the other hand, superstructures in external flows are only found in the logarithmic region and are somewhat shorter compared to the VLSMs. Their spectral peak occurs at $\lambda_x/h \approx 6$, but instantaneous meandering structures may be significantly longer (Hutchins and Marusic, 2007a). The VLSM and superstructures carry a significant amount of turbulent kinetic energy and Reynolds stress (Guala, Hommema, and Adrian, 2006), and have an imprint in the near-wall region. A series of recent work has shown that the very large scale motions have an amplitude modulation effect on the near wall cycle (Hutchins and Marusic, 2007b; Mathis, Hutchins, and Marusic, 2009): a negative large-scale excursion reduces the velocity gradient at the wall, which weakens turbulence production and reduces the intensity of the near-wall cycle, while a positive large-scale excursion has the opposite effect. This amplitude modulation effect seems to become important above $\mathrm{Re}_\tau \approx 2000$, and becomes stronger with increasing Reynolds number (Mathis, Hutchins, and Marusic, 2009). The near-wall cycle is therefore autonomous in the sense described earlier, but not independent of the flow in the logarithmic and core region. Finally, we note that the streamwise velocity spectra indicate another energetically important family of scales. They are characterized by a streamwise wavelength of $\lambda_x/h \approx 2-3$, and are usually referred to as very large scale motions (LSMs) (Adrian, Meinhart, and Tomkins, 2000). LSMs occur in internal and external flows throughout the logarithmic and outer layer, but their imprint is more pronounced in the outer flow, where the VLSMs and superstructures weaken (Monty et al., 2009).

Many numerical simulations, and to a lesser extent experiments, are limited to low Reynolds numbers. The above discussion shows that numerical studies have inherent limitations which arise from the insufficient scale separation. For example, the present study will consider a turbulent channel flow at $\mathrm{Re}_\tau = 180$, which implies that the inner region ($y^+ \leq 30$) occupies about 17% of the channel half-height and the streak length ($\lambda_x^+ \approx 1000$) is of the same order as h. Moreover, the amplitude modulation effect of the VLSMs is absent in this flow regime. Low Reynolds number studies are therefore helpful to understand the near-wall dynamics, but it is important to keep in mind that flows at technologically relevant Re_τ exhibit much richer physics, and observations at low Reynolds number may not hold at larger Re_τ (and vice-versa).

1.2 Turbulent Flow Control

Enhanced mixing due to turbulent flow motions is undesired in most engineering applications, and a natural question is whether detrimental effects can be removed or at least reduced by providing a suitable perturbation to the flow. This is a control problem, and defines the broad field of turbulent flow control. The control objective depends on the problem at hand, and for the purpose of this study, we focus on control to reduce the turbulent drag contribution. We therefore limit the following review to the drag reduction problem as well and further narrow the scope to control schemes that have a clear physical interpretation and provide the control input at or close to the wall. As we will see, almost all such control schemes target the near-wall cycle and aim to disrupt or at least weaken it with their control input. Most of the studies are conducted through DNS of low Reynolds number flows, and the above comments about missing scale separation should therefore be kept in mind.

Broadly speaking, one can differentiate between active control schemes, where the actuators require power input, and passive schemes, where the actuators do not need external power supply. For active schemes, a a further distinction can be made between closed-loop control, where the actuator input depends on the flow state, and open-loop control, where the actuator input is predetermined and independent of the flow state. The current study builds on a well-established active closed-loop control scheme known as opposition control (Choi, Moin, and Kim, 1994). We will therefore first review the literature results on opposition control, and subsequently introduce other closed-loop control approaches of relevance. We omit active open-loop techniques, but will discuss a few passive control methods, which will be important for later comparison.

1.2.1 Active Closed-Loop Control

The idea at the heart of opposition control is to reduce turbulent drag by detecting the quasi-streamwise vortices of the near-wall cycle and suppressing their momentum mixing. To this end, the control scheme measures the wall-normal velocity v at a detection plane located at a distance y_d above the wall (denoted by y_w) and generates blowing and suction with opposite sign and scaled by a factor A_d at the wall

$$v(y_w) = -A_d v(y_d). \tag{1.1}$$

A schematic of this scheme is shown in fig. 1.3. Previous DNS studies of turbulent channel (Choi, Moin, and Kim, 1994) and pipe flow (Fukagata and Kasagi, 2002) at $\mathrm{Re}_\tau \approx 180$ show that opposition control with $A_d = 1$ can reduce drag by up to

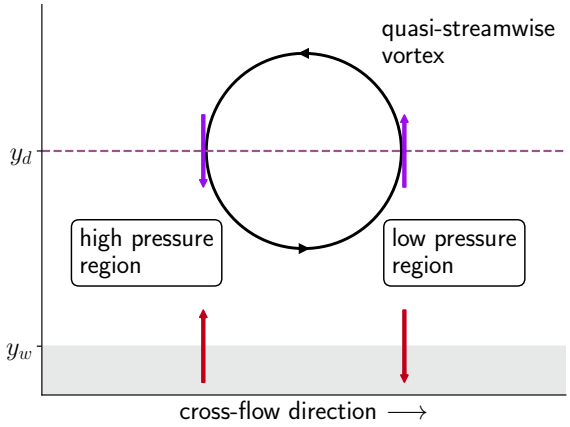

Figure 1.3: Schematic of opposition control. The dashed purple line indicates the sensor location (y_d) and the gray shaded area denotes the wall (y_w). The arrows indicate the sensor measurement (purple) and actuator response (red). The pressure regions outline the conceptual model of Xu, Rempfer, and Lumley (2003).

25%. The control effectiveness strongly depends on the sensor location, and the largest drag reduction (DR for short) occurs around $y_d^+ = 15$ (Hammond, Bewley, and Moin, 1998; Chung and Talha, 2011), which roughly coincides with the center of the streamwise vortices ($y^+ \approx 20$ on average, see Kim, Moin, and Moser, 1987). Less drag reduction is achieved if the sensors are located below or slightly above $y^+ = 15$, and the control scheme results in drag increase if $y_d^+ > 23$ (Choi, Moin, and Kim, 1994; Chung and Talha, 2011). The range of sensor locations leading to drag reduction can be increased by reducing A_d (Chung and Talha, 2011), and the maximum DR can be increased by either using upstream sensor information (Lee, 2015), or adding an integral term to the control law (Kim and Choi, 2017). The control scheme is sensitive to the spanwise alignment of the sensor measurement and control input, and a spanwise misalignment of more than $10\,l_v$ results in drag increase (Chung and Sung, 2003). The effectiveness of the control scheme depends on the Reynolds number and decreases with increasing Re_τ. For example, the maximum DR drops from approximately 25% at $\mathrm{Re}_\tau = 180$ to 18% at $\mathrm{Re}_\tau = 1000$ (Chang, Collis, and Ramakrishnan, 2002; Deng, Huang, and Xu, 2016). The deterioration with increasing Reynolds number can possibly be explained in terms of a decreasing ratio between outward shift of the mean velocity profile and the centerline velocity, analogous to patterned surfaces (Spalart and McLean, 2011; García-Mayoral, Gómez-de-Segura, and Fairhall, 2019). The data of Deng, Huang, and Xu (2016) provide some support for this argument, but the authors are not aware of a systematic validation in the context of opposition control.

The opposition control scheme requires flow measurements inside the flow field, which is not feasible in practical applications. One approach to mitigate this limitation is to formally retain the opposition control law (1.1), but estimate the velocity field at the sensor location from wall quantities, for example through a Taylor series approximation (Choi, Moin, and Kim, 1994), a convolutional neural network (Park and Choi, 2020), or a spectral linear stochastic estimation (Samie et al., 2020). Accurate estimation of the near-wall flow state from wall variables requires spanwise alignment between the wall measurement and the surrogate sensor location within the flow. For example, the correlation between the wall-shear stress and the streamwise velocity at $y^+ = 15$ vanishes for spanwise separations larger than $20\,l_v$ (Samie et al., 2020), which is reminiscent of the sensitivity of opposition control to spanwise misalignment. It seems plausible that the sensitivity of the estimation and control problem to spanwise shifts are related, and ultimately a consequence of the relatively small diameter ($20 - 50\,l_v$) of the quasi-streamwise vortices (Samie et al., 2020). Of course, the estimation and control problem are independent and one could use general estimation techniques as well (among many others Chevalier et al., 2006; Encinar and Jiménez, 2019). A different approach is to abandon the opposition control law and base the actuation input directly on wall quantities. In most cases, the goal remains to detect the quasi-streamwise vortices and to counteract them with wall transpiration, but the detection of the vortices is now based on their wall signature. Examples of such schemes are the suboptimal control laws of Lee, Kim, and Choi (1998), which use the second spanwise derivative of the wall pressure or the spanwise derivative of the spanwise shear to inform the blowing and suction and result in 16% and 22% DR, respectively ($\mathrm{Re}_\tau = 110$). It is also interesting that the control input of suboptimal control with spanwise shear is remarkably similar to a neural network control architecture based on the same quantity (Lee, Kim, Babcock, et al., 1997). A different view on wall-based control can be obtained from the vorticity field, and Koumoutsakos (1999) showed that a manipulation of the wall-vorticity flux through blowing and suction can result in DR as large as 40% at low Reynolds numbers.

A fundamental challenge of opposition control, and in fact of any control scheme that acts on the near-wall region, is the Reynolds number scaling of the targeted structures and the resulting resolution requirements for the control hardware. As mentioned earlier, the structures of the near-wall cycle scale in inner units, which decrease as Re_τ increases. The viscous length and time scales at technologically relevant Reynolds numbers are microscopic ($O(\mu m)$ and $O(\mu s)$, respectively), which poses severe

challenges for the practical realization of control hardware (Abbassi et al., 2017). A handful of studies raise hope that control of the near-wall region is feasible even if the actuation input is limited to significantly larger (and more practical) length scales (Choi, Moin, and Kim, 1994; Schoppa and Hussain, 1998). However, it is important to point out that these studies were conducted at relatively low Reynolds numbers as well. Another promising approach to avoid the resolution problem is to abandon the near-wall region all-together and target the flow in the log-region instead. The experimental and numerical challenges associated with higher Reynolds number flows have rendered such studies impossible until recently, but first ideas have now been explored, even if with limited success (e.g. Abbassi et al., 2017; Ibrahim, Guseva, and Garcia-Mayoral, 2020). The lesser known dynamics of the log region complicate the formulation of effective control objectives, and the larger distance from the wall complicates wall-based actuation. In addition, the cost of DNS at moderate Reynolds numbers still precludes exploration of large parameter spaces for control design.

1.2.2 Passive Control

Passive control techniques are easier to implement in practice than active closed-loop schemes, because they do not require flow information and do not involve moving parts. However, they trade simplicity for effectiveness in the sense that the achievable drag reduction is typically lower than with active schemes.

An important class of passive control strategies are carefully patterned surfaces, so-called riblets. The riblet geometry is typically aligned with the streamwise direction so as to not obstruct the mean flow, and a well-defined spanwise shape (rectangle, triangle, etc.) provides resistance to the near-wall cross-flow. Riblets have been tested in numerical simulations and experiments, with maximum DR of the order 10% (among many e.g. Walsh and Lindemann, 1984; Choi, Moin, and Kim, 1993; Bechert et al., 1997; García-Mayoral and Jiménez, 2011). The performance of riblets strongly depends on the details of their geometry, but a robust feature is the initial occurrence of a so-called viscous regime in which drag reduction increases with riblet size, up to a geometry-dependent optimum size after which the performance deteriorates and eventually results in a drag increase. The breakdown of the viscous regime seems to be associated to some extent with the failure of large riblets to inhibit the quasi-streamwise vortices, and to a larger extent with the appearance of spanwise coherent rollers above the riblet tops (Choi, Moin, and Kim, 1993; García-Mayoral and Jiménez, 2011; Chavarin and Luhar, 2020).

A similar drag reduction mechanism is observed for a range of anisotropic permeable materials. Specifically, a material with large streamwise and small spanwise permeability provides little obstruction to the streamwise mean flow, but suppresses the cross-flow in the near-wall region, very analogous to the riblet geometry. A recent DNS study showed that suitably designed anisotropic materials can reduce drag by up to 25% at low Reynolds numbers (Gómez-de-Segura and García-Mayoral, 2019). For equal spanwise and wall-normal permeabilities, which are chosen to be proportional to but much smaller than the streamwise permeability, the DR initially increases linearly with permeability (analogous to the viscous regime of riblets), until it reaches a maximum and then deteriorates. The deterioration coincides with the appearance of spanwise rollers (Gómez-de-Segura and García-Mayoral, 2019), again analogous to flow over riblets. The appearance of spanwise rollers seems to be related to the relaxation of the impermeability condition, since similar rollers are also observed in isotropic permeable materials and porous materials, which are permeable only in the wall-normal direction (Jiménez, Uhlmann, et al., 2001; Breugem, Boersma, and Uittenbogaard, 2006; Efstathiou and Luhar, 2018). Both cases result in a large drag increase as well.

We conclude the discussion of passive control techniques with a short review of compliant walls, which are flexible surfaces that deform under and modify the surrounding flow. Their design parameter space is quite large, and tested configurations include spring-damper supported plates, which are purely driven by wall pressure (e.g. Xu, Rempfer, and Lumley, 2003), and anisotropic compliant walls, which are driven by wall pressure as well as wall-shear stress fluctuations (e.g. Koumoutsakos, 1999). The literature results are inconclusive as to whether compliant walls can achieve turbulent drag reduction (Lee, Fisher, and Schwarz, 1993; Xu, Rempfer, and Lumley, 2003; Fukagata, Kern, et al., 2008; Kim and Choi, 2014), but a few observations are fairly robust and will be interesting for later comparison. Stiff walls are not able to modify the turbulent flow and do therefore not lead to a significant drag change (Xu, Rempfer, and Lumley, 2003; Kim and Choi, 2014). Soft walls on the other hand are susceptible to a resonance mechanism between the flexible wall and the flow, which leads to downstream traveling spanwise-constant wall deformations. The near-wall flow changes significantly under this type of deformation and results in a pronounced form and skin friction drag increase (Kim and Choi, 2014). While somewhat reminiscent of the spanwise rollers discussed in the context of riblets and permeable walls, it is important to keep in mind that these deformations are a function of the flow and the wall material properties. Another interesting

aspect is the conjectured drag reduction mechanism of purely pressure driven compliant walls: unlike riblets or porous surfaces, which reduce drag by obstructing the cross flow, it is believed that such deformable surfaces reduce drag by inducing a wall-normal velocity above the wall which then counteracts the streamwise vortices, analogous to the opposition control scheme. This interpretation is supported by Kang and Choi (2000), who showed that drag reduction with compliant walls is possible if their deformation is based on the opposition control or suboptimal control law instead of pressure. However, the inconclusive literature results on drag reduction indicate that it is difficult to reproduce a similar control effect if the wall deformation is based on the wall pressure. Xu, Rempfer, and Lumley (2003) attribute the difficulty to an inherently different phase relation between wall velocity and pressure in both control scenarios. A quasi-streamwise vortex likely creates a high wall pressure in the downwash region and a low wall pressure in the upwash region, see fig. 1.3. Under opposition control, the downwash is countered with a positive wall-normal velocity, so that pressure and wall-normal velocity are both positive, or in-phase (the same is true with opposite sign in the upwash region). On the other hand, most compliant walls depress below the high pressure region and induce a negative wall-normal velocity, so that pressure and vertical velocity have opposite sign and are out-of-phase. One would therefore have to design a compliant wall that induces a positive wall-normal velocity in high pressure regions instead, but this does not seem to be possible and may indicate a fundamental limitation for this type of compliant wall (Xu, Rempfer, and Lumley, 2003).

1.3 Low-Order Modeling

The robustness and energetic importance of coherent structures raises hopes that perhaps they are elemental building blocks of turbulence, whose superposition gives rise to the complex flow patterns observed in the real world. A natural question to ask then is whether one can formulate a simplified flow model that reproduces these elemental building blocks and, in extension, the key physical mechanisms of the flow. The discovery of coherent structures, new mathematical tools, and an unprecedented amount of experimental and numerical data have spurred enormous interest in the area of low-order flow modeling for well over the last decade. Broadly speaking, low-order models can be classified into data-driven approaches, which aim to extract important flow features and build models from flow data alone, and equation-based approaches, which aim to derive models from the governing equations themselves. The distinction is not sharp in the sense that some of the data-driven and equation-

based approaches are formally related, at least under certain assumptions, and the combination of both approaches can often lead to synergies. In this study we will utilize low-order models for flow control design, and by the very nature of the problem we will not have data about the controlled flow available. We therefore limit our approach and this review to the equation-based models, which require minimal data input. The first part of the review addresses low-order models for canonical (uncontrolled) flows, while the second part summarizes literature results about low-order models for flow control.

1.3.1 Canonical Flows

Research efforts over the past 25 years have shown that linear mechanisms play a key role in the transition to turbulence (among others Trefethen et al., 1993; Jovanović and Bamieh, 2005) and in the dynamics of fully-developed wall-bounded turbulent flows (for example Kim and Lim, 2000). Most of the equation-based low-order models aim to shed light on these linear mechanisms through an analysis of the linearized Navier-Stokes operator. Formally, the governing equations are linearized about a turbulent mean velocity profile, and either the natural (unforced) or forced response of the resulting system are analyzed (Schmid, 2007). Canonical turbulent mean profiles are thought to be linearly stable (Reynolds and Tiederman, 1967), so that the first class of problems focuses on the transient growth characteristics of the linearized Navier-Stokes operator. Various studies have shown that the optimal perturbations to the transient problem resemble the streaky flow motions in the near-wall and logarithmic region (Butler and Farrell, 1993; Del Álamo et al., 2004). Even though these results reproduce important features of wall-bounded turbulent flows, the conceptual link between the optimal initial value problem and the turbulent steady state is not necessarily obvious. A second class of problems therefore considers the response of the linearized system to continuous forcing, which can either be stochastic (e.g. Hwang and Cossu, 2010) or have specific frequency content (Zare, Jovanović, and Georgiou, 2017).

Of particular importance for this study is the resolvent interpretation of the forced linearized Navier-Stokes system, which identifies the nonlinear terms as intrinsic forcing and seeks modes (basis functions) that are most amplified by the linear dynamics (McKeon and Sharma, 2010). Past studies have shown that this framework is able to reproduce many of the key structural and statistical features of wall-bounded turbulent flows (e.g. McKeon and Sharma, 2010; Sharma and McKeon, 2013; Moarref, Jovanović, et al., 2014). The resolvent basis can be improved by

accounting for some nonlinearity, for example through the incorporation of an eddy viscosity (e.g. Morra, Semeraro, et al., 2019; Symon, Illingworth, and Marusic, 2021; Pickering et al., 2021) or a subset of nonlinear interactions in case of a periodic mean flow (Padovan, Otto, and Rowley, 2020). An interesting special case is the resolvent operator of turbulent channel flow, which along the lines of modal stability analysis can be split into an Orr-Sommerfeld and Squire operator. The decomposition also results in an improved resolvent basis and hints at a competition between the contribution of the Orr-Sommerfeld and Squire modes (Rosenberg and McKeon, 2019; McMullen, Rosenberg, and McKeon, 2020).

1.3.2 Controlled Flows

The large cost of DNS, which limits numerical studies to low Reynolds numbers and often precludes the exploration of large parameter spaces, motivates the use of low-order models for flow control. In particular, low-order models may enable analysis and synthesis controllers at technologically relevant Reynolds numbers, which are currently not tractable with DNS.

The insight that linear mechanisms play a key role in wall-bounded turbulence has popularized the use of linear system theory for turbulent flow control, and the approaches can again be classified based on whether they study the natural or forced response of the system. For example, Lim and Kim (2004) used a singular value analysis to assess the effect of opposition control on optimal initial disturbances to the linearized Navier-Stokes equations. In agreement with previous DNS results, their analysis shows that the growth of the disturbances, which is interpreted as a proxy for turbulence intensity, decreases for a narrow range of sensor locations y_d^+ and increases if the sensor is located too far away from the wall. In a similar manner, Duque-Daza et al. (2012) used the linearized Navier-Stokes equations to study how streamwise-traveling waves of spanwise wall velocity affect the energy amplification of initial perturbations that resemble elongated streamwise vortices. Their results indicate a strong correlation between the change in energy amplification of the initial perturbation, and the drag reduction observed in DNS for traveling waves of various frequencies and wavelengths. With regards to the forced response, the resolvent approach has recently been extended to various control configurations, which include opposition control (Luhar, Sharma, and McKeon, 2014b), suboptimal control (Nakashima, Fukagata, and Luhar, 2017), compliant walls (Luhar, Sharma, and McKeon, 2015), riblets (Chavarin and Luhar, 2020), and permeable walls (Chavarin, Gómez-de-Segura, et al., 2021). Typically, these studies consider the

control effect on individual resolvent modes and show that the amplification changes at energetically important wave number combinations follow the drag reduction trends that were already known from DNS.

Studies that evaluate resolvent-based control designs in DNS are scarce and remain inconclusive for wall-bounded flows. For example, Kawagoe et al. (2019) used the resolvent formulation to design a modified version of the suboptimal control law, but the agreement between resolvent and DNS was mixed: the study considered two modified controllers, and while the resolvent was able to correctly predict the DNS flow response for one of them, the approximation was poor in the other case. We also note that the resolvent framework has been used to design control for other classes of flows, such as airfoils (Yeh and Taira, 2019) or open-cavity flows (Leclercq et al., 2019).

1.4 Thesis Objectives and Outline

The above discussion shows that the flow control problem is far from being solved, even after decades of active research. For example, the study and design of flow control schemes at technologically relevant Reynolds numbers remains an open challenge. Direct numerical simulations have become an indispensable tool for the development of flow control approaches at low Re_τ, but our current DNS capabilities are well below the technologically relevant Reynolds number regime. The literature data show that the flow physics become significantly more complex with increasing Re_τ, and it may not come as a surprise that the performance of control schemes developed at low Reynolds numbers typically deteriorate with Re_τ. The control design problem can therefore not be reduced to the low Reynold number regime accessible by DNS. A first step towards control at high Reynolds numbers would therefore be the development of novel design tools that capture the essential flow physics in this flow regime. Of course, these tools have to be computationally tractable to be of any use, and ideally they would be cheap to evaluate, which enables large parameter sweeps in the design process.

Other open questions exist even in the low Reynolds number regime. The discussion of active and passive control approaches showed that many schemes rely on some form of wall transpiration for actuation. This is strictly speaking true for opposition control, but the notion of wall transpiration applies at least conceptually to a much broader class of schemes. For example, if one considers a wall-parallel plane located at the riblet tops or at the interface with a permeable substrate as a surrogate domain

boundary, then the notion of wall transpiration also applies to these configurations. The literature results suggest that control through wall transpiration can attenuate the near-wall cycle and achieve drag reduction for some controller parameters or surface geometries. However, for different parameters, the control schemes trigger large spanwise rollers, which produce a significant drag increase. It remains unclear if these different control strategies leading similar phenomena can be subsumed under a unifying wall-transpiration framework, or if they have to be considered separate problems.

The goal of the present thesis is to contribute towards the two aforementioned open questions, which can be summarized succinctly as follows: i) what are suitable controller design tools for high Reynolds number flows? ii) how does actuation through closed-loop wall transpiration change the flow physics? We will study these questions through a combination of direct numerical simulations and modal analyses. The starting point is previous work by Luhar, Sharma, and McKeon (2014b), who used resolvent analysis to study opposition control in a turbulent pipe flow. Their analysis suggests that the controller performance can be increased if a phase shift is introduced between the Fourier transformed sensor measurement and actuator response, but this model prediction has not been validated in DNS yet. The first part of the study contributes to the first question and assesses whether the resolvent framework is a suitable tool for flow control design by example of this generalized opposition control scheme (which we will denote varying-phase opposition control hereafter). Specifically, we repeat the pipe flow calculations of Luhar, Sharma, and McKeon (2014b) for a channel geometry and compare the resolvent drag reduction prediction for a wide range of parameters with DNS calculations. The DNS results will show that the phase shift between the sensor measurement and actuator response encodes how the flow responds to the wall transpiration. Depending on the phase shift, the wall transpiration can suppress or amplify the near-wall cycle, or it can trigger spanwise rollers. These patterns are reminiscent of the flow response to passive control. The second part of the study will concern question number two and demonstrate that these flow patterns can be understood as the response of individual scales to various phase shifts.

The thesis is structured as follows: Chapter 2 gives a formal problem definition and introduces the methods used in this study. The assessment of the resolvent model for flow control design at low Reynolds numbers along with an analytical scaling that enables cheap evaluation of the model at high Re_τ are presented in Chapter 3. We

then switch gears and analyze how individual scales respond to wall transpiration with phase shifts in two steps: Chapter 4 gives an overview of the structural and spectral features of a few select controlled flows, and Chapter 5 outlines the physical mechanisms that underlie the observed behavior. Chapter 6 presents some evidence that the drag changes can be understood from a pressure perspective, and Chapter 7 summarizes the findings and outlines future research directions.

Chapter 2

METHODS

The thesis objectives outlined in the previous section will be studied with a combination of direct numerical simulation and modal analyses of a low Reynolds number turbulent channel flow. The present chapter formally introduces these methods and further outlines statistical tools to analyze flow data. We start the discussion with an overview of the relevant governing equations and a mathematical problem statement (section 2.1). We then outline the framework to solve the governing equations numerically (section 2.2), and discuss statistical tools to analyze the flow data (section 2.3). The modal analysis techniques are introduced last in section 2.4.

2.1 Mathematical Problem Formulation

This section provides a mathematical problem statement and summarizes important analytical results and techniques. We start the discussion with an overview of the governing equations (section 2.1.1), and description of the channel geometry (section 2.1.2). Relevant analytical results for turbulent channel flow are summarized in section 2.1.3, and the Fourier transforms, which will be used heavily in this study, are defined in section 2.1.4.

2.1.1 Governing Equations

This study concerns the incompressible flow of a Newtonian fluid. The equations governing the fluid flow can be obtained from the conservation laws of mass and momentum, which result in a set of partial differential equations (PDEs for short) known as Naiver-Stokes equations (abbreviated as NSE hereafter)

$$\frac{\partial \boldsymbol{u}}{\partial t} + \boldsymbol{u} \cdot \nabla \boldsymbol{u} = -\nabla p + \frac{1}{\mathrm{Re}} \nabla^2 \boldsymbol{u} \tag{2.1a}$$

$$\nabla \cdot \boldsymbol{u} = 0 \tag{2.1b}$$

with appropriate initial and boundary conditions. Bold symbols in eq. (2.1) denote vector quantities, while plain symbols represent scalars: $\boldsymbol{u} = [u_1, u_2, u_3]$ is the velocity vector, t denotes time, and p is pressure. It is important to note that velocity and pressure themselves are not conserved quantities, and are therefore commonly referred to as "primitive variables." All physical quantities in eq. (2.1) are made dimensionless with a reference length scale L and velocity scale U, which together

with the kinematic viscosity ν of the fluid define the Reynolds number $\mathrm{Re} = UL/\nu$. The Reynolds number parametrizes the family of solutions for a given boundary geometry and initial condition, in the sense that any combination of U, L, and ν that gives rise to the same Re is described by the same nondimensional solution (see e.g. Batchelor, 2000, Chapter 4.7 for more details). The appropriate choice of reference length and velocity scale is problem-dependent and will be specified in section 2.1.2.

The NSE can also be expressed in terms of other flow variables. For example, taking the curl of eq. (2.1a) gives the NSE in vorticity form

$$\frac{\partial \boldsymbol{\omega}}{\partial t} - \nabla \times \underbrace{(\boldsymbol{u} \times \boldsymbol{\omega})}_{=\boldsymbol{H}} = \frac{1}{\mathrm{Re}} \nabla^2 \boldsymbol{\omega} \tag{2.2}$$

where $\boldsymbol{\omega} = \nabla \times \boldsymbol{u} = [\omega_1, \omega_2, \omega_3]$ is the vorticity vector, and $\nabla \times \boldsymbol{H}$ subsumes the advection and vortex stretching term. Note that the pressure does not appear in the vorticity formulation, which indicates that the pressure in incompressible flow is not a thermodynamic quantity that contributes to the evolution of the flow field. Instead, it is an implicit dynamic variable that adjusts itself such that the flow is divergence-free at all times. The nature of pressure complicates the numerical solution of the NSE in primitive variables (see Canuto et al., 1988, chapter 7 for details), and pressure-free vorticity formulations are therefore advantageous for numerical purposes. However, the presence of boundaries poses a challenge for the vorticity formulation, because boundary conditions are typically expressed in terms of the velocity field, not the vorticity field. Several approaches for translating the velocity boundary conditions to vorticity exist and a summary can be found in Cottet and Koumoutsakos (2000) (Chapter 6).

The most straight-forward approach is to recast eq. (2.2) into the so-called velocity-vorticity form, which is well-known from the stability literature (see e.g. Schmid and Henningson, 2001, Chapter 3) To this end, we retain the second component of eq. (2.2) and take a linear combination of derivatives of the first and third component. The linear combination can be recast into a fourth order equation for u_2, and for a Cartesian coordinate system $\boldsymbol{x} = [x_1, x_2, x_3]$, the final result reads

$$\begin{aligned} \frac{\partial}{\partial t}\omega_2 &= \frac{\partial H_1}{\partial x_3} - \frac{\partial H_3}{\partial x_1} + \frac{1}{\mathrm{Re}}\nabla^2\omega_2 \\ \frac{\partial}{\partial t}\nabla^2 u_2 &= -\frac{\partial}{\partial x_2}\left(\frac{\partial H_1}{\partial x_1} + \frac{\partial H_3}{\partial x_3}\right) + \left(\frac{\partial^2}{\partial x_1^2} + \frac{\partial^2}{\partial x_3^2}\right) H_2 + \frac{1}{\mathrm{Re}}\nabla^4 u_2. \end{aligned} \tag{2.3}$$

It will be shown in section 2.2.1 that boundary conditions for u_2 and ω_2 at a solid wall are readily available. Further note that the remaining velocity and vorticity components can be obtained from the incompressibility constraint (2.1b) and the definition of ω_2 once the wall-normal velocity and vorticity are known.

As mentioned earlier, the pressure is not required to determine the evolution of the vorticity field and does not appear in eqs. (2.2) and (2.3). However, the pressure can be recovered from a separate equation, known as the pressure Poisson equation, which is obtained by taking the divergence of eq. (2.1a)

$$\nabla^2 p = -\nabla \cdot (\boldsymbol{u} \cdot \nabla \boldsymbol{u}) \,. \tag{2.4}$$

Note that the equation is forced by the (known) velocity field and is time-independent, which reflects the nature of pressure as a dynamic variable that adjusts itself instantaneously. The pressure Poisson equation has to be supplied with appropriate boundary conditions, which are obtained by evaluating the momentum equation at the domain boundary. A more detailed description of the boundary conditions will be given in the following section.

2.1.2 Geometry

The governing equations of the previous section are usually studied in a particular domain, and throughout this study, we consider a channel geometry, which is shown in fig. 2.1. In this configuration, a fluid flows between two parallel plates, which are represented by the shaded rectangles and which are spaced $2h$ apart. As mentioned earlier, h is usually referred to as channel half-height and is one of the characteristic length scales of this geometry. The flow is driven by a possibly time-dependent pressure gradient, which aligns with one of the wall-parallel directions. That direction is referred to as streamwise direction, while the wall-parallel direction perpendicular to it is dubbed the spanwise direction. Theoretical studies typically assume infinitely large plates, while computational studies use finite plates and periodic boundary conditions to mimic the infinite extent. The present study is computational, so that the channel domain is finite with streamwise and spanwise length L_x and L_z, respectively. We use a Cartesian coordinate system with coordinate vector $\boldsymbol{x} = [x, y, z] = [x_1, x_2, x_3]$, which contains the streamwise (x, x_1), wall-normal (y, x_2), and spanwise (z, x_3) directions. The corresponding velocity and vorticity vectors are $\boldsymbol{u} = [u, v, w] = [u_1, u_2, u_3]$ and $\boldsymbol{\omega} = [\omega_x, \omega_y, \omega_z] = [\omega_1, \omega_2, \omega_3]$, respectively. The origin of the coordinate system is at the channel center, so that the walls are located at $y_w/h = \pm 1$.

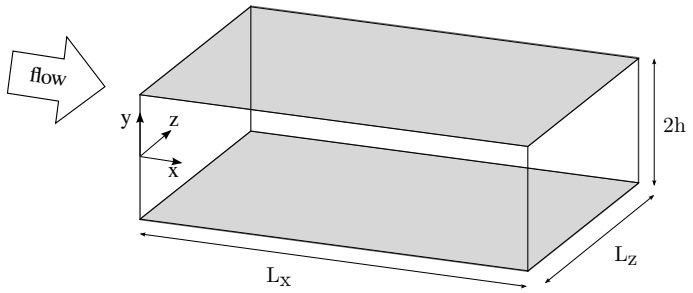

Figure 2.1: Definition of the channel geometry used in this study. The streamwise, wall-normal, and spanwise coordinate are denoted by x, y, and z, respectively.

The geometry also imposes boundary conditions on the flow field, which will be discussed next. We first consider the velocity boundary conditions and then turn our attention to the pressure field. The boundary conditions for the velocity field are periodic in the streamwise and spanwise direction

$$\begin{aligned} \boldsymbol{u}(x + L_x, y, z, t) &= \boldsymbol{u}(x, y, z, t) \\ \boldsymbol{u}(x, y, z + L_z, t) &= \boldsymbol{u}(x, y, z, t) \end{aligned} \tag{2.5}$$

to mimic the infinite extent of the plates. The fluid motion in the vertical direction is constrained by the presence of the wall, which is much more restricting in comparison. The wall-parallel velocities obey the no-slip condition

$$u(x, y_w, z, t) = w(x, y_w, z, t) = 0, \tag{2.6}$$

and a general Dirichlet boundary condition is prescribed for the vertical velocity at the wall

$$v(x, y_w, z, t) = g(\boldsymbol{x}, t, \boldsymbol{u}). \tag{2.7}$$

Equation (2.7) recovers the no-through condition of a canonical channel flow if $g(\boldsymbol{x}, t, \boldsymbol{u}) = 0$. However, the bulk of this study will concern flows with $g(\boldsymbol{x}, t, \boldsymbol{u}) \neq 0$, which physically means that the no-through condition is replaced with some form of wall transpiration. We are particularly interested in the case of closed-loop wall transpiration, where $v(y_w)$ depends on the flow state $\boldsymbol{u}$. An example for this type of boundary condition is the opposition control law discussed in eq. (1.1). The closed-loop boundary conditions of interest in this study will be introduced in section 3.2.

The boundary conditions for the pressure field are more subtle and require careful consideration. The pressure is not periodic in the streamwise direction due to the mean gradient that drives the flow. In addition, it will be shown later that the

instantaneous spanwise pressure gradient in a numerical simulation may be nonzero as well, so that the pressure field is not periodic in the spanwise direction either. The analytical results presented in section 2.1.3 will clarify the x and z dependence of the pressure field and allow the definition of appropriate boundary conditions in these directions. However, we note that the pressure gradient is periodic in the streamwise and spanwise direction, which follows from eq. (2.5) and a subtraction of the momentum equations evaluated at x_i and $x_i + L_i$, where $i = \{x, z\}$. A boundary condition for the pressure at the wall can be derived from the momentum equation. The wall-normal component of eq. (2.1a) gives a Neumann boundary condition for the pressure field, while a linear combination of the tangential components results in a Dirichlet boundary condition (after a Fourier transform in x and z). We follow the vast majority of the literature and use the Neumann condition, which in the presence of wall transpiration reads

$$\begin{aligned}\frac{\partial p}{\partial y}(y_w) &= \frac{1}{\mathrm{Re}}\nabla^2 v(y_w) - \frac{\partial v}{\partial t}(y_w) \\ &= \frac{1}{\mathrm{Re}}\left(\frac{\partial \omega_z}{\partial x}(y_w) - \frac{\partial \omega_x}{\partial z}(y_w)\right) - \frac{\partial v}{\partial t}(y_w).\end{aligned} \tag{2.8}$$

Note that in the absence of wall transpiration, i.e. $v(y_w) = 0$, eq. (2.8) recovers the boundary condition of the canonical channel (see e.g. Kim, 1989)

$$\frac{\partial p}{\partial y}(y_w) = \frac{1}{\mathrm{Re}}\frac{\partial^2 v}{\partial y^2}(y_w). \tag{2.9}$$

It is important to point out that the solution of the Dirichlet and Neumann problem may be different (Moin and Kim, 1980). Whether this is true for the flows considered in this study has not been analyzed yet and should be addressed in future work.

We next summarize very briefly the characteristics of the known NSE solutions (analytical or numerical) for the canonical channel flow. An analytical, so-called laminar solution can be found in the idealized scenario of steady, two-dimensional flow with no streamwise variation. This is the solution shown earlier in fig. 1.1a. The streamwise velocity is the only nonzero component of this laminar solution and has a parabolic profile in the wall-normal direction. The laminar solution becomes linearly unstable at $\mathrm{Re}_c = U_c h/\nu \approx 5772$, where $U_c = u(y = 0)$ is the velocity at the centerline of the channel (Orszag, 1971). We note that transition may also occur subcritically, since the linearized NSE for channel flow are non-normal, which implies that substantial energy amplification can occur even in the linearly stable flow regime (see e.g. Schmid and Brandt, 2014). The details of the transition process

are not relevant for this study; the important point is that both transition scenarios in general result in a turbulent flow, characterized by an unsteady three-dimensional flow field with a broad range of spatial and temporal scales (see fig. 1.1b). This is the flow state that is typically observed in experiments (e.g. Laufer, 1948; Schultz and Flack, 2013) and numerical simulations (e.g. Kim, Moin, and Moser, 1987; Lee and Moser, 2015) at large enough Reynolds numbers. We note that special nonlinear solutions, whose complexity falls in-between the laminar and turbulent state, can be computed numerically. They are usually referred to as exact coherent states and are important for the dynamical system interpretation of turbulence. However, they are unstable at sufficiently large Reynolds numbers, and it is thus unlikely that they can be realized in an experiment or time-marching simulation (see Kawahara, Uhlmann, and Veen, 2012, for more details). The present study only concerns the fully turbulent regime, and the other flow states will not be considered subsequently.

We conclude this section with a discussion of the characteristic velocity and length scales for a turbulent channel flow. We have already encountered the channel half-height h, which is the length scale imposed by the geometry, and the centerline velocity U_c, which characterizes the velocity field in the core flow region. Together they define the centerline Reynolds number Re_c. However, the turbulent flow field varies in space and time, so that the centerline velocity has to be defined in a statistical sense. To this end, we introduce various averages, which will be used throughout this study to define statistical flow quantities. In this context, the symbol $\langle f \rangle$ denotes the average of an arbitrary flow quantity $f(x, y, z, t)$, and the terms average and mean are used interchangeably. A frequently used average is the wall-parallel mean, which is defined as

$$\langle f \rangle_{x,z}(y, t) = \frac{1}{L_x L_z} \int_0^{L_x} \int_0^{L_z} f(x, y, z, t) \, \mathrm{d}x \, \mathrm{d}z. \tag{2.10}$$

Note that we indicate the averaged coordinates in the subscript to the angular brackets. Similarly, one can average a flow quantity in time

$$\langle f \rangle_t(x, y, z) = \lim_{T \to \infty} \frac{1}{T} \int_{t_0}^{t_0+T} f(x, y, z, t) \, \mathrm{d}t. \tag{2.11}$$

The temporal mean is used most often in conjunction with the wall-parallel average, and their concatenation is the spatio-temporal mean

$$\overline{f}(y) = \langle f \rangle_{x,z,t}(y). \tag{2.12}$$

For notational compactness, we follow the literature convention and denote the spatio-temporal mean with an overbar.

The appropriate notion of U_c in the turbulent channel flow is now given by the spatio-temporal mean at the centerline

$$U_c = \overline{u}(y = 0). \tag{2.13}$$

Note that averaging is implied for statistical velocity and length scales, so that we omit the angular brackets or the overbar for compactness, unless they are needed to distinguish different types of averages. Another commonly used velocity scale is the bulk velocity U_b, which quantifies the instantaneous mass flux through the channel. It is obtained by integrating $\langle u \rangle_{x,z}$ in the wall-normal direction

$$U_b(t) = \frac{1}{2} \int_{-1}^{1} \langle u \rangle_{x,z} \, \mathrm{d}\left(\frac{y}{h}\right). \tag{2.14}$$

The bulk velocity can be used to define the bulk Reynolds number $\mathrm{Re}_b = 2U_b h/\nu$, which will be shown to be particularly relevant for numerical simulations. Note that the definition of the bulk Reynolds number has an additional factor of two compared to Re_c. Finally, the viscous or inner scales introduced earlier are based on the mean wall-shear stress $\overline{\tau}_w$

$$\overline{\tau}_w = \frac{1}{\mathrm{Re}} \frac{\mathrm{d}\overline{u}}{\mathrm{d}y}(y_w). \tag{2.15}$$

Note that the time-averaged wall-shear stress is denoted by an overbar, so that it can be distinguished from its instantaneous counterpart. The friction velocity u_τ is defined as

$$u_\tau = \sqrt{\overline{\tau}_w} \tag{2.16}$$

where the possibly somewhat unfamiliar definition without fluid density is a consequence of the normalization, and the viscous length scale l_v is given by

$$l_v = \nu/u_\tau. \tag{2.17}$$

Variables normalized with the viscous length and velocity scale are denoted by a superscript +, as already mentioned in the Introduction. The friction velocity (or, equivalently l_v) together with the channel half-height define the friction Reynolds number $\mathrm{Re}_\tau = u_\tau h/\nu$. Note that the wall-shear stress and viscous scales are statistical quantities.

2.1.3 Analytical Results

We next consider a few analytical results for turbulent channel flow that will be important for the subsequent discussion. These results follow from the governing

equations and the averages defined in eqs. (2.10) to (2.12). Interested readers may also refer to Chapter 5 of Tennekes and Lumley (1972) for more details about the derivation and an in-depth discussion of the material.

We first consider the velocity-vorticity formulation of the NSE in eq. (2.3) and derive an analytical expression for the (instantaneous) spatial mean of the two state variables v and ω_y. The definition of the wall-normal vorticity

$$\omega_y = \frac{\partial u}{\partial z} - \frac{\partial w}{\partial x} \tag{2.18}$$

together with the periodic boundary conditions of the velocity field in x and z imply that the wall-parallel mean of ω_y is identically zero at all wall-normal locations and times

$$\langle \omega_y \rangle_{x,z}(y,t) = 0. \tag{2.19}$$

Similarly, an integration of the continuity equation (2.1b) in the wall-parallel directions reveals that the (instantaneous) mean vertical velocity is constant across the channel

$$\frac{\partial \langle v \rangle_{x,z}}{\partial y} = 0. \tag{2.20}$$

The constant is set by the boundary condition eq. (2.7), as can be seen by integrating the above equation from the wall to a wall-normal location inside the flow

$$\langle v \rangle_{x,z}(y,t) = \langle v \rangle_{x,z}(y_w,t) = 0. \tag{2.21}$$

The constant is zero for a no-through wall, but nonzero values would be possible in case of wall-transpiration, the only constraint being that the values at the top and bottom wall are identical. A nonzero constant would imply a mean mass flux in the wall-normal direction, which is undesired for the purpose of the present study. We therefore explicitly set the constant to zero even in the case of wall transpiration, as indicated by the last equality of eq. (2.21).

Next, we consider the wall-normal component of the momentum equation (2.1a), which can give some insight into the pressure field. After averaging in the streamwise and spanwise direction, the equation reads

$$\frac{\partial}{\partial y}\langle vv \rangle_{x,z}(y,t) = -\frac{\partial}{\partial y}\langle p \rangle_{x,z}(y,t) \tag{2.22}$$

where eq. (2.21) is required to see that the time-derivative and viscous term drop out. It is important to note that the y-derivative of eq. (2.22) recovers the wall-parallel mean of the pressure Poisson equation (2.4), so that the two averaged equations are

redundant. The indefinite integral of eq. (2.22) introduces a yet to be determined function ζ, which can depend on all coordinates except y

$$\langle p \rangle_{x,z}(y,t) = -\langle vv \rangle_{x,z}(y,t) + \zeta(x,z,t). \tag{2.23}$$

The function ζ is constrained by the streamwise and spanwise mean momentum equations, in which it has to produce the mean pressure gradients. A suitable form is

$$\zeta(x,z,t) = \Pi_x(t)x + \Pi_z(t)z + p_0(t) \tag{2.24}$$

where Π_x and Π_z are the mean streamwise and spanwise pressure gradients, which are at most a function of time, and $p_0(t)$ is an (undetermined) background pressure. Note that any p_0 added to a permissible pressure field produces another pressure field that satisfies all governing equations and boundary conditions. The reason for this is that the NSE only constrain the pressure gradient, not the pressure itself. As a consequence, the pressure Poisson equation is ill-posed and p_0 has to be fixed to obtain a unique solution. Further note that Π_x and Π_z are time-dependent in the above equations, and an overbar will be used to denote their time averages. The full pressure field is therefore given by

$$p(x,y,z,t) = p_0(t) - \langle vv \rangle_{x,z}(y,t) + \Pi_x(t)x + \Pi_z(t)z + p'(x,y,z,t). \tag{2.25}$$

The pressure fluctuations p' have zero wall-parallel mean (any non-zero contribution could be absorbed into p_0) and are typically modeled as periodic in x and z (see e.g. Kim, 1989).

Finally, we consider the streamwise momentum equation, which will give further insight into the stress profile across the channel. Averaging the streamwise component of eq. (2.1a) in x, z and using eq. (2.25) gives

$$\frac{\partial}{\partial t}\langle u \rangle_{x,z}(y,t) + \frac{\partial}{\partial y}\langle uv \rangle_{x,z}(y,t) = -\Pi_x(t) + \frac{1}{\mathrm{Re}}\cdot\frac{\partial^2}{\partial y^2}\langle u \rangle_{x,z}(y,t) \tag{2.26}$$

If the bulk velocity (or equivalently mass flux) of the channel is held constant, which will be the case for the numerical simulations considered in this study, then the integral of eq. (2.26) from the wall to the centerline shows that the mean pressure gradient is balanced by the mean wall-shear stress at any instant in time

$$\underbrace{\frac{1}{\mathrm{Re}}\frac{\partial \langle u \rangle_{x,z}}{\partial y}(t)\bigg|_{y/h=-1}}_{=\tau_w(t)} = -\Pi_x(t). \tag{2.27}$$

Note that τ_w above denotes the time-dependent wall-shear stress (no overbar). The instantaneous balance between τ_w and Π_x also holds in the presence of control, as long as the mean Reynolds stress at the wall is zero at all times, which will be true for all flow configurations considered in this study. The time average of eq. (2.26) is given by

$$\frac{\mathrm{d}}{\mathrm{d}y}\overline{uv}(y) = -\overline{\Pi}_x + \frac{1}{\mathrm{Re}}\frac{\mathrm{d}^2\overline{u}}{\mathrm{d}y^2}(y) \tag{2.28}$$

and its integral from the wall to an arbitrary wall-normal location in the flow reveals that the total stress varies linearly across the channel

$$\frac{1}{\mathrm{Re}}\frac{\mathrm{d}\overline{u}}{\mathrm{d}y}(y) - \overline{uv}(y) = -\overline{\tau}_w y. \tag{2.29}$$

The slope is given by the time-averaged wall-shear stress, which is a consequence of eq. (2.27). The definition of the friction velocity, eq. (2.16), further implies that the total stress profiles for different Re_τ collapse if u_τ is used as characteristic velocity scale

$$\frac{1}{\mathrm{Re}_\tau}\frac{\mathrm{d}\overline{u^+}}{\mathrm{d}y}(y) - \overline{u^+v^+}(y) = -y. \tag{2.30}$$

2.1.4 Fourier Domain Representation

Besides the physical-domain representation, we will often turn to a Fourier decomposition in the wall-parallel coordinates to numerically solve the governing equations and analyze the results. The forward Fourier transform of a generic flow quantity f in the streamwise and spanwise direction is defined as

$$\hat{f}(l,m,y,t) = \frac{1}{L_x L_z}\int_0^{L_x}\int_0^{L_z} f(x,z,y,t)\, e^{-i\left(l\frac{2\pi}{L_x}x + m\frac{2\pi}{L_z}z\right)}\,\mathrm{d}x\,\mathrm{d}z \tag{2.31}$$

where we have reordered the coordinates to highlight the transformed directions. Fourier coefficients and other complex quantities will be labeled with a superscript hat from now on, in order to distinguish them from their physical-domain and real counterparts. Recall that the domain is periodic in x and z, with period L_x and L_z, respectively. The periodicity restricts the streamwise (k_x) and spanwise wave number (k_z) to integer multiples of the fundamental wave number, $k_x = l\ (2\pi/L_x)$, $k_z = m\ (2\pi/L_z)$ with $\{l,m\} \in \mathbb{Z}$. A single Fourier mode can be characterized by its streamwise and spanwise indices $[l,m]$, its spatial wave number vector $\boldsymbol{\kappa} = [k_x, k_z]$, or its spatial wavelength vector $\boldsymbol{\lambda} = [\lambda_x, \lambda_z]$, where $\lambda_i = 2\pi/k_i$ for $i = \{x,z\}$. All three descriptors are equivalent and will be used interchangeably. Note that the Fourier coefficient at a particular wave number combination is a function of the wall-normal coordinate and time.

The inverse transform is given by the Fourier series

$$f(x,z,y,t) = \sum_{l=-\infty}^{\infty} \sum_{m=-\infty}^{\infty} \hat{f}(l,m,y,t)\, e^{i\left(l\frac{2\pi}{L_x}x + m\frac{2\pi}{L_z}z\right)}. \tag{2.32}$$

The discrete nature of the inverse transform is also a consequence of the spatial periodicity, which reduces the integral of the general Fourier transform to a sum.

We will occasionally also transform the time coordinate to Fourier domain, in particular in the context of modal analyses, which will be introduced in section 2.4. The temporal coordinate lacks periodicity and therefore transforms differently than the spatial directions. The missing periodicity implies a continuous temporal frequency ω, and necessitates to use the general (integral) form of the Fourier transform. The forward transform is defined as

$$\hat{f}(\omega,x,y,z) = \frac{1}{2\pi} \int_{-\infty}^{\infty} f(t,x,y,z)\, e^{i\omega t}\, \mathrm{d}t \tag{2.33}$$

and includes the normalization factor $1/(2\pi)$. The corresponding backwards transform is given by

$$f(t,x,y,z) = \int_{-\infty}^{\infty} \hat{f}(\omega,x,y,z)\, e^{-i\omega t}\, \mathrm{d}\omega. \tag{2.34}$$

As written in eqs. (2.33) and (2.34), the temporal transform is applied in isolation. However, the temporal transform is only used in conjunction with the spatial transforms in this study, and only in the context of modal analyses. A quantity that has been transformed in all three coordinates will be characterized by the wave number triplet $\boldsymbol{k} = [k_x, k_z, \omega] = [\boldsymbol{\kappa}, \omega]$. If $k_x \neq 0$ we will occasionally also characterize the Fourier coefficient in terms of wave speed $c = \omega/k_x$ rather than ω. Note that the Fourier coefficients at each $\boldsymbol{k}$ are a function of the wall-normal coordinate only. It is also important to point out that the sign convention of the complex exponential is different for the spatial and temporal transforms. This is a deliberate choice, so that Fourier modes with positive k_x and ω can be interpreted as downstream propagating structures with positive wave speed $c = \omega/k_x$.

An important property of the Fourier transform of real-valued functions is an induced symmetry in wave number space, which is usually referred to as Hermitian symmetry. It relates the Fourier coefficients at negative wave numbers to the coefficients at the corresponding positive wave numbers and follows directly from the definition of the transform. For example, applying the spatial transform to an

arbitrary real-valued function $f(x, y, z, t)$ and comparing the Fourier coefficients at $\boldsymbol{\kappa} = [k_x, k_z]$ and $-\boldsymbol{\kappa}$ reveals that

$$\hat{f}(-\boldsymbol{\kappa}) = \hat{f}^*(\boldsymbol{\kappa}). \tag{2.35}$$

This symmetry is not particular to $\boldsymbol{\kappa}$ and applies to any transform coordinate, including time. It also holds for any number of transformed directions, as long as $\boldsymbol{\kappa}$ in eq. (2.35) is replaced with the corresponding wave number vector. Flow quantities like velocity or pressure are real-valued functions in the physical domain and their Fourier transforms are therefore Hermitian symmetric.

2.2 Direct Numerical Simulation

The majority of the data presented in this study are obtained from direct numerical simulation (DNS) of the full nonlinear NSE in a channel domain. DNS resolves all dynamically relevant scales of the flow and therefore provides a numerical solution of the NSE without further modeling assumptions. Two different numerical solvers are used in this study and introduced in this section. The first one integrates the velocity-vorticity form of the NSE in time, and is described in section 2.2.1. A second solver is used to recover the pressure field in postprocessing, and its details are given in section 2.2.2.

2.2.1 Navier-Stokes Solver

We first outline the solver for the Navier-Stokes equations, which is based on the code framework developed by Flores and Jiménez (2006). The numerical method follows the formulation of Kim, Moin, and Moser (1987) and solves the NSE in the velocity-vorticity form of eq. (2.3) by integrating the wall-normal vorticity and the Laplacian of the vertical velocity in time.

We start the discussion with the discretization of the three spatial coordinates and time. The periodic wall-parallel directions (x and z) are discretized by means of a spectral Fourier-Galerkin method, and the nonlinear term $\boldsymbol{H}$ in eq. (2.3) is evaluated pseudospectrally. The pseudospectral evaluation can be summarized as follows: use a discrete inverse Fourier transform to recover $\boldsymbol{u}$ and $\boldsymbol{\omega}$ in physical space, evaluate $\boldsymbol{H}$ by point-wise multiplication, and transform the result back to Fourier domain. This must be done carefully in order to prevent aliasing and the code framework uses a method known as the 3/2-rule to dealise the transforms. The basic idea of this approach is to evaluate the discrete Fourier transforms on a finer grid and zero-pad the missing wave numbers, which cancels the aliasing error. Interested readers may

refer to Canuto et al. (1988) (Chapter 3) for more details. The wall-normal direction is discretized by a finite difference method based on a sinusoidal mesh with a grid stretching factor to control the clustering of grid points near the wall (see e.g. Lee and Moser, 2015). Compact finite difference schemes with five point stencils are used to discretize the wall-normal derivatives on this mesh. The first derivative operator has fourth-order accuracy and is optimized to reduce phase errors at high wave numbers (see Flores and Jiménez, 2006, for details). The second derivative operator on the other hand has sixth-order accuracy, but no phase error optimization is done in this case. It should be noted that the fourth order equation (2.3) for v can be split into two second order equations for $\nabla^2 v$ and v, respectively, so that y-derivatives of order higher than two are not required. Finally, a third-order low-storage Runge-Kutta scheme is used to advance the solution in time. The nonlinear terms are treated explicitly, while the viscous terms are integrated implicitly, and the time step size is adjusted based on a Courant-Friedrichs-Lewy (CFL) condition to ensure numerical stability.

It is important to point out that the wall-parallel mean of eq. (2.3) does not carry any information. Recall that $\langle v \rangle_{x,z} = \langle \omega_y \rangle_{x,z} = 0$ due to eqs. (2.19) and (2.21), and the streamwise and spanwise derivatives that otherwise allow to back out the missing flow variables all vanish. A different strategy is therefore required to advance the mean flow in time, and the DNS instead integrates the mean streamwise and spanwise momentum equation, which can be written in term of $\boldsymbol{H}$ as well

$$\begin{aligned} \frac{\partial}{\partial t}\langle u \rangle_{x,z} + \langle w\omega_y \rangle_{x,z} - \langle v\omega_z \rangle_{x,z} &= -\Pi_x + \frac{1}{\mathrm{Re}}\frac{\partial^2}{\partial y^2}\langle u \rangle_{x,z} \\ \frac{\partial}{\partial t}\langle w \rangle_{x,z} + \langle v\omega_x \rangle_{x,z} - \langle u\omega_y \rangle_{x,z} &= -\Pi_z + \frac{1}{\mathrm{Re}}\frac{\partial^2}{\partial y^2}\langle w \rangle_{x,z}. \end{aligned} \tag{2.36}$$

Note that the equation for $\langle v \rangle_{x,z}$ need not be integrated, because it is identically zero. Equation (2.36) is also important because it illustrates how the mean flow is driven. Recall from our earlier discussion that the mean pressure gradients Π_x and Π_z induce the mean flow, and they have to be chosen therefore as part of the simulation setup. Two options are common in the literature: the first option is to fix the pressure gradient to a constant, for example $\Pi_x = C$ and $\Pi_z = 0$. This configuration is known as "fixed pressure gradient" for obvious reasons and implies a constant wall-shear stress (recall eq. (2.27)) and Re_τ, but a time-dependent bulk velocity (mass flux). The other option is to fix the bulk velocity, which is known as the "fixed mass flux" configuration, and implies a time-dependent mean pressure gradient and wall-shear

stress. The present code framework is driven by a fixed mass flux, so that

$$\begin{aligned} U_b &= C \neq 0 \\ W_b &= 0. \end{aligned} \tag{2.37}$$

Above, C is a suitable constant and W_b is defined analogous to eq. (2.14). The DNS setup is therefore best characterized by its bulk Reynolds number, which remains constant over time. For all simulations in this study, we use $\mathrm{Re}_b = 5600$, which results in an $\mathrm{Re}_\tau \approx 180$ for the canonical flow configuration. Note that the Re_τ based on the instantaneous wall-shear stress is time-dependent, just like the mean pressure gradient, and the above value is a temporal average. Further note that the instantaneous spanwise pressure gradient may be nonzero in order to balance the Reynolds stresses and enforce $W_b = 0$. However, Π_z tends to zero in a time-average sense.

Next, we revisit the discussion of boundary conditions in the context of the DNS code framework. As outlined in Kim, Moin, and Moser (1987), the solution of the NSE in velocity-vorticity form requires boundary conditions for v, $\partial v/\partial y$, and ω_y. The boundary conditions for ω_y follow from its definition (see eq. (2.18)) and the no-slip condition in eq. (2.6)

$$\omega_y(y_w) = \frac{\partial}{\partial z}\underbrace{u(y_w)}_{=0} - \frac{\partial}{\partial x}\underbrace{w(y_w)}_{=0} = 0. \tag{2.38}$$

Similarly, the boundary condition for $\partial v/\partial y$ can be obtained from the continuity equation (2.1b) and the no-slip condition

$$\frac{\partial}{\partial y} v(y_w) = -\left(\frac{\partial}{\partial x}\underbrace{u(y_w)}_{=0} + \frac{\partial}{\partial z}\underbrace{w(y_w)}_{=0} \right) = 0. \tag{2.39}$$

Note that both boundary conditions are zero even in the presence of wall transpiration. The appropriate boundary condition for v was already discussed and is given by eq. (2.7). Further note that the mean flow equations have to be supplied with boundary conditions as well. Those are no-slip, i.e. $\langle u \rangle_{x,z}(y_w) = \langle w \rangle_{x,z}(y_w) = 0$.

We close this section with a discussion of the discretization parameters of the DNS. These are chosen to match the domain size and resolution of previous numerical simulations such as Flores and Jiménez (2006) and Lee and Moser (2015). The size of the computational domain in the streamwise and spanwise direction is $L_x = 4\pi h$ and $L_z = 2\pi h$, respectively, and $N_x = N_z = 256$ Fourier modes are used in these

directions. This corresponds to a resolution of $\Delta x^+ \approx 8.8$ and $\Delta z^+ \approx 4.4$ in terms of Fourier modes before dealiasing at the nominal $\mathrm{Re}_\tau = 180$ of the canonical flow. A sinusoidal grid with $N_y = 172$ points is used in the wall-normal direction, which gives a resolution of $\Delta y^+_{\mathrm{min}} \approx 0.37$ at the wall and $\Delta y^+_{\mathrm{max}} \approx 3.09$ at the channel center. The adequacy of these settings for flows with and without wall transpiration will be confirmed in section 3.3.2. The actuator spectra of fig. 4.4 will further show that the most energetic control scales are typically shorter than or equal to the fundamental wavelength, which suggests that the computational domain is sufficiently large for the purpose of this study. All simulations are started from a fully-developed turbulent flow field at $\mathrm{Re}_\tau = 180$ and statistics are collected over at least 10 eddy turnover times (h/u_τ) once a statistically steady state is reached.

2.2.2 Pressure Solver

Next, we discuss the solver for the pressure Poisson equation (2.4). Recall that the pressure is not required to advance the solution in velocity-vorticity formulation, and the code framework of section 2.2.1 does therefore not solve for p. However, the pressure is still of interest in this study, as will be shown in Chapter 6, and is therefore recovered in postprocessing. A separate Poisson solver was written to this end. The details are given below, but it should be noted that this is an early version with a crude wall-normal discretization that should be improved in the future.

Before introducing the numerical method, it is instructive to revisit the expression for the full pressure field, eq. (2.25), and illustrate its relation to the pressure Poisson equation. Taking the Laplacian of eq. (2.25) reveals that only two terms enter the Poisson equation

$$\nabla^2 p = -\frac{\partial^2}{\partial^2 y}\langle vv \rangle_{x,z} + \nabla^2 p'. \tag{2.40}$$

The absence of the mean pressure gradient terms Π_x and Π_z is consistent with our earlier observation that these terms are determined by the mean momentum equations. The first term in eq. (2.40) can be added to the right-hand side and the pressure Poisson equation therefore only governs the fluctuations

$$\nabla^2 p' = -\nabla \cdot (\boldsymbol{u} \cdot \nabla \boldsymbol{u}) + \frac{\partial^2}{\partial^2 y}\langle vv \rangle_{x,z}. \tag{2.41}$$

The wall-parallel mean of eq. (2.41) is trivially satisfied and reflects its equivalence with the wall-normal mean momentum equation, whose information is already incorporated in the expression for p. Since the pressure fluctuations are assumed to be periodic, eq. (2.41) is best solved using Fourier transforms, which has further

implications. First, the additional term on the right-hand side is constant in x and z, and after a Fourier transform only contributes to the equation for the mode $\boldsymbol{\kappa} = \mathbf{0}$. Second, it will be shown in eq. (2.46) that the equation for $\boldsymbol{\kappa} = \mathbf{0}$ corresponds to the wall-parallel mean of the Poisson equation, which does not have to be solved since it is trivially satisfied. In other words, the Fourier-transformed pressure Poisson equation for the fluctuations is no different from the original formulation of eq. (2.4), except that the mode $\boldsymbol{\kappa} = \mathbf{0}$ does not have to be solved for. The following discussion therefore only regards the fluctuations, and we drop the prime for notational convenience.

We next consider the numerical discretization. Again, the pressure fluctuations are periodic in x and z, and we therefore discretize the streamwise and spanwise direction with the same pseudospectral Fourier Galerkin method used in the NSE solver. The nonlinear forcing term in eq. (2.41) is evaluated in physical domain, and the 3/2-rule is used to dealise the discrete Fourier transforms. The stretched sinusoidal mesh of the NSE solver is used in the wall-normal direction and the second derivative operator in y is approximated by a central finite difference scheme with three point stencil, which at each $\boldsymbol{\kappa} \neq \mathbf{0}$ reads

$$\frac{\mathrm{d}^2}{\mathrm{d}y^2}\hat{p}(y_j) \approx A_j\hat{p}(y_{j-1}) + B_j\hat{p}(y_j) + C_j\hat{p}(y_{j+1}) \tag{2.42}$$

where $\{y_j\}_{j=0}^{N_y-1}$ denotes the wall-normal grid. The coefficients are given by

$$\begin{aligned} A_j &= \frac{2}{\Delta y_j(\Delta y_j + \Delta y_{j+1})} \\ B_j &= -\frac{2}{\Delta y_j \Delta y_{j+1}} \\ C_j &= \frac{2}{\Delta y_{j+1}(\Delta y_j + \Delta y_{j+1})} \end{aligned} \tag{2.43}$$

where $\Delta y_j = y_j - y_{j-1}$. Note that the coefficients are different at each mesh point, since the grid is non-uniform. The local truncation error of this scheme is $O(\Delta y_j)$ for a non-uniform mesh, which improves to $O(\Delta y^2)$ for the special case of a uniform grid.

The mesh points on the wall, y_0 and y_{N_y-1}, require special attention, because one function value in each stencil is not available ($\hat{p}(y_{-1})$ and $\hat{p}(y_{N_y})$, respectively). A standard approach for finite difference methods with Neumann boundary data is to introduce so-called ghost points outside of the domain, and use the Neumann data to approximate the function value at the ghost points. Once those function values are

known, the interior stencil can also be used at the boundaries. In the present case, we need two ghost points, y_{-1} and y_{N_y}, i.e. one for each wall. The ghost points are created symmetrically about the walls so that, for example, $y_0 - y_{-1} = y_1 - y_0$. The function values at the ghost points are then approximated as

$$\begin{aligned}\hat{p}(y_{-1}) &= \hat{p}(y_1) - 2\Delta y_1 \frac{\mathrm{d}\hat{p}}{\mathrm{d}y}(y_0) + O(\Delta y_1^3) \\ \hat{p}(y_{N_y}) &= \hat{p}(y_{N_y-2}) + 2\Delta y_{N_y-1} \frac{\mathrm{d}\hat{p}}{\mathrm{d}y}(y_{N_y-1}) + O(\Delta y_{N_y-1}^3).\end{aligned} \tag{2.44}$$

Applying the interior scheme and using the ghost points gives the following approximation at the domain boundaries

$$\begin{aligned}\frac{\mathrm{d}^2\hat{p}}{\mathrm{d}y^2}(y_0) &\approx B_0\hat{p}(y_0) + (A_0 + C_0)\hat{p}(y_1) - \frac{2}{\Delta y_1}\frac{\mathrm{d}\hat{p}}{\mathrm{d}y}(y_0) \\ \frac{\mathrm{d}^2\hat{p}}{\mathrm{d}y^2}(y_{N_y-1}) &\approx (A_{N_y-1} + C_{N_y-1})\hat{p}(y_{N_y-2}) + B_{N_y-1}\hat{p}(y_{N-1}) + \frac{2}{\Delta y_{N_y-1}}\frac{\mathrm{d}\hat{p}}{\mathrm{d}y}(y_{N_y-1})\end{aligned} \tag{2.45}$$

with A_j, B_j, and C_j according to eq. (2.43), and the pressure boundary conditions from eq. (2.8). Note that the local truncation error of this approximation is also $O(\Delta y_j)$.

Section 6.2 will show that the current solver reproduces literature data of canonical channel flow and is appropriate for postprocessing purposes. However, a more accurate solver would be preferable, especially if the pressure were no longer a passive variable. An example for this scenario would be if the pressure were used to inform the wall transpiration.

2.3 Statistical Analysis

After describing the numerical solvers to generate flow data, we introduce the statistical tools to analyze them. Sections 2.3.1 and 2.3.2 outline different averages, which define the first and second order flow statistics. The spatial power spectra, which will be used to quantify how much each scale contributes to the second order moments, are defined in section 2.3.3. The symbols f and g are used throughout this section as placeholder for any component of the velocity vector $\boldsymbol{u}$ or pressure. It is also important to keep in mind that fully-developed turbulent channel flow is statistically homogeneous in x and z, and stationary in time. Furthermore, the channel is statistically symmetric about the centerline and averaging over symmetric planes in y is implied in all definitions.

2.3.1 Averages

We start the discussion by introducing various spatial and temporal averages, which represent the first order flow statistics. Recall that the terms mean and average are used interchangeably.

We first consider two different spatial averages. The first one, the wall-parallel mean $\langle f \rangle_{x,z}$, was already defined in eq. (2.10). It is important to note that the spatial mean corresponds to the (spatial) Fourier coefficient at the wave number combination $[l = 0, m = 0]$

$$\langle f \rangle_{x,z}(y,t) = \hat{f}(l = 0, m = 0, y, t) \tag{2.46}$$

which follows from a comparison of eqs. (2.10) and (2.31). A second type of spatial average will be used for periodic quantities, which are characterized by their wavelength λ_x. If more than one wavelength occurs in the flow domain, an average over all wavelengths can be computed, which is usually referred to as phase average

$$\langle f \rangle_{\lambda_x}(x,y,z,t) = \frac{1}{N_\lambda} \sum_{j=0}^{N_\lambda - 1} f(x + j\lambda_x, y, z, t) \tag{2.47}$$

where $N_\lambda = L_x/\lambda_{xc}$ is the number of wavelengths in the flow domain. As written above, the phase average is taken in the streamwise direction, but the same procedure could be applied to the spanwise direction. Note that the phase average is still a function of all coordinates, but the averaged one is restricted to a single wavelength, i.e. $x \in [0, \lambda_x]$ above.

Flow quantities are often also averaged in time. The temporal average $\langle f \rangle_t$ was defined in eq. (2.11), and we note that there is again a relation to the (temporal) Fourier coefficients

$$\langle f \rangle_t(x,y,z) = \hat{f}(\omega = 0, x, y, z). \tag{2.48}$$

Finally, the spatio-temporal mean $\overline{f}$ is obtained by averaging in the wall-parallel directions and time. The definition is given in eq. (2.12) and the relation to the (spatial and temporal) Fourier coefficients is in this case

$$\overline{f}(y) = \hat{f}(l = 0, m = 0, \omega = 0, y). \tag{2.49}$$

The spatio-temporal mean is used to define the so-called Reynolds decomposition, which is commonly used in turbulence research to express a flow quantity as a sum of a mean, which only depends on the wall-normal coordinate, and fluctuations about that mean

$$f(x,y,z,t) = \overline{f}(y) + f'(x,y,z,t). \tag{2.50}$$

Note that the fluctuations have no spatio-temporal mean by construction.

2.3.2 Variance and Root-Mean-Square Deviation

Next, we consider averages of products like fg, which will introduce the notion of variance and root-mean-square deviation to quantify the fluctuations about the mean. The definition of spatial and temporal averages given in eqs. (2.10) to (2.12) also apply to quadratic products. However, expressing averages of quadratic products in terms of their Fourier coefficients is more complicated, because a multiplication in physical domain implies a convolution in Fourier space. The relation between quadratic averages and Fourier coefficients is known as Parseval's theorem, and for the spatial wave number reads

$$\begin{aligned}\langle fg\rangle_{x,z}(y,t) &= \sum_{l=-\infty}^{\infty}\sum_{m=-\infty}^{\infty} \hat{f}(l,m,y,t)\hat{g}(-l,-m,y,t) \\ &= \sum_{m=-\infty}^{\infty} \Re\left\{\hat{f}(l=0,m,y,t)\,\hat{g}^*(l=0,m,y,t)\right\} \\ &\quad + \sum_{l=1}^{\infty}\sum_{m=-\infty}^{\infty} 2\Re\left\{\hat{f}(l,m,y,t)\,\hat{g}^*(l,m,y,t)\right\}\end{aligned} \tag{2.51}$$

where $\Re\{\hat{f}\}$ denotes the real part of the complex quantity $\hat{f}$, and the second equality holds because of Hermitian symmetry, eq. (2.35). A similar relation holds for the time average

$$\begin{aligned}\langle fg\rangle_t(x,y,z) &= \int_{-\infty}^{\infty} \hat{f}(\omega,x,y,z)\,\hat{g}(-\omega,x,y,z)\,\mathrm{d}\omega \\ &= \int_{0}^{\infty} 2\Re\left\{\hat{f}(\omega,x,y,z)\,\hat{g}^*(\omega,x,y,z)\right\}\,\mathrm{d}\omega,\end{aligned} \tag{2.52}$$

but now involves an integral, because the temporal frequency is continuous. The two relations can also be combined to express the spatio-temporal mean as a convolution integral of the form

$$\overline{fg}(y) = \sum_{l=-\infty}^{\infty}\sum_{m=-\infty}^{\infty}\int_{-\infty}^{\infty} \hat{f}(\boldsymbol{k},y)\hat{g}^*(\boldsymbol{k},y)\,\mathrm{d}\omega, \tag{2.53}$$

and a reduction to a subset of the wave number space analogous to the above cases is outlined in appendix B for the special case of modal analysis approximations.

The spatio-temporal mean of the product $f'g'$ corresponds to the covariance, which follows from the definition of the Reynolds decomposition

$$\overline{f'g'}(y) = \overline{fg}(y) - \overline{f}(y)\,\overline{g}(y). \tag{2.54}$$

Note that eq. (2.54) reduces to the variance in the special case $f = g$. Another comment regards the terminology in the turbulence literature. A common scenario in the analysis of turbulent flows is that f and g are both velocity components, in which case the variance and covariance are usually referred to as Reynolds stresses. The fluctuations of a single flow variable about its mean can also be quantified in terms of the root-mean square deviation (abbreviated as rms and sometimes called standard deviation), which is closely related to the variance

$$f_{\mathrm{rms}}(y) = \left(\overline{f'f'}(y)\right)^{1/2} = \left(\overline{f^2}(y) - \left(\overline{f}(y)\right)^2\right)^{1/2}. \tag{2.55}$$

The root-mean square of velocity components is also called turbulence intensity in the literature.

2.3.3 Spectra

The statistical tools introduced so far allow quantification of flow variables in terms of a spatio-temporal mean and fluctuations about that mean. Next, we define the spatial power (co-)spectrum, which can be used to quantify how much each scale contributes to the (co-)variance.

The starting point for the discussion is Parseval's theorem for the spatial Fourier coefficients. After taking the time average of eq. (2.51) and defining

$$\tilde{\Phi}_{fg}(l, m, y) = \begin{cases} \Re\left\{\langle \hat{f}(l=0, m, y)\hat{g}(l=0, m, y)\rangle_t\right\} & \text{if } l = 0 \\ 2\Re\left\{\langle \hat{f}(l, m, y)\hat{g}^*(l, m, y)\rangle_t\right\} & \text{else,} \end{cases} \tag{2.56}$$

we can write the spatio-temporal mean of the product fg as

$$\overline{fg}(y) = \overline{f}(y)\overline{g}(y) + \overline{f'g'}(y) = \sum_{l=0}^{\infty}\sum_{m=-\infty}^{\infty} \tilde{\Phi}_{fg}(l, m, y). \tag{2.57}$$

One can think of $\tilde{\Phi}_{fg}(l, m, y)$ as a density of $\overline{fg}$ in wavenumber space. If the absolute value of $\tilde{\Phi}_{fg}$ is large, then the wavenumber combination $[l, m]$ contributes significantly to the spatio-temporal mean. Conversely, if the absolute value of $\tilde{\Phi}_{fg}$ is small, then the contribution of that wavenumber combination is negligible. If $f = g$, then $\tilde{\Phi}_{ff}$ is called the (two-sided) time-averaged spatial power spectrum of f. The power spectrum at each wavenumber is proportional to $\langle|\hat{f}(l, m)|^2\rangle_t$, and $\tilde{\Phi}_{ff}$ is therefore non-negative. If $f \neq g$, then $\tilde{\Phi}_{fg}$ is called the (two-sided) time-averaged spatial co-spectrum of f and g. The co-spectrum can attain positive or negative values, depending on the relative phase of $\hat{f}$ and $\hat{g}$ at each wavenumber

combination. Note that both $\tilde{\Phi}_{ff}$ and $\tilde{\Phi}_{fg}$ are functions of the wavenumbers, but are real-valued quantities (therefore they have no superscript hat).

The two-sided spectra of eq. (2.56) are defined over the half-plane $l \geq 0$. Since the $\pm z$ direction in a turbulent channel flow are indistinguishable in a statistical sense, it is common practice to fold the $m < 0$ part of the spectrum onto the $m > 0$ part. In other words, we introduce the new quantity for $m \geq 0$

$$\Phi_{fg}(l,m,y) = \begin{cases} \tilde{\Phi}_{fg}(l,m,y) & \text{if } m = 0 \\ \tilde{\Phi}_{fg}(l,m,y) + \tilde{\Phi}_{fg}(l,-m,y) & \text{else} \end{cases} \tag{2.58}$$

which allows to express the spatio-temporal mean of fg as

$$\overline{fg}(y) = \overline{f}(y)\overline{g}(y) + \overline{f'g'}(y) = \sum_{l=0}^{\infty}\sum_{m=0}^{\infty} \Phi_{fg}(l,m,y). \tag{2.59}$$

The function $\Phi_{fg}(l,m,y)$ is the one-sided time-averaged cospectrum of f and g, and is preferred over the two-sided spectrum in the literature. The present study will therefore only report one-sided time-averaged spectra and simply refer to them as cospectrum ($f \neq g$) and spectrum ($f = g$), respectively. One special case of eq. (2.59) is important to point out: if either $\overline{f} = 0$ or $\overline{g} = 0$, then the spectrum sums to the covariance $\overline{f'g'}$.

2.4 Modal Analysis

Besides the DNS introduced in section 2.2, which is used to solve the full nonlinear NSE numerically, we will make frequent use of modal analyses to elucidate linear mechanisms that underlie or at least contribute to the flow phenomena observed in DNS. Specifically, we will use two equation-driven modal analysis techniques, the temporal eigenspectrum and resolvent analysis, which are described in more detail in this section.

The starting point for both techniques is a Reynolds decomposition of the NSE in primitive variables, which allows to split eq. (2.1) into an equation for the spatio-temporal mean and an equation for the fluctuations about that mean. The streamwise velocity $\overline{u}(y)$ is the only nonzero mean component in the present channel flow configuration, and is governed by eq. (2.28). For both modal analyses, we will assume that the mean velocity profile is known, for example from an experiment, a numerical simulation, or an eddy-viscosity approximation. More details about the generation and selection of the mean velocity profiles will be given in section 2.4.2.

The problem then reduces to the turbulent fluctuations, which are governed by

$$\begin{aligned}\frac{\partial \boldsymbol{u}'}{\partial t} &= -\overline{u}\frac{\partial \boldsymbol{u}'}{\partial x} + \frac{1}{\mathrm{Re}}\nabla^2\boldsymbol{u}' - v'\frac{\mathrm{d}\overline{u}}{\mathrm{d}y}\boldsymbol{e}_x - \nabla p' + \underbrace{\overline{\boldsymbol{u}'\cdot\nabla\boldsymbol{u}'} - \boldsymbol{u}'\cdot\nabla\boldsymbol{u}'}_{=\tilde{\boldsymbol{f}}(\boldsymbol{u}')} \\ \nabla\cdot\boldsymbol{u}' &= 0\end{aligned} \tag{2.60}$$

where $\boldsymbol{e}_x$ is the unit vector in the streamwise direction. The fluctuation equations have to be supplied with appropriate initial and boundary conditions, which are identical to the ones described in section 2.1.2. Note that the spatio-temporal mean of eq. (2.60) is trivially satisfied, which is to be expected since the fluctuations have zero mean by construction. For notational convenience, we drop the superscript prime from here on and introduce the symbol $\tilde{\boldsymbol{f}} = [f_u, f_v, f_w]$ for the nonlinear terms (in the fluctuations) on the right-hand-side.

Both modal analysis techniques rely on a Fourier-domain representation in (at least) the streamwise and spanwise direction, so that we transform eq. (2.60) in x and z, and rewrite it at each spatial wave number pair $\boldsymbol{\kappa}$ as

$$\frac{\partial}{\partial t}\boldsymbol{M}\hat{\boldsymbol{q}}(y,t) = \boldsymbol{L}(\boldsymbol{\kappa})\hat{\boldsymbol{q}}(y,t) + \hat{\boldsymbol{f}}(\hat{\boldsymbol{q}}) \tag{2.61}$$

where $\hat{\boldsymbol{q}} = (\hat{u}, \hat{v}, \hat{w}, \hat{p})$ and $\hat{\boldsymbol{f}} = [\hat{f}_u, \hat{f}_v, \hat{f}_w, 0]$ denote the state vector and nonlinear advection terms, respectively, $\boldsymbol{M}$ is a weight matrix to enforce the right-hand side of the continuity equation

$$\boldsymbol{M} = \begin{pmatrix} 1 & 0 & 0 & 0 \\ 0 & 1 & 0 & 0 \\ 0 & 0 & 1 & 0 \\ 0 & 0 & 0 & 0 \end{pmatrix} \tag{2.62}$$

$\boldsymbol{L}$ is the linearized Navier-Stokes operator

$$\boldsymbol{L} = \begin{pmatrix} -ik_x\overline{u} + \frac{\Delta}{\mathrm{Re}} & -\frac{\mathrm{d}\overline{u}}{\mathrm{d}y} & 0 & -ik_x \\ 0 & -ik_x\overline{u} + \frac{\Delta}{\mathrm{Re}} & 0 & -\frac{\mathrm{d}}{\mathrm{d}y} \\ 0 & 0 & -ik_x\overline{u} + \frac{\Delta}{\mathrm{Re}} & -ik_z \\ -ik_x & -\frac{\mathrm{d}}{\mathrm{d}y} & -ik_z & 0 \end{pmatrix} \tag{2.63}$$

and $\Delta = \mathrm{d}^2/\mathrm{d}y^2 - k_x^2 - k_z^2$ is the Laplacian. It is important to point out that eq. (2.61) is an exact representation of the full nonlinear fluctuation equations. This particular

formulation is instructive, because it highlights that the nonlinear advection terms can be interpreted as an intrinsic forcing to the remaining linear dynamics of the NSE, which is the view put forward by McKeon and Sharma (2010). The two modal analysis techniques introduced subsequently will approximate the flow state $\hat{\boldsymbol{q}}$ based on an analysis of the linear operators in eq. (2.61). The challenge is that the forcing $\hat{\boldsymbol{f}}$ depends nonlinearly on $\hat{\boldsymbol{q}}$ as well, which at first seems to obstruct further progress. However, previous studies (e.g. McKeon and Sharma, 2010; Sharma and McKeon, 2013; Luhar, Sharma, and McKeon, 2014b) suggest that significant physical insight can be gained from eq. (2.61) if the nonlinear forcing term is modeled, so that it becomes independent of $\hat{\boldsymbol{q}}$, i.e by approximation of the action of the operator. Each modal analysis technique considered subsequently is based on a different forcing model: the temporal eigenspectrum will analyze eq. (2.61) under the assumption $\hat{\boldsymbol{f}} = \boldsymbol{0}$, while resolvent analysis will model $\hat{\boldsymbol{f}}$ as the harmonic forcing that is most amplified by the remaining linear terms.

2.4.1 Interpretation of Modal Analyses

The abundance of modal analysis techniques can easily obscure what aspect of the flow state $\hat{\boldsymbol{q}}$ each method models. Before formally introducing the two modal analysis techniques considered in this study, we therefore provide an intuitive understanding of what each of them tries to achieve. To this end, we consider a variation of eq. (2.61), given by

$$\frac{\mathrm{d}}{\mathrm{d}t}\hat{\boldsymbol{q}}(t) = \boldsymbol{L}(\boldsymbol{\kappa})\hat{\boldsymbol{q}}(t) + \hat{\boldsymbol{f}}(t). \tag{2.64}$$

In this form, the weight matrix is absent, which prevents difficulties associated with the rank deficiency of $\boldsymbol{M}$. One could formally eliminate $\boldsymbol{M}$ from eq. (2.61) by transforming from primitive variables to velocity-vorticity form, so that this is not a significant modification. Of course, the operator $\boldsymbol{L}$ and vectors $\hat{\boldsymbol{q}}$, $\hat{\boldsymbol{f}}$ would change under such a transformation as well, but the details of these objects are not relevant for the purpose of this discussion. We further reduced the system of PDEs (2.61) to a system of ordinary differential equations (ODEs, eq.(2.64)), which can be easily achieved by discretizing the wall-normal coordinate. The one significant difference between eqs. (2.61) and (2.64) is that the forcing $\hat{\boldsymbol{f}}$ is assumed to be independent of $\hat{\boldsymbol{q}}$ in the latter. This assumption is necessary in order to apply tools from ODE theory to the system (2.64), which will lead to an expression that enables an intuitive interpretation of the two modal analysis techniques.

Under the above assumptions, we can find an analytical expression for the solution of eq. (2.64) at each $\boldsymbol{\kappa}$

$$\hat{\boldsymbol{q}}(t) = e^{\boldsymbol{L}(\boldsymbol{\kappa})t}\hat{\boldsymbol{q}}_0 + \int_0^t e^{\boldsymbol{L}(\boldsymbol{\kappa})(t-\tau)}\hat{\boldsymbol{f}}(\tau)\,\mathrm{d}\tau \tag{2.65}$$

where $e^{\boldsymbol{L}(\boldsymbol{\kappa})t}$ is the matrix exponential and $\hat{\boldsymbol{q}}_0$ denotes the initial condition (see e.g. the review by Jovanović, 2021). The first term in eq. (2.65) represents the natural response of the system in the absence of external forcing (note that $\hat{\boldsymbol{f}}$ does not appear in this expression). In contrast, the second term describes the response of the system due to the external forcing $\hat{\boldsymbol{f}}$.

The natural response is fully determined by the temporal eigenspectrum of the linearized Navier-Stokes operator $\boldsymbol{L}$. Its temporal eigenvalues are complex and the amplitude of the associated eigenmodes can therefore grow, decay, or remain constant over time. If all eigenvalues at a particular $\boldsymbol{\kappa}$ are damped, then the natural response of that Fourier mode decays over a sufficiently long time horizon. Moreover, the natural response does not contribute to the long-term dynamics of the system if all eigenvalues at all $\boldsymbol{\kappa}$ are damped. On the other hand, if at least one eigenvalue at a particular $\boldsymbol{\kappa}$ is neutral or amplified, then the natural response does not decay. In particular, Fourier modes with amplified eigenvalues grow over time and the natural response of the system eventually diverges. In the context of modal analyses, we will utilize the temporal eigenspectrum of $\boldsymbol{L}$ to characterize the flow response in the absence of intrinsic nonlinear forcing. The details of this analysis and a discussion of the implications will be given in section 2.4.3. It is important to emphasize that the above conclusions apply to the linear system (2.64). Caution is required when drawing conclusions about the NSE from the eigenspectrum of $\boldsymbol{L}$, because the former is intrinsically nonlinear. Implications of the nonlinearity for the interpretation of the eigenspectrum will also be discussed in section 2.4.3.

Next, we consider the forced response of the linear system, and limit our analysis to the case of damped temporal eigenvalues of $\boldsymbol{L}$. In this scenario, the natural response decays, and the system enters a steady-state response under a given forcing. We are in particular interested in harmonic forcing of the form $\hat{\boldsymbol{f}}(\tau) \propto e^{-i\omega\tau}$, where $\omega \in \mathbb{R}$ is a real frequency. The Fourier transform can then be utilized to rewrite the forced response in eq. (2.65) as (see e.g. review by Jovanović, 2021)

$$\hat{\boldsymbol{q}}(\omega) = \underbrace{(-i\omega\boldsymbol{I} - \boldsymbol{L}(\boldsymbol{\kappa}))^{-1}}_{\mathcal{H}(\boldsymbol{k})}\hat{\boldsymbol{f}}(\omega). \tag{2.66}$$

The operator $\mathcal{H}(\boldsymbol{k})$ that maps the forcing to the state vector is called the resolvent operator. The second modal analysis technique used in this study aims to derive an efficient basis for $\hat{\boldsymbol{q}}$ from a singular value decomposition of the operator $\mathcal{H}(\boldsymbol{k})$. This basis can then be used to study the flow response of the forced (i.e. modeled nonlinear) system under various control configurations. The details of this analysis will be introduced in section 2.4.4.

It is important to note the different temporal behavior implied in the eigenspectrum and resolvent analysis. The frequencies (eigenvalues) of the eigenspectrum are complex, which can lead to temporal growth, decay, or limit cycle behavior. In contrast, resolvent analysis only considers real frequencies and all modes are therefore neutrally stable. The steady state response described by eq. (2.66) is only meaningful if all eigenvalues of the temporal eigenspectrum are damped, so that the natural response decays. The notion of a steady state forced response does not exist if the natural response diverges, and the resolvent is not defined if $\boldsymbol{L}$ has neutrally stable eigenvalues, because $(-i\omega\boldsymbol{I} - \boldsymbol{L})$ is singular at those frequencies. It is also important to emphasize that while the above discussion assumed the forcing vector to be independent of $\hat{\boldsymbol{q}}$, this is not a prerequisite of the resolvent framework. The resolvent operator can equally be defined for the full nonlinear system (2.61), which will be done in section 2.4.4.

2.4.2 Discretization and Mean Profile Selection

The previous section shows that the definition of the temporal eigenspectrum and the resolvent operator are based on spatial differential operators, which have to be discretized for numerical evaluation. Before introducing the two modal analyses in detail, we therefore describe the discretization of $\boldsymbol{L}$, which is identical for both frameworks.

The spatial Fourier transforms implied in eq. (2.61) provide a natural discretization in x and z, and the streamwise and spanwise wave numbers are again constrained to be integer multiples of the fundamental wave number imposed by the domain size. The wall-normal coordinate is discretized by the Chebyshev collocation method described in Weideman and Reddy (2000), and the collocation points can be chosen to correspond to the DNS grid points up to the grid stretching factor. It should be emphasized that the discretized operators incorporate boundary conditions, which are no-slip for the streamwise and spanwise velocity fluctuations (see eq. (2.6)) and Dirichlet boundary conditions for v according to eq. (2.7). A change in boundary

conditions therefore alters the linear operators, which in turn modifies the temporal eigenspectrum of $\boldsymbol{L}$ and singular value decomposition of $\mathcal{H}$.

It is further important to point out that the effect of control enters the modal analyses in two places. First, the no-through boundary condition is relaxed to allow wall transpiration. This can be interpreted as a linear effect of control, which only acts on the wave number combination currently under consideration and which does not require a priori knowledge of the controlled flow. Second, the turbulent mean profile underlying the linearized Navier-Stokes operator $\boldsymbol{L}$ changes when control is applied. This is a nonlinear effect: changes at individual wave numbers alter the mean Reynolds stress, which in turn changes the mean velocity profile through eq. (2.28). A priori knowledge of the controlled flow, namely the modified mean profile, is required to incorporate this effect into the modal analyses.

For both, the temporal eigenspectrum and resolvent analysis of controlled flows, we will consider two problem formulations of increasing complexity: the first one considers the modal analysis about an uncontrolled turbulent mean, but replaces the no-through boundary condition with a nonzero closed-loop wall transpiration. In other words, this first formulation incorporates the change in boundary condition, but neglects changes in the mean. This is a model assumption, with the intention to understand what the minimum required information is to approximate the behavior of the full nonlinear system. The uncontrolled turbulent mean is approximated by the semi-empirical eddy viscosity model proposed by Reynolds and Tiederman (1967), with parameters $\alpha = 25.4$ (constant in the Van Driest wall law) and $\kappa = 0.426$ (constant in the von Kármán logarithmic law). Of course, the uncontrolled mean profiles could also be obtained from DNS, but the eddy viscosity approach is advantageous because it can be easily extended to regimes where DNS or experimental data are not available. The second formulation considers the modal analysis about the controlled turbulent mean with control boundary conditions. That is, the second formulation incorporates both the linear and nonlinear effect of control. The controlled mean profiles are obtained from a DNS with matching transpiration boundary conditions. It is worth noting that the eddy viscosity is only used to approximate the uncontrolled mean profile. It is not incorporated in the linearized Navier-Stokes operator $\mathbf{L}$ when formulating either of the modal analyses. In other words, higher-order effects due to the nonlinear interactions of the fluctuations are neglected in the modal analyses.

2.4.3 Temporal Eigenspectrum

We now introduce the details of the first modal analysis techniques, the temporal eigenspectrum. Formally, the temporal eigenspectrum is derived by linearizing the fluctuation equations about the turbulent mean $\overline{u}(y)$, which is equivalent to setting $\hat{\boldsymbol{f}}(\hat{\boldsymbol{q}}) = \boldsymbol{0}$ in eq. (2.61), and making a normal mode ansatz $\hat{\boldsymbol{q}}(y,t) = \hat{\boldsymbol{q}}(y)e^{-i\hat{\omega}t}$ with complex frequency $\hat{\omega} = \omega_r + i\omega_i$ and $\{\omega_r, \omega_i\} \in \mathbb{R}$. Equation (2.61) then reduces to a temporal eigenvalue problem of the form

$$\boldsymbol{L}(\boldsymbol{\kappa})\hat{\boldsymbol{q}} = -i\hat{\omega}\boldsymbol{M}\hat{\boldsymbol{q}} \tag{2.67}$$

with $\boldsymbol{L}$ and $\boldsymbol{M}$ according to eqs. (2.62) and (2.63), respectively. Equation (2.67) employs the sign convention of the stability literature so that temporal amplification corresponds to $\omega_i > 0$, and results will often be presented in terms of complex wave speed $\hat{c} = \hat{\omega}/k_x = c_r + ic_i$ instead of temporal frequency.

The temporal eigenvalue problem is formulated in primitive variables, and the weight matrix $\boldsymbol{M}$ is singular due the continuity equation, which leads to spurious numerical eigenvalues. Following Jiménez, Uhlmann, et al., 2001 we label eigenvalues as spurious if their value changes significantly for a small change in grid resolution, and spurious eigenvalues are discarded in the analysis. This method was validated against the results of Orszag (1971) for a laminar base profile and excellent agreement was found for $N_y = 201$ collocation points.

Further recall that the eddy viscosity is not incorporated in $\boldsymbol{L}$ to model the effect of Reynolds stresses. An interpretation of eq. (2.67) as stability analysis of the turbulent mean is therefore not valid, even if it looks formally equivalent. Instead, one should think of eq. (2.67) as an eigenvalue problem for $\boldsymbol{L}$, which characterizes the natural response of the unforced (linearized) NSE, as discussed in section 2.4.1. However, caution is required when drawing conclusions about the full NSE from the eigenvalues of $\boldsymbol{L}$, because the former are inherently nonlinear. In particular, the interpretation of amplified eigenvalues about a well-defined turbulent mean profile is challenging due to the discrepancy between the diverging natural response of the linearized equation and the stable nonlinear system. The neglected nonlinearity may have a stabilizing effect in the former, but we will not further address this question here. Damped eigenvalues are less problematic to interpret and indicate that the corresponding eigenmodes of the unforced system are not relevant for the long-term dynamics of the full nonlinear flow.

The boundary conditions are enforced in eq. (2.67) by replacing the linearized fluctuation equations at the wall with the boundary conditions described in eqs. (2.6) and (2.7). A change in boundary condition therefore alters the temporal eigenvalue problem, and our main focus will be on analyzing how the eigenvalues change under closed-loop wall transpiration.

2.4.4 Resolvent Analysis

The second modal analysis used in this study is the resolvent approach of McKeon and Sharma (2010). Under the resolvent formulation, the nonlinear term is viewed as intrinsic forcing to the remaining linear dynamics (see eq. (2.61)), and the goal is to characterize the forced flow response, which corresponds to the turbulent steady state. To this end, a low-order approximation of the flow state $\hat{\boldsymbol{q}}$ is sought by identifying an efficient basis from the resolvent operator.

Formally, we wish to identify in each dimension the basis whose first N functions capture most kinetic energy $|\boldsymbol{u}|^2$ of the flow under an $\mathcal{L}^2$-norm. It can be shown analytically that the Fourier basis is the optimal one in the statistically homogeneous streamwise and spanwise directions and in the stationary temporal coordinate (Holmes, Lumley, and Berkooz, 1996). We therefore start the model development by applying a Fourier transform in those coordinates. Recall that the streamwise and spanwise direction are already transformed in eq. (2.61), so that we only need to apply a transform in time. The forced response can then be written as

$$\hat{\boldsymbol{q}}(y) = \underbrace{\left(-i\omega\boldsymbol{M} - \boldsymbol{L}(\boldsymbol{\kappa})\right)^{-1}}_{\mathcal{H}(\boldsymbol{k})} \hat{\boldsymbol{f}}(\hat{\boldsymbol{q}}, y) \tag{2.68}$$

where $\mathcal{H}(\boldsymbol{k})$ is the resolvent operator, which in contrast to eq. (2.66) includes the mass matrix, and is given by

$$\mathcal{H}(\boldsymbol{k}) = \begin{pmatrix} -i\omega + ik_x\overline{u} - \frac{\Delta}{\mathrm{Re}_\tau} & \frac{\mathrm{d}\overline{u}}{\mathrm{d}y} & 0 & ik_x \\ 0 & -i\omega + ik_x\overline{u} - \frac{\Delta}{\mathrm{Re}_\tau} & 0 & \frac{\mathrm{d}}{\mathrm{d}y} \\ 0 & 0 & -i\omega + ik_x\overline{u} - \frac{\Delta}{\mathrm{Re}_\tau} & ik_z \\ ik_x & \frac{\mathrm{d}}{\mathrm{d}y} & ik_z & 0 \end{pmatrix}^{-1}. \tag{2.69}$$

The optimal basis in the remaining wall-normal direction is obtained from a singular value decomposition of the discretized resolvent operator, and the method described in Luhar, Sharma, and McKeon (2014a) is used to enforce an energy norm within

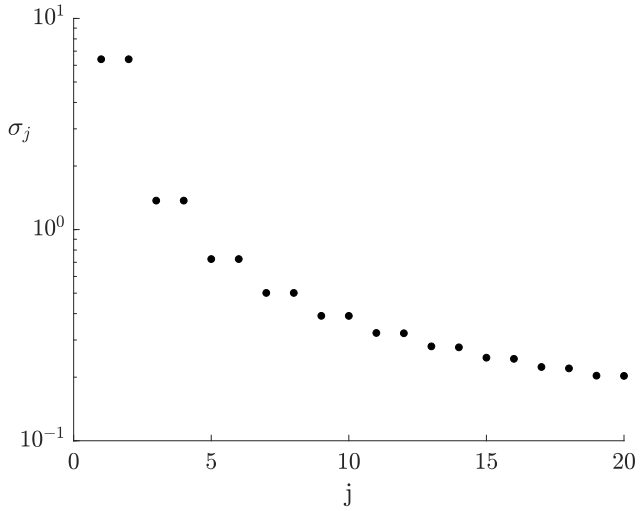

Figure 2.2: The twenty largest singular values σ_j of the canonical channel flow resolvent operator at the wave number combination $[\lambda_x^+ = 2262, \lambda_z^+ = 103, c^+ = 10]$.

the primitive variable formulation. The singular value decomposition returns an ordered basis pair $\{\hat{\boldsymbol{\psi}}_j, \hat{\boldsymbol{\phi}}_j\}$, which can be used to rewrite eq. (2.68) at each $\boldsymbol{k}$

$$\hat{\boldsymbol{q}}(y) = \mathcal{H}(\boldsymbol{k})\hat{\boldsymbol{f}}(\boldsymbol{q}, y) = \sum_{j=1}^{\infty} \sigma_j \hat{\boldsymbol{\psi}}_j(y) \left\langle \hat{\boldsymbol{\phi}}_j(y), \hat{\boldsymbol{f}}(\hat{\boldsymbol{q}}, y) \right\rangle \tag{2.70}$$

where $\sigma_1 \geq \sigma_2 \geq \cdots > 0$ denote the singular values (gains) of $\mathcal{H}$, $\hat{\boldsymbol{\psi}}_j = [\hat{u}_j, \hat{v}_j, \hat{w}_j, \hat{p}_j]$ and $\hat{\boldsymbol{\phi}}_j = [\hat{f}_{uj}, \hat{f}_{vj}, \hat{f}_{wj}, 0]$ are, respectively, the left and right singular vectors (wall-normal basis functions) associated with σ_j and $\langle \cdot, \cdot \rangle$ denotes the $\mathcal{L}^2$-inner product in the wall-normal direction for vector-valued functions. We will refer to the left singular vectors $\hat{\boldsymbol{\psi}}_j$ as resolvent modes hereafter. The basis elements are ranked in order of descending gain, σ_j, and the singular values come in pairs of equal or at least same order of magnitude values, as can be seen from fig. 2.2. This is a peculiarity of the channel geometry and reflects its statistical symmetry about the centerline. The paired singular vectors are not unique (any linear combination of them is also a permissible singular vector) and an additional constraint is required to ensure uniqueness. Following Moarref, Sharma, et al. (2013), we therefore impose an additional wall-normal symmetry constraint on the paired singular vectors, which results in distinct wall-normal symmetries of the resolvent modes: $\hat{u}_j$, $\hat{w}_j$ and $\hat{p}_j$ of the first paired mode are even, while $\hat{v}_j$ is odd in y. The symmetries of all components are inverted for the second mode of the pair. It is important to point out that eq. (2.70) is still an exact representation of the fluctuation equations. In particular, the nonlinearity is retained in $\hat{\boldsymbol{f}}(\hat{\boldsymbol{q}})$, unlike in section 2.4.1.

Previous work has shown that the resolvent operator at each $\boldsymbol{k}$ is low-rank (among others McKeon and Sharma, 2010; Moarref, Sharma, et al., 2013), and owing to the particular choice of bases the low-rank nature is reflected in expansion (2.70): typically, the first two singular values are an order of magnitude larger than the remaining ones, which is shown in fig. 2.2 for the mode $[\lambda_x^+ = 2262, \lambda_z^+ = 103, c^+ = 10]$. It can therefore be assumed that the flow is reasonably approximated by just the first two terms of the expansion. Since almost all singular values are paired and the corresponding singular vectors only differ in their wall-normal symmetry, it is often possible to simplify further and just consider the first singular value and vector, which gives a so-called rank-1 approximation of the operator at each $\boldsymbol{k}$

$$\hat{\boldsymbol{q}}(y) \approx \sigma_1 \hat{\boldsymbol{\psi}}_1(y) \left\langle \hat{\boldsymbol{\phi}}_1(y), \hat{\boldsymbol{f}}(\hat{\boldsymbol{q}}, y) \right\rangle \tag{2.71}$$

It will be shown in section 3.4.2 and appendix C that a rank-1 approximation is indeed sufficient for the purpose of this study.

While the singular values and vectors can be calculated directly from the resolvent, the nonlinear forcing $\hat{\boldsymbol{f}}(\hat{\boldsymbol{q}})$ depends on the flow state $\hat{\boldsymbol{q}}$, which creates a circular dependence. To make further progress, we therefore have to model $\hat{\boldsymbol{f}}(\hat{\boldsymbol{q}})$. It is well-known that the resolvent operator is a very selective amplifier (McKeon and Sharma, 2010) and it is therefore reasonable to assume that the exact form of forcing is irrelevant as long as the real flow contains some forcing in the dominant directions. Note, however, that there is an increasing body of work devoted to determining and modeling the shape of the forcing to accurately reconstruct the flow field (Moarref, Jovanović, et al., 2014; Zare, Jovanović, and Georgiou, 2017; Towne, Schmidt, and Colonius, 2018; McMullen, Rosenberg, and McKeon, 2020; Morra, Semeraro, et al., 2019; Morra, Nogueira, et al., 2021). In the present study, we seek the simplest representation of the forcing that captures the control trends for this system, and therefore we use the so-called rank-1, broadband forcing model $\langle \hat{\boldsymbol{\phi}}_1(y), \hat{\boldsymbol{f}}(\hat{\boldsymbol{q}}, y) \rangle = 1$ instead of the more complex models mentioned above. It is important to emphasize that the resolvent formulation of the NSE with broadband forcing is not a linearization in the sense of small perturbations relative to a fixed point solution. A linearization would set $\hat{\boldsymbol{f}}(\hat{\boldsymbol{q}}) = \boldsymbol{0}$ (as was done for the temporal eigenspectrum), while the rank-1 broadband forcing assumption employed here explicitly retains the nonlinearity and models it as $\hat{\boldsymbol{f}}(\boldsymbol{q}, y) = \hat{\boldsymbol{\phi}}_1(y)$ at all $\boldsymbol{k}$. The resulting rank-1 broadband forcing approximation of the NSE at $\boldsymbol{k}$ is given by

$$\hat{\boldsymbol{q}}(y) \approx \sigma_1 \hat{\boldsymbol{\psi}}_1(y) \tag{2.72}$$

and will be referred to as "resolvent analysis" or "resolvent model" hereafter. We note that this framework was developed in a series of previous publications (McKeon and Sharma, 2010; Moarref, Sharma, et al., 2013; Luhar, Sharma, and McKeon, 2014b), and we validated the present resolvent implementation against results reported therein. Excellent agreement in singular values and vectors was found for $N_y = 172$ collocation points.

The resolvent operator includes boundary conditions, which are enforced by replacing the forced fluctuation equations at the wall with eqs. (2.6) and (2.7). A change in boundary conditions therefore alters the resolvent operator, and our focus will be on analyzing how the singular values and vectors change under closed-loop wall transpiration. The analysis will either focus on individual wave number triplets, or on mean flow quantities, which can be obtained by summing over resolvent modes at different $\boldsymbol{k}$. Interested readers may also refer to Luhar, Sharma, and McKeon (2014b) for an in-depth discussion of the shape and control response of individual resolvent modes.

It is also important to point out that we excluded the mean velocity equation from the model development, because $\overline{u}(y)$ was assumed to be known. The resolvent model is therefore not constrained to satisfy the mean momentum equation. In other words, the mean Reynolds stress resulting from a superposition of resolvent modes is not necessarily compatible with the mean velocity profile in $\mathcal{H}$, some implications of which will be discussed in section 3.4.

Chapter 3

LOW-ORDER MODELS FOR FLOW CONTROL

Portions of this chapter have been previously published in:

Toedtli, S., Luhar, M., and McKeon, B. (2019). "Predicting the response of turbulent channel flow to varying-phase opposition control: Resolvent analysis as a tool for flow control design". In: *Physical Review Fluids* 4 (7), p. 073905. DOI: 10.1103/PhysRevFluids.4.073905.

The literature review in the Introduction showed that turbulent flow control remains a challenging open problem of immense practical importance. Even though the Navier-Stokes equations provide a very accurate model for many fluid systems of practical interest, they are so complex that even their most basic mathematical properties remain inscrutable and their numerical solutions are only feasible for simple geometries and Reynolds numbers well below the technologically relevant regime (Rowley and Dawson, 2017). These challenges limit the usefulness of the NSE for controller design and motivate the development of approximate low-order flow models. The present chapter evaluates the capabilities of one such low-order flow model, which will be referred to as resolvent model hereafter and which is based on the eponymous linear analysis introduced earlier in section 2.4.4. The evaluation is done by the example of the so-called varying-phase opposition control scheme, which is introduced in section 3.2 and applied to a turbulent channel flow at $\mathrm{Re}_\tau = 180$, based on u_τ of the uncontrolled flow. We first conduct a DNS study to evaluate the drag reduction for varying-phase opposition control with different controller parameters (section 3.3). The resolvent model is then used to compute an approximation of the drag reduction over the same parameter range and its capabilities are judged based on the overall agreement between model and DNS drag reduction. These results are presented in section 3.4, together with a strategy to evaluate the resolvent model at technologically relevant Re_τ.

3.1 Prologue: Symmetries in Fourier Domain

Before introducing the control scheme, we revisit the wave number symmetries introduced in section 2.1.4 specifically for the DNS and resolvent model. As will be shown, the resolvent model with broadband forcing has an additional symmetry,

which is an important aspect to keep in mind whenever the resolvent model is linked to DNS or experiments. In the present case, the additional symmetry will have implications for the formulation of the control scheme, as will be shown in section 3.2.

A first wave number symmetry, the so-called Hermitian symmetry, was already introduced in eq. (2.35). Recall that it follows from the properties of the Fourier transform for real-valued quantities (like velocity or pressure) and holds for any number of transformed directions. The symmetry is therefore present in both, DNS data and the resolvent model, but has to be defined with respect to a different wave number vector, since the resolvent framework also transforms time. For DNS, Hermitian symmetry applies to the spatial wave numbers at each instant in time and at each wall-normal location. For example, the velocity vector satisfies $\hat{\boldsymbol{u}}(-\boldsymbol{\kappa}, y, t) = \hat{\boldsymbol{u}}^*(\boldsymbol{\kappa}, y, t)$. The wave number vector for resolvent modes, $\boldsymbol{k} = [k_x, k_z, \omega]$, additionally includes the temporal frequency, and the corresponding relation for resolvent modes is $\hat{\boldsymbol{u}}(-\boldsymbol{k}, y) = \hat{\boldsymbol{u}}^*(\boldsymbol{k}, y)$.

Relation (2.35) is the only (instantaneous) symmetry present in the DNS. The resolvent model on the other hand has an additional symmetry, which relates $\boldsymbol{k} = [k_x, k_z, \omega]$ and $\tilde{\boldsymbol{k}} = [k_x, -k_z, \omega]$, and which follows from the structure of the resolvent operator and the broadband forcing assumption. To see this, consider the resolvent operator $\mathcal{H}$ as defined in eq. (2.69) at $\tilde{\boldsymbol{k}}$. The only difference to $\mathcal{H}(\boldsymbol{k})$ is a sign change in the off-diagonal terms of the last two rows, which can be absorbed into the velocity and forcing vector. This allows reformulating the forcing-response relation at $\tilde{\boldsymbol{k}}$ in terms of the resolvent operator $\mathcal{H}(\boldsymbol{k})$

$$\underbrace{\begin{pmatrix} u(\tilde{\boldsymbol{k}}, y) \\ v(\tilde{\boldsymbol{k}}, y) \\ -w(\tilde{\boldsymbol{k}}, y) \\ p(\tilde{\boldsymbol{k}}, y) \end{pmatrix}}_{=\hat{\boldsymbol{u}}^\dagger(\tilde{\boldsymbol{k}}, y)} = \mathcal{H}(\boldsymbol{k}) \underbrace{\begin{pmatrix} f_u(\tilde{\boldsymbol{k}}, y) \\ f_v(\tilde{\boldsymbol{k}}, y) \\ -f_w(\tilde{\boldsymbol{k}}, y) \\ 0 \end{pmatrix}}_{=\hat{\boldsymbol{f}}^\dagger(\tilde{\boldsymbol{k}}, y)}. \tag{3.1}$$

In general, $\hat{\boldsymbol{f}}^\dagger(\tilde{\boldsymbol{k}}, y) \neq \hat{\boldsymbol{f}}(\boldsymbol{k}, y)$, and the velocity and pressure response $\hat{\boldsymbol{u}}^\dagger(\tilde{\boldsymbol{k}}, y)$ may be different from $\hat{\boldsymbol{u}}(\boldsymbol{k}, y)$. However, the rank-1 broadband forcing assumption sets $\hat{\boldsymbol{f}}^\dagger(\tilde{\boldsymbol{k}}, y) = \hat{\boldsymbol{f}}(\boldsymbol{k}, y) = \hat{\boldsymbol{\phi}}_1(\boldsymbol{k}, y)$, which induces the additional symmetry

$$\hat{\boldsymbol{u}}^\dagger(\tilde{\boldsymbol{k}}, y) = \hat{\boldsymbol{u}}(\boldsymbol{k}, y). \tag{3.2}$$

In the resolvent framework, this holds for any temporal frequency ω. We note that relation (3.2) holds in DNS for the special case $\omega = 0$, at least approximately if a finite time interval is considered. This is because the channel geometry has no preferential orientation in the spanwise direction, which implies that modes with $\boldsymbol{k}$ and $\tilde{\boldsymbol{k}}$ should be equal in a time-average ($\omega = 0$) sense.

Recall that the Fourier coefficients are complex numbers and can be represented in terms of a magnitude and a phase. The symmetries have implications for the physical interpretation of the Fourier coefficient phase. As will be shown next by example of the wall-normal velocity component, the phase in the resolvent framework has a clear physical interpretation, while the interpretation of the phase in DNS data is more complicated because of the missing second symmetry. We first consider the rank-1 resolvent approximation, and write the Fourier coefficient at a fixed y in terms of magnitude and phase, i.e. $\hat{v}_1(\boldsymbol{k}, y) = A_1 e^{i\phi_1}$ with $\{A_1, \phi_1\} \in \mathbb{R}$. Due to the additional symmetry (3.2), we also have $\hat{v}_1(\tilde{\boldsymbol{k}}, y) = A_1 e^{i\phi_1}$. Summing $\hat{v}(\boldsymbol{k})$, $\hat{v}(\tilde{\boldsymbol{k}})$ and their complex conjugates results in a physical-domain structure $v_{\boldsymbol{k}}^{\mathrm{RES}}$ given by

$$v_{\boldsymbol{k}}^{\mathrm{RES}}(x, y, z, t) = 4A_1 \cos(k_x x - \omega t + \phi_1) \cos(k_z z) \tag{3.3}$$

where the factor 4 results from Hermitian symmetry and the trigonometric sum-to-product identity. Further note that eq. (3.3) corresponds to a building block of the inverse spatial Fourier transform (2.32). Due to the symmetries, the phase of the Fourier coefficient only enters the first term, and a nonzero ϕ_1 can be interpreted as a streamwise or temporal shift of the structure. Conversely, the spanwise position of the structure is not affected by a change in ϕ_1.

On the other hand, the instantaneous DNS Fourier coefficients at $\boldsymbol{\kappa} = [k_x, k_z]$ are not related to $\tilde{\boldsymbol{\kappa}} = [k_x, -k_z]$. For example, $\hat{v}(\tilde{\boldsymbol{\kappa}}, t, y) \neq \hat{v}(\boldsymbol{\kappa}, t, y)$, and the missing symmetry in k_z complicates the physical interpretation of the phase. Similarly to before, we write the DNS Fourier coefficients of v at a fixed y in terms of magnitude and phase, i.e. $\hat{v}(\boldsymbol{\kappa}, t, y) = A_1 e^{i\phi_1}$ and $\hat{v}(\tilde{\boldsymbol{\kappa}}, t, y) = A_2 e^{i\phi_2}$, where $\{A_1, A_2, \phi_1, \phi_2\} \in \mathbb{R}$. Summing $\hat{v}(\boldsymbol{\kappa})$, $\hat{v}(\tilde{\boldsymbol{\kappa}})$, and their complex conjugates results again in a physical-domain structure $v_{\boldsymbol{\kappa}}^{\mathrm{DNS}}$ which can also be interpreted as a building block of the spatial inverse Fourier transform

$$\begin{aligned} v_{\boldsymbol{\kappa}}^{\mathrm{DNS}}(x, y, z, t) = {} & 4A_1 \cos\left(k_x x + \frac{\phi_1 + \phi_2}{2}\right) \cos\left(k_z z + \frac{\phi_1 - \phi_2}{2}\right) \\ & + 2(A_2 - A_1) \cos(k_x x - k_z z + \phi_2)\,, \end{aligned} \tag{3.4}$$

where we can assume $A_2 > A_1$ without loss of generality. The first term, for which x and z factor into different trigonometric functions, is the equivalent of $v_{\boldsymbol{k}}^{\mathrm{RES}}$. The

phase of the Fourier coefficients, ϕ_1 and ϕ_2, have a clear physical interpretation for this structure: if the mean of the two phases changes, the structure is shifted in streamwise direction. If their difference changes, the structure is shifted in the spanwise direction. However, the missing symmetry in k_z introduces an additional term with mixed arguments in x and z, which has no counterpart in eq. (3.3). The phase has no clear physical interpretation for this term, because the argument is mixed, so that a change in ϕ_2 can correspond to a streamwise or spanwise shift. We will refer to the second term in eq. (3.4) as "oblique wave" hereafter, even if it does not necessarily have a well-defined wave speed. It is also important to point out that eq. (3.4) is a generalization of eq. (3.3), and the latter can be recovered by setting $A_2 = A_1$ and $\phi_2 = \phi_1$ (i.e. by enforcing the additional symmetry).

3.2 Control Scheme

Next we introduce the control scheme, which provides the foundation for the present and the following chapters. The controller is a generalization of the well-known opposition control scheme, which was introduced in eq. (1.1) and which we will occasionally denote "classical opposition control" to make the distinction clear. In contrast to the original formulation by Choi, Moin, and Kim (1994), who defined the control law for points in physical space, we define the control law for individual Fourier modes. This allows the controller gain $\hat{A}_d$ to be complex (note the superscript hat), so that it not only has an amplitude $|\hat{A}_d|$, but also a phase $\angle\hat{A}_d$. We will term the generalized Fourier domain scheme "varying-phase opposition control," and refer to $\angle\hat{A}_d$ as "phase shift" from here on. The significance of the amplitude has been studied in the past and is reasonably well understood (see e.g. Chung and Talha, 2011; Luhar, Sharma, and McKeon, 2014b). We will therefore assign a fixed value to $|\hat{A}_d|$ and focus on understanding the role of the phase shift. As will be shown, a nonzero $\angle\hat{A}_d$ changes the phase of individual Fourier modes and has an interpretation in the physical domain, which is tied to the symmetries of the Fourier coefficients discussed in section 3.1. The control law is therefore a good example for the importance of these symmetries, and we will have to formulate two slightly different controllers for the resolvent model and DNS to ensure that we study the same physical phenomena in both cases. We first introduce the formulation for the resolvent model and then present the definition for DNS.

3.2.1 Resolvent Model

Varying phase opposition control was first introduced by Luhar, Sharma, and McKeon (2014b) in the context of a resolvent analysis of turbulent pipe flow. They defined the control law as

$$\hat{v}(\boldsymbol{k}, y_w) = -\hat{A}_d(\boldsymbol{k})\hat{v}(\boldsymbol{k}, y_d). \tag{3.5}$$

In general, the controller gain can be a function of the wave number vector, constrained only by Hermitian symmetry. This gives the scheme great flexibility, but also introduces a plethora of tuning parameters. To reduce the complexity of the controller, we consider a special case of eq. (3.5), where we fix $|\hat{A}_d| = 1$ and set $\angle\hat{A}_d$ to a (nonzero) constant in wave number space. The exception are the streamwise-constant modes, for which $\angle\hat{A}_d = 0$. A justification for this choice will be given subsequently. The resulting control scheme is given by

$$\begin{aligned} \hat{v}(\boldsymbol{k}, y_w) &= -\hat{A}_d^{\mathrm{RES}}(\boldsymbol{k})\hat{v}(\boldsymbol{k}, y_d) \\ \hat{A}_d^{\mathrm{RES}}(\boldsymbol{k}) &= \begin{cases} 0 & \text{if } k_x = k_z = 0 \\ 1 & \text{if } k_x = 0, k_z \neq 0 \\ e^{i\phi} & \text{if } k_x > 0 \end{cases} \end{aligned} \tag{3.6}$$

and the superscript RES labels the gain for the resolvent model, which is slightly different from its DNS counterpart. We will refer to eq. (3.6) as the varying-phase opposition control law for the resolvent model from here on and note that a similar scheme was used by Luhar, Sharma, and McKeon (2014b) in their section 3.6. The control scheme (3.6) only has two parameters: the sensor location y_d and the phase shift $\hat{A}_d = \phi$. Note that the definition of A_d^{RES} does not include an expression for $k_x < 0$. This is because the actuator input for $k_x < 0$ is fully determined by $v(y_w)$ at $k_x \geq 0$ and Hermitian symmetry.

It is instructive to write eq. (3.6) in terms of the magnitude and phase of the Fourier coefficients. The magnitude part is trivial and states that the sensor measurement and actuator response are equal in magnitude. The phase part, which can be written as

$$\angle\hat{v}(\boldsymbol{k}, y_w) = \angle\hat{v}(\boldsymbol{k}, y_d) + \pi + \angle\hat{A}_d \tag{3.7}$$

is more insightful. This form of eq. (3.6) shows that the control law takes the phase of the sensor measurement, adds π (sign inversion) and a possible phase shift $\angle\hat{A}_d$ to determine the phase of the actuator input. Note that the phase shift $\angle\hat{A}_d = \phi$ is

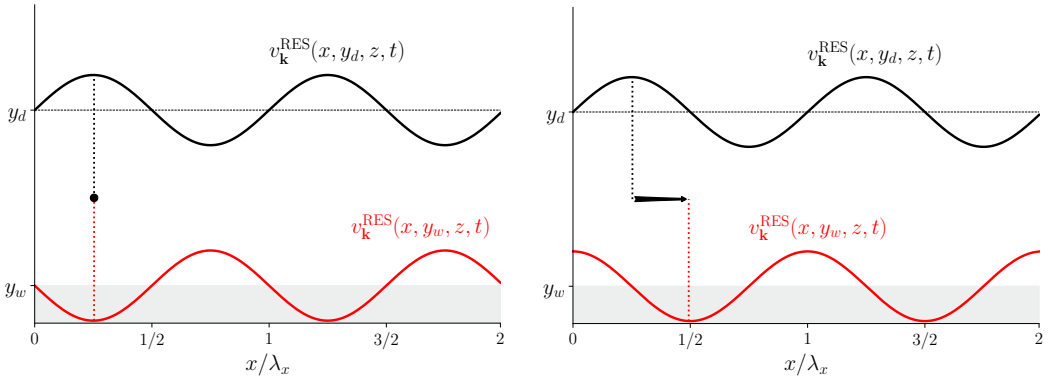

(a) $\angle \hat{A}_d = 0$ (b) $\angle \hat{A}_d = -\pi/2$

Figure 3.1: Interpretation of the phase shift in physical domain. Figure 3.1a shows classical opposition control with no additional phase shift, while fig. 3.1b displays varying-phase opposition control with a negative phase shift. In both figures, the black curve denotes an example sensor measurement of structure $v_{\boldsymbol{k}}^{\mathrm{RES}}$ defined in eq. (3.3), and the red curve is the corresponding actuator response. The shaded gray area indicates the wall and the dashed horizontal line is the sensor location. The vertical lines draw out an example sensor signal maximum and corresponding actuator signal minimum to aid the comparison. The figure shows the situation for fixed z and t, but conceptually applies at all spanwise locations and times.

constant in $\boldsymbol{k}$ and therefore preserves the wave number symmetries of section 3.1, so that the relation $\hat{v}(\tilde{\boldsymbol{k}}, y) = \hat{v}(\boldsymbol{k}, y)$ also holds in the controlled case.

The persistence of the wave number symmetries gives the phase shift a clear physical interpretation. To see this, assume $\hat{v}(\boldsymbol{k}, y_d) = A_1 e^{i\phi_1}$. The sensor measurement in physical space then consists of building blocks according to eq. (3.3) with y replaced by y_d. The actuation consists of the same structures with identical magnitude, but the phase shift changes the argument of the first term in eq. (3.3). For $k_x \neq 0$, we can write

$$v_{\boldsymbol{k}}^{\mathrm{RES}}(x, y_w, z, t) = -4A_1 \cos\left(k_x \left(x + \frac{\angle \hat{A}_d}{k_x}\right) - \omega t + \phi_1\right) \cos\left(k_z z\right) \tag{3.8}$$

where we expressed the π phase difference in eq. (3.7) as a sign inversion. In other words, the phase shift between sensor measurement and actuator response in Fourier domain corresponds to a scale-dependent streamwise shift in physical domain. A visualization of eq. (3.8) for two different phase shifts is shown in fig. 3.1. Figure 3.1a on the left shows the spatial relation between sensor measurement and actuator response of $v_{\boldsymbol{k}}$ for classical opposition control, which corresponds to $\angle \hat{A}_d = 0$. In this case the two structures only differ by their sign, and the maxima of the sensor signal align with the minima of the actuator response as indicated by the dashed

vertical line. On the other hand, the sensor signal and actuator response not only differ by a sign, but are offset in the streamwise direction if $\angle \hat{A}_d \neq 0$. Figure 3.1b illustrates the situation for an example negative phase shift $\angle \hat{A}_d = -\pi/2$. The actuator signal leads the sensor measurement in the streamwise direction in case of a negative phase shift and in this particular case the lead amounts to a quarter wavelength. Contrary, a positive phase shift corresponds to a streamwise lag of the actuator response. The physical interpretation of the phase shift shows that control with eq. (3.6) is related to the work of Lee (2015), who studied opposition control with streamwise shifts between sensor measurement and actuator response. The two controllers are different in that the current one applies a constant shift in Fourier domain, which corresponds to a scale-dependent shift in physical space (see eq. (3.8)), while Lee's scheme applies a constant shift in physical domain, which corresponds to a scale-dependent phase shift in Fourier domain.

The physical interpretation also motivates the special treatment of the $k_x = 0$ modes in eq. (3.6). The interpretation of the phase shift as a displacement in the streamwise direction is by definition lost for streamwise-constant modes. If the temporal frequency content is accessible, as in resolvent analysis, the phase shift at $k_x = 0$ could be interpreted as a temporal lead or lag, which is the point of view taken by Luhar, Sharma, and McKeon (2014b). However, the frequency content is not easily accessible in real time in an experiment or DNS and individual temporal frequencies can not be controlled at present in these settings. The notion of a temporal shift is therefore problematic for the DNS, and consequently no phase shift is applied to $k_x = 0$. For consistency between the two frameworks, we impose this constraint also for the resolvent model in eq. (3.6). Finally, the zero gain for $k_x = k_z = 0$ follows from eq. (2.21) and is a consequence of continuity in the periodic channel domain.

The discussion thus far has focused on the change in boundary condition due to control. It is important to keep in mind that the resolvent framework also requires a mean velocity profile as input. Control can alter the mean velocity nonlinearly, and this effect can possibly be accounted for in the model by choosing a different, controlled mean profile. Unless stated otherwise, we will not pursue this approach here and instead formulate the resolvent model about the eddy viscosity approximation of the uncontrolled mean, which corresponds to the first problem formulation of section 2.4.2. Some implications of the mean flow choice will be discussed in section 3.4.5

3.2.2 DNS

The varying-phase opposition control scheme has not been formulated for DNS before, and we thus need to derive a suitable form first. A straight-forward but somewhat naive approach would be to apply the resolvent model control law eq. (3.6) directly to DNS. The problem with this formulation arises from the missing symmetry in k_z, which introduces additional physics that were not present in the resolvent model. To see this, suppose that $\hat{v}(\boldsymbol{\kappa}, y_d, t) = A_1 e^{i\phi_1}$ and $\hat{v}(\tilde{\boldsymbol{\kappa}}, y_d, t) = A_2 e^{i\phi_2}$, with $A_2 > A_1$. The sensor signal in physical space then consists of building blocks of the form eq. (3.4), with y replaced by y_d. Applying the control law (3.6) to DNS would change the phase of the Fourier coefficients at $\boldsymbol{\kappa}$ and $\tilde{\boldsymbol{\kappa}}$ by $\angle\hat{A}_d$ and result in physical-domain structures of the form

$$\begin{aligned} v_{\boldsymbol{\kappa}}^{\mathrm{DNS}}(x, y_w, z, t) = &4A_1 \cos\left(k_x\left(x + \frac{\angle\hat{A}_d}{k_x}\right) + \frac{\phi_1 + \phi_2}{2}\right)\cos\left(k_z z + \frac{\phi_1 - \phi_2}{2}\right) \\ &+ 2(A_2 - A_1)\cos(k_x x - k_z z + \phi_2 + \angle\hat{A}_d) \end{aligned} \tag{3.9}$$

for $k_x \neq 0$. The phase shift results in a scale-dependent streamwise shift of the first term, as desired. However, note that the phase shift also enters the oblique wave, which has a mixed argument in x and z, and implies that the actuator signal is shifted in the streamwise and spanwise direction. The oblique wave thus forbids to interpret $\angle\hat{A}_d$ as a streamwise-only shift. Previous work has shown that spanwise misalignment between the sensor measurement and actuator input can lead to large drag increase (Chung and Sung, 2003). It is therefore possible that the resolvent model and DNS respond very differently to the control law eq. (3.6), just because the resolvent model is not rich enough to capture all the physics of the real flow. In order to exclude the detrimental effect of spanwise shifts and enable a meaningful comparison with the resolvent model, we wish to eliminate the oblique wave from the control input. This can be achieved by modifying the control gain $\hat{A}_d$, so that the resulting control input satisfies $A_1 = A_2$, which is equivalent to $|\hat{v}(\boldsymbol{\kappa}, y_w, t)| = |\hat{v}(\tilde{\boldsymbol{\kappa}}, y_w, t)|$. Note that the phase of the Fourier coefficients remain unconstrained, so that this is a weaker constraint than the k_z symmetry in the resolvent.

The resulting varying-phase opposition control scheme for DNS, that preserves the

interpretation of $\angle\hat{A}_d$ as streamwise-only spatial shifts, is given by

$$\hat{v}(\boldsymbol{\kappa}, t, y_w) = -\hat{A}_d^{\mathrm{DNS}}(\boldsymbol{\kappa})\hat{v}(\boldsymbol{\kappa}, t-\Delta t, y_d)$$

$$\hat{A}_d^{\mathrm{DNS}}(\boldsymbol{\kappa}) = \begin{cases} 0 & \text{if } k_x = k_z = 0 \\ 1 & \text{if } k_x = 0, k_z \neq 0\,. \\ e^{i\phi} & \text{if } k_x > 0, k_z = 0 \\ \frac{\min(|\hat{v}(\boldsymbol{\kappa},t-\Delta t,y_d)|,|\hat{v}(\tilde{\boldsymbol{\kappa}},t-\Delta t,y_d)|)}{|\hat{v}(\boldsymbol{\kappa},t-\Delta t,y_d)|}e^{i\phi} & \text{if } k_x > 0, k_z \neq 0 \end{cases} \tag{3.10}$$

Analogous to the resolvent case, $\hat{A}_d^{\mathrm{DNS}}$ only specifies the controller gain for $k_x \geq 0$, since the gains for $k_x < 0$ are determined by Hermitian symmetry. The particular values of $\hat{A}_d$ are explained as follows. Continuity dictates that control should not induce any mean wall-normal velocity (see eq. (2.21)) so that the gain is zero if $k_x = k_z = 0$. The other Fourier modes with $k_x = 0$ have no streamwise dependence, so that any phase shift would lead to a spanwise shift, by definition. The gain for modes $[k_x > 0, k_z \neq 0]$ is therefore equal to one, which is identical to classical opposition control. On the other hand, the gain for spanwise-constant modes ($k_z = 0$) is equivalent to the resolvent model. This is a special case, because $\tilde{\boldsymbol{\kappa}} = \boldsymbol{\kappa}$ for these modes and a streamwise-only shift is guaranteed by Hermitian symmetry. Finally, the entry for $k_x > 0, k_z \neq 0$ enforces $|\hat{v}(\boldsymbol{\kappa}, y_w, t)| = |\hat{v}(\tilde{\boldsymbol{\kappa}}, y_w, t)|$, so that the oblique wave in eq. (3.9) cancels out. As written, the controller assigns the smaller of $|\hat{v}(\boldsymbol{\kappa}, y_w))|$ and $|\hat{v}(\tilde{\boldsymbol{\kappa}}, y_w))|$ to both modes, so that the control signal is less energetic than the sensor measurement. Another valid option would be to formulate the control input based on the larger of the two amplitudes, but a larger control magnitude is not desirable in general. Note that either choice leaves the oblique wave uncontrolled. Furthermore, the DNS control law is a generalization of the resolvent formulation and recovers the latter if $|\hat{v}(\boldsymbol{\kappa}, y_d, t)| = |\hat{v}(\tilde{\boldsymbol{\kappa}}, y_d, t)|$.

It is important to point out that there is a time delay of one time step between the sensor measurement and the actuator response in eq. (3.10), because the actuation is implemented as Dirichlet boundary condition. The time delay is equivalent to an additional frequency-dependent phase $e^{i\omega\Delta t}$ in Fourier domain, which is not represented in the resolvent model. The time step in the DNS varies subject to a CFL condition, but is of the order $\Delta t u_\tau/h = O(1\mathrm{e}{-3})$. The phase error introduced to the structures of the near-wall cycle, which are expected to dominate the control signal and can be characterized by $\lambda_x^+ \approx 1000, c^+ \approx 10-12$ (Luhar, Sharma, and McKeon, 2014b), is $\omega\Delta t \approx \pi/450$. This is two orders of magnitude smaller than the phase shifts induced by the controller and it can therefore be expected that the phase

error due to the time delay is negligible. Simulations with smaller Δt and therefore smaller phase errors were performed to validate this assumption and it was indeed confirmed that the drag reduction obtained for smaller Δt changed by less than 1%.

3.3 Direct Numerical Simulation

We first study varying-phase opposition control by means of DNS and compute the drag reduction for various sensor locations and phase shifts. These DNS data provide the ground truth to which we will subsequently compare the resolvent model predictions. All computations were carried out with the numerical method described section 2.2, and control is applied to a channel flow at $\mathrm{Re}_b = 5600$, which corresponds to $\mathrm{Re}_\tau = 180$ in the uncontrolled configuration. We first introduce the drag reduction measure (section 3.3.1) and outline a few select test cases to validate the DNS framework against literature data (section 3.3.2). The drag reduction results and some aspects of the controlled flows are reported in section 3.3.3.

3.3.1 DNS: Drag Reduction Measure

We start the discussion of DNS results with the definition of an appropriate drag reduction measure. The flow is driven by a fixed mass flux (see discussion in section 2.2), which is purposely kept constant when control is applied, so that the controlled flows and the uncontrolled reference flow have the same bulk Reynolds number. In this configuration, the mean pressure gradient required to induce the fixed mass flux changes based on the flow state. A decrease of the mean pressure gradient magnitude relative to the uncontrolled flow is the desirable control outcome, because it implies less power input to induce the same mass flux. Conversely, an increase in mean pressure gradient magnitude is undesirable, because it implies a larger power input to produce the same mass flux. A common definition of drag reduction for constant mass flux simulations is therefore based on the relative change in mean pressure gradient

$$\Delta\overline{\tau} = 1 - \frac{\left(\overline{\Pi}_x\right)_c}{\left(\overline{\Pi}_x\right)_0} \tag{3.11}$$

where $\Delta\overline{\tau}$ denotes drag reduction and $\overline{\Pi}_x$ is the time-averaged mean pressure gradient. From here on, the subscript 0 will denote uncontrolled quantities, while a subscript c is used to label controlled variables. A positive value of $\Delta\overline{\tau}$ implies drag reduction (DR for short), while a negative value indicates drag increase (abbreviated as DI).

Recall from eq. (2.27) that the mean pressure gradient is balanced by the wall-shear stress, so that drag reduction can equivalently be written in terms of $\overline{\tau}_w$

$$\Delta\overline{\tau} = 1 - \frac{(\overline{\tau}_w)_c}{(\overline{\tau}_w)_0} = 1 - \frac{\left(\mathrm{Re}_\tau^2\right)_c}{\left(\mathrm{Re}_\tau^2\right)_0} \tag{3.12}$$

and the last equality follows from the definition of u_τ and Re_τ. A drag reduction can therefore also be thought of as a decrease in wall-shear stress or Re_τ. Additional insight into the generation of wall stresses, and into the mechanisms of drag reduction, can be obtained from various decompositions of the normalized skin friction coefficient. One of these decompositions, which is commonly named FIK identity after its inventors Fukagata, Iwamoto, and Kasagi (2002), is of particular relevance for the present study. It allows to express $\Delta\overline{\tau}$ in terms of a weighted integral of the mean Reynolds stress (see Appendix A)

$$\Delta\overline{\tau} = \frac{\int_{-1}^{1} \left(\frac{y}{h}\right) \left[\left(\overline{u'v'}\right)_0 - \left(\overline{u'v'}\right)_c\right] \mathrm{d}\left(\frac{y}{h}\right)}{\frac{\mathrm{Re}_b}{\mathrm{Re}^2} + \int_{-1}^{1} \left(\frac{y}{h}\right) \left(\overline{u'v'}\right)_0 \mathrm{d}\left(\frac{y}{h}\right)} \tag{3.13}$$

where Re is the Reynolds number based on the velocity scale used to nondimensionalize the Reynolds stresses. This expression is particularly amenable to modal analyses, because the mean Reynolds stress can be computed on a mode-by-mode basis. Other decompositions may offer greater physical insight, but are less suited for modal analyses (see e.g. Renard and Deck, 2016). Here we only note that the denominator of eq. (3.13) is a sum of a laminar contribution (first term), which is fully determined by the mean velocity profile, and a turbulent contribution (second term), which is fully determined by the weighted integral of the Reynolds stress.

From here on, we will use the term "drag reduction" to refer to $\Delta\tau$ as defined in eqs. (3.11) to (3.13). It is important to emphasize that all three definitions are equivalent and can be derived from each other by analytic manipulations of the governing equations. This definition of drag reduction is fairly standard in the literature and has in particular been used in previous opposition control studies (see e.g. Choi, Moin, and Kim, 1994; Chung and Talha, 2011). However, other definitions are possible and well-defined as well. For example, another approach is to quantify drag reduction in terms of an outward shift of the mean velocity profile (Ibrahim, Guseva, and Garcia-Mayoral, 2020). This choice is motivated by the total stress equation (2.29), which indicates that a decrease in local Reynolds stress leads to an increase in mean velocity gradient and therefore to an outward shift of $\overline{u}$.

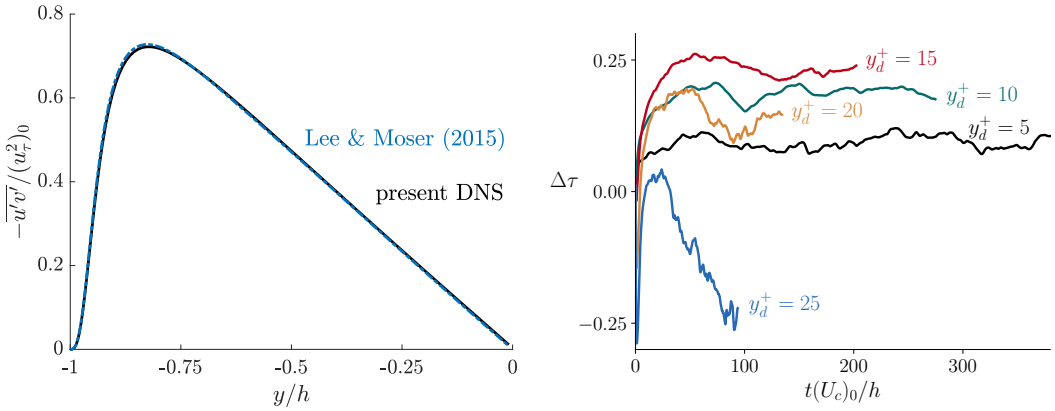

(a) Uncontrolled flow (b) Classical opposition control

Figure 3.2: Validation of DNS framework. Figure 3.2a compares the Reynolds stress profile of the uncontrolled flow as a function of the wall-normal coordinate. The solid black line is data from the present DNS, the blue dash-dotted line is data from Lee and Moser (2015). Figure 3.2b shows the time history of drag change under classical opposition control with various sensor locations y_d. Figure 3.2a reproduced from Toedtli, Luhar, and McKeon (2019). © 2019 American Physical Society.

Finally, it should be noted that the present study considers drag reduction due to active control, which implies that the actuators do work on the system. The definition of $\Delta\overline{\tau}$ neglects the power input of the actuation and is therefore not a measure of net energy savings. Related to that, the definition of drag reduction in terms of the mean pressure gradient alone cannot distinguish between mean flux contribution (pumping) and turbulence reduction due to control (Hoepffner and Fukagata, 2009). However, throughout Chapters 3 to 5, we use drag reduction only to delineate distinct flow regimes, for which we deem the above definition sufficient. Control efficiency considerations will be presented separately in section 6.4.

3.3.2 DNS: Validation

Prior to simulating flows under varying-phase opposition control, we validate results of the present code framework against literature data. Two validation cases are presented: First, a simulation of an uncontrolled channel flow at $\mathrm{Re}_\tau = 180$, which will also be the reference flow to drag reduction. And second, a simulation of classical opposition control with sensors located at various distances from the wall. The main goal of this validation case is to ensure the adequacy of the grid parameters in the presence of wall transpiration.

The statistics of the uncontrolled flow are compared to the data of Lee and Moser (2015), and fig. 3.2a shows an example comparison of the mean uv-Reynolds stresses. The two curves show excellent agreement over the entire channel height and the same was found for all other flow statistics available for comparison, which confirms the adequacy of the numerical parameters to simulate uncontrolled flows.

The literature data are more sparse when it comes to controlled flows. In particular, the statistics are not available from online databases, which limits the comparison of controlled flows to more qualitative aspects. Previous studies have shown that the DR of classical opposition control strongly depends on the sensor location (Choi, Moin, and Kim, 1994; Hammond, Bewley, and Moin, 1998; Chung and Talha, 2011), and reported the time history as well as time-averaged values of $\Delta\tau$. The control response for various sensor locations is therefore a good test to validate the numerical framework. Figure 3.2b shows the time history of the instantaneous drag reduction for a range of sensor locations. All controlled runs are started from the same uncontrolled flow field at $t = 0$ and run for the same number of time steps. A constant number of time steps leads to a different simulated physical time in each case. This is because the actuation magnitude changes with y_d and a larger wall transpiration magnitude requires smaller timesteps to satisfy the CFL condition. It is apparent that sensors located close to the wall ($y_d^+ \leq 20$) lead to drag reduction, while control with $y_d^+ = 25$ leads to a drag increase. These qualitative trends agree with literature results. For example, compare fig. 3.2b with fig. 2 of Choi, Moin, and Kim (1994) or fig. 2 of Chung and Talha (2011), which all show the same trends. A maximum drag reduction of 23.4% occurs for sensor located at $y_d^+ = 15$, which agrees with results reported by Hammond, Bewley, and Moin (1998) and Chung and Talha (2011), who both found a maximum DR of 25% at the same sensor location. The good agreement of the classical opposition control results confirm that the numerical parameters are appropriate for the study of flows with wall transpiration as well. For later comparison, it is important to keep in mind that classical opposition control also acts on the oblique wave in eq. (3.9). This is a key difference to varying-phase opposition control, which leaves the oblique wave uncontrolled. Some implications of this difference in control setup will be discussed in section 3.3.3.

Finally, it should be pointed out that Re_τ, and therefore also the grid resolution in inner units, change when control is applied. The resolution increases if the drag is decreased and vice-versa and runs with $\mathrm{Re}_\tau > 245$ may be considered slightly

under-resolved. We conducted a grid convergence study in order to rule out any grid effects in the DNS results of varying-phase opposition control. We simulated a drag-reducing ($y_d^+ = 15, \angle\hat{A}_d = -\pi/4$) and a drag-increasing ($y_d^+ = 15, \angle\hat{A}_d = \pi/2$) configuration with higher resolution ($N_x = 512, N_y = 272, N_z = 512$), and confirmed that the flow statistics did not change.

3.3.3 DNS: Drag Reduction Behavior

After validating the code framework for known flow configurations, we now consider varying-phase opposition control and investigate the DR behavior for various sensor locations and phase shifts. To this end, we performed a total of 50 DNS runs covering five sensor locations, $y_d^+ = [5, 10, 15, 20, 25]$, and ten phase shifts, $\angle\hat{A}_d \in [-3\pi/4, +3\pi/4]$. Note that $\angle\hat{A}_d$ is 2π-periodic, so that the above settings cover the entire range except for $\angle\hat{A}_d = \pm\pi$. A π phase shift corresponds to a sign inversion and leads to in-phase control, where $v(y_w) = v(y_d)$. Previous studies have shown that in-phase opposition control leads to significant drag increase (Choi, Moin, and Kim, 1994), so that we do not consider this scenario further. Two of the tested configurations, namely control with $\angle\hat{A}_d = 3\pi/4$ and sensors located at $y_d^+ = [20, 25]$, lead to the largest drag increase and diverged before a statistically steady state was reached. The cause was not further investigated, because the DR trend could already be estimated from the partially completed runs, but it is possible that the grid resolution was insufficient in these cases. The maximum drag increase observed in all successfully completed runs was assigned to these two control cases, which is a lower bound for the effective drag increase. The raw data were then interpolated using bilinear splines to produce the DR map of fig. 3.3. Bright shading (positive numbers) represent drag reduction, while dark shading (negative numbers) indicate drag increase and the solid black lines outline a few select contour levels.

Figure 3.3 indicates that the DR behavior is a function of the sensor location and phase shift. A closer inspection further reveals that the relevance of each parameter varies across the tested configurations. For example, many contour lines in the range $-3\pi/8 \leq \angle\hat{A}_d \leq \pi/8$ are close to horizontal, which indicates a weak dependence of the drag reduction on the phase shift. On the other hand, the contours outside of this range become more vertical, which suggests that the phase shift becomes more important in this parameter region.

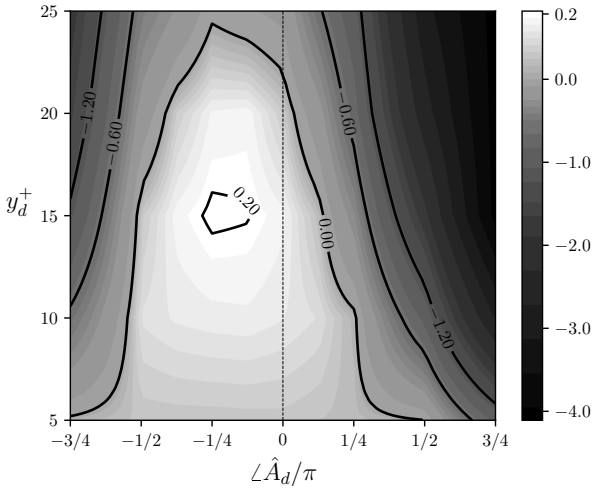

Figure 3.3: Contour map showing the DNS drag reduction of varying-phase opposition control as a function of the sensor location y_d^+ and phase shift $\angle\hat{A}_d$. Positive numbers (light colors) indicate drag reduction, while negative numbers (dark colors) represent drag increase. Note that the color scale is nonlinear in order to highlight the region of drag reduction. The dashed vertical line denotes $\angle\hat{A}_d = 0$, which is closely related to classical opposition control. Figure after Toedtli, Luhar, and McKeon (2019) and Toedtli, Yu, and McKeon (2020).

We first discuss the effect of the sensor location for a fixed phase shift, which corresponds to vertical lines in fig. 3.3. The effect of the sensor location is strongest for $-\pi/2 \leq \angle\hat{A}_d \leq \pi/4$, which includes the region with almost horizontal contour lines. In this region, the drag reduction initially increases as the sensors move away from the wall, reaches a maximum around $y_d^+ \approx 15$, and then decreases as the sensors move further out. The optimal sensor location of $y_d^+ = 15$ is consistent with classical opposition control results, as can be confirmed from fig. 3.2b or e.g. Chung and Talha (2011). The importance of the sensor location tapers off for large negative ($\angle\hat{A}_d < -\pi/2$) and positive phase shifts ($\angle\hat{A}_d > \pi/4$), and in both cases the drag increases as soon as the sensors move away from the wall.

Next, we consider the effect of the phase shift at a fixed sensor location, which corresponds to horizontal lines in fig. 3.3. The trend is quite uniform for all tested sensor locations. Going from negative to positive phase shifts, we initially observe a drag increase, followed by a region of drag reduction and another subsequent drag increase. Slightly negative phase shifts seem to be optimal, and a maximum drag reduction of 21% is achieved with $\angle\hat{A}_d = -\pi/4$ and $y_d^+ = 15$. The largest drag increases are observed for large positive phase shifts. In some of these cases,

drag increases by more than 400% or, equivalently, Re_τ increases by more than a factor of two. These findings are all consistent with related literature results. Lee (2015) showed that upstream sensor information increases the maximum DR of opposition control, while downstream sensor information decreases it. As explained in section 3.2.1, $\angle\hat{A}_d < 0$ corresponds to a downstream shift of the actuator, which can also be interpreted as the actuator using upstream sensor information. Similarly, $\angle\hat{A}_d > 0$, which corresponds to an upstream shift of the actuator, is equivalent to using downstream sensor information. The results of both studies agree qualitatively, but it is important to emphasize again that the nature of the streamwise shift is different in each case. Another comparison can be made to the study of Kim and Choi (2017), which showed that the maximum drag reduction of opposition control can be increased by adding an integral term to the control law. For a linear system, a proportional-integral controller is equivalent to a proportional controller with phase shift, so that the two approaches would be identical. Since the flow dynamics are nonlinear, the equivalence does not hold exactly, but a recent study on control of vortex shedding in a low Reynolds number cylinder flow suggests that a proportional-integral and proportional controller with phase shift lead to a similar response, at least in the flow regime considered therein (Son, Jeon, and Choi, 2011). The present study suggests that the two controllers are also related for a low Reynolds number turbulent channel flow, because the addition of a phase shift to the controller gain and an integral term to the control law both improve the drag reduction.

Further note that the controller with $\angle\hat{A}_d = 0$, which corresponds to the dotted vertical line in fig. 3.3, is closely related to the original opposition control scheme. The two control laws are identical except for the oblique wave in eq. (3.9), which is controlled in the original scheme, but left uncontrolled under the present formulation. The qualitative drag reduction trends of the two schemes are very similar, as can be seen by comparing figs. 3.2b and 3.3. In both cases, the drag reduction increases as the sensors move away from the wall, and reaches a maximum around $y_d^+ = 15$. From there on, the drag reduction decreases with increasing sensor distance. However, the maximum DR is significantly different in both cases. The varying-phase opposition control scheme achieves a maximum drag reduction of 17%, while the original scheme with sensors located at the same location reduces drag by 23%. The difference indicates that the oblique waves play an important role in the drag characteristics of the controlled flow, but this aspect is not further investigated here. We only note that the role of the oblique waves could be studied by an alternative control scheme, which only generates the second term of eq. (3.9) as control input.

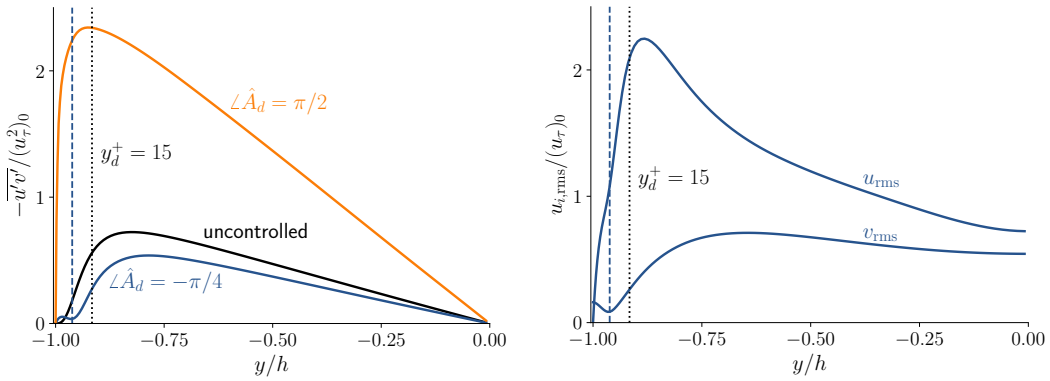

(a) Reynolds stresses

(b) Turbulence intensities for $\angle\hat{A}_d = -\pi/4$

Figure 3.4: Flow statistics of two example controlled flows with sensors located at $y_d^+ = 15$ and different phase shifts. Figure 3.4a compares the mean Reynolds stress profiles with the uncontrolled flow and fig. 3.4b displays the streamwise and wall-normal turbulence intensities of controller $\angle\hat{A}_d = -\pi/4$. The dotted black vertical line denotes the sensor location, while the dashed blue vertical line indicates the location of the minimum in the v_{rms} profile. Figure 3.4a after Toedtli, Luhar, and McKeon (2019).

Finally, we consider a few select Reynolds stress profiles to illustrate the connection between mean Reynolds stresses and drag reduction (3.13). Figure 3.4a compares the mean Reynolds stress of the uncontrolled flow with two example controlled flows with sensors located at $y_d^+ = 15$ and $\angle\hat{A}_d = [-\pi/4, \pi/2]$. All profiles are normalized with the uncontrolled friction velocity, so that the weighted area between the uncontrolled and controlled curve corresponds to the numerator in eq. (3.13). Control with $\angle\hat{A}_d = -\pi/4$ reduces the Reynolds stresses and therefore leads to drag reduction. On the other hand, control with a positive phase shift increases the Reynolds stresses, which implies drag increase. It is interesting to note that the flow changes under this normalization are not confined to the sensor location, which is indicated by the dotted black vertical line. The prominent change in the core flow is the modified slope of the profiles, which reflects the change in wall-shear stress under control. The mean shear in the core is negligible, so that the slope of the $\overline{uv}$-curve is essentially τ_w (see eq. (2.29)). The normalization of fig. 3.4a with $(u_\tau)_0$ is therefore appropriate to visually interpret the DR, but eq. (2.30) shows that all curves would collapse in the core flow if the actual $(u_\tau)_c$ were used instead. The control effect on the outer flow can therefore be fully attributed to the wall-shear stress, which is also consistent with Townsend's outer-layer-similarity hypothesis (Townsend, 1956).

The profile of the drag-reduced flow further shows an interesting feature in the near-wall region. There is a clearly distinguishable local minimum close to the wall, which roughly occurs at the dashed blue vertical line and which is not observed in the uncontrolled and drag-increased configuration. A possible connection between the local minimum and drag reduction is supported by eq. (3.13), which shows that reductions of Reynolds stress in the near-wall region have most importance in the weighted integral. The origin of the local minimum can be understood by considering the profiles of the u and v turbulence intensities shown in fig. 3.4b. The distinguishing feature of all controlled flows is that the vertical velocity can be non-zero at the wall, which is apparent from a statistical point of view in fig. 3.4b. Starting from a non-zero $v_{\mathrm{rms}}(y_w)$, the profile initially decreases with distance from the wall and has a local minimum, whose location is indicated by the dashed blue vertical line in fig. 3.4b. The location of the v_{rms} minimum is also plotted in fig. 3.4a to highlight a potential connection between the minima in both profiles. The streamwise turbulence intensity on the other hand is zero at the wall due to the no-slip condition, and increases monotonically throughout the near-wall region. It is interesting to note that the u_{rms}-profile has an outward shift at the location of the minimum in v_{rms}. Since the Reynolds stress is a combination of both quantities, it is subject to the competing effect of the increasing u_{rms} and the decreasing v_{rms} in the near-wall region. The matching location of the minima in v_{rms} and $\overline{uv}$ suggest that the dip in the wall-normal intensity profile indeed causes the minimum in the Reynolds stress. The significance of the v_{rms}-minimum will be further explored in section 4.4, and it will be shown that the drag-increasing controller $\angle\hat{A}_d = \pi/2$ has such a local minimum as well, but it does not translate to $\overline{uv}$, as can be seen from fig. 3.4a.

3.4 Resolvent Model

After studying the properties of varying-phase opposition control by means of DNS, we now switch our approach and use the resolvent model instead. We first generalize the drag reduction measure in order to account for model errors (section 3.4.1) and present model calculations for an uncontrolled flow at $\mathrm{Re}_\tau = 180$ to get a sense for the model characteristics (section 3.4.2). The initial calculations have the same wave number resolution as DNS, which allows a meaningful comparison, but makes the model similarly expensive to evaluate. Section 3.4.3 outlines a subsampling strategy to speed up the model calculations, which will be used in subsequent sections of this chapter. The drag reduction of varying-phase opposition control for various

sensor locations and phase shifts obtained from the resolvent model is presented in section 3.4.4. The role of the mean velocity profile is analyzed in section 3.4.5 and section 3.4.6 outlines how known scaling relations can be used to efficiently evaluate the model at high Reynolds numbers.

3.4.1 Resolvent: Drag Reduction Measure

Before introducing the details of the resolvent model, we have to revisit the drag reduction measure and generalize the DNS expression in order to account for model errors. The starting point for the discussion is the drag reduction definition given in eq. (3.13), but keep in mind that all definitions in section 3.3.1 are equivalent and any of the other ones could be used as well. Equation (3.13) is preferred because the mean Reynolds stress can be computed from contributions of individual Fourier modes, which themselves can be approximated by resolvent modes. The challenge in applying eq. (3.13) to the resolvent model stems from the denominator, which consists of two parts. A laminar contribution (first part), which is fully determined by the mean velocity profile, and a turbulent contribution (second part), which is fully determined by the weighted integral of the Reynolds stresses (Fukagata, Iwamoto, and Kasagi, 2002). In the real flow, the mean velocity and Reynolds stresses that underlie each term are connected through the mean momentum equation (2.28). The resolvent model on the other hand is not constrained to satisfy the mean momentum equation (recall the discussion in section 2.4.4), so that the mean velocity and Reynolds stress do not necessarily balance each other. In fact, it will be shown in section 3.4.2 that the model Reynolds stress under a broadband forcing assumption is orders of magnitude larger than in the real flow. The resolvent model can therefore not predict the correct relative magnitude of each term in the denominator, and a direct application of eq. (3.13) would not return a meaningful result.

As outlined in Appendix A, the DR expression can be recast into an appropriate form that accounts for model errors such as the mismatch between the model Reynolds stresses and the mean velocity profile. The final expression reads

$$\begin{aligned}\Delta\tau = &\underbrace{\frac{\int_{-1}^{1}\frac{y}{h}\left[(\overline{u'v'})_0-(\overline{u'v'})_c\right]\mathrm{d}\left(\frac{y}{h}\right)}{\int_{-1}^{1}\frac{y}{h}(\overline{u'v'})_0\,\mathrm{d}\left(\frac{y}{h}\right)}}_{=T_1(y_d,\angle\hat{A}_d)}\underbrace{\left(1-\frac{3}{2}\frac{\mathrm{Re}_b}{(\mathrm{Re}_\tau^2)_0}\right)}_{=T_2}\\ &\times\underbrace{\frac{\int_{-1}^{1}\frac{y}{h}\left[(\overline{u'v'})_0^{\mathrm{DNS}}-(\overline{u'v'})_c^{\mathrm{DNS}}\right]\mathrm{d}\left(\frac{y}{h}\right)}{\int_{-1}^{1}\frac{y}{h}\left[(\overline{u'v'})_0-(\overline{u'v'})_c\right]\mathrm{d}\left(\frac{y}{h}\right)}}_{=T_3(y_d,\angle\hat{A}_d)}\underbrace{\frac{\int_{-1}^{1}\frac{y}{h}(\overline{u'v'})_0\,\mathrm{d}\left(\frac{y}{h}\right)}{\int_{-1}^{1}\frac{y}{h}(\overline{u'v'})_0^{\mathrm{DNS}}\,\mathrm{d}\left(\frac{y}{h}\right)}}_{=T_4}\end{aligned}\tag{3.14}$$

where the superscript DNS labels a quantity that is obtained from DNS and which therefore satisfies the mean momentum equation. Depending on the context, quantities without superscript can originate from DNS or the resolvent model, and they may not satisfy the mean momentum equation. The term $T_1(y_d, \angle\hat{A}_d)$ represents the turbulent DR predicted by the model under consideration (resolvent or DNS) and as such depends on the sensor location and the phase shift. The second term T_2 is the ratio of the turbulent drag to the total drag in the real uncontrolled flow, which is a constant for fixed Re_b. The product T_1T_2 represents the total change in wall shear stress (or equivalently drag), possibly subject to model errors represented by the following two terms. $T_3(y_d, \angle\hat{A}_d)$ is the model error in turbulent DR, which is a function of the control parameters, and the constant T_4 is the model error in the uncontrolled Reynolds stress profile. Note that $T_3 = T_4 = 1$ for DNS data, so that the definition of eq. (3.13) is recovered.

DNS data allows to evaluate all terms of eq. (3.14), while the resolvent model alone can only quantify T_1, which solely depends on model data, and T_2, which can be obtained from the input $(\mathrm{Re}_\tau)_0$ and the eddy-viscosity approximation of the mean profile. The model errors T_3 and T_4 can only be evaluated if higher fidelity data are available as well. In other words, the resolvent model alone can only estimate the change in mean wall shear stress up to a model error

$$\Delta\tilde{\overline{\tau}} = T_1(y_d, \angle\hat{A}_d)\, T_2 = \frac{\Delta\overline{\tau}}{T_3(y_d, \angle\hat{A}_d)\, T_4} \tag{3.15}$$

and we will report $\Delta\tilde{\overline{\tau}}$ instead of the true change in wall shear stress when presenting resolvent data. In order to compare different control configurations it can be advantageous to normalize the model drag reduction by a reference value, for example the maximum DR ($\Delta\tilde{\overline{\tau}}_{\max}$ for short)

$$\xi = \frac{\Delta\tilde{\overline{\tau}}}{\Delta\tilde{\overline{\tau}}_{\max}} = \frac{\Delta\overline{\tau}}{\Delta\overline{\tau}_{\max}} \frac{T_3(y_{d,\max}, \angle\hat{A}_{d,\max})}{T_3(y_d, \angle\hat{A}_d)}. \tag{3.16}$$

This allows the elimination of T_4, the model error in the uncontrolled profile.

3.4.2 Resolvent: Baseline Model

In order to evaluate $\Delta\tilde{\overline{\tau}}$, we need to compute the model Reynolds stress for the uncontrolled flow and each control configuration of interest. This section outlines the calculation of the model Reynolds stresses, characterizes the resulting uncontrolled profile, and compares it with the true one, which will give a sense for the model

error of the uncontrolled flow, T_4. The controlled configurations and resulting drag reduction will be discussed subsequently in section 3.4.4.

The resolvent framework described in section 2.4.4 returns an approximation of the Fourier coefficients at each wave number triplet $\boldsymbol{k}$. The resolvent modes can be connected to the mean Reynolds stress by first writing the latter in terms of Fourier coefficients

$$\overline{u'v'}(y) = \sum_{l=-\infty}^{\infty} \sum_{m=-\infty}^{\infty} \int_{-\infty}^{\infty} \hat{u}(\boldsymbol{k}, y)\, \hat{v}^*(\boldsymbol{k}, y)\, \mathrm{d}\omega \tag{3.17}$$

which follows from eq. (2.53). The Fourier coefficients at each $\boldsymbol{k}$ can subsequently be approximated by resolvent modes up to a suitable order. Figure 2.2 has shown that the first two singular values are typically an order of magnitude larger than the following ones, which suggests a rank-2 approximation of the resolvent. Under a rank-2 broadband forcing approximation, the integrand in eq. (3.17) becomes

$$\begin{aligned} \hat{u}(\boldsymbol{k}, y)\hat{v}^*(\boldsymbol{k}, y) \approx{}& \sigma_1^2 \hat{u}_1(\boldsymbol{k}, y)\hat{v}_1^*(\boldsymbol{k}, y) + \sigma_1\sigma_2 \hat{u}_1(\boldsymbol{k}, y)\hat{v}_2^*(\boldsymbol{k}, y) \\ &+ \sigma_1\sigma_2 \hat{u}_2(\boldsymbol{k}, y)\hat{v}_1^*(\boldsymbol{k}, y) + \sigma_2^2 \hat{u}_2(\boldsymbol{k}, y)\hat{v}_2^*(\boldsymbol{k}, y). \end{aligned} \tag{3.18}$$

Recall from the discussion about the wall-normal symmetry of resolvent modes (section 2.4.4) that if the singular values are paired, then the first and second resolvent modes are equal in magnitude, but opposite in wall-normal symmetry. In particular, $\hat{u}_1$ and $\hat{v}_2$ are even functions of y, while $\hat{u}_2$ and $\hat{v}_1$ are odd. The cross-terms ($\sigma_1\sigma_2\hat{u}_1\hat{v}_2^*$ and $\sigma_1\sigma_2\hat{u}_2\hat{v}_1^*$) are therefore even and their y-weighted wall-normal integral vanishes. Consequently, they do not contribute to $\Delta\tilde{\tilde{\tau}}$. The diagonal terms ($\sigma_1^2\hat{u}_1\hat{v}_1^*$ and $\sigma_2^2\hat{u}_2\hat{v}_2^*$) are equal and odd in y, so that they contribute equally to $\Delta\tilde{\tilde{\tau}}$. The only difference between a rank-1 and rank-2 approximation is therefore a factor of two. This factor appears in the nominator and denominator of the first term in eq. (3.14) and cancels, which makes a rank-1 and rank-2 approximation equivalent. Recall that almost all singular values are paired, so that the above statement is true for almost all resolvent modes. It can therefore be expected that $\Delta\tilde{\tilde{\tau}}$ resulting from rank-1 and rank-2 model is almost identical and this has indeed been confirmed in numerical experiments (data not shown). For the purpose of this chapter, it thus suffices to consider a rank-1 approximation, as anticipated in section 2.4.4

The expression for the model Reynolds stress can be simplified by taking advantage of the resolvent wave number symmetries. As shown in Appendix B, eq. (3.17) can be rewritten as

$$\overline{u'v'}(y) = \sum_{l=0}^{\infty} \sum_{m=0}^{\infty} \int_{-\infty}^{\infty} B_{lm}\, \sigma_1^2 \Re\{\hat{u}_1(\boldsymbol{k}, y)\hat{v}_1^*(\boldsymbol{k}, y)\}\, \mathrm{d}\omega \tag{3.19}$$

	baseline model	subsampled model
k_x	$k_x h = l/2,\ l \in [0, 84]$	$k_x h = [0, 0.5, \ldots, 5, 7.5, 10, 20, 31, 42]$
k_z	$k_z h = m,\ m \in [0, 84]$	$k_z h = [0, 1, \ldots, 10, 12, 14, 16, 20, 25, 30, 40, \ldots, 70, 84]$
c (for $k_x \neq 0$)	$\{c_i^+ = \overline{u}^+(y_i)\}_{i=1}^{N_y/2}$	$\{c_i^+ = \overline{u}^+(y_{2i-1})\}_{i=1}^{N_y/4+1}$
ω (for $k_x = 0$)	$\Delta\omega h/(u_\tau)_0 = \begin{cases} 0.01 & \text{for } \lvert\omega h/(u_\tau)_0\rvert \leq 0.25 \\ 0.05 & \text{for } 0.25 < \lvert\omega h/(u_\tau)_0\rvert \leq 0.5 \\ 0.25 & \text{for } 0.5 < \lvert\omega h/(u_\tau)_0\rvert \leq 3.5 \end{cases}$	

Table 3.1: Resolution of the baseline and subsampled resolvent model in wave number space.

where

$$B_{lm} = \begin{cases} 1 & \text{if } l = m = 0 \\ 2 & \text{if either } l = 0 \text{ or } m = 0 \\ 4 & \text{else} \end{cases}. \tag{3.20}$$

In practice, the sums have to be truncated and the integral has to be discretized and evaluated over a finite interval of temporal frequencies. The same truncation as in the DNS is used whenever possible, so that model errors due to resolution discrepancies can be ruled out and a meaningful comparison can be made. This choice has the additional benefit that minimal empirical knowledge is required to select an appropriate model resolution. In this spirit, the model resolves the same streamwise and spanwise wavenumbers as the DNS (after dealiasing), which are specified in table 3.1. Note that the wave numbers are integer multiples of the fundamental wave number corresponding to the domain sizes $L_x = 4\pi h$ and $L_z = 2\pi h$, respectively. In the wall-normal direction the resolvent operator is discretized on a set of $N_y = 172$ Chebyshev collocation points so that the grid of the model and the DNS are identical up to a stretching factor described in Lee and Moser (2015).

The only coordinate requiring additional empirical knowledge for parameter selection is the temporal frequency. The continuous range of frequencies resolved in the DNS is too large to be handled reasonably by the numerical framework of the model, and furthermore the DNS does not provide a well-defined sampling rate because the timestep changes subject to a CFL condition. However, there is compelling empirical evidence that the temporal frequency content of each Fourier mode is

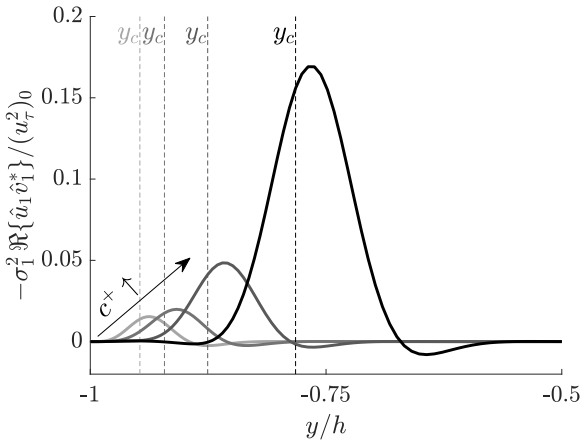

Figure 3.5: Effect of wave speed on the mean Reynolds stress contribution of individual resolvent modes. The figure shows the $\overline{uv}$ contribution of resolvent modes characterized by $k_x h = 5.5, k_z h = 2$ and wave speeds $c^+ = [8, 10, 12, 24]$ with darker colors indicating faster wave speeds. The dashed vertical lines indicate the critical layer of each mode. Reproduced from Toedtli, Luhar, and McKeon (2019). © 2019 American Physical Society.

approximately sparse, so that the entire frequency spectrum does not need to be resolved. As summarized by Bourguignon et al. (2014), the dominant temporal frequencies at $k_x \neq 0$ can be parametrized by the wave speed $c = \omega/k_x$ and fall in between the empirical range $10\,u_\tau \leq c \leq U_c$. This suggests picking the temporal frequency vector ω at each k_x such that at least the range $10\,u_\tau \leq \omega/k_x \leq U_c$ can be resolved. For reasons that will become clear shortly, we use the slightly more conservative range $0 \leq \omega/k_x \leq U_c$ in this study. Note that the range of wave speeds is kept constant across all $\boldsymbol{k}$, so that the corresponding temporal frequencies change for different k_x.

An appropriate sampling rate in c can be derived from the wall-normal localization of the resolvent modes. Figure 3.5 shows that the mean Reynolds stress contribution of a single resolvent mode is localized around its critical layer, i.e. around the wall-normal location y_c where its wave speed equals the local mean velocity $c \approx \overline{u}(y_c)$. Conversely, one can say that the dominant contribution to the Reynolds stress at a fixed y comes from modes whose critical layer y_c correspond to that y. The discretization of the wall-normal coordinate naturally samples the mean velocity profile and defines the critical wave speeds resolved by the grid. From the previous argument we expect that the dominant Reynolds stress contribution at each gridpoint y_i is given by modes with wave speed $c = \overline{u}(y_i)$. This suggests that the sampled wave speeds should correspond to the discretized mean velocity profile, and justifies the

resolved wave speeds in the left column of table 3.1. Note that empirical knowledge is required to justify this range of ω, but no empirical knowledge is required to evaluate it. The temporal frequency vector is fully determined by the given mean velocity profile and wall-normal grid.

The exception to the above discussion are streamwise constant modes ($k_x = 0$). For such modes, the wave speed c is not defined and a different, for now empirical, approach is needed to determine an appropriate frequency vector. The amplification of streamwise constant modes peaks at $\omega = 0$ and drops off very quickly and symmetrically as ω moves away from the origin. For example, the maximum σ_1 across all k_z drops from $\sigma_1 = 696$ at $\omega = 0$ to $\sigma_1 = 2$ at $\omega h/(u_\tau)_0 = \pm 3.5$ and further decreases as $|\omega|$ increases (data not shown in the interest of brevity). Recall that the Reynolds stress contribution depends on the square of the singular value and therefore contributions beyond $\omega h/(u_\tau)_0 = \pm 3.5$ can be neglected. We thus restrict the temporal frequency vector of $k_x = 0$ to $-3.5 \leq \omega h/(u_\tau)_0 \leq 3.5$, and sample as indicated in table 3.1.

It was verified that the results do not depend on the particular choice of c or ω. The mean Reynolds stress only varies minimally if the bandwidth of ω is increased or if the sampling frequency $\Delta\omega$ is changed. For reasons that will become more clear in section 3.4.3, we will refer to the resolvent model with parameters according to the left column in table 3.1 as baseline model. Also, for future reference, it is worth mentioning that one baseline model run costs around 160 core hours at the time of writing. This is similarly expensive as a single DNS run at $\mathrm{Re}_\tau = 180$, which took about 120 core hours.

The Reynolds stress profile predicted by the baseline model for an uncontrolled channel flow at $\mathrm{Re}_\tau = 180$ is shown as dash-dotted blue line in fig. 3.6. The model baseline resolves all dynamically relevant spatial and temporal scales, and can therefore be considered a resolvent model calculation at DNS resolution. However, it is apparent from the figure that the model profile does not match the true Reynolds stress. The model largely overpredicts the peak magnitude, as can be seen from a comparison of the y-axes in figs. 3.2a and 3.6. Moreover, the modeled profile peaks closer to the wall than the real one and exhibits a plateau between $-0.75 \leq y/h < -0.4$ instead of a near-linear decrease. Recall that the model is not constrained to satisfy the mean momentum equation, since we neglected the latter in the model development. Yet it is interesting to note that the modeled Reynolds stress exhibits a near-linear decrease in the outer flow, as indicated by the gray line in fig. 3.6. But

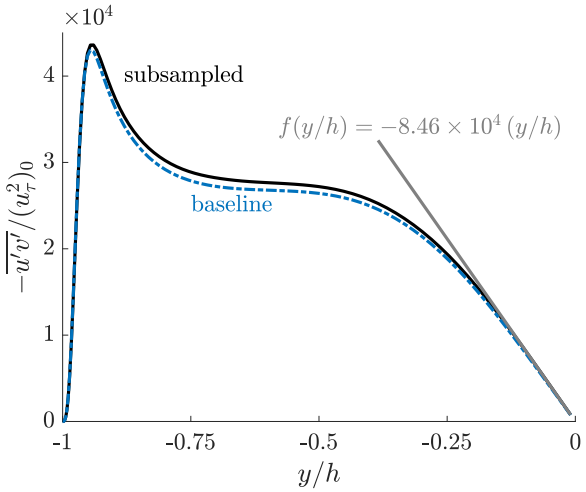

Figure 3.6: Uncontrolled mean Reynolds stress profiles computed with two different resolvent models. The blue dashed curve shows the baseline model, while the black curve denotes the subsampled model. The gray curve is a linear fit to the model Reynolds stress in the core flow. Reproduced from Toedtli, Luhar, and McKeon (2019). © 2019 American Physical Society.

in agreement with the overpredicted magnitude of the Reynolds stress, the slope is steeper than what one would expect from an analysis of the mean momentum equation.

The features of fig. 3.6 can also be compared to results from a similar study of a turbulent pipe flow by Luhar, Sharma, and McKeon (2014b). The mean Reynolds stress profiles of both studies agree qualitatively and the only difference to the pipe flow result is the heavier tail in the outer channel ($y/h > -0.5$), which can be ascribed to the streamwise constant ($k_x = 0$) modes with zero temporal frequency and low spanwise wave numbers. These dominant streamwise constant modes peak close to the channel center and have the largest singular values of all resolved wave numbers. Under the broadband forcing assumption, their contributions have a strong footprint on the integrated Reynolds stress profile, and therefore give rise to the observed heavy tail. The role of the $k_x = 0$ modes within the resolvent framework remains to be fully understood and an in-depth analysis is beyond the scope of this investigation, but we would like to point out that largest amplification occurring for streamwise constant modes is reminiscent of transient growth, where streamwise constant vortices are well-known to be the optimal perturbations (Butler and Farrell, 1992).

Given that the resolvent model is not constrained to satisfy the mean momentum equation and the numerous model assumptions, in particular the broadband forcing, the observed deviations between model and DNS profile may not be surprising. But in view of recent work on more complex forcing models that approximate the correct flow statistics (e.g. Moarref, Jovanović, et al., 2014; Zare, Jovanović, and Georgiou, 2017; Towne, Schmidt, and Colonius, 2018; McMullen, Rosenberg, and McKeon, 2020; Morra, Nogueira, et al., 2021), one may ask whether a rank-1 model with broadband forcing is still adequate. However, the key point not to forget in a control context is this: a useful control-oriented model mainly needs to capture the relation between inputs and outputs, it need not produce the correct flow statistics of the system (Kim and Bewley, 2007). In this spirit the goal should be to find the simplest possible model that is able to approximate the response of the full nonlinear system to control, and in this sense, the broadband forcing assumption is preferred over the aforementioned more complex models. Furthermore, unlike the other models, the broadband forcing assumption does not require flow data as input, which minimizes the dependency on empirical data.

3.4.3 Resolvent: Subsampling in Wavenumber Space

The baseline model presented in the previous section is the appropriate starting point for comparison with DNS, but its evaluation is computationally too expensive for practical applications that may require extensive parameter studies or controller design at higher Re_τ. An analysis of the mean Reynolds stress contribution of individual resolvent modes reveals that their contribution varies smoothly over at least parts of the wave numbers. This observation suggests that the resolvent model can subsample the wave number space to reduce the number of resolved scales and the computational cost. This approach has already been used in previous studies (for example Moarref, Sharma, et al., 2013; Luhar, Sharma, and McKeon, 2014b), but without formal justification. The goal of this section is to demonstrate that subsampling is indeed appropriate.

As can be seen from fig. 3.5, the mean Reynolds stress contribution of a single mode is localized around the critical layer y_c and therefore its wall-normal profile is mainly determined by the wave speed c. The wall-normal profiles for different c look very similar and the location of their peak moves slowly away from the wall as the wave speed increases. This suggests that not all the wave speeds resolved in the baseline model are required to capture the wall-normal shape of the mean Reynolds stress profile, since resolvent modes with similar wave speeds largely overlap in

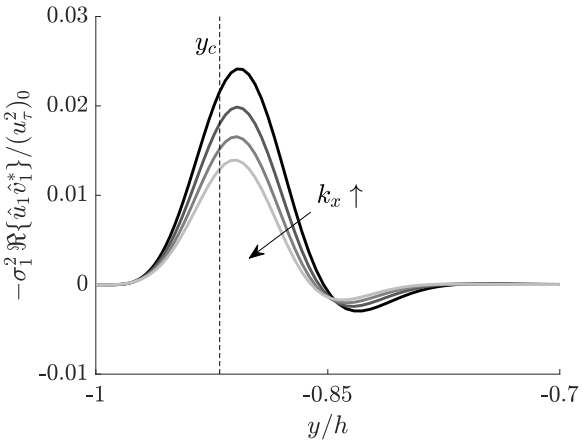

Figure 3.7: Effect of streamwise wave number on the mean Reynolds stress contribution of individual resolvent modes. The figure shows the resolvent modes $k_x h = [5, 5.5, 6, 6.5]$, $k_z h = 2$ and $c^+ = 10$, with darker colors indicating smaller wave numbers. The dashed vertical line indicates the critical layer, which is identical for all modes. Reproduced from Toedtli, Luhar, and McKeon (2019). © 2019 American Physical Society.

y. Figure 3.7 further shows the mean Reynolds stress contribution for modes with various k_x at fixed k_z and c. It is again apparent that the wall-normal localization of the modes is determined by the wave speed. Furthermore, it can be seen that the wall-normal profiles look very similar for various k_x and that the peak magnitude slowly decreases as k_x increases. This observation holds for all sufficiently large streamwise and spanwise wave numbers ($k_x h \gtrapprox 5$, $k_z h \gtrapprox 10$) and suggests that the spatial wave numbers can be subsampled as well as the wave speeds.

Based on these insights, the wave number space is subsampled as indicated in the right column of table 3.1. This corresponds to a reduction from 85×85×86 (baseline) to $16 \times 22 \times 44$ (subsampled model) resolved wave numbers. The missing wave numbers are linearly interpolated and ω is not subsampled if $k_x = 0$. The resulting Reynolds stress profile of the uncontrolled flow is shown as solid black line in fig. 3.6. The good agreement with the baseline model (dash-dotted blue line) confirms that the wave number space can indeed be sampled very sparsely. The subsampled model only resolves about 2% of the wave numbers of the baseline, which reduces the computational time to 2 core hours, i.e. almost two orders of magnitude less compared to DNS. This is cheap enough to allow, for example, extensive parameter searches for controller design. Furthermore, the memory requirements and operation count of the subsampled model are small enough so that it can be run on an off-the-shelf laptop and no high-performance computing facilities are required to evaluate

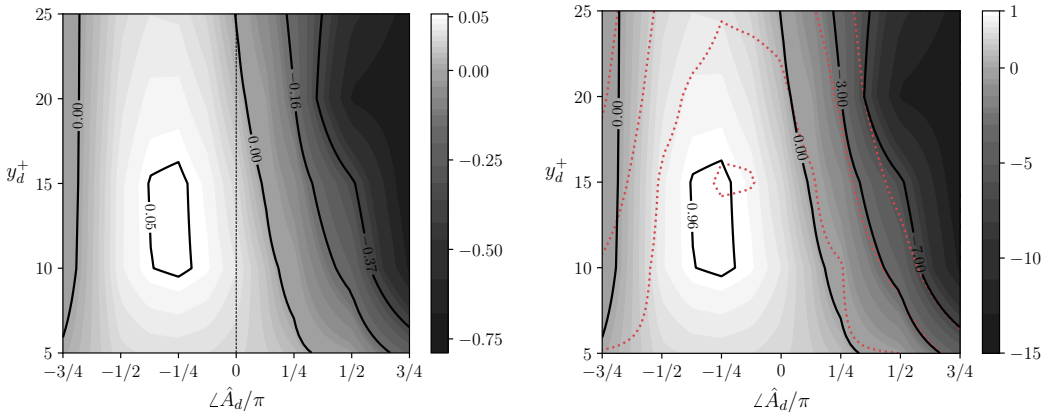

(a) $\Delta\tilde{\tilde{\tau}}$ (b) ξ

Figure 3.8: Contour maps showing the resolvent model drag reduction as a function of sensor location y_d^+ and phase shift $\angle \hat{A}_d$. Figure 3.8a shows the absolute drag reduction $\Delta\tilde{\tilde{\tau}}$, while fig. 3.8b displays $\xi = \Delta\tilde{\tilde{\tau}}/\Delta\tilde{\tilde{\tau}}_{\max}$. The black lines draw out equivalent contour levels in each figure and the dotted red lines indicate the corresponding ξ-contours of the DNS data shown in fig. 3.3. The dashed vertical line in fig. 3.8a denotes $\angle \hat{A}_d = 0$, which is closely related to opposition control. Note that the color scale is nonlinear to highlight the region of drag reduction. Figure 3.8a reproduced from Toedtli, Luhar, and McKeon (2019). Figure 3.8b after Toedtli, Luhar, and McKeon (2019). © 2019 American Physical Society.

it. Motivated by the results of this section, we will use the subsampled model for all resolvent calculations hereafter, and we will make all comparisons between subsampled resolvent model and DNS.

3.4.4 Resolvent: Drag Reduction Behavior

Now that we have defined a suitable drag reduction measure for the resolvent model and identified an appropriate resolution that also enables efficient model evaluation, we repeat the parameter study for varying-phase opposition control with the subsampled resolvent model. Again, five sensor locations $y_d^+ = [5, 10, 15, 20, 25]$ and ten phase shifts $\angle \hat{A}_d \in [-3\pi/4, +3\pi/4]$ are evaluated and the raw data are interpolated using bilinear splines to create a smooth drag reduction map. The capabilities of the resolvent model for controller design are then assessed from the agreement between the model and DNS drag reduction map.

Figure 3.8a shows $\Delta\tilde{\tilde{\tau}}$, which is the drag reduction measure compromised by the model error terms T_3 and T_4. It is apparent that the resolvent model reproduces trends previously observed in DNS. For example, a small negative phase shift improves the drag reduction and the maximum DR occurs at $y_d^+ \approx 10 - 15$ and $\angle \hat{A}_d = -\pi/4$.

On the other hand, large negative phase shifts are detrimental for drag reduction and so are positive shifts of any magnitude. The qualitative agreement between resolvent model and DNS can be better illustrated by overlaying contour levels of the normalized drag reduction ξ, which is shown in fig. 3.8b. The normalization is required to account for the different drag reduction magnitude in both frameworks, which will be discussed subsequently. A comparison of the contour lines shows that the resolvent model is capable of approximating the response of the full nonlinear system over a large range of the parameter space. In particular, the DNS and resolvent model contours of ξ collapse for positive phase shifts over the entire range of tested sensor locations. The agreement is lesser for $\angle\hat{A}_d < 0$, especially for large negative phase shifts. However, the resolvent model is still able to capture the trend of the DNS results reasonably well and it can in particular capture the location of the maximum drag reduction.

The collapse of the ξ-contour lines for positive phase shifts allows to draw conclusions about the model error in turbulent DR, denoted $T_3(y_d, \angle\hat{A}_d)$, in this parameter regime. First, the definition of ξ according to eq. (3.16) implies that the ratio $T_{3,\max}/T_3$ must be approximately one for all positive phase shifts. Further note that $T_{3,\max}$ is a constant, so that $T_3 \approx$ const for $\angle\hat{A}_d > 0$ as well. On the other hand, the error T_3 changes with y_d and $\angle\hat{A}_d$ for negative phase shifts. The ratio $T_{3,\max}/T_3$ is still of order one, but $\Delta\tilde{\overline{\tau}}/\tilde{\overline{\tau}}_{\max} > \Delta\overline{\tau}/\overline{\tau}_{\max}$, which indicates that T_3 decreases for more negative phase shifts. It also changes sign in parts of the parameter space, which indicates that the model expects drag reduction in regions where the DNS produces drag increase.

The parameter-dependent qualitative agreement also highlights an important aspect of the forcing model selection. The good agreement between the resolvent model, which uses the simplistic broadband forcing, and the DNS for $\angle\hat{A}_d > 0$ suggests that a positive phase amplifies all modes in spectral space. In this scenario, the error arising from the broadband forcing assumption cancels in the ratio $T_{3,\max}/T_3$, and the contour levels collapse as observed. On the other hand, the disagreement for $\angle\hat{A}_d < 0$ suggests that the control effect for negative phases is mixed in spectral space, so that the model error from the broadband forcing assumption does not cancel. It has been shown by Luhar, Sharma, and McKeon (2014b) that the broadband forcing puts too much weight on modes which are further suppressed by a negative phase shift. This is consistent with a decrease of T_3 in this part of the parameter space. The discrepancy between DNS and resolvent model for these parameter combinations

shows that the more mixed the effect of control in spectral space is, the more careful one has to be with the selection of forcing model. However, in this regard the resolvent model with broadband forcing can always be used as a first order design to estimate how mixed the response is and a more refined forcing model can be added in a second step if needed.

The discussion thus far was qualitative, and we next discuss quantitative aspects. A comparison between figs. 3.3 and 3.8a shows that the resolvent model underestimates the drag reduction over the entire parameter range. For example, the resolvent model predicts a maximum DR of 5% at $y_d^+ = 15$ and $\angle\hat{A}_d = -\pi/4$, while a 21% DR results at the same parameter combination in the DNS. Similarly, the drag increase at positive and large negative phase shifts is less pronounced in the resolvent model. We can therefore conclude that the model error terms $T_3(y_d^+, \angle\hat{A}_d)\, T_4 > 1$ for all parameters considered. These errors have a geometric interpretation in the Reynolds stress profiles of fig. 3.4a (DNS) and fig. 3.9 (resolvent model), which can thus be used to estimate their order of magnitude. Note that multiple Reynolds stress profiles are shown in both figures. The focus for now is on the black and blue line in fig. 3.4a and the thin and thick black line in fig. 3.9, respectively. In each figure, these two curves outline the $\overline{uv}$ profile of the uncontrolled and an example controlled flow ($y_d^+ = 15, \angle\hat{A}_d = -\pi/4$). The model error in the uncontrolled profile, i.e. term T_4, is the ratio between the weighted area under the thin black curve in fig. 3.9 and the black curve in fig. 3.4a. A comparison of both ordinates shows that $T_4 \gg 1$. The model error in turbulent drag reduction, $T_3(y_d, \angle\hat{A}_d)$, is the ratio of the weighted area between the black and blue curve of fig. 3.4a and the weighted area between the thin and thick black line in fig. 3.9. Here, the different order of magnitudes of the ordinates implies $T_3 \ll 1$. Both terms are dominated by the model contribution, which in T_3 appears in the denominator and in T_4 in the numerator. This suggests that the broadband forcing could be rescaled by a constant factor, which would cancel out in the DR measure (3.14) and bring both terms closer to order one.

3.4.5 Resolvent: Role of the Mean Velocity Profile

Figure 3.9 further provides an interesting insight into the role of the mean velocity profile in the controlled flow. As can be seen from comparing the thin (uncontrolled) and thick (example controlled flow) black curves, the control effect in the resolvent model is localized around the sensor location ($y_d^+ \approx 15$, indicated by the vertical line), where an attenuation as well as a slight outward shift of the peak can be observed. In particular, it is interesting to note that the two profiles collapse beyond

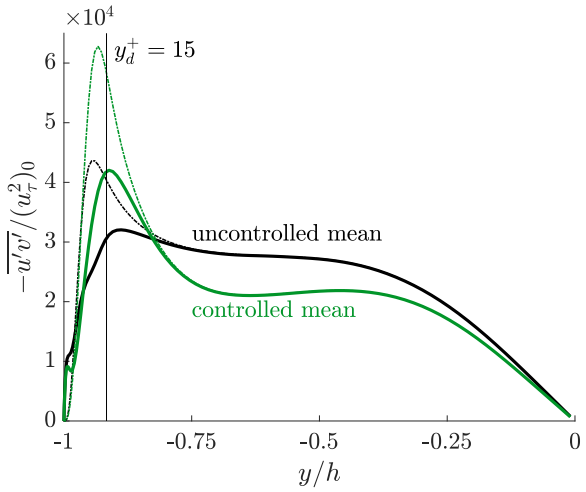

Figure 3.9: Reynolds stress profiles of the uncontrolled and an example controlled flow ($y_d^+ = 15, \angle\hat{A}_d = -\pi/4$). The black curves are computed from a resolvent analysis about the uncontrolled mean and the thin line outlines the uncontrolled profile, while the thick line shows the Reynolds stresses of the controlled flow. The green curves are obtained from a resolvent analysis about the controlled DNS mean and the thin and thick line again outline the uncontrolled and controlled flow in terms of boundary conditions. The vertical line indicates the sensor location. Figure after Toedtli, Luhar, and McKeon (2019).

$y/h \approx -0.8$, which indicates that the core flow remains unaffected by control. From the perspective of the resolvent model, the Reynolds stress in the core flow is produced by fast moving modes with no velocity signature close to the wall (Luhar, Sharma, and McKeon, 2014b), so that these modes cannot be detected by the sensor and therefore remain uncontrolled. Furthermore, recall that the uncontrolled mean profile is used to formulate the resolvent operator, so that the core flow feels the same $\overline{\tau}_w$ as in the uncontrolled case. From the resolvent perspective there is therefore really no difference in the core region between the uncontrolled and the controlled case and it is no surprise that the two profiles coincide.

The DNS data in fig. 3.4a on the other hand present a different picture for the core flow. A comparison of the uncontrolled (black line) and the controlled (blue line for $\angle\hat{A}_d = -\pi/4$) profile shows that the Reynolds stress decreases throughout the channel, similar to the results reported by Choi, Moin, and Kim (1994). As explained earlier, the tilting of the DNS profile in the core flow can be ascribed to the change in wall-shear stress and is determined by the mean momentum equation. The resolvent model does not satisfy the mean momentum equation, so that a similar analysis is not meaningful, but ideas like Townsend's outer-layer similarity hypothesis (Townsend,

1956) also suggest that changes in the core flow are mainly due to changes in τ_w, without relying on the mean momentum equation. One therefore may speculate that the change in the outer flow can be captured in the resolvent model if a controlled mean with different τ_w is used in the resolvent operator.

To test this hypothesis, we constructed the resolvent operator with the controlled DNS mean velocity profile and repeated the model prediction for the example controlled flow ($y_d^+ = 15, \angle \hat{A}_d = -\pi/4$). The resulting Reynolds stress profile is shown as thick green line in fig. 3.9. The thin green line shows the Reynolds stress profile with controlled mean but no-slip boundary conditions, to illustrate which changes are due to the change in mean and which ones are due to the boundary conditions. It is apparent that the change in mean profile alters the shape of the uncontrolled Reynolds stress profile throughout the channel. The near-wall peak is further increased and the Reynolds stresses decrease above $y/h = -0.8$. The effect of control is again limited to the sensor location, and both green curves collapse above $y/h = -0.8$. A comparison between the uncontrolled profile with uncontrolled mean (thin black line) and the controlled profile with controlled mean (thick green line) illustrates that a change in mean profile and boundary condition can reproduce the control effect in the entire channel. This supports the hypothesis that the change in the outer flow is indeed mainly due to the change in τ_w. In addition, the predicted DR increases from 5% (uncontrolled mean) to 10% (controlled mean), which is closer to the DNS value of 21%. This suggests that the modeling errors $T_3 T_4$ also decrease when the controlled mean is used. Finally, note that the resolvent model is able to capture the local minimum of $\overline{uv}$ in the near-wall region, especially if the controlled mean is used.

3.4.6 Resolvent: Reynolds Number Scaling

The results thus far outline how the resolvent model can be used for controller design in internal flows and suggest that it can approximate the DR of the real flow for our example controller at $(\mathrm{Re}_\tau)_0 = 180$. At these low Reynolds numbers, the (subsampled) resolvent model is almost two orders of magnitude cheaper to evaluate than DNS. However, DNS is still feasible and relatively cheap at these low Reynolds numbers, so that the value of the resolvent model may not be immediately apparent. As mentioned in the Introduction, the ultimate goal is to develop tools that allow controller design for internal flows at technologically relevant Reynolds numbers, which are currently not tractable with DNS. This is where the resolvent model has most potential in the future, because it can be applied relatively easily to

high Reynolds number flows. This section outlines two approaches to evaluate the resolvent model at technologically relevant Re_τ.

Two aspects of the model are central for its applicability to high Reynolds numbers. First, the smooth variation of the Reynolds stress profile in at least parts of the wave number space, which allows subsampling the model as described in section 3.4.3. As was shown for $\mathrm{Re}_\tau = 180$, the contributions of high wave numbers decay quickly, which makes the incorporation of additional high wave numbers cheap as Re_τ increases. The results presented here and in Moarref, Sharma, et al. (2013) show that this approach is well-justified and allows the model to easily handle flows at $\mathrm{Re}_\tau = O(10^4)$. In a naive approach, one could proceed at these higher Reynolds number in the same way as we did in this section. Use the eddy viscosity to obtain an approximation of the mean velocity profile, compute the resolvent modes at individual wave number triplets, and subsample the wave number space to efficiently compute the mean Reynolds stress profile. Enough resolution is still required in the wall-normal direction to resolve all features of the resolvent modes and this is particularly challenging in the near-wall region where structures scale with viscous units. These resolution requirements may still be practical at moderate Reynolds number, but they become prohibitive at large Re_τ and a different approach is required.

This is where the second key aspect of the resolvent model comes in. Moarref, Sharma, et al. (2013) derived scaling laws for different classes of resolvent modes (categorized based on their wave speed) from the properties of the resolvent operator alone. This allows to compute resolvent modes at a low Reynolds number, where resolution requirements in y are mild, and use the scaling laws to obtain the singular values and vectors at arbitrary high Reynolds numbers. The remainder of this section explores whether the scaling laws also apply to controlled flows, which would greatly simplify the applicability of the model to high Re_τ. The validation is based on two model calculations at higher Reynolds numbers: $\mathrm{Re}_\tau = 6000$, which is approximately the upper end of available experimental (Schultz and Flack, 2013) and DNS (Lee and Moser, 2015; Yamamoto and Tsuji, 2018) data, and $\mathrm{Re}_\tau = 30000$, which is well above current DNS and experimental capabilities and at the lower end of the technologically relevant Reynolds numbers (Smits and Marusic, 2013). To illustrate our point, we select the so-called inner class of resolvent modes, which scales in viscous units (Moarref, Sharma, et al., 2013), and is therefore the most challenging to calculate with the naive approach described above. It has been verified that the scaling laws apply to the other classes of modes as well.

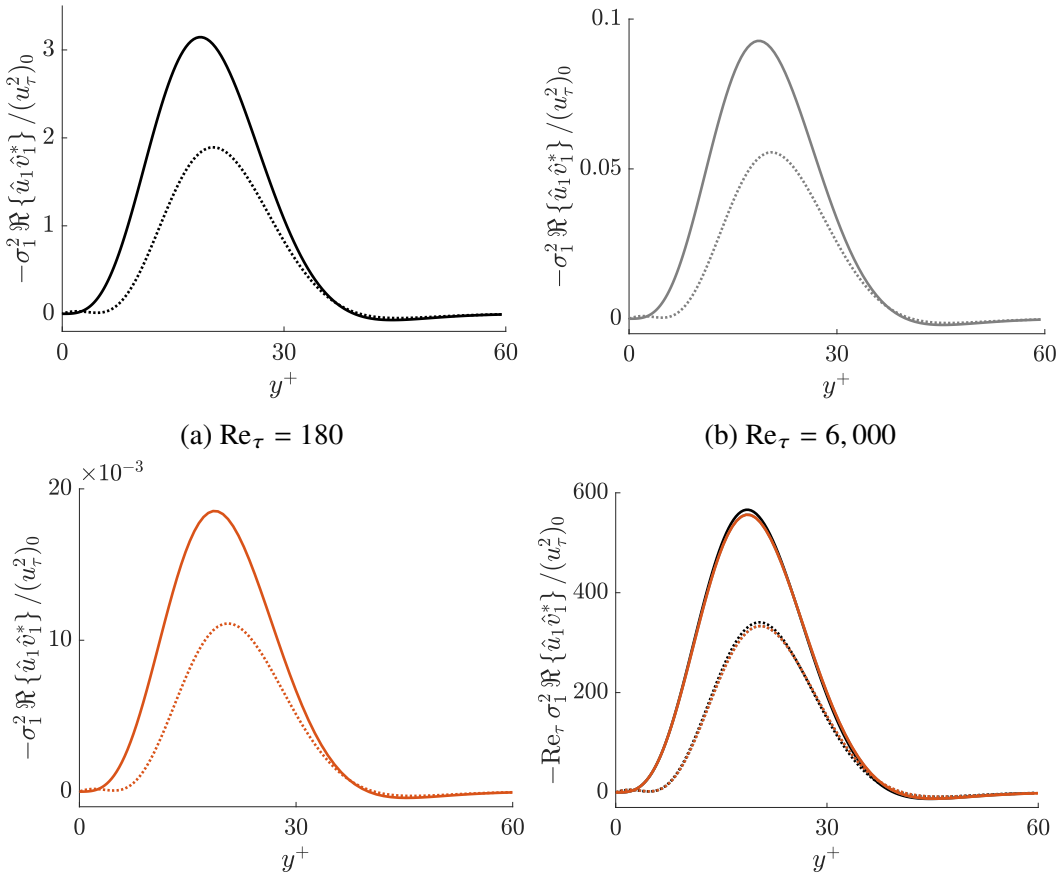

(a) $\mathrm{Re}_\tau = 180$ (b) $\mathrm{Re}_\tau = 6,000$

(c) $\mathrm{Re}_\tau = 30,000$ (d) rescaled profiles

Figure 3.10: Mean Reynolds stress contribution of an example resolvent mode characterized by $\lambda_x^+ = 1000$, $\lambda_z^+ = 100$, and $c^+ = 10$. Figures 3.10a to 3.10c show the profile normalized by the uncontrolled wall-shear stress at different Reynolds numbers, while fig. 3.10d displays the same data rescaled according to the scaling law of Moarref, Sharma, et al. (2013). In all figures, the solid line shows the profile of the uncontrolled flow, while the dotted line displays the profile of an example control configuration ($y_d^+ = 10$ and $\angle \hat{A}_d = -\pi/4$). Reproduced from Toedtli, Luhar, and McKeon (2019). © 2019 American Physical Society.

Figures 3.10a to 3.10c show the mean Reynolds stress contribution of a single resolvent mode characterized by $\lambda_x^+ = 1000$, $\lambda_z^+ = 100$ and $c^+ = 10$, where the solid and dotted line represent the uncontrolled and an example controlled flow ($y_d^+ = 10$, $\angle \hat{A}_d = -\pi/4$), respectively. Note that this mode belongs to the inner class according to the classification by Moarref, Sharma, et al. (2013). These resolvent modes are computed using the naive approach, i.e.they are computed with sufficient resolution at the indicated Reynolds numbers. To obtain DNS resolution, one would require $N_y = 172, 1700$ and 8500 grid points in the wall-normal direction (with an

appropriate grid stretching factor in the high Re_τ cases), respectively. However, the singular values are already converged for $N_y = 90, 130$, and 300, respectively. We therefore used somewhat coarser grids with $N_y = 172, 800, 1230$ (without grid stretching to ensure sufficient resolution in the near-wall region) to produce the results shown in Figures 3.10a to 3.10c. It can first be observed that the energy content of the near-wall structure decreases as the Reynolds number increases. Moreover, the plots suggest that the shape of the uncontrolled and the controlled structure remains unchanged. The last panel, fig. 3.10d, confirms that the mean Reynolds stress contributions indeed follow the scaling law proposed by Moarref, Sharma, et al. (2013), since all the profiles collapse when scaled appropriately. The scaling does therefore not only hold in the uncontrolled flow, which was already known, but also in the controlled flow. This is a key property of the model, which supersedes the naive approach by far. There is no need to compute the resolvent modes at high Re_τ. All one has to do is compute the resolvent modes at low Reynolds number, which is cheap, and then use the known scaling laws to obtain their contribution at an arbitrary high Re_τ.

We close this section with two comments. First, it should be pointed out that the scaling laws assume the presence of a logarithmic region in the mean velocity profile (Moarref, Sharma, et al., 2013). The empirical results of fig. 3.10d show good agreement between all the profiles, but strictly speaking at least $\mathrm{Re}_\tau = 180$ is too low to argue for the existence of a logarithmic region. In fact, there is a slight deviation between the $\mathrm{Re}_\tau = 180$ profile and the two other ones which may be a Reynolds number effect, even if small. One may therefore consider a slightly higher Re_τ when generating the profiles for scaling. Second, there is a small subset of wave number combinations that do not belong to any similarity class (see (Moarref, Sharma, et al., 2013) for details). Depending on their significance in the resolvent model, these modes may have to be computed explicitly at high Reynolds numbers. Note, however, that when combined with the subsampling strategy, this is only required for very few modes.

3.5 Chapter Summary

The present chapter introduced a variant of the opposition control scheme dubbed varying-phase opposition control. It is formulated for individual Fourier modes and introduces a phase shift between sensor measurements and actuator response. The phase shifts in Fourier domain can be thought of as scale-dependent streamwise shifts of the actuation relative to the sensor measurement, and in a linear system the

phase shift would be equivalent to an additional differential or integral term of the control law.

Direct numerical simulations showed that the drag reduction of varying-phase opposition control strongly depends on both control parameters considered, the sensor location y_d^+ and the phase shift $\angle\hat{A}_d$. There is an optimal sensor location at $y_d^+ \approx 15$, which agrees well with literature data of opposition control (e.g. Hammond, Bewley, and Moin, 1998; Chung and Talha, 2011). Furthermore, slightly negative phase shifts lead to optimal drag reduction, with maximum DR occurring at $\angle\hat{A}_d = -\pi/4$, while large negative or positive phase shifts lead to drag increase.

The varying-phase opposition control scheme served as a benchmark problem to evaluate the capabilities of a resolvent model for controller design. The model is constructed with the simplest assumptions possible: the resolvent is formulated about an eddy viscosity approximation of the uncontrolled mean profile and truncated at rank-1, and the nonlinear weighting terms are modeled with a broadband forcing assumption. Great care was taken to ensure that the resolvent model resolves the same spatial and temporal scales as the DNS and represents the same physics, so that a meaningful comparison could be made. The mean momentum equation and FIK identity were used to derive an analytical expression for the conventional drag reduction measure, enriched with model error terms that have a clear physical interpretation and can be quantified if high-fidelity data are available. The Reynolds stress contribution of individual resolvent modes, which are required to evaluate the drag reduction, varies smoothly in wave number space, which allows coarse subsampling. Indeed, a subsampled model, which only resolves 2% of the original wave numbers, is able to recover the fully-resolved model Reynolds stress profile at a fraction of the computational cost. A comparison between the model and DNS drag reduction calculations of varying-phase opposition control show that the model is able to approximate the behavior of the full nonlinear system over the entire parameter range considered, and confirms that the model is a suitable tool for controller design. There are quantitative differences between the model and the DNS regarding the maximum drag reduction, which can mainly be ascribed to the broadband forcing assumption. The uncontrolled mean velocity profile is sufficient to predict the trend of the nonlinear system, but cannot reproduce control changes in the outer flow. These changes are only represented in the model if the true controlled mean is used to construct the resolvent operator.

The resolvent model is about two orders of magnitude cheaper to evaluate than DNS at $\mathrm{Re}_\tau = 180$ and the savings increase with increasing Reynolds number. Importantly, the controlled resolvent modes follow known scaling laws of the canonical flow, which is a key advantage of the model. One can compute the resolvent modes at relatively low Reynolds numbers, which is cheap due to the mild resolution requirements in the wall-normal direction, and then scale the modes to arbitrary high Reynolds numbers without having to actually evaluate the resolvent operator. The validation at low Reynolds number and the scaling laws suggest that the model is suitable to design controllers at technologically relevant Re_τ.

Chapter 4

STRUCTURAL AND SPECTRAL FEATURES OF CONTROLLED FLOWS

Portions of this chapter have been previously published in[1]:

Toedtli, S., Yu, C., and McKeon, B. (2019). "Structural and spectral analysis of varying-phase opposition control in turbulent channel flow". In: *Proceedings of TSFP 11*.

Toedtli, S., Yu, C., and McKeon, B. (2020). "On the origin of drag increase in varying-phase opposition control". In: *International Journal of Heat and Fluid Flow* 85, p. 108651. DOI: 10.1016/j.ijheatfluidflow.2020.108651.

The results of the previous chapter suggest that the drag reduction attainable by varying-phase opposition control strongly depends on the phase of the controller gain $\angle\hat{A}_d$ and the sensor location y_d. We have further shown that the resolvent model is able to approximate the response of the full nonlinear system to control over the considered parameter range. From a resolvent perspective, control with a given $\angle\hat{A}_d$ and y_d changes the singular values and associated singular vectors, which leads to a change in mean Reynolds stress and ultimately drag. However, it remains unclear how control alters the real flow to bring about changes in flow structure and drag. The goal of this and the following chapter is therefore to elucidate the mechanisms that underlie the drag reduction map in fig. 3.3. The analysis is done in two parts. The present chapter is observational and characterizes DNS data of four example controlled flows, two that lead to drag reduction and two that result in drag increase. The subsequent chapter is theoretical and uses DNS and modal analyses of a simplified control problem to explain the characteristics of the example flows and the structure of the drag reduction map.

4.1 Prologue: Opposition Control Objective and Drag Reduction

Before describing the selection of the example controlled flows, it is instructive to review two concepts that will be important for the following discussion: the objective of the opposition control scheme and drag reduction. At first, it may seem

[1] C. Yu laid the groundwork for the visualizations presented in this chapter during a Summer Undergraduate Research Fellowship (SURF) in our group.

surprising that the two are not the same, and it will be shown that the two concepts are indeed related. Yet, many of the results reported in this and the following chapter only allow to draw conclusions for either the drag reduction or the opposition control objective, so that it is important to distinguish between the two.

As pointed out by Kim and Choi (2017), the opposition control scheme can be considered a proportional controller, which seeks to drive the wall-normal velocity fluctuations at the sensor location to zero. To see this, we define the control objective as $d = v(y_d) = 0$. The control error, which quantifies the deviation between the control objective and the system state, becomes $e = d - v(y_d) = -v(y_d)$. In other words, the control error corresponds to the sensor measurement with inverted sign. The actuator input under opposition control $v(y_w)$ is then proportional to the control error

$$v(y_w) = A_d\, e = -A_d\, v(y_d) \tag{4.1}$$

with proportionality constant A_d. Note that the last expression recovers the control law defined in eq. (1.1). In order to decide whether the controller achieves its control objective, we thus have to interrogate the wall-normal velocity at the sensor location. As for any turbulent flow quantity, a statistical measure is required to make a meaningful statement. The mean wall-normal velocity $\langle v \rangle_{x,z}(y,t)$ is identically zero at all wall-normal locations and times (see eq. (2.21)) and does not provide useful information. The appropriate statistical measure is therefore the variance of the wall-normal velocity at the sensor location, $\overline{v'v'}(y_d)$. Equation (2.55) implies that we can equally consider the root-mean-square (rms) fluctuation $v_{\mathrm{rms}}(y_d)$, and we will often switch back and forth between the two metrics to quantify the control error. In terms of rms fluctuations, the controller achieves its objective, at least partially, if

$$\Delta v_{\mathrm{rms}}(y_d) = (v_{\mathrm{rms}})_0\,(y_d) - (v_{\mathrm{rms}})_c\,(y_d) > 0 \tag{4.2}$$

where as before the subscript 0 and c label the uncontrolled and controlled flow, respectively. It is important to note that the control objective is a local measure. For example, the control objective would still be met if $(v_{\mathrm{rms}})_c$ decreased around the sensor plane relative to the uncontrolled case, but increased everywhere else. The terminology "opposition control objective" may be somewhat ambiguous and confusing in the current context. We will therefore refer to the formal control objective outlined above as "fluctuation suppression" from here on.

The primary goal of opposition control, even if not formally part of the control law and objective, is drag reduction. There is a significant leap between fluctuation

suppression and drag reduction, which can be best illustrated by revisiting the last form of the drag reduction definition in eq. (3.13). The drag decreases if $\Delta\tau > 0$, which is achieved if the numerator is positive, i.e.

$$\int_{-1}^{1} \frac{y}{h} \left[\left(\overline{u'v'} \right)_0 - \left(\overline{u'v'} \right)_c \right] \mathrm{d}\left(\frac{y}{h} \right) > 0. \tag{4.3}$$

The integral expression makes clear that drag reduction is a global quantity, in contrast to fluctuation suppression which is purely local. In addition, drag reduction not only depends on v, but also on the streamwise velocity and its relative phase to the wall-normal velocity. One can thus, at least in theory, imagine scenarios where opposition control successfully suppresses fluctuations, but fails to reduce drag, or vice-versa. For example, control may lead to a local decrease of v_{rms} around y_d and an increase everywhere else. In this case, the controller successfully suppresses fluctuations, but may lead to a drag increase. Conversely, the drag may decrease even if the fluctuations at the sensor location remain unchanged or increase. Such a scenario would for example be possible if control altered the relative phase between u and v.

Even though it is not obvious from the formal definitions, previous studies suggest that fluctuation suppression and drag reduction are correlated, at least in an integral sense and when control is applied in the near wall region (see, for example, the discussions in Choi, Moin, and Kim, 1994; Chung and Talha, 2011). The link between the two concepts is the flow structure in the near-wall region. The quasi-streamwise vortices that populate the near-wall region efficiently mix momentum by transporting low-speed fluid away from the wall and bringing high-speed fluid from further out towards the wall (Robinson, 1991). If the sensors of the opposition control scheme pick up the wall-normal velocity associated with the quasi-streamwise vortices, then suppressing $v_{\mathrm{rms}}(y_d)$ is equivalent to suppressing their motions. Weaker quasi-streamwise vortices lead to less momentum mixing, which results in a gentler mean velocity gradient at the wall and therefore drag reduction (Choi, Moin, and Kim, 1994).

The results in this chapter will confirm that the two concepts are correlated in an average sense. The distinction will be more important in the following chapter when we analyze the effect of control on individual spatial scales. In general, we will build on the results of Chapter 3 and use the drag reduction as starting point for our discussion. We will analyze fluctuation suppression where it provides additional insights.

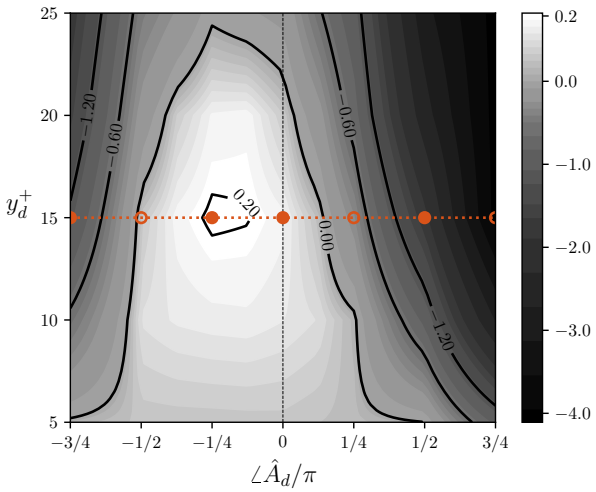

Figure 4.1: Contour map showing the drag reduction of varying-phase opposition control as a function of the sensor location y_d^+ and phase shift $\angle \hat{A}_d$. Positive numbers (light colors) indicate drag reduction, while negative numbers (dark colors) represent drag increase. Note that the color scale is nonlinear in order to highlight the region of drag reduction. The dotted horizontal line denotes the sensor location $y_d^+ = 15$ and the filled circles along this line indicate the example controllers considered subsequently. The dashed vertical line denotes $\angle \hat{A}_d = 0$, which is closely related to classical opposition control. Figure after Toedtli, Yu, and McKeon (2020).

4.2 Selection of Example Controlled Flows

Figure 4.1 shows again the DNS drag reduction map of fig. 3.3. Its properties have been discussed in detail in section 3.3.3, and we just restate the main observation, which is that the drag reduction strongly depends on both the sensor location and the phase shift.

The dependence of drag reduction on the sensor location for classical opposition control, which roughly corresponds to the dashed vertical line along $\angle \hat{A}_d = 0$ in fig. 4.1, has been studied extensively in the literature. The general consensus is that effective drag reduction occurs if the sensor location roughly coincides with the center of the quasi-streamwise vortices (Hammond, Bewley, and Moin, 1998; Chung and Sung, 2003). In contrast, the control scheme fails to inhibit momentum mixing if the sensors are located too far above the vortex center, and for sensors located above $y_d^+ \approx 23$, control even enhances momentum transport and leads to drag increase (Hammond, Bewley, and Moin, 1998; Chung and Talha, 2011). These observations are consistent with a previous resolvent analysis study, which suggest that more modes are amplified under control as the sensors move further away from the wall (Luhar, Sharma, and McKeon, 2014b).

The drag change under varying-phase opposition control for $\angle\hat{A}_d = 0$ agrees well with the aforementioned literature results. As discussed in section 3.3.3, the dependence on the phase shift is rather weak for $-3\pi/8 \leq \angle\hat{A}_d \leq \pi/8$, and it thus seems reasonable to assume that the drag change with increasing y_d in this parameter range is due to the mechanisms reported in the literature. For phase shifts outside of this parameter range, the dependence on the sensor location is weak, which suggests that this part of the drag reduction map is driven by phase shifts.

Since the dependence of DR on the sensor location can be explained by mechanisms reported in the literature, we focus our attention for the remainder of the following two chapters on the effect of the phase shift, which has not been explored so far. To reduce the parameter space, we fix the sensor location at $y_d^+ = 15$ and only vary $\angle\hat{A}_d$ between $-3\pi/4$ and $+3\pi/4$, which corresponds to the dotted orange horizontal line in fig. 4.1. We choose this particular sensor location because it contains all features of the drag reduction map, including the maximum DR. Controllers with $-\pi/2 \leq \angle\hat{A}_d \leq +\pi/8$ lead to drag reduction, with a (global) maximum DR for $\angle\hat{A}_d = -\pi/4$. Large positive and negative phase shifts on the other hand lead to drag increase (abbreviated as DI). In particular, we will study four example controllers, which are indicated by the filled orange circles in fig. 4.1. From the drag-reducing regime, we will consider the controllers with $\angle\hat{A}_d = -\pi/4$ (21% DR, corresponds to maximum DR) and $\angle\hat{A}_d = 0$ (17% DR, closely related to classical opposition control). A comparison between the two will provide insights into why a slightly negative phase shift leads to more drag reduction. For convenience, we will refer to these two controllers together as the "drag-reducing" controllers from here on. From the drag-increasing regime, we will analyze the controllers with $\angle\hat{A}_d = -3\pi/4$ (110% DI) and $\angle\hat{A}_d = +\pi/2$ (180% DI), and we will term the two controllers together the "drag-increasing" controllers. The goal of analyzing these two controllers is to understand what mechanisms cause the drag increase and whether these mechanisms are different for positive and negative phase shifts. For convenience, we will refer to individual controllers by their phase shift, e.g. $\angle\hat{A}_d = -\pi/4$. The sensor location $y_d^+ = 15$ is implied and will be omitted.

4.3 Flow Structure

We start our analysis and comparison of the controlled flows with visualizations of instantaneous flow fields. The intent of this discussion is to develop an intuition for how the flow changes under various control conditions. Representative structural features of the four example controlled flows are shown in fig. 4.2. Each row

represents a different controller in order of increasing phase shift, starting at the top with $\angle\hat{A}_d = -3\pi/4$. The left column displays volume renderings of vortical flow structures, which are identified by means of the λ_2-criterion (Jeong and Hussain, 1995). The threshold in all figures is $\lambda_2 h^2/(u_\tau)_0^2 = -940$, the absolute value of which corresponds to approximately 5% of the typical maximum of $|\lambda_2|$ in an uncontrolled channel flow at the same Reynolds number. In the drag-reducing cases, figs. 4.2c and 4.2e, the vortical activity is confined to the near-wall region and individual vortices are discernible. It is interesting to note that the vortical structure in both figures looks similar, which suggests that the flow structure at maximum DR is not significantly different from classical opposition control. On the other hand, the drag-increasing configurations shown in figs. 4.2a and 4.2g look quite different. In both cases, the vortical activity is strongly enhanced and vortices are found not only in proximity of the wall, but throughout the channel. Most vortical activity is found for $\angle\hat{A}_d = +\pi/2$, which is also the controller that leads to the largest drag increase. Comparing across all example controllers confirms the intuition that there is less vortical activity in drag-reduced flows and more in drag-increased configurations. It is interesting to observe that the wall-based actuation does not only change the structure of the flow in proximity of the wall, but throughout the channel, at least for the drag-increasing controllers.

The second column of fig. 4.2 shows instantaneous snapshots of the actuation at the wall. The velocities are made dimensionless with the centerline velocity $(U_c)_0$ of the uncontrolled flow at $\mathrm{Re}_\tau \approx 180$ and red regions indicate positive v (blowing), while blue regions represent negative v (suction). Example instantaneous control inputs for the drag-reducing controllers are shown in figs. 4.2d and 4.2f. The actuator response of both drag-reducing configurations looks again very similar. The wall actuation is dominated by a few spatial scales, which give rise to streamwise elongated streaky regions of positive and negative v. Typically, a region of positive v is surrounded on both sides in the spanwise direction by regions of negative v and vice-versa. One may speculate that the spatial structure of the control signal is the imprint of the streamwise vortices detected at the sensor location and the subsequent statistical analysis will support this hypothesis.

The actuator response of the drag-increasing controllers is shown in figs. 4.2b and 4.2h. It is interesting to note that both control inputs are about an order of magnitude larger compared to the drag-reducing cases (note the different color scales), but the larger input results in drag increase rather than drag reduction. This

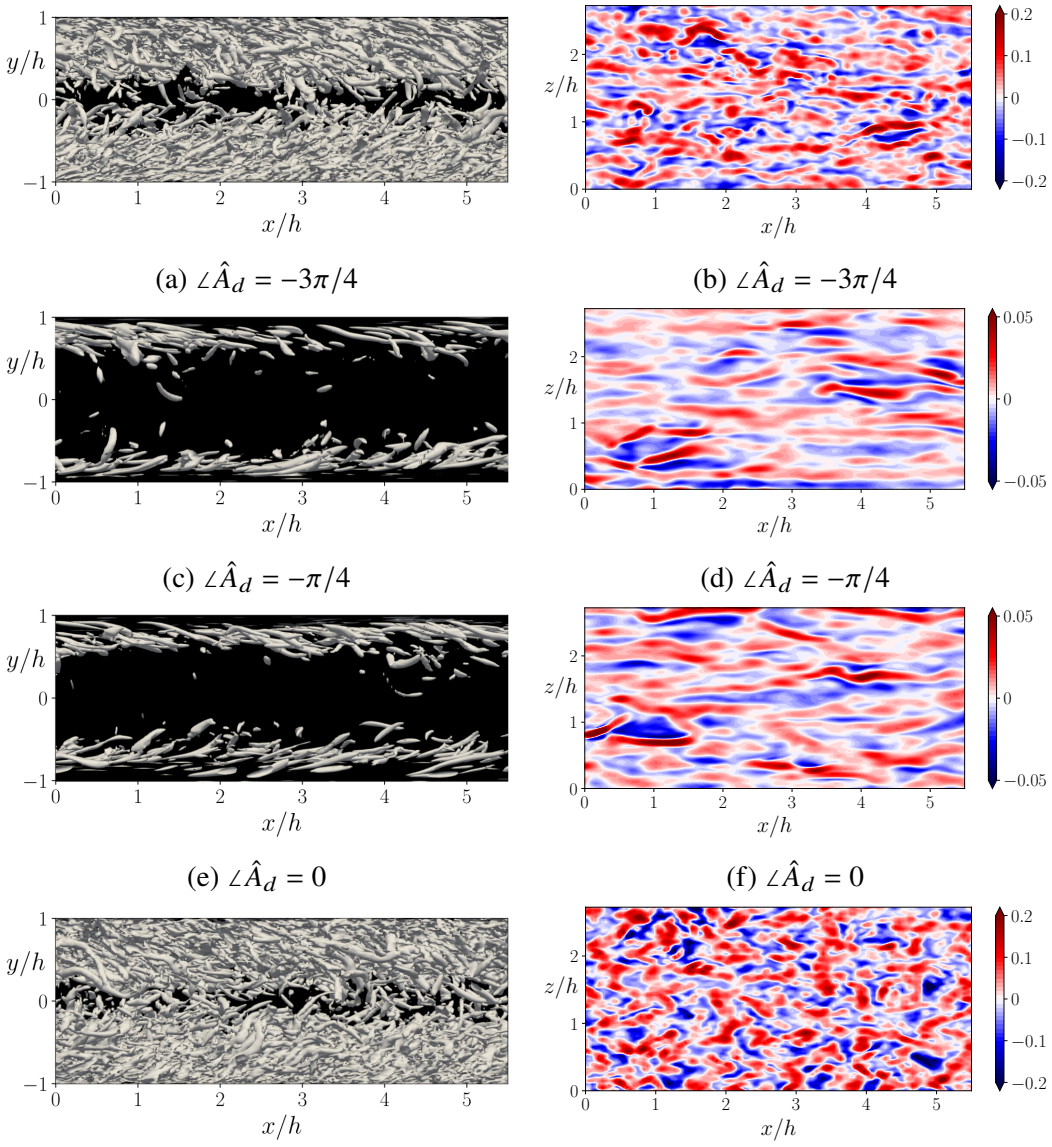

(a) $\angle\hat{A}_d = -3\pi/4$ (b) $\angle\hat{A}_d = -3\pi/4$

(c) $\angle\hat{A}_d = -\pi/4$ (d) $\angle\hat{A}_d = -\pi/4$

(e) $\angle\hat{A}_d = 0$ (f) $\angle\hat{A}_d = 0$

(g) $\angle\hat{A}_d = +\pi/2$ (h) $\angle\hat{A}_d = +\pi/2$

Figure 4.2: Representative instantaneous flow structure and actuator input. Each row corresponds to a different phase shift, with sensors located at $y_d^+ = 15$ in all cases. Figures 4.2a, 4.2c, 4.2e and 4.2g show a volume rendering of instantaneous λ_2 isosurfaces seen from the plane $z/h = 0$. The threshold used in all figures is $\lambda_2 h^2/(u_\tau)_0^2 = -940$. Figures 4.2b, 4.2d, 4.2f and 4.2h display a snapshot of the actuation at the wall, $v(x, y_w, z)$. Note that the color scale in figs. 4.2b and 4.2h is different from the one in figs. 4.2d and 4.2f. In all cases, the color scales are saturated (indicated by the arrows at both ends) to make the flow structure more apparent. Figure after Toedtli, Yu, and McKeon (2020).

suggests that the sensor measurement and actuator response lock-on and that their feedback with large negative or positive phase shift drives the flow to a new state of enhanced turbulence. This hypothesis will later be supported by the analysis in Chapter 5.

The spatial structure of the actuator response for $\angle \hat{A}_d = -3\pi/4$ is similar to the drag-reducing cases. It consists of elongated regions of positive and negative wall-normal velocity, but the structures are somewhat shorter and more slender compared to the drag-reducing configurations, and the signal looks more multi-scale overall. The actuator response for $\angle \hat{A}_d = +\pi/2$ exhibits quite different characteristics. Instead of the streaky structure typical for the previous cases, we observe a more unorganized control input. The streamwise coherence of the velocity signal is largely lost, but some organization is vaguely perceptible, with structures inclined with respect to the streamwise direction or even oriented along the span.

4.4 Wall-Normal Velocity Fluctuations

The characterization of flow structure thus far was based on instantaneous flow fields, but it is important to keep in mind that the actuation, and therefore also the flow structure, may be time-dependent. A time-series analysis shows that the spatial localization and amplitude of the control signal indeed change over time. In the following two sections, we thus analyze the flow structure from a statistical point of view, in order to validate whether the observed features persist over extended periods of time. We start the statistical analysis by looking at the wall-normal rms velocity fluctuations. As discussed in section 4.1, this flow diagnostic indicates whether the controller has achieved its objective. It further allows to quantify the actuator input at the wall and helps illustrate a few basic characteristics of the control scheme.

The wall-normal velocity fluctuations of the example controlled flows are shown in fig. 4.3, along with the profile of the uncontrolled flow. The first observation is that the two drag-reducing controllers reduce v_{rms} at the sensor location and beyond relative to the uncontrolled flow, while the drag-increasing controllers increase v_{rms}. In other words, the drag-reducing controllers achieve the control objective partially, because the wall-normal velocity fluctuations are smaller than in the uncontrolled case, but larger than zero. The drag-increasing controllers increase v_{rms} at the sensor location by more than a factor of two and do not achieve the control objective. Fluctuation suppression and drag reduction therefore correlate for all four example flows.

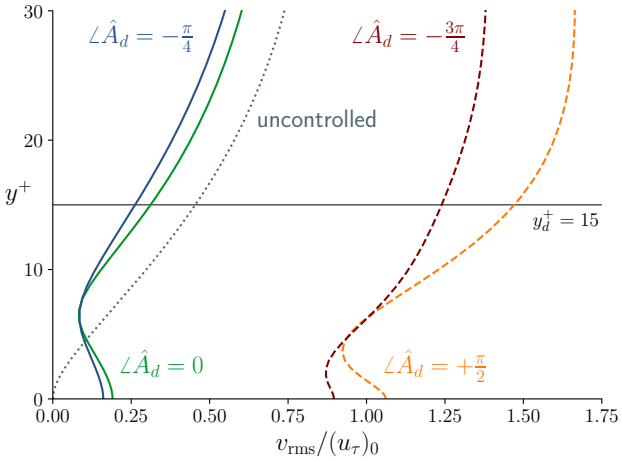

Figure 4.3: Wall-normal rms velocity profile as a function of the wall-normal coordinate. Each profile corresponds to a different phase shift $\angle\hat{A}_d$. Solid lines denote profiles of drag-reducing controllers, while dashed lines outline drag-increasing configurations. The dotted line outlines the profile of the uncontrolled fluctuations and the horizontal line corresponds to the sensor location $y_d^+ = 15$.

Each controlled profile in fig. 4.3 shows a local minimum of v_{rms} between the wall and the sensor plane. In the scenarios where control successfully reduces drag, the location of the minimum is usually referred to as a "virtual wall" (Hammond, Bewley, and Moin, 1998). The much reduced wall-normal velocity fluctuations at that plane inhibit momentum transfer in the wall-normal direction, and therefore shield the flow region below from high-speed fluid. Figure 4.3 shows that the drag-reducing controllers establish a virtual wall half-way between the sensor location and the physical wall, which agrees with previous DNS studies (for example Choi, Moin, and Kim, 1994; Hammond, Bewley, and Moin, 1998). The location of the virtual wall may be somewhat surprising, because the previous discussion about fluctuation suppression would suggest that the minimum should occur at the sensor location. A possible explanation for the location mismatch is that a proportional controller generates actuator inputs that are not large enough to reach all the way to the sensor location. The addition of an integral term to the control law increases the actuator input, since it is no longer solely proportional to $v_{\mathrm{rms}}(y_d)$, and can push the virtual wall outwards to the sensor plane (Kim and Choi, 2017). It is interesting to note that the profile of the drag-increasing controllers also exhibits a local minimum between the sensor plane and the wall. The wall-normal velocity fluctuations at the minimum location are still much larger than in the uncontrolled case, which indicates that they do not inhibit momentum transfer and that an interpretation of them as

virtual walls is not appropriate. It is also apparent that the minima of v_{rms} for the drag-increasing controllers occur closer to the wall compared to the drag-reducing controllers. A possible explanation for the location of the minimum for controller $\angle\hat{A}_d = +\pi/2$ will be given in section 5.4.3.

Figure 4.3 also allows to statistically quantify the control input, which corresponds to $v_{\mathrm{rms}}(y_w^+) = v_{\mathrm{rms}}(0)$. The previous comments about the wall-normal velocity fluctuations at the sensor plane also apply to the actuator, since the two are directly related by the control law. For classical opposition control the fluctuation intensity at the sensor and actuator would be identical, because the sensor measurement and actuator response only differ by a sign. Figure 4.3 shows that the fluctuation intensity at the wall is smaller than at the sensor location in case of varying-phase opposition control. This is a consequence of the additional symmetry constraint in Fourier domain. Recall that the control law eq. (3.10) selects the smaller of $|\hat{v}(k_x, k_z, y_d)|$ and $|\hat{v}(k_x, -k_z, y_d)|$ to generate the actuator response. This constraint ensures that phase shifts in Fourier domain correspond to streamwise shifts in physical domain (see discussion in section 3.2.2 for details). As a consequence, the magnitude of the control input is typically smaller than the magnitude of the sensor measurement and an oblique wave at the sensor location, namely the last term in eq. (3.4), remains uncontrolled. The wall-normal velocity fluctuations at the sensor location can be significantly larger than at the actuator, which can be seen for example from the profile for $\angle\hat{A}_d = +\pi/2$. The difference suggests that the oblique waves are instantaneously quite energetic, even if they must average to zero in order to preserve the statistical symmetry of the channel in z. We also note that the exception to the above discussion are modes with $k_x = 0$ or $k_z = 0$, for which the control amplitude is equal to the sensor measurement (see eq. (3.10)). However, the discussion in this and the following chapter will show that the slight difference in amplitude does not affect the qualitative behavior of these scales.

When comparing the drag-reducing controllers, it is interesting to note that v_{rms} at the sensor location and at the wall is smaller for the controller $\angle\hat{A}_d = -\pi/4$ than $\angle\hat{A}_d = 0$. Further recall that controller $\angle\hat{A}_d = -\pi/4$ leads to the maximum drag reduction, and it does so using the smallest control input among the four example flows. The control input of the drag-increasing controllers is significantly larger compared to the drag-reducing ones, which confirms the instantaneous observations of the previous section in a statistical sense. It should be emphasized that this discussion regards velocity input, not power. Power and efficiency considerations will be further discussed in section 6.4.

4.5 Actuation Spectra

The two previous sections have shown that the structure of drag-increased and drag-reduced flows is quite different. In particular, the wall-normal velocity fluctuations at the sensor plane (control error) and at the wall (actuator input) are much larger in the drag-increasing configurations. The instantaneous snapshots of the actuator signal further suggest that different spatial scales are active for different $\angle \hat{A}_d$. The goal of the present section is to analyze which scales contribute most to the actuator input from a statistical point of view. This will also allow quantification of the robustness of the instantaneous control signal characteristics described in section 4.3.

We will use the time-averaged power spectrum of the actuator input $\Phi_{vv}(y_w)$, shown in fig. 4.4, to characterize the most energetic scales. Recall that Φ_{vv} is related to $\overline{v'v'}$ and v_{rms} through eq. (2.59), which visually means that the sum over each spectrum in fig. 4.4 is equal to the square of $v_{\mathrm{rms}}(y_w)$ of the corresponding profile in fig. 4.3. The spectrum can thus be thought of as a density of v_{rms} in wave number space at a fixed wall-normal location: scales that are more energetic in the spectrum contribute more to the wall-normal velocity fluctuations at that y. In this sense, the time-averaged power spectrum is the appropriate diagnostic to characterize the most energetic scales of the actuator input.

Each plot in fig. 4.4 shows $\Phi_{vv}(y_w)$ of a different controller, in order of increasing phase shift and starting with $\angle \hat{A}_d = -3\pi/4$ at the top left. Unless stated otherwise, the friction velocity of the uncontrolled flow $(u_\tau)_0$ is used to rescale velocities and lengths to inner units. The spectra are shown as a function of wavelength to facilitate comparison with well-known flow structures, and the wavelengths $\lambda_x^+ < 45$ and $\lambda_z^+ < 28$ are omitted in fig. 4.4. This choice was motivated by the observation that the actuator input at these small wavelengths is almost zero. It should further be noted that the color scale in each plot is different, except for figs. 4.4b and 4.4c. Since each spectrum sums to the square of the corresponding v_{rms}, this reflects the different magnitude of the actuator inputs observed in fig. 4.3.

We first turn our attention to the drag-reducing configurations shown in figs. 4.4b and 4.4c. Both spectra are dominated by long and relatively slender structures, which confirms the earlier characterization of the instantaneous control input from a statistical point of view. Each spectrum has a global maximum, which is indicated by the green open square in fig. 4.4 and characterized in table 4.1. We also report the peak location normalized by the controlled viscous length scale for comparison, and label this normalization with an additional subscript tilde, e.g. $\tilde{\lambda}_x^+ = \lambda_x (u_\tau)_c / \nu$.

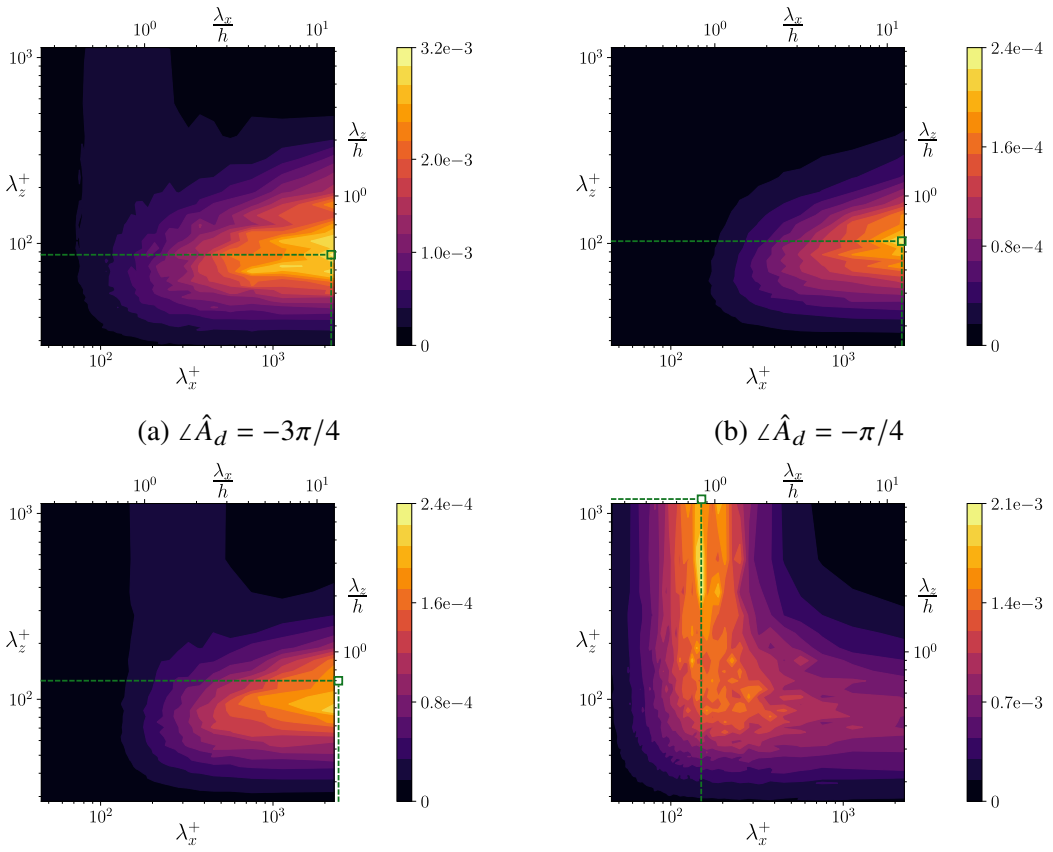

(a) $\angle\hat{A}_d = -3\pi/4$ (b) $\angle\hat{A}_d = -\pi/4$

(c) $\angle\hat{A}_d = 0$ (d) $\angle\hat{A}_d = +\pi/2$

Figure 4.4: Time-averaged spatial power spectrum $\Phi_{vv}/(u_\tau)_0^2$ of the actuator input $v(y_w)$ as a function of the streamwise (λ_x^+) and spanwise (λ_z^+) wavelength. In all cases the sensors are located at $y_d^+ = 15$ and each figure shows the spectrum for a different phase shift $\angle\hat{A}_d$. The green open square indicates the most energetic spatial scale of the control input, which is characterized in table 4.1. Note that the color scale is different in each figure. Figure after Toedtli, Yu, and McKeon (2020).

$\angle\hat{A}_d$	Most energetic scale	
	$\lambda^+ = \lambda\,(u_\tau)_0\,/\nu$	$\tilde{\lambda}^+ = \lambda\,(u_\tau)_c\,/\nu$
$-3\pi/4$	$\left[\lambda_x^+ \approx 2262,\ \lambda_z^+ \approx 87\right]$	$\left[\tilde{\lambda}_x^+ \approx 3278,\ \tilde{\lambda}_z^+ \approx 126\right]$
$-\pi/4$	$\left[\lambda_x^+ \approx 2262,\ \lambda_z^+ \approx 103\right]$	$\left[\tilde{\lambda}_x^+ \approx 2000,\ \tilde{\lambda}_z^+ \approx 91\right]$
0	$\left[\lambda_x^+ \to \infty,\ \lambda_z^+ \approx 126\right]$	$\left[\tilde{\lambda}_x^+ \to \infty,\ \tilde{\lambda}_z^+ \approx 114\right]$
$+\pi/2$	$\left[\lambda_x^+ \approx 174,\ \lambda_z^+ \to \infty\right]$	$\left[\tilde{\lambda}_x^+ \approx 290,\ \tilde{\lambda}_z^+ \to \infty\right]$

Table 4.1: Most energetic spatial scale of $\Phi_{vv}(y_w)$for various phase shifts. The entries in the second column characterize the scale in terms of the uncontrolled viscous length and correspond to the green open squares in fig. 4.4. The third column uses the viscous length of the controlled flow to normalize the peak location.

In both cases, the scales are reminiscent of the near-wall cycle and support the hypothesis that the distinct spatial structure of the control signal is an imprint of the quasi-streamwise vortices. It is interesting to note that scales with $150 \leq \lambda_x^+ \leq 800$ are more energetic for $\angle\hat{A}_d = 0$ than $\angle\hat{A}_d = -\pi/4$. This is most apparent for large spanwise widths, but the observation applies to all scales with $\lambda_z^+ > 40$. Recall from fig. 4.3 that the controller $\angle\hat{A}_d = 0$ induces somewhat larger velocity fluctuations at the wall than controller $\angle\hat{A}_d = -\pi/4$. Taking the difference between the two spectra shows that the additional energy in the velocity fluctuations for $\angle\hat{A}_d = 0$ is associated with the aforementioned region in spectral space.

Next, we consider the drag-increasing configurations in figs. 4.4a and 4.4d. It is apparent that the structure of the two spectra is quite different. The spectrum of the actuator $\angle\hat{A}_d = -3\pi/4$ is similar to the drag-reducing configurations, but the scales are much more energetic, as can be seen by comparing the color scales. The actuation is dominated by large streamwise scales, with somewhat more activity in smaller scales compared to the drag-reduced flows. This is consistent with the earlier observations about the instantaneous control input. The peak for this spectrum occurs at wavelengths that are again reminiscent of the near-wall cycle, at least when normalized with the uncontrolled viscous length scale. As can be seen from table 4.1, the difference between λ^+ and $\tilde{\lambda}^+$ is more pronounced in this case, because the change in Re_τ is much larger in the drag-increasing than in the drag-reducing configurations. The spectrum for $\angle\hat{A}_d = +\pi/2$ looks remarkably different from the ones discussed previously. It is apparent that the control input is dominated by structures that are relatively short in the streamwise direction, but wide in the span. In fact, the signature of the near-wall cycle is not apparent and instead the region around $\lambda_x^+ \approx 170$, which was vaguely perceptible in some of the other spectra, is now very energetic. The spectrum confirms the earlier visual observations, which suggested that the actuation signal is less coherent in the streamwise direction, but shows some organization along the span.

We close this section by mentioning once again that the wall-normal velocity at the wall is related to v at the sensor location through the varying-phase opposition control law, eq. (3.10). The power spectrum of the actuation is therefore also a proxy for the spectrum of v at y_d and for the near-wall region in general. The qualitative features of the spectra shown in fig. 4.4 persist until at least $y_d^+ = 31$, which is the last plane at which spectra were accumulated during the DNS runs. It therefore seems that the structure of the controlled flows does not change much within the near-wall region.

4.6 Conclusion: Two Families of Scales

The present chapter characterized the structure of controlled flows from an instantaneous and a statistical point of view by example of four controllers with identical y_d, but different $\angle\hat{A}_d$. The two example drag-reducing controllers attenuate the wall-normal velocity fluctuations in the near-wall region compared to the uncontrolled case, and their control input shows an imprint of the near-wall cycle structures. The two example drag-increasing controllers have a much larger control input compared to the drag-reducing configurations, but rather than attenuating the wall-normal velocity fluctuations, they amplify v_{rms} in the near-wall region. The scales contributing to the control input are quite different for each of the drag-increasing examples. The most energetic control scales for large negative phase shifts are similar to the drag-reducing configurations and are reminiscent of near-wall cycle structures. On the other hand, the most energetic spatial scales for large positive phase shifts are much shorter and wider and do not resemble near-wall cycle structures at all.

The picture that emerges from the present analysis is that of two important families of scales. Streamwise-elongated scales, which are reminiscent of the near-wall cycle and dominate the control input for $-3\pi/4 \leq \angle\hat{A}_d \leq 0$, and spanwise-elongated scales, which are most active for $\angle\hat{A}_d > 0$. Each family comprises a range of scales, which can be loosely defined from the spectra in fig. 4.4 as scales that lie close to each other in spectral space and behave similarly under various $\angle\hat{A}_d$. This raises hopes that the drag reduction behavior of varying-phase opposition control can be understood by considering an example scale of each family and such an analysis will be done in the following chapter.

Chapter 5

MECHANISMS OF DRAG CHANGE

Portions of this chapter have been previously published in:

Toedtli, S., Yu, C., and McKeon, B. (2019). "Structural and spectral analysis of varying-phase opposition control in turbulent channel flow". In: *Proceedings of TSFP 11*.

Toedtli, S., Yu, C., and McKeon, B. (2020). "On the origin of drag increase in varying-phase opposition control". In: *International Journal of Heat and Fluid Flow* 85, p. 108651. DOI: 10.1016/j.ijheatfluidflow.2020.108651.

The observations of the previous chapter suggest that two regions in spectral space, dubbed streamwise-elongated and spanwise-elongated scales, respectively, determine the drag reduction behavior of varying-phase opposition control for various phase shifts. The problem of understanding the drag reduction map, fig. 4.1, therefore may reduce to understanding the response of the two spectral regions to control.

The control response of individual spatial scales, which we characterize as Fourier modes with a wave number vector $\boldsymbol{\kappa} = [k_x, k_z]$ and which may belong to one of the two families, is composed of two parts. First, each scale responds to the change in boundary condition. This is a linear effect, because the boundary condition acts on each wave number individually and contains information from only that $\boldsymbol{\kappa}$. And second, each scale responds to changes that control induces at other scales. This is a nonlinear mechanism, and can be considered a secondary effect in the sense that at least one scale has to be modified by the boundary condition for the nonlinear mechanism to kick in. The goal of the present chapter is to understand whether the linear boundary condition effect alone is sufficient to characterize the control response of the streamwise-elongated and spanwise-elongated scales.

Following our previous approach, we fix the sensor location at $y_d^+ = 15$ and allow the phase shift to vary, so that $\angle \hat{A}_d \in [-3\pi/4, 3\pi/4]$. With this restriction, changes in boundary condition are limited to changes in phase shift, and our problem reduces to analyzing the response of individual scales to changes in $\angle \hat{A}_d$. In order to isolate the effect of the boundary condition, we seek to minimize the nonlinear interactions of controlled scales. This can be achieved by restricting control to a small set of wave

numbers, which cannot feed back on each other directly, and leaving all other spatial scales uncontrolled. We will refer to such controllers as "scale-restricted" and they will be used in this chapter to analyze the response of the streamwise-elongated and spanwise-elongated structures to control with various $\angle \hat{A}_d$.

The analysis of scale-restricted controllers will be based on a mix of direct numerical simulations and modal analyses. The DNS are used to study the response of the real flow to scale-restricted control, and nonlinear interactions are still present in this case. The controlled scales are the only ones to feel the boundary condition (i.e. linear) effect of control, while all scales feel the secondary (i.e. nonlinear) effect. This includes the controlled scales, but since they cannot feed back on each other, the nonlinear effect will be shown to be weak. On the other hand, modal analyses allow to fully single out the linear mechanism, because the nonlinear secondary effect only enters through the mean flow and forcing, which can both be chosen as part of the problem formulation. The modal analyses can thus provide further evidence that linear mechanisms relate the scale response to $\angle \hat{A}_d$. In addition, the linear analyses can characterize the amplification mechanisms by relating the behavior of each scale family to properties of the temporal eigenspectra and pseudospectra.

5.1 Prologue: Scale-by-Scale Fluctuation Suppression

Before introducing the scale-restricted controllers, it is instructive to revisit the concepts of fluctuation suppression and drag reduction from a scale-by-scale perspective, and the former will be mainly quantified in terms of $\overline{v'v'}$ rather than v_{rms} (see discussion in section 4.1). The discussion and results in Chapter 4 have shown that the two concepts are distinct, but often correlated. Fluctuation suppression is a local measure in y, which depends on $\overline{v'v'}$ at the sensor location, while drag reduction is a global measure in y, which depends on a weighted integral of $\overline{u'v'}$ in the vertical direction. It is important to note that despite their different nature in the wall-normal direction, both quantities are average measures in wave number space. To see this, consider Parseval's theorem (2.51), which shows that the spatial average of quadratic quantities implied in $\overline{u'v'}$ or $\overline{v'v'}$, corresponds to the sum over all wave numbers.

The analysis in the present chapter will consider controllers that only act on a small set of wave numbers and leave all the others uncontrolled. Average measures in wave number space remain important also in this setting to quantify the overall change of the flow. But they are only informative if the response of the controlled

scales is strong enough to significantly change the mean Reynolds stresses. In some cases, control may alter the scales it acts on, but the changes are weak in a mean sense and not detectable through the diagnostics developed in section 4.1. And even if the modification of the controlled scales is reflected in the mean, it may be more insightful to consider the effect of control on each scale individually. This suggests refining the notion of scale suppression and drag reduction to a scale-by-scale basis.

Ideally, one would keep track of four quantities when analyzing the scale-restricted controllers: scale suppression and drag reduction for individual Fourier modes, and averaged in wave number space. Since this chapter presents DNS and modal analysis data, the diagnostics would have to be formulated and evaluated for each frameworks, which quickly leads to a confusing multitude of statistics. To make the analysis more tractable, we limit the discussion to drag reduction when looking at mean quantities, and to fluctuation suppression when looking at the effect of control on a scale-by-scale basis. The results of Chapter 4 suggest that mean drag reduction and scale suppression correlate for the parameter range considered here, so that it is reasonable to assume that a decrease (increase) in mean drag goes hand in hand with a decrease (increase) of $\overline{v'v'}$ at the sensor location. The same correlation has not yet been verified for scale-by-scale diagnostics, so that one cannot necessarily relate a decrease (increase) in scale-by-scale fluctuation contribution to a decrease (increase) in scale-by-scale drag contribution. However, such a correlation seems well-supported if the integral drag change and scale fluctuation contribution point in the same direction. For example, if both the mean drag and scale-by-scale fluctuation contribution decrease under scale-restricted control, then it is likely that the mean drag contribution of the controlled scales also decreases. If the mean drag contribution remains unchanged, then the correlation is more speculative, even if it may be intuitive. We have chosen fluctuation suppression over drag reduction as a scale-by-scale diagnostic, because the former is related to the power spectra of the wall-normal velocity at the sensor location, as will be shown next. The discussion of fluctuation suppression therefore naturally includes an analysis of the near-wall flow structure, while drag reduction as an integral measure in y does not.

The goal for the remainder of this section is to derive a statistical measure to quantify the scale-by-scale fluctuation suppression in DNS and resolvent analysis. A similar approach could be used to define a scale-by-scale drag contribution, but the derivation is omitted here since this diagnostic is not reported. The starting point is the definition of the mean fluctuation suppression, eq. (4.2), but now expressed in

terms of $\overline{v'v'}$ rather than v_{rms}. Using eq. (2.51), we can write the scale suppression in terms of time-averaged Fourier coefficients

$$\begin{aligned}\Delta\overline{v'v'}(y_d) &= \left(\overline{v'v'}\right)_0(y_d) - \left(\overline{v'v'}\right)_c(y_d) \\ &= \sum_{l=-\infty}^{\infty}\sum_{m=-\infty}^{\infty} \left\langle|\hat{v}|_0^2\right\rangle_t(l,m,y_d) - \left\langle|\hat{v}|_c^2\right\rangle_t(l,m,y_d).\end{aligned} \tag{5.1}$$

The difference at each wave number can be positive or negative, and we recall that $\Delta\overline{v'v'}$ is the desired outcome. If the difference at a particular wave number combination is positive, then that scale contributes to mean fluctuation suppression, and we denote that scale "suppressed under control." Conversely, if the difference at a particular wave number combination is negative, then that scale amplifies the mean fluctuation, and we denote that scale "amplified under control." These will be our notions of scale-by-scale fluctuation suppression. In the following, we bring eq. (5.1) into forms that are suitable to evaluate with DNS data or resolvent calculations.

5.1.1 DNS Formulation

For DNS, it is most convenient to express the scale suppression in terms of the time-averaged power spectrum at the sensor location, $\Phi_{vv}(l,m,y_d)$. Using eqs. (2.56) and (2.59), we can rewrite eq. (5.1) as

$$\begin{aligned}\Delta\overline{v'v'}(y_d) &= \sum_{l=0}^{\infty}\sum_{m=0}^{\infty} (\Phi_{vv})_0(y_d) - (\Phi_{vv})_c(y_d) \\ &= \sum_{l=0}^{\infty}\sum_{m=0}^{\infty} \frac{\Delta\Phi_{vv}(y_d)}{(\Phi_{vv})_0(y_d)}(\Phi_{vv})_0(y_d)\end{aligned} \tag{5.2}$$

where

$$\frac{\Delta\Phi_{vv}(y_d)}{(\Phi_{vv})_0(y_d)} = 1 - \frac{(\Phi_{vv})_c(y_d)}{(\Phi_{vv})_0(y_d)} \tag{5.3}$$

and we omitted the dependence of the spectrum on the streamwise and spanwise wave number for compactness. Recall that the notion of scale suppression or amplification depends on the sign of the corresponding term in eq. (5.2), each of which is the product of two factors. The factor $(\Phi_{vv})_0$ is non-negative and describes the overall energetic importance of that scale in the uncontrolled flow. The other factor, $\Delta\Phi_{vv}/(\Phi_{vv})_0$, can be positive or negative and determines the sign of the product. In order to decide whether a particular scale is amplified or suppressed, it is thus sufficient to consider $\Delta\Phi_{vv}/(\Phi_{vv})_0$. The interpretation of its sign and

magnitude are as follows

$$\frac{\Delta\Phi_{vv}}{(\Phi_{vv})_0} \in \begin{cases} [0,1] & \text{scale is suppressed (more positive is better)} \\ (-\infty, 0) & \text{scale is amplified (more negative is worse).} \end{cases} \tag{5.4}$$

5.1.2 Resolvent Analysis Formulation

Next, we derive a suitable expression for resolvent analysis. An important formal difference between DNS and resolvent analysis is their treatment of the temporal coordinate. In contrast to DNS, the resolvent framework operates with temporal frequencies, which implies an additional dimension in Fourier domain. A single scale in the resolvent sense is therefore characterized by a wave number triplet $\boldsymbol{k} = [k_x, k_z, \omega]$, with the temporal frequency ω as additional descriptor. This also means that the resolvent framework refines the notion of scale suppression to contributions of individual temporal frequencies.

In order to find a suitable definition for scale suppression, we first need to express $\overline{v'v'}$ as a function of wave numbers and temporal frequencies. Using eq. (2.53), we can write

$$\overline{v'v'}(y) = \sum_{l=-\infty}^{\infty} \sum_{m=-\infty}^{\infty} \int_{-\infty}^{\infty} |\hat{v}|^2(l, m, y, \omega)\, \mathrm{d}\omega. \tag{5.5}$$

The individual Fourier modes $\hat{v}(l, m, y, \omega)$ can now be approximated by resolvent modes up to a desired order. As shown in Appendix C, the scale suppression for a rank-1 broadband forcing resolvent model can be written as

$$\begin{aligned} \Delta\overline{v'v'}(y_d) &= \sum_{l=0}^{\infty} \sum_{m=0}^{\infty} \int_{-\infty}^{\infty} \left(B_{lm}\, \sigma_1^2\, |\hat{v_1}|^2(y_d)\right)_0 - \left(B_{lm}\, \sigma_1^2\, |\hat{v_1}|^2(y_d)\right)_c \, \mathrm{d}\omega \\ &= \sum_{l=0}^{\infty} \sum_{m=0}^{\infty} B_{lm} \int_{-\infty}^{\infty} \frac{\Delta\left(\sigma_1^2 |\hat{v}_1|^2(y_d)\right)}{\left(\sigma_1^2 |\hat{v}_1|^2(y_d)\right)_0} \left(\sigma_1^2 |\hat{v}_1|^2(y_d)\right)_0 \, \mathrm{d}\omega \end{aligned} \tag{5.6}$$

where

$$\frac{\Delta\left(\sigma_1^2\, |\hat{v}_1|^2(y_d)\right)}{\left(\sigma_1^2\, |\hat{v}_1|^2(y_d)\right)_0} = 1 - \frac{\left(\sigma_1^2\, |\hat{v}_1|^2(y_d)\right)_c}{\left(\sigma_1^2\, |\hat{v}_1|^2(y_d)\right)_0} \tag{5.7}$$

and

$$B_{lm} = \begin{cases} 1 & \text{if } l = m = 0 \\ 2 & \text{if either } l = 0 \text{ or } m = 0 \\ 4 & \text{else} \end{cases}. \tag{5.8}$$

Further note that we have omitted the dependence on $\boldsymbol{k}$ for compactness. The notion of scale suppression again depends on the sign of each term, whose structure is very

analogous to the DNS formulation. The factor $\left(\sigma_1^2|\hat{v}_1|^2\right)_0$ is non-negative and describes the energetic importance of that scale under a broadband forcing assumption. The sign of each term is therefore determined by the factor $\Delta\left(\sigma_1|\hat{v}_1|^2\right)/\left(\sigma_1^2|\hat{v}_1|^2\right)_0$, and it is sufficient to consider its value in order to determine if a scale is amplified or suppressed

$$\frac{\Delta\left(\sigma_1^2|\hat{v}_1|^2\right)}{\left(\sigma_1^2|\hat{v}_1|^2\right)_0} \in \begin{cases} [0,1] & \text{scale is suppressed (more positive is better)} \\ (-\infty,0) & \text{scale is amplified (more negative is worse).} \end{cases} \tag{5.9}$$

In order to make the distinction between frequency-dependent resolvent scales and time-averaged DNS scales clear, we will usually refer to eq. (5.9) as "resolvent mode suppression." A comparison between eqs. (5.2) and (5.6) further shows that the two definitions are related by

$$\Delta\Phi_{vv} \approx B_{lm} \int_{-\infty}^{\infty} \Delta\left(\sigma_1^2|\hat{v}_1|^2\right) \mathrm{d}\omega = B_{lm}\, k_x \int_{-\infty}^{\infty} \Delta\left(\sigma_1^2|\hat{v}_1|^2\right) \mathrm{d}c. \tag{5.10}$$

The approximate equality indicates that a rank-1 broadband forcing resolvent approximation does not reproduce the true statistics. The last equality only holds if $k_x \neq 0$, so that the wave speed $c = \omega/k_x$ is well-defined. The parametrization in terms of wave speed is advantageous, because the energetic content of the real flow is limited to a narrow band of c (Bourguignon et al., 2014), which allows to restrict the range of wave speeds to consider (see section 3.4.2). Our analysis will consider spatial scales with $k_x \neq 0$ and we will therefore report resolvent mode suppression as a function of wave speed rather than temporal frequency.

When studying the spanwise-elongated scales, we will also work with an approximation to eq. (5.7), which is given by

$$\frac{\Delta\sigma_1^2}{\left(\sigma_1^2\right)_0} = 1 - \frac{\left(\sigma_1^2\right)_c}{\left(\sigma_1^2\right)_0} \tag{5.11}$$

and does not account for changes in singular vectors due to control. The approximation is useful because it emphasizes the behavior of the singular values, which will be shown to be the main driver for amplification of spanwise-elongated scales. It should be pointed out that the approximation qualitatively reproduces the trends of eq. (5.7) for the cases considered and that the interpretation of $\Delta\sigma_1^2/\left(\sigma_1^2\right)_0$ is analogous to eq. (5.9).

5.2 Scale-Restricted Control

After alluding to them for several times, we now finally define the scale-restricted controllers. Again, the general idea is to only control a small number of spatial scales and leave all others uncontrolled. Individual spatial scales are characterized as Fourier modes and identified by means of their spatial wave number vector $\boldsymbol{\kappa} = [k_x, k_z]$. We will denote the controlled scales by $\boldsymbol{\kappa}_c$, which can refer to an individual scale or a set of scales, depending on the context. If $\boldsymbol{\kappa}_c$ contains more than two spatial scales, we require them to not be triadically consistent, i.e. $\boldsymbol{\kappa}_1 + \boldsymbol{\kappa}_2 \neq \boldsymbol{\kappa}_3$ for any triplets in $\boldsymbol{\kappa}_c$. This requirement ensures that the controlled scales cannot feed back on each other and minimizes the secondary (nonlinear) control effect for scales in $\boldsymbol{\kappa}_c$. The scale-restricted controllers now simply apply varying-phase opposition control to the scales in $\boldsymbol{\kappa}_c$, and leave all other spatial scales uncontrolled. The scale restriction corresponds to a modified controller gain $\hat{A}_{d,\boldsymbol{\kappa}}$

$$\hat{A}_{d,\boldsymbol{\kappa}} = \begin{cases} \hat{A}_d & \text{if } \boldsymbol{\kappa} \in \boldsymbol{\kappa}_c \\ 0 & \text{else} \end{cases} \tag{5.12}$$

where $\hat{A}_d$ without subscript $\boldsymbol{\kappa}$ is the gain according to eq. (3.6) and eq. (3.10) for resolvent and DNS, respectively. If $\boldsymbol{\kappa}_c$ contains a single spatial scale, for example $\boldsymbol{\kappa}_c = \{[k_x h = 6.5, k_z h = 0]\}$, we will refer to the control law as "single scale control," or SS control for short. If $\boldsymbol{\kappa}_c$ contains all spanwise scales at a single streamwise wave number, for example $\boldsymbol{\kappa}_c = \{[k_x h = 0.5, k_z]\}$, we will refer to the control law as "single wave number control," or SW control for short.

5.2.1 Scale Selection

The control scales $\boldsymbol{\kappa}_c$ are an additional parameter of the scale-restricted scheme, besides the sensor location y_d and phase shift $\angle \hat{A}_d$ that it inherits from varying-phase opposition control. The selection of the control scale is guided by the observations of Chapter 4, which suggest choosing scales that belong to either the streamwise-elongated or spanwise-elongated family. In order to separate their effects, we consider a scale-restricted controller for each family in isolation. The selection of $\boldsymbol{\kappa}_c$ within each family of scales is somewhat arbitrary, but ideally the control scales are energetic enough, so that their effect is detectable in the flow in a mean sense. In order to identify energetic scales, we revisit the actuation spectra of varying-phase opposition control in fig. 4.4 and outline the scale selection for each family below.

5.2.2 Example Streamwise-Elongated Scale

The streamwise-elongated scales are active for $\angle\hat{A}_d \leq 0$, and one of the main aspects we hope to understand from this family is the drag reduction behavior for negative phase shifts. We therefore consider the actuation spectrum at $\angle\hat{A}_d = -\pi/4$ (maximum DR), show in fig. 4.4b, to select $\boldsymbol{\kappa}_c$. Based on the requirement that control should lead to as large of a flow response as possible, we select the most energetic scale, which we identified in table 4.1, and which occurs at $\boldsymbol{\lambda}_s = \left[\lambda^+_{xs} \approx 2262, \lambda^+_{zs} \approx 103\right]$. The subscript s labels the example streamwise-elongated scale from here on and is shorthand for "streak," which characterizes the spatial shape of the actuation associated with this scale (see e.g. fig. 4.2d). The scale can equivalently be characterized in terms of its wave numbers normalized by the channel half-height, which corresponds to $\boldsymbol{\kappa}_s = [k_{xs}h = 0.5, k_{zs}h = 11]$. The first scale-restricted controller of the streamwise-elongated family is a SS controller defined by

$$\boldsymbol{\kappa}_c = \{\boldsymbol{\kappa}_s = [k_{xs}h = 0.5, k_{zs}h = 11]\}. \tag{5.13}$$

Section 5.3.1 will show that the flow response to control with $\boldsymbol{\kappa}_s$ is rather weak, so that the drag does not change significantly. We therefore consider an additional controller which acts on all spanwise scales at $k_{xs}h = 0.5$, and which we will denote by $\{\boldsymbol{\kappa}\}_{k_{xs}}$. The control scales for this case are given by

$$\boldsymbol{\kappa}_c = \left\{\{\boldsymbol{\kappa}\}_{k_{xs}} = [k_{xs}h = 0.5, k_z]\right\} \tag{5.14}$$

and this corresponds to a SW controller by our earlier name convention. Note that all control scales share the same streamwise wave number, which makes them triadically inconsistent.

5.2.3 Example Spanwise-Elongated Scale

The spanwise-elongated scales are particularly active at large positive phase shifts, and we thus consider the actuation spectrum for $\angle\hat{A}_d = +\pi/2$, shown in fig. 4.4d, to select $\boldsymbol{\kappa}_c$. A wide range of spanwise-elongated scales centered around $\lambda^+_x \approx 174$ contributes to the control signal at this phase shift. Following the same approach as for the streamwise-elongated family, we choose the most energetic scale, which corresponds to $\boldsymbol{\lambda}_r = \left[\lambda^+_{xr} \approx 174, \lambda^+_{zr} \to \infty\right]$ or, equivalently, $\boldsymbol{\kappa}_r = [k_{xr}h = 6.5, k_{zr}h = 0]$. The subscript r labels the example spanwise-elongated scale from here on and is shorthand for "roller," since this scale will later be shown to induce spanwise rollers for a range of phase shifts. The scale-restricted controllers of the spanwise-elongated

family only act on this one scale so that

$$\boldsymbol{\kappa}_c = \{\boldsymbol{\kappa}_r = [k_{xr}h = 6.5, k_{zr}h = 0]\}. \tag{5.15}$$

Note that this corresponds to a single scale controller by our earlier name convention.

5.3 Response of Streamwise-Elongated Scales to Control

This section explores the response of streamwise-elongated scales to varying-phase opposition control with various $\angle\hat{A}_d$. The analysis is based on the two scale-restricted controllers introduced earlier: the SS controller with $\boldsymbol{\kappa}_s$ defined in eq. (5.13), and the SW controller with $\{\boldsymbol{\kappa}\}_{k_{xs}}$ defined in eq. (5.14). The sensors are fixed at $y_d^+ = 15$ and the phase shift is varied from $-3\pi/4$ to $3\pi/4$. The first two parts of the analysis use DNS data to characterize mean drag reduction and scale suppression, and the following two parts use modal analyses to explore the temporal eigenspectrum and analyze resolvent mode suppression.

5.3.1 Streamwise-Elongated Scales: DNS Drag Reduction

We start the discussion by considering the drag reduction of the scale-restricted controllers. The green open squares in fig. 5.1 represent the drag reduction under single scale control with $\boldsymbol{\kappa}_s$. Note that the figure has two ordinates with different colors, one on the left and one on the right. Each ordinate quantifies the drag reduction for the curve with the same color, and the green ordinate on the left is the relevant one for SS control. Recall from the definition of DR in eqs. (3.11) to (3.13) that a positive value (symbol above the black horizontal in fig. 5.1) corresponds to drag reduction, while a negative value (symbol below the black horizontal) indicates drag increase. It is apparent from fig. 5.1 that the DR is a function of the phase shift. The most pronounced flow response occurs for $\angle\hat{A}_d = +3\pi/4$, which leads to a 12% drag increase. A smaller drag increase of about 1% can also be observed for $\angle\hat{A}_d = -3\pi/4$. The drag changes for the remaining phase shifts are smaller, and while fig. 5.1 may hint at a slight drag decrease for $-\pi/4 \leq \angle\hat{A}_d \leq +\pi/4$, these differences are not large enough to be statistically significant.

It is somewhat surprising that the strongest flow response occurs for large positive phase shifts. The streamwise-elongated scales were not particularly pronounced in the actuation spectrum for $\angle\hat{A}_d = +\pi/2$ shown in fig. 4.4d, and the same observation holds for the corresponding spectrum at $\angle\hat{A}_d = +3\pi/4$ (data not shown). Even so, the drag reduction trends from fig. 5.1 indicate that the streamwise-elongated scales contribute to drag increase at large positive phase shifts. An interpretation consistent

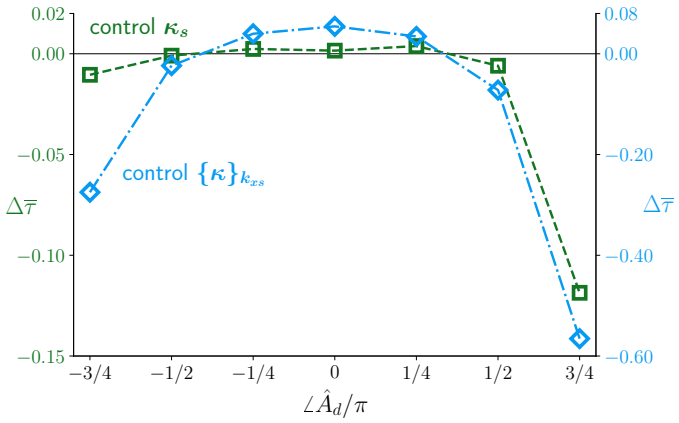

Figure 5.1: Drag reduction of varying-phase opposition control with sensors located at $y_d^+ = 15$ as a function of the phase shift $\angle\hat{A}_d$. The green open squares show SS control with $\boldsymbol{\kappa}_s$, while the blue diamonds indicate SW control with $\{\boldsymbol{\kappa}\}_{k_{xs}}$. Each curve has its own ordinate, which can be identified by the matching text color, and its own scale.

with the spectrum and fig. 5.1 is that streamwise-elongated scales do contribute to drag increase, but to a much smaller extent than the spanwise-elongated scales, so that their imprint in the spectrum is not very prominent. The slight drag increase for $\angle\hat{A}_d = -3\pi/4$ on the other hand is consistent with the actuation spectrum in fig. 4.4a, which showed that the streamwise-elongated scales are the most energetic and therefore likely drive the flow response in this parameter range. The drag changes for $-\pi/2 \leq \angle\hat{A}_d \leq +\pi/2$ are within the statistical uncertainty and should not be used to draw further conclusions. An explanation for why the drag change in this regime is so weak will be given in section 5.3.2.

We first reconsider whether control with the single scale $\boldsymbol{\kappa}_s$ is adequate for our purposes. The study of scale-restricted controllers is most insightful if the simplified controllers reproduce the drag trend of the full scheme in at least parts of the parameter space. This is because matching trends suggest that linear mechanisms that link phase shift to scale response are at least partially responsible for the drag change in varying-phase opposition control. We chose the streamwise-elongated scales mainly to understand the drag reduction for slightly negative phase shifts, but the flow response in precisely this parameter range is too weak to establish a trend.

In order to clarify whether linear mechanisms at the streamwise-elongated scales are significant for the behavior of the full control scheme in the range $-\pi/2 \leq \angle\hat{A}_d \leq +\pi/2$, we can add more scales from the streamwise-elongated family to the restricted controller. Adding more scales increases the magnitude of the control input and

possibly leads to a stronger mean flow response. The streamwise-elongated family consists of a range of scales located close to $\boldsymbol{\kappa}_s$ in spectral space, as can be seen from fig. 4.4b. Ideally, the additional scales should also be energetic for control with $\angle\hat{A}_d = -\pi/4$ and triadically inconsistent, so that they cannot feed back on each other. The most energetic scales in fig. 4.4b all occur at $k_x h = k_{xs} h = 0.5$, which suggests controlling all spanwise wave numbers at this particular k_x. This corresponds to the single wave number controller with scales $\{\boldsymbol{\kappa}\}_{k_{xs}}$ defined in eq. (5.14). It is important to point out that even though the SW controller acts on all spanwise wave numbers at a given k_x, this only corresponds to approximately 1% of all Fourier modes.

The drag reduction behavior of the SW controller is shown as blue curve in fig. 5.1, and the DR is quantified by the blue ordinate on the right. Note that the scale of the ordinate is larger by a factor of four, which confirms that adding more control scales increases the flow response and indicates that the drag changes are statistically significant over the entire parameter range. It is apparent that the SS and SW controller have similar trends, which confirms that all scales in $\{\boldsymbol{\kappa}\}_{k_{xs}}$ respond similarly to control, even if there is a weak dependence in k_z, since the two curves are not just offset by a constant factor. For SW control, we observe drag reduction for $-\pi/4 \leq \angle\hat{A}_d \leq +\pi/4$, with a maximum DR of 5% at $\angle\hat{A}_d = 0$. Large negative or positive phase shifts again increase the drag. A maximum drag increase of 56% occurs at $\angle\hat{A}_d = +3\pi/4$, while the increase at $\angle\hat{A}_d = -3\pi/4$ is only about half as large.

Since the drag changes for SW control are statistically significant, we can now relate the response of the streamwise-elongated family to the drag change of the full control scheme. Figure 5.2 compares the drag reduction of the two control schemes as a function of the phase shift. It is important to point out again that each curve has its own ordinate, with the one on the left axis corresponding to varying-phase opposition control and the one on the right to SW control. The qualitative behavior of the two curves matches well, which suggests that the response of streamwise-elongated scales to $\angle\hat{A}_d$ is relevant for the behavior of varying-phase opposition control over the entire parameter range. The relevance of the streamwise-elongated scales for $\angle\hat{A}_d \leq 0$ could already be inferred from the spectra in fig. 4.4, but the matching trend for positive phase shifts reinforces the earlier observation that these scales also contribute to the drag increase, even if their imprint in the actuation spectrum is weak. One interesting difference to note between the two curves is the symmetry

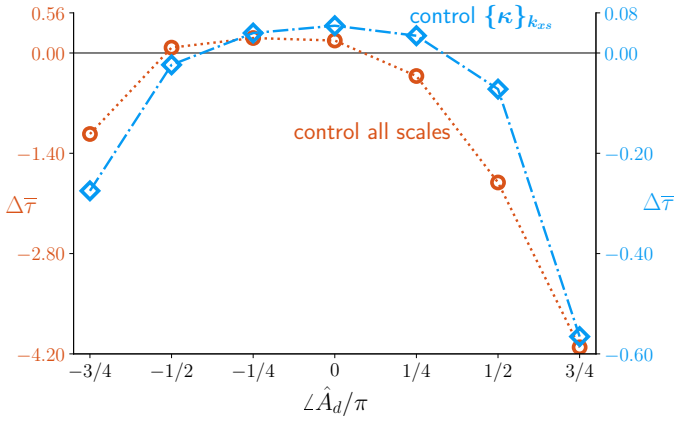

Figure 5.2: Drag reduction of varying-phase opposition control with sensors located at $y_d^+ = 15$ as a function of the phase shift $\angle\hat{A}_d$. The blue open diamonds denote SW control with $\{\kappa\}_{k_{xs}}$, while the orange circles show varying-phase opposition control with all scales and correspond to the orange line in fig. 4.1. Note that each curve has its own ordinate, which can be identified by the matching text color, and its own scale.

about $\angle\hat{A}_d = 0$. The maximum DR for SW control occurs at $\angle\hat{A}_d = 0$, and the curve is approximately symmetric for small phase shifts. On the other hand, the maximum DR for varying-phase opposition control occurs at $\angle\hat{A}_d = -\pi/4$, and there is no apparent symmetry about zero phase shift. In fact, varying-phase opposition control increases drag at $\angle\hat{A}_d = +\pi/4$, while the SW scheme still achieves drag reduction. The streamwise-elongated scales in isolation can therefore not explain why a slightly negative phase shift leads to maximum drag reduction in varying-phase opposition control. The analysis in section 5.5.1 will show that one has to include the spanwise-elongated scales to understand this aspect. The other notable difference occurs at $\angle\hat{A}_d = -\pi/2$, where the single wave number scheme leads to a slight drag increase, while the full scheme can achieve a drag reduction. The difference at this phase shift has not yet been fully investigated, but is likely due to a heterogeneous (i.e. weakly wave number dependent) response of the streamwise-elongated scales at this phase shift.

It is important to emphasize again the relevance of qualitative versus quantitative agreement between the drag reduction curves in figs. 5.1 and 5.2. The drag reduction trends do not match quantitatively, which is reflected in the need for two ordinates in each plot. The drag change under varying-phase opposition control is about a factor of seven larger compared to SW control. And the drag change under single wave number control in turn is about a factor of four larger compared to SS control.

Recall that the scale-restricted controllers only act on a small subset of the Fourier modes, so that these quantitative differences are expected. They simply indicate that scales other than $k_x = k_{xs}$ contribute to the drag change. The important observation here is the generally good qualitative agreement between the curves, which suggests that the streamwise-elongated family contributes to the control response of the flow. Since we minimized the nonlinear interactions between controlled scales, we can make an even stronger statement and directly relate the response of the streamwise-elonagted scales, and in extension the DR of varying-phase opposition control, to changes in $\angle \hat{A}_d$. Furthermore, fig. 5.1 suggests that $\boldsymbol{\kappa}_s$ is a suitable representative of the streamwise-elongated family and will be used instead of $\{\boldsymbol{\kappa}\}_{k_{xs}}$ whenever the study of a single scale in isolation is advantageous.

5.3.2 Streamwise-Elongated Scales: DNS Scale Suppression

The previous section considered the drag change and confirmed that the streamwise-elongated scales determine at least a part of the flow response to varying-phase opposition control. The drag change is an average measure in wave number space, and we next turn our attention to the effect of control on individual scales. For the reasons given in section 5.1, this discussion is focused on scale suppression. Recall that the quantification of scale suppression for DNS data is based on the power spectrum of the wall-normal velocity at the sensor plane. We will therefore first discuss a few example controlled spectra, which also allows to analyze the flow structure under scale-restricted control.

Figure 5.3 shows the power spectrum of the wall-normal velocity Φ_{vv} at the sensor location of the uncontrolled flow (top) and two example SW controllers (bottom). The spectra are shown as a function of wave number and the range $k_x h > 5$, and $k_z h > 30$ are omitted. The close-up view helps highlight the important changes to the flow, but it should be noted that the omitted wave numbers carry a non-negligible amount of energy, especially in fig. 5.3b. Figure 5.3a shows the spectrum of the uncontrolled flow, with respect to which we define scale suppression. If a controlled scale is less energetic than in fig. 5.3a, we say the scale is suppressed. In contrast, if a scale is more energetic, we say the scale is amplified. The most energetic spatial scales in the wall-normal velocity signal of the uncontrolled flow at $y^+ = 15$ are located around $[k_x h = 0.5, k_z h = 11]$. Single wave number control with $\{\boldsymbol{\kappa}\}_{k_{xs}}$ targets this region in spectral space and acts on all spanwise wave numbers at $k_x h = 0.5$, which are indicated by the vertical blue line. Figures 5.3b and 5.3c show the corresponding spectra for two example SW controllers with various phase

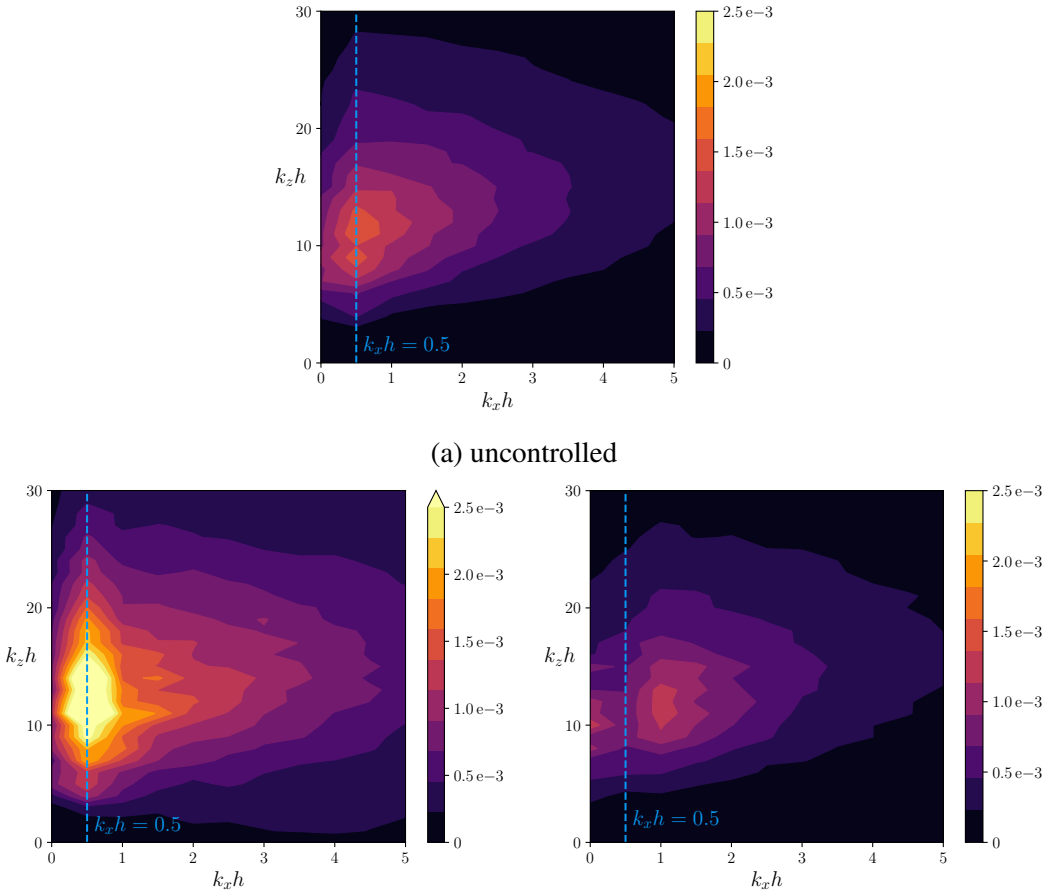

(a) uncontrolled

(b) $\angle \hat{A}_d = -3\pi/4$

(c) $\angle \hat{A}_d = -\pi/4$

Figure 5.3: Time-averaged power spectrum $\Phi_{vv}/\left(u_\tau^2\right)_0$ of the wall-normal velocity at the sensor location $y_d^+ = 15$ as a function of the streamwise (k_x) and spanwise wave number (k_z). Figure 5.3a shows the spectrum of the uncontrolled flow, while figs. 5.3b and 5.3c show controlled spectra for different phase shifts $\angle \hat{A}_d$. The blue vertical line in each figure indicates the control scales $\{\boldsymbol{\kappa}\}_{k_{xs}}$ to aid the visual comparison of the figures. Note that the color scale in fig. 5.3b is saturated, so that the same color scale can be used in each figure.

shifts. The figure on the bottom left shows control with $\angle \hat{A}_d = -3\pi/4$, which leads to a 27% drag increase, while the figure on the bottom right shows the controller with $\angle \hat{A}_d = -\pi/4$, which decreases drag by 4%. The shape of the controlled spectra is quite similar to the uncontrolled one, which indicates that control may damp or amplify certain scales, but does not fundamentally alter the flow structure.

The control scales in the drag-increasing configuration of fig. 5.3b are significantly amplified, in particular for $9 \leq k_z h \leq 16$. In other words, control of the streamwise-elongated scales with large negative phase shifts does not achieve the

control objective. The spectra together with the mean drag increase further suggest that the controlled scales are at least partially responsible for the DI. It is also interesting to note that other scales, like the ones along $k_x h = 1.0$, become more energetic, even though they are not controlled. These scales highlight the potential importance of secondary, nonlinear control effects. The scales $k_x h = 1.0$ are the first harmonic of the control input, and can receive energy from the self-interaction of the controlled scales. It is quite conceivable that these scales also contribute to the drag increase. We note that the difference between the controlled and uncontrolled spectrum could be used to quantify nonlinear effects, and to understand how the control input propagates through the nonlinear flow, but this aspect is not further investigated in the present study. We also note that the control spectra for large positive phase shifts look similar to fig. 5.3b, but the scale amplification is more pronounced (data not shown). This suggests that the drag increase mechanism for large positive phase shifts is identical and relies on amplification of the controlled scales.

On the other hand, the drag-reducing configuration suppresses the control scales, as can be seen from fig. 5.3c. The change is most pronounced for $9 \leq k_z h \leq 16$, and a saddle appears in this part of the spectrum. The control scales still contain some energy, which indicates that the controller achieves its goal only partially. These observations apply to all drag-reducing phase shifts, and together with the mean drag change, they suggest that suppression of the controlled scales is the main drag reduction mechanism. Uncontrolled scales may be slightly attenuated as well, but the nonlinear effects seem less strong than in the drag-increasing case.

The observations thus far were qualitative, and in the following, we will make quantitative statements about scale suppression for the entire range of phase shifts. This is best done for a single scale, and we therefore turn from the SW controller back to the SS controller with $\boldsymbol{\kappa}_s$. Figure 5.4 shows the suppression of the control scale $\boldsymbol{\kappa}_s$ as a function of $\angle \hat{A}_d$. Recall that scale suppression occurs for positive values (symbols above the black line) with a maximum value of one, which means that the controller annihilates the fluctuation contribution of that scale completely. On the other hand, negative values (symbols below the black line) indicate scale amplification and more negative values mean that control amplifies the scale more strongly.

Scale suppression occurs for $-\pi/2 \leq \angle \hat{A}_d \leq +\pi/4$, while smaller and larger phase shifts result in scale amplification. The controller achieves its control objective in

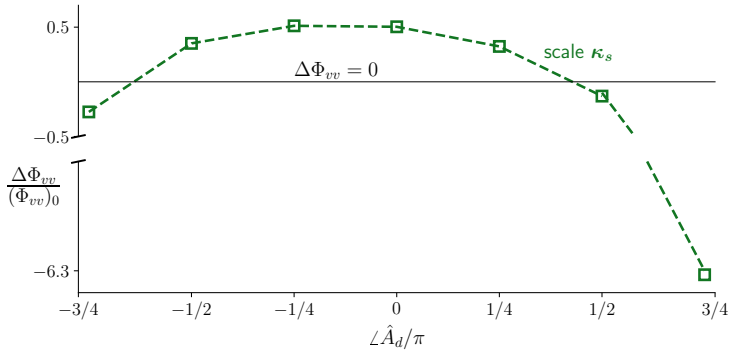

Figure 5.4: Suppression of scale $\boldsymbol{\kappa}_s$ for SS control with that same scale and sensors located at $y_d^+ = 15$ for various phase shifts $\angle\hat{A}_d$. Note that a portion of the ordinate is cut out to accommodate the strong scale amplification for $\angle\hat{A}_d = +3\pi/4$. The black horizontal line delineates the region of scale suppression (above) and scale amplification (below).

the scale-suppressing range only partially, and the largest attenuation of about 50% occurs at $\angle\hat{A}_d = -\pi/4$ and $\angle\hat{A}_d = 0$. The largest scale amplification is observed for $\angle\hat{A}_d = +3\pi/4$ and corresponds to 630%. The amplification curve is not symmetric about $\angle\hat{A}_d = 0$, and positive phase shifts lead to larger scale amplification than negative ones. A similar bias was already apparent in the drag reduction curves of fig. 5.1.

The control scale $\boldsymbol{\kappa}_s$ is the most energetic scale in the uncontrolled flow at $y_d^+ = 15$ and accounts for about 0.84% of the $\overline{v'v'}$ Reynolds stress at that y. Even so, the scale suppression is not strong enough to change the flow response in a mean sense and induce a statistically significant drag change, as can be seen by comparing figs. 5.1 and 5.4. Interestingly, a weak mean drag increase is perceivable for $\angle\hat{A}_d = -3\pi/4$, even if the scale amplification is of the same order of magnitude. The reason for this difference has not been investigated in detail. But fig. 5.3 suggests that a possible explanation may be the stronger nonlinear effects in case of scale amplification, which energize scales beyond $\boldsymbol{\kappa}_s$, and thus lead to a stronger control response. The strongest scale amplification at $\angle\hat{A}_d = +3\pi/4$ also coincides with the most pronounced drag increase.

Figure 5.3 suggests that the control response of most spanwise scales at k_{xs} is similar to that of $\boldsymbol{\kappa}_s$. We can therefore also compare the scale suppression trends of $\boldsymbol{\kappa}_s$ with the drag reduction of SW control, which acts on all $\{\boldsymbol{\kappa}\}_{k_{xs}}$. The overall good correlation between scale suppression and drag reduction support the hypothesis that the mean flow response is at least partially driven by changes at the control scales.

The one exception is, just as in the previous section, $\angle\hat{A}_d = -\pi/2$, which presents an interesting edge case. Figure 5.4 shows that $\boldsymbol{\kappa}_s$ is suppressed quite effectively, but the drag under SW control increases, while a drag decrease results under varying-phase opposition control (fig. 5.2). These differences suggest that the control response of the streamwise-elongated family at $\angle\hat{A}_d = -\pi/2$ is heterogeneous, which is confirmed by $\Phi_{vv}(y_d)$ under the SW control at this phase shift (data not shown). Conclusions from $\boldsymbol{\kappa}_s$ and $\{\boldsymbol{\kappa}\}_{k_{xs}}$ about the entire streamwise-elongated family at this phase shift should therefore be considered with some skepticism.

Figure 5.4 further shows why a mean drag reduction is less likely observed under single scale control than a drag increase. In the best case scenario, control can suppress the one scale it acts on completely and remove its mean Reynolds stress contribution from the flow. The example of $\boldsymbol{\kappa}_s$ shows that any single spatial scale contributes at most around 1% to the Reynolds stress components, at least at a fixed y, so that the resulting change is small. In addition, the controller does typically not suppress the scale completely (see fig. 5.4), so that the resulting mean change to the flow is negligible. Of course, control could affect other scales nonlinearly, but the spectrum in fig. 5.3c suggests that nonlinear effects are weak in case of scale suppression. From this perspective, it is not surprising that SS control did not change the mean flow for the scale-suppressing regime and that multiple scales had to be included in order to observe drag reduction. On the other hand, scale amplification is not bounded. A scale can become much more energetic than in its uncontrolled state, as the example of $\angle\hat{A}_d = 3\pi/4$ with an amplification of 630% shows. The mean flow response in case of scale amplification can therefore be much more pronounced, as we observed in fig. 5.1. In addition, the spectrum in fig. 5.3b shows that nonlinear effects lead to amplification of uncontrolled scales as well.

5.3.3 Streamwise-Elongated Scales: Temporal Eigenspectrum

The previous analysis of DNS data showed that the response of streamwise-elongated scales to phase shifts is mixed. Large positive or negative phase shifts lead to scale amplification and a significant mean drag increase under SS and SW control. Smaller phase shifts result in scale suppression, but the mean flow response is weak in this case. Drag reduction is therefore only observed under SW control. Overall, the drag reduction trends suggest that the streamwise-elongated scales contribute to the flow response to varying-phase opposition control at least partially. We also noted nonlinear effects in the DNS, in particular we observed uncontrolled scales becoming more energetic when the scales $\{\boldsymbol{\kappa}\}_{k_{xs}}$ were amplified under control. We now switch

gears and use tools from modal analysis rather than DNS to interrogate the behavior of the streamwise-elongated scales. Per the discussion in the chapter introduction, modal analyses allow full isolation of linear mechanisms and can provide further evidence that the scales respond primarily to their boundary condition. The modal analyses follow the approach of the DNS and consider the single scale controller with $\boldsymbol{\kappa}_s$ as a representative for the streamwise-elongated scales. The sensors are again fixed at $y_d^+ = 15$, so that the phase shift $\angle\hat{A}_d$ is the only free control parameter. The current section analyzes SS control by means of the temporal eigenspectrum (natural system response), while the following section considers resolvent analyses (forced system response).

The main objective of this section is to understand how the temporal eigenvalues move in the complex plane as a function of the phase shift and whether there is a correlation between the location of the eigenvalues and scale suppression or drag change in DNS. We will use the eddy viscosity approximation of the uncontrolled mean profile as linearization point and incorporate the effect of control only through a change in boundary conditions (this corresponds to the first problem formulation of section 2.4). As pointed out earlier, this is a model assumption made in order to minimize the dependence on empirical mean profile data. The change in mean due to SS control with $\boldsymbol{\kappa}_s$ is insignificant (recall that the largest drag change is 12%), so that the effect of the mean profile is limited anyways in this part of the study. Implications of the mean profile choice in case of stronger control effects will be discussed in section 5.4.4. It is worth pointing out that our approach is similar to the analysis of Jiménez, Uhlmann, et al. (2001) of flow over porous surfaces. However, in contrast to their analysis, we use the eddy viscosity only to approximate the mean profile and do not incorporate it into the eigenvalue problem to model the effect of the Reynolds stresses. An interpretation of the following analysis as stability problem about the turbulent mean is not valid. Instead, one should think of the temporal eigenvalues as governing the long-term response of the unforced linearized Navier-Stokes system (see discussion in section 2.4.1).

Example temporal spectra for the scale $\boldsymbol{\kappa}_s$ are shown in fig. 5.5 for two different phase shifts of the controller. Figure 5.5a is the eigenspectrum for $\angle\hat{A}_d = -3\pi/4$, which is a drag-increasing configuration, while fig. 5.5b shows $\angle\hat{A}_d = -\pi/4$, which resulted in drag reduction, at least when all spanwise scales at k_{xs} were controlled. The spectra are shown in terms of wave speed $\hat{c} = \hat{\omega}/k_x$, where the complex $\hat{\omega}$ are the temporal eigenvalues. The real part c_r corresponds to the phase speed of the

mode, while the imaginary part c_i is the growth rate and $c_i > 0$ means amplification. The phase speed and growth rate are normalized with the centerline velocity of the uncontrolled mean flow $(U_c)_0$.

The spectrum has a branch structure reminiscent of laminar Poiseuille flow (e.g. Schmid and Henningson, 2001, Ch. 3), and following the nomenclature of the stability literature, we dub the left branch ($c_r \to 0$) "wall modes" and the right branch ($c_r \to (U_c)_0$) "center modes." The wall modes come in pairs of (almost) equal eigenvalues which are indistinguishable from each other in figs. 5.5a and 5.5b. It is possible to construct symmetric and anti-symmetric eigenvectors for paired $\hat{\omega}$, since any linear combination of the corresponding eigenvectors is again a valid eigenvector. In other words, the paired wall modes only differ in their wall-normal symmetry, and we therefore refer to these paired eigenvalues as a single eigenvalue for simplicity. The other branches do not have two coincident eigenvalues, but they each still have eigenvalues that lie close to each other in the complex plane. The eigenmodes associated with two close eigenvalues share similarities with the Orr-Sommerfeld and Squire modes known from the stability literature (e.g. Schmid and Henningson, 2001, Ch. 3): one eigenmode only has a nonzero u and w component, and resembles the unforced Squire modes, while the other has nonzero entries for all velocity components as well as pressure, and resembles the Orr-Sommerfeld modes, including the contribution from the forced Squire equation. This partitioning of modes is not enforced in the formulation, but naturally results from the solution of the eigenproblem in primitive variables. It should be noted, however, that the analogy is approximate, because the two modes have slightly different eigenvalues.

All eigenvalues in fig. 5.5a have a negative imaginary part, which indicates that the eigenmodes for $\angle \hat{A}_d = -3\pi/4$ decay over a sufficiently long time horizon and have no significance for the long-term dynamics of the flow. The most unstable eigenvalue is a center mode with wave speed $\hat{c} = 0.99 - 0.09i$. Also note that the wall modes only consist of two paired modes here, both of which are damped. Changing the phase shift to $\angle \hat{A}_d = -\pi/4$ barely alters the structure of the eigenspectrum, as can be seen by comparing figs. 5.5a and 5.5b. The most apparent change occurs for one of the wall modes, highlighted by the yellow circle, whose phase speed decreases and amplification remains approximately constant as the phase shift increases. The other wall mode does not change with $\angle \hat{A}_d$ and neither do many of the modes on the other branches. The robustness of the eigenvalue location to changes in phase shift can be best understood from a physical perspective: only eigenmodes with substantial

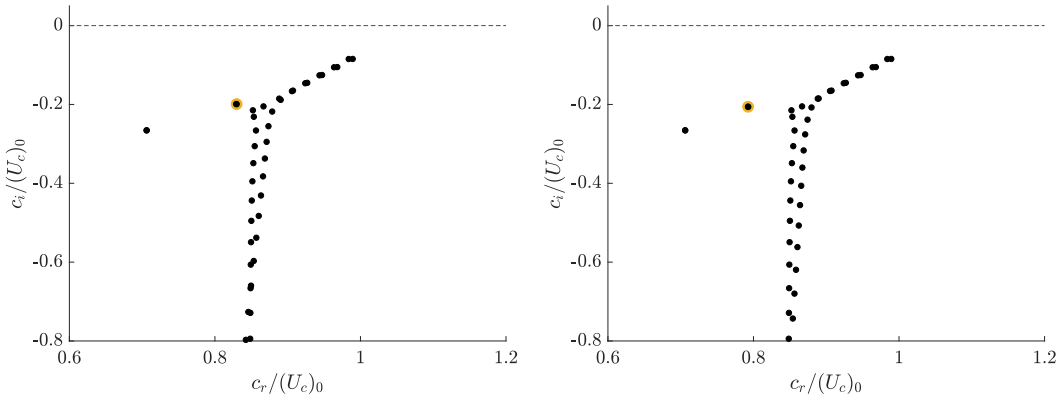

(a) $\angle\hat{A}_d = -3\pi/4$ (b) $\angle\hat{A}_d = -\pi/4$

Figure 5.5: Temporal eigenspectrum of single scale control with $\boldsymbol{\kappa}_s$ as a function of wave speed. Figure 5.5a shows the eigenspectrum of a drag-increasing configuration, while fig. 5.5b is a drag-reducing controller, at least when all spanwise scales at k_{xs} are controlled. The yellow circles track the location of the wall mode that is most affected by the change in phase shift and the dashed horizontal delineates the regions of damped (below) and amplified (above) eigenvalues.

nonzero v at y_d can be detected by the sensors and acted upon by the actuators. The eigenvalues associated with such modes can be shifted in the complex plane by changing $\angle\hat{A}_d$. In contrast, eigenmodes with a zero (very small) wall-normal velocity at y_d are not (hardly) detected by the sensors and are therefore not (very little) affected by control. For example, the wall mode unaffected by control is a Squire mode according to our earlier classification. It has no v component and does therefore not change with $\angle\hat{A}_d$. The modes of the other branches are localized around their critical layers (i.e. the location where their phase speed matches the mean velocity), which occur far away from the wall due to the large c_r. Their wall-normal velocity signature at the sensor location is, if present at all, very weak and so is their dependence on the phase shift.

Similar calculations can be repeated for the other phase shifts of interest, and lead to the same conclusion. The wall mode identified above moves in the complex plane as a function of the phase shift and approaches lower phase speeds as $\angle\hat{A}_d$ increases. Its amplification increases slightly to a maximum of $c_i = -0.14i$ at $\angle\hat{A}_d = -3\pi/4$, but it clearly remains damped over the entire parameter range. The other modes vary minimally as a function of phase shift, and the center mode at $\hat{c} = 0.99 - 0.09i$ remains the most amplified one for all configurations. These observations indicate that the unforced linearized dynamics of $\boldsymbol{\kappa}_s$ are not significantly affected by changes in the phase shift. The eigenvalues are damped for all phase

shifts and the corresponding eigenmodes decay over a sufficiently long time horizon, so that the eigenmodes have no significance for the long-term control response of the streamwise-elongated family.

5.3.4 Streamwise-Elongated Scales: Resolvent Analysis

Since the temporal eigenvalues of the linearized Navier-Stokes operator are damped for all phase shifts, the contributions of its eigenvectors decay over a sufficiently long time horizon. The long-term scale response is therefore governed by the response of the forced linearized Navier-Stokes system, which is characterized in this section by means of a resolvent analysis. Recall that the resolvent framework operates in temporal frequency domain, so that the following analysis will consider individual temporal frequencies at $\boldsymbol{\kappa}_s$.

In contrast to the previous section, all resolvent modes are neutrally stable and do not grow or decay in time. The frequency ω and wave speed $c = \omega/k_x$ are therefore purely real (note that there is no superscript hat) and describe the oscillation frequency and propagation speed of the mode, respectively. For resolvent modes, we use the terms wave speed and phase speed interchangeably, and prefer the former to avoid confusion with the phase shift. The goal of this section is to analyze if the suppression of individual resolvent modes, defined earlier in eq. (5.7), is linked to changes in $\angle \hat{A}_d$. Since the uncontrolled and controlled mean profiles do not differ significantly, we formulate the resolvent about the eddy viscosity approximation of the uncontrolled mean profile and incorporate the effects of control only through a change in boundary conditions. This again corresponds to the first problem formulation of section 2.4.

Figure 5.6 shows various aspects of scale suppression as a function of the wave speed and phase shift. The top panel shows the scale suppression $\Delta\Phi_{vv}/(\Phi_{vv})_0$ computed from DNS data as a function of the phase shift and corresponds to fig. 5.4. The large panel on the bottom left shows $\Delta\left(\sigma_1^2|\hat{v}_1|^2\right)/\left(\sigma_1^2|\hat{v}_1|^2\right)_0$, which is the resolvent mode suppression metric derived in eq. (5.7), as a function of c and $\angle \hat{A}_d$. Finally, the panel on the bottom right shows the uncontrolled mode weight under a broadband forcing assumption as a function of the wave speed. These three panels are closely related, which is best explained by considering the dotted vertical line in the bottom left panel of fig. 5.6. The product of the values along this line and the panel on the right equals the resolvent mode suppression metric at each wave speed, $\Delta\left(\sigma_1^2|\hat{v}_1|^2\right)$. The integral of this product along the line (which corresponds to an integral in c) returns

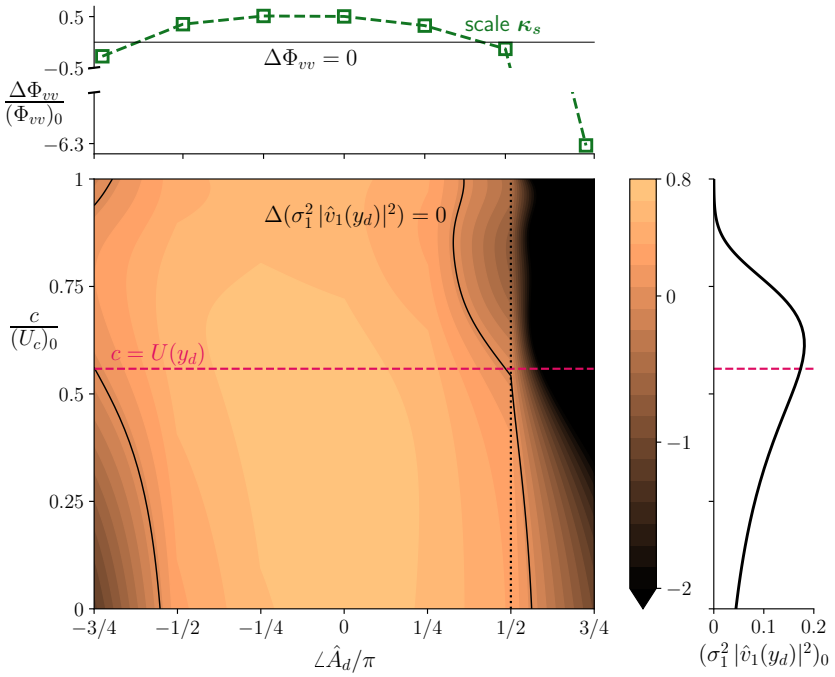

Figure 5.6: Suppression of scale κ_s as a function of the wave speed c and phase shift $\angle\hat{A}_d$. The top panel shows the DNS scale suppression as a function of $\angle\hat{A}_d$ and corresponds to fig. 5.4. The panel on the bottom left displays the suppression $\Delta\left(\sigma_1^2|\hat{v}_1|^2\right)/\left(\sigma_1^2|\hat{v}_1|^2\right)_0$ of resolvent modes as a function of c and $\angle\hat{A}_d$. The bottom right panel shows the uncontrolled mode weight at y_d under a broadband forcing assumption as a function of the phase speed c. The solid black line in the top and bottom left panel delineate the regions of scale suppression and amplification, while the dotted vertical line outlines the suppression of resolvent modes for the example controller $\angle\hat{A}_d = \pi/2$. The red dashed line in the bottom panels indicates the critical phase speed, defined as the uncontrolled mean velocity at the sensor location. Note that the color scale of the bottom left contour plot is saturated (indicated by the triangle at the end) to highlight the region of scale suppression.

the time-averaged resolvent mode suppression, which can then be compared to the DNS metric in the panel above. The comparison between the integrated resolvent scale suppression and the DNS metric is essentially the visual representation of eq. (5.10). When comparing the two plots, we look for qualitative similarities, not quantitative agreement. Recall that the resolvent is not constrained to reproduce flow statistics, and instead uses a simple broadband forcing model. It is therefore expected that the DNS and resolvent mode suppression do not match quantitatively. The qualitative agreement is of interest because it will allow to relate the DNS results to linear mechanisms encoded in the resolvent. If scale κ_s is suppressed (amplified) in DNS and suppression (amplification) of the corresponding resolvent

modes is observed over a significant range of wave speeds, then the modal analysis provides further evidence for a linear scale suppression (amplification) mechanism due to control. How important each region of phase speed is in the mean sense can only be partially answered here, because the nonlinear weights are not known explicitly. However, recall our earlier discussion in Chapter 3, which showed that the details of the forcing model only matter if the scale response is mixed in spectral space. This is also true for the following analysis. Further note that fig. 5.6 only shows phase speeds in the range $0 \leq c \leq (U_c)_0$, while the integral in eq. (5.10) is over all phase speeds. The restriction to this range of phase speeds is justified by the results in Chapter 3 and earlier studies, which showed that the singular values in the resolvent operator and energetic content in the real flow drop off rapidly outside this range (Bourguignon et al., 2014).

Figure 5.6 shows that all resolvent modes are suppressed for $-\pi/2 \leq \angle\hat{A}_d \leq \pi/4$. The suppression is strongest around $\angle\hat{A}_d = 0$, and decreases almost symmetrically for increasing $|\angle\hat{A}_d|$, except for large phase shifts and large wave speeds. The resolvent mode suppression is in good agreement with DNS data, which report a maximum suppression around $\angle\hat{A}_d = 0$ and also indicate a degradation for increasing $|\angle\hat{A}_d|$. In contrast, we observe that all resolvent modes are amplified at $\angle\hat{A}_d = +3\pi/4$. Note that the color scale of the contour plot is saturated, which indicates that the resolvent mode amplification for large c is significantly larger than the maximum reported value. This is consistent with the DNS data, which report the most pronounced scale amplification at this phase shift. There is further a region of mixed response for $\angle\hat{A}_d = -3\pi/4$ and $\angle\hat{A}_d = +\pi/2$, where control can lead to resolvent mode amplification or suppression, depending on the wave speed of the mode. These two phase shifts are examples for where the details of the forcing model matter if one wants to predict whether scale amplification or suppression occurs in the full nonlinear system. The DNS data agree with our crude model in the sense that DNS scale amplification is weakest at these two phase shifts, which is consistent with competing amplification behavior across c. Overall, the resolvent mode suppression agrees remarkably well with DNS data and provides further evidence that the response of streamwise-elongated scales to control is dominated by the change in boundary condition. The linear mechanism that relates scale suppression to $\angle\hat{A}_d$ seems to be well captured in the resolvent.

In addition, we would like to draw the reader's attention to two aspects of fig. 5.6 that shed some light on previous DNS observations. First, recall that we identified

$\angle\hat{A}_d = -\pi/2$ as an interesting edge case, where some spanwise scales at k_{xs} are amplified, while others are damped. As can be seen from fig. 5.6, the boundary between amplification and suppression is close to this phase shift for a wide range of wave speeds. It is plausible that the boundary depends on k_z and small variations would result in scale suppression for some k_z and scale amplification for others, thus leading to the mixed response. The same observation is true for $\angle\hat{A}_d = +\pi/2$, but this case is less relevant because it will be shown that the streamwise-elongated family only plays a secondary role in this parameter range.

The second aspect regards an apparent change in the resolvent mode response around the wave speed that corresponds to the mean velocity at the sensor location, which is indicated by the dashed red line. Consider for example $\angle\hat{A}_d = +\pi/2$, which corresponds to the dotted vertical line in fig. 5.6. Modes moving slower than $U_0(y_d)$ are suppressed, while modes moving faster are amplified under control. The opposite holds for $\angle\hat{A}_d = -3\pi/4$. A similar change in behavior can be observed in the range $-\pi/2 \leq \angle\hat{A}_d \leq \pi/4$: within this range, the most effective damping for modes with $c \leq U_0(y_d)$ occurs at $\angle\hat{A}_d = 0$, while faster moving modes are most damped for slightly negative phase shifts. These response changes are not tied to the sensor location, but occur because resolvent modes switch from "attached" to "critical" behavior around $c^+ = 10$. The terms were coined by Luhar, Sharma, and McKeon (2014b), who binned resolvent modes into two groups based on their wave speed. So-called attached modes move at approximately $c^+ < 10$, have a footprint at the wall, and peak at the same wall-normal location, irrespective of wave speed. The other class of modes is termed critical modes. They move at $c^+ > 10$ and peak at their respective critical layer, which is a function of c. The partition of these modes is not sharp and there is overlap between the two classes of modes, but $c^+ = 10$ can roughly be taken as the divide between them. Luhar, Sharma, and McKeon (2014b) further showed that attached modes are best suppressed by classical opposition control, or $\angle\hat{A}_d = 0$, while critical modes need a slightly negative phase shift to maximize suppression. The transition from attached to critical is therefore what underlies the change in scale response. The fact that this change occurs at the critical speed of the sensor location seems to be a mere coincidence, since the uncontrolled mean velocity at the sensor location corresponds to $U^+(y_d) \approx 10$ and therefore coincides with the divide. Further, recall that the DNS drag reduction and scale suppression curves for SW control with streamwise-elongated scales were not symmetric about $\angle\hat{A}_d = 0$ for large phase shifts. Figure 5.6 suggests that the critical modes are responsible for the lack of symmetry. While the response of the attached

modes is approximately symmetric, the critical modes favor negative phase shifts. Their preference for negative phase shifts leads to less scale amplification and drag increase for large negative $\angle\hat{A}_d$ compared to large positive ones.

Finally, we connect the resolvent observations to the eigenspectra of section 5.3.3. As mentioned in section 2.4.4 and shown in fig. 5.6, the control boundary conditions change the singular values and singular vectors of the resolvent, which ultimately results in mode amplification or suppression. With regards to the singular values, two mechanisms can lead to large gains (e.g. Symon, Rosenberg, et al., 2018): resonance, which occurs when an eigenvalue of the linearized Navier-Stokes operator is close to the neutral stability axis, and pseudoresonance, which is related to the non-orthogonality of the eigenvectors of the linearized NSE. The relative importance of these two mechanisms in wall-bounded flows depend on multiple factors, including the spatial wave number and wave speed of the mode as well as its wall-normal localization. It is further possible that control with various $\angle\hat{A}_d$ alters the relative importance of the two mechanisms, which can contribute to the observed changes in singular values. Since the movement of the eigenvalues in the complex plane is known from section 5.3.3, we can give a partial answer on how resonance changes under control. The example streamwise-elongated scale $\boldsymbol{\kappa}_s$ is characteristic for near-wall cycle structures at this Re_τ, and it has been shown for the uncontrolled case that the relatively large singular values at these wave numbers are due to the pseudoresonant mechanism (Symon, Rosenberg, et al., 2018). We further know from fig. 5.5 that the eigenvalues are insensitive to changes in $\angle\hat{A}_d$, so that the resonant mechanism does not become more important with control. It can thus be speculated that the changes in singular values and scale amplification in fig. 5.6 are due to a more pronounced pseudoresonance mechanism.

5.3.5 Streamwise-Elongated Scales: Summary

We close this section with a brief summary of the most important observations thus far. The matching drag change trends between varying-phase opposition control and SW control with $\{\boldsymbol{\kappa}\}_{k_{xs}}$ confirm that the streamwise-elongated scales shape the control response of the flow over the entire parameter range, at least partially. Control of the streamwise-elongated scales leads to drag reduction for $-\pi/4 \leq \angle\hat{A}_d \leq \pi/4$ and drag increase for phase shifts outside this regime. The control response is not symmetric about $\angle\hat{A}_d = 0$, especially for large phase shifts, because fast-moving (so-called critical) modes identified by resolvent analysis prefer negative phase shifts over positive ones and bias the curve. A combination of DNS and modal analysis

provides strong evidence that the control response of the streamwise-elongated scales is due to the change in boundary condition and therefore essentially a linear effect. A change in $\angle\hat{A}_d$ at one scale primarily changes the amplification of that scale, which translates into a mean drag change provided that the scale response is strong enough. The resolvent operator encodes this linear mechanism and simplified models based on its singular values and vectors reproduce DNS trends quite well. On the other hand, the temporal eigenspectrum has no significance for the control response of the streamwise-elongated family. We further observed a fundamental difference between scale suppression and scale amplification, which is not specific to the streamwise-elongated family, but applies in general. A scale can at best be annihilated by control, which leads to small changes in a mean sense. It is therefore difficult to obtain a substantial drag reduction by targeting a single scale alone. On the other hand, there is no bound on how strongly a scale is amplified by control. The drag can therefore increase substantially even if only a single scale is controlled.

5.4 Response of Spanwise-Elongated Scales to Control

Next, we explore the control response of the other scale family, the spanwise-elongated structures. The analysis is based on the scale-restricted controller introduced in eq. (5.15), which acts on the single scale $\boldsymbol{\kappa}_r = [k_{xr}h = 6.5, k_{zr}h = 0]$. All control configurations considered in this section have sensors located at $y_d^+ = 15$ and the phase shift $\angle\hat{A}_d$ is varied between $-3\pi/4$ and $3\pi/4$. The approach is identical to section 5.3 and involves DNS and modal analysis. As will be shown, the eigenspectrum is more important for control with spanwise-elongated scales, and we will discuss this aspect in more depth compared to the previous section. In particular, we will compare the spatial structure of eigenmodes with phase-averaged DNS flow fields, which is an aspect that we did not explore for the streamwise-elongated scales.

5.4.1 Spanwise-Elongated Scales: DNS Drag Reduction

We start the discussion by considering the mean drag reduction, shown in fig. 5.7. The green open squares show the DR of SS control with $\boldsymbol{\kappa}_r$ as a function of $\angle\hat{A}_d$. For reference, the figure also shows the DR obtained under varying-phase opposition control as orange circles. This line corresponds to the cross-section of fig. 4.1 along the horizontal $y_d^+ = 15$. It is apparent from the figure that the drag change due to SS control is a strong function of $\angle\hat{A}_d$, and that the trends are similar to control with all scales in parts of the parameter regime. The mean flow response is strong for $\angle\hat{A}_d \geq \pi/2$, but much weaker for smaller phase shifts, and it is difficult to conclude

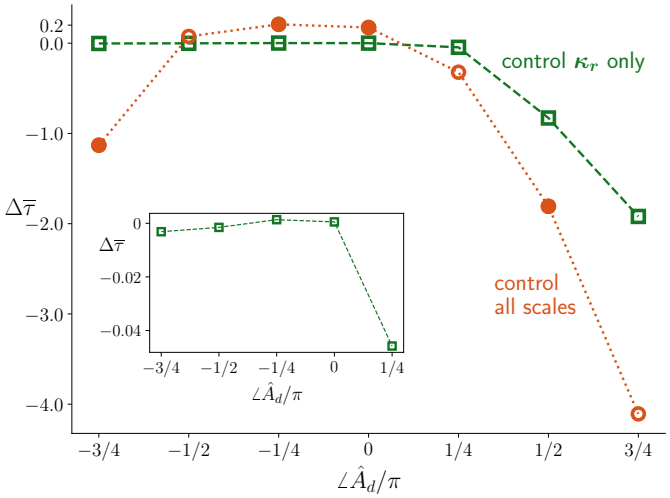

Figure 5.7: Drag reduction of varying-phase opposition control with sensors located at $y_d^+ = 15$ as a function of the phase shift $\angle\hat{A}_d$. The orange circles denote control with all scales and correspond to the orange line in fig. 4.1. The green open squares represent single-scale control with $\boldsymbol{\kappa}_r$. The inset shows a magnification of the DR due to single scale control for the range $-3\pi/4 \leq \angle\hat{A}_d \leq +\pi/4$. Figure after Toedtli, Yu, and McKeon (2020).

whether there is any change at all due to the scale of the ordinate. The inset therefore shows a magnification of the DR for $\angle\hat{A}_d \leq \pi/4$, and it becomes clear that there is indeed no statistically significant change for $\angle\hat{A}_d \leq 0$. An analysis of the control input for this regime further shows that the control scale is virtually inactive. In the absence of a significant control input, the flow is no different from an uncontrolled one and it is no surprise that the drag remains unchanged. The discussion of the streamwise-elongated scales showed that the mean effect of single scale controllers can be weak, especially in the drag-reducing regime, and that a clearer picture of the drag trend can be obtained if the control signal strength is increased by including more scales. Figure 4.4d shows that the most energetic scales of the spanwise-elongated family occur at $k_x h = 6.5$ ($\lambda_x^+ \approx 170$) for a phase shift of $+\pi/2$. Following the reasoning of section 5.3.1, we can construct a single wave number controller by including all spanwise scales at $k_x h = 6.5$ and repeat the control experiments for $-3\pi/4 \leq \angle\hat{A}_d \leq 0$. However, the SW controller does not lead to a statistically significant drag change either, and suggests that the spanwise-elonated scales truly are of secondary importance in this parameter regime. This is consistent with our earlier observations of the control spectra in fig. 4.4, which suggested that the streamwise-elongated scales are most active at these phase shifts. An explanation for the weak flow response to control with the spanwise-elongated scales for these $\angle\hat{A}_d$ will be given in section 5.4.2.

In contrast, SS control with $\boldsymbol{\kappa}_r$ can significantly increase the drag for positive $\angle\hat{A}_d$. A small positive phase shift only leads to a slight increase in drag, as can be seen from the inset at $\angle\hat{A}_d = +\pi/4$. The drag increase becomes more pronounced for larger positive phase shifts, analogous to the trends of varying-phase opposition control. For example, single-scale control with $\angle\hat{A}_d = +\pi/2$ leads to a 82% drag increase, notably through control of a single spatial length scale only. At the same phase shift, the varying-phase opposition control scheme, which acts on all spatial scales, increases drag by 180%. The matching DR behavior suggests that single-scale control with $\boldsymbol{\kappa}_r$ is a suitable model to understand at least parts of the mechanism that lead to drag increase at positive phase shifts. We say parts of the mechanisms, because the streamwise-elongated scales were shown to contribute to drag increase in this regime as well. However, note the different order of magnitude of the drag increase: SS control with the streamwise-elongated scale $\boldsymbol{\kappa}_s$ leads to a 12% drag increase at $\angle\hat{A}_d = 3\pi/4$ (fig. 5.1), while SS control with $\boldsymbol{\kappa}_r$ increases the drag by more than 190%. The spanwise-elongated scales therefore dominate the flow response in this parameter regime, which is consistent with the actuator spectrum fig. 4.4d.

It is also important to keep in mind that $\boldsymbol{\kappa}_r$ is a representative for the family of spanwise-elongated scales. The observations from figs. 4.4d and 5.7 suggest that the other scales of this family follow the behavior of $\boldsymbol{\kappa}_r$ and also contribute to drag increase. This hypothesis is supported by an additional control experiment, in which varying-phase opposition control with $\angle\hat{A}_d = +\pi/2$ was applied to all scales except $[k_{xr}h = 6.5, k_z h]$. Note that this controller excluded $\boldsymbol{\kappa}_r$ and all other spanwise wave numbers at k_{xr}. This configuration resulted in a 170 % drag increase, which is comparable to control with all scales and confirms that the observations are not a peculiarity of $\boldsymbol{\kappa}_r$.

5.4.2 Spanwise-Elongated Scales: DNS Scale Suppression

After considering the change in drag, which is an average measure in wave number space, we turn our attention to the control effect on a single scale, $\boldsymbol{\kappa}_r$. As before, the discussion focuses on scale suppression, and we first discuss a few example spectra of controlled flows before quantifying the suppression of $\boldsymbol{\kappa}_r$ for various phase shifts.

Figure 5.8 shows the power spectrum of the wall-normal velocity Φ_{vv} at the sensor location for various flows as a function of wave number. Note that the wave numbers $k_x h > 20$ and $k_z h > 40$ are omitted, because these scales are not energetic at this

wall-normal location. Figure 5.8a shows the power spectrum of the uncontrolled flow, with respect to which we define scale amplification. The portion within the blue rectangle was already shown in fig. 5.3a, and a brief discussion of the uncontrolled spectrum can be found in section 5.3.2. Figures 5.8b and 5.8c on the other hand are two example spectra for SS control with $\boldsymbol{\kappa}_r$, which is indicated by the green open square, and different phase shifts.

Figure 5.8b on the bottom left shows the spectrum for $\angle\hat{A}_d = -\pi/4$, which did not lead to a significant drag change. Consistent with that, the imprint of the control scale is not discernible in the spectrum. In fact, a comparison between figs. 5.8a and 5.8b shows that the spectrum of $\angle\hat{A}_d = -\pi/4$ is visually not distinguishable from the uncontrolled one over the entire range of wave numbers shown. The unchanged flow structure provides further evidence that control at this phase shift is very weak and does not alter the flow at all.

The spectrum for $\angle\hat{A}_d = +\pi/2$, which resulted in a large drag increase, is shown in fig. 5.8c on the bottom right. Note that the color scale of this figure is logarithmic, and its limits are different from the ones in figs. 5.8a and 5.8b. It is apparent that the wall-normal velocity at the sensor location is dominated by the control scale $\boldsymbol{\kappa}_r$ (indicated by the green open square), which is significantly more energetic than in the uncontrolled case. In other words, control with $\angle\hat{A}_d = +\pi/2$ amplifies the control scale rather than suppressing it. It is interesting to note that scales different from $\boldsymbol{\kappa}_r$ are active as well, even if much weaker. In particular, note that the harmonic of the control signal, i.e. $[k_x h = 13, k_z = 0]$ is the second most energetic scale. The presence of the harmonic is a consequence of the quadratic nonlinearity, which allows the control signal to interact with itself to transfer energy across scales, and illustrates the possible importance of nonlinear interactions when all scales are controlled. It is also worth noting that the signature of the near-wall cycle is very weak in fig. 5.8c, which suggests that control with $\angle\hat{A}_d = +\pi/2$ fundamentally alters the flow structure close to the wall.

The discussion so far focused on the spectra and showed that the control scale is not discernible in case of $\angle\hat{A}_d = -\pi/4$ and very energetic for $\angle\hat{A}_d = +\pi/2$. We next quantify the scale suppression of $\boldsymbol{\kappa}_r$ according to eq. (5.3) over the entire range of phase shifts. This comparison is shown in fig. 5.9. Recall that a positive value of $\Delta\Phi_{vv}/(\Phi_{vv})_0$ indicates scale suppression, and a value of one corresponds to the best case where control completely suppresses any contribution of $\boldsymbol{\kappa}_r$ to $\overline{v'v'}$. A negative value on the other hand indicates that control amplifies the scale, and more negative

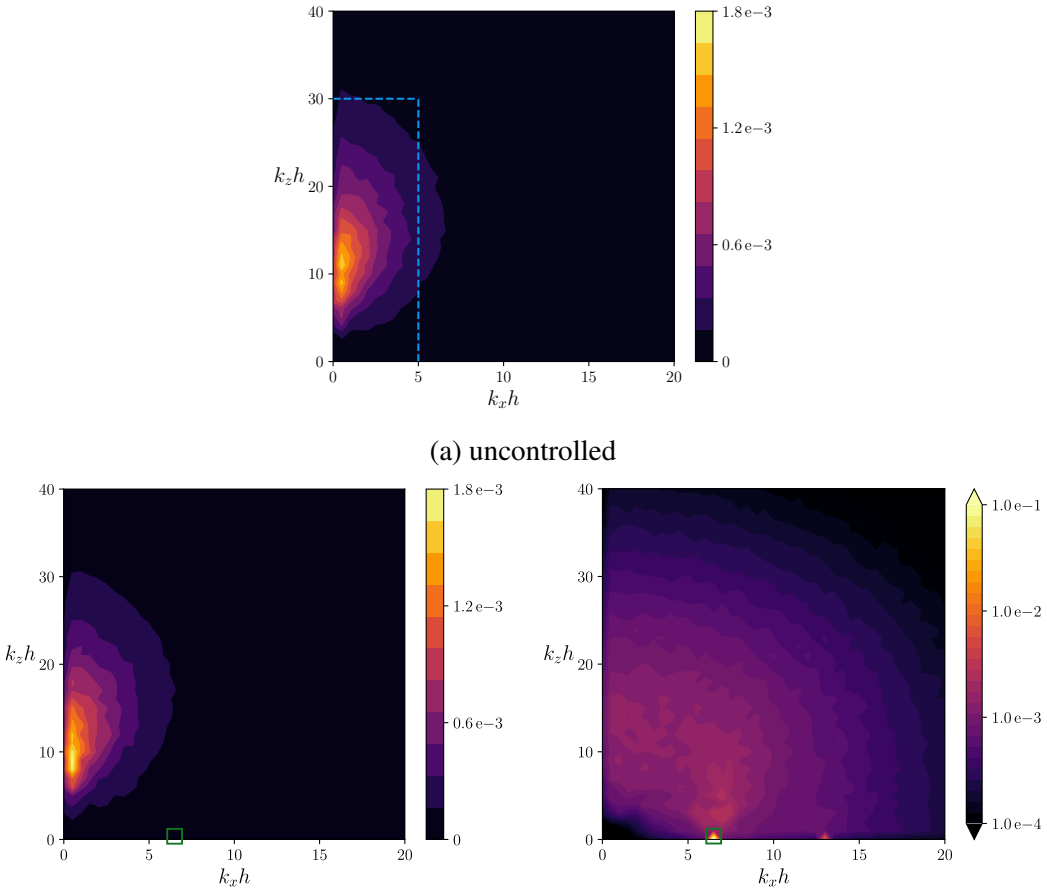

(a) uncontrolled

(b) $\angle \hat{A}_d = -\pi/4$

(c) $\angle \hat{A}_d = +\pi/2$

Figure 5.8: Time-averaged power spectrum $\Phi_{vv}/(u_\tau^2)_0$ of the wall-normal velocity at the sensor location $y_d^+ = 15$ as a function of the streamwise (k_x) and spanwise wave number (k_z). Figure 5.8a shows the spectrum of the uncontrolled flow, while figs. 5.8b and 5.8c show controlled spectra for different phase shifts. Nonlinear effects seem to be strong at $\angle \hat{A}_d = +\pi/2$, since scales far away from the control scale have been amplified. The blue rectangle in fig. 5.8a outlines the portion of the uncontrolled spectrum shown in fig. 5.3a, and the green open squares in figs. 5.8b and 5.8c indicate the control scale. The color scale in fig. 5.8c is different from figs. 5.8a and 5.8b. In particular, note that it is logarithmic and saturated at both ends. Figure 5.8c reproduced from Toedtli, Yu, and McKeon (2020). © 2020 Elsevier Inc.

values indicate larger amplification. The ordinate in fig. 5.9 is logarithmic, which implies that the scale amplification changes order of magnitude as the phase shift is varied. Further note the inset graph, which shows a magnification of $\Delta\Phi_{vv}/(\Phi_{vv})_0$ for the range $-3\pi/4 \leq \angle \hat{A}_d \leq 0$ for which the scale amplification is of order one.

The most apparent feature of fig. 5.9 is the strong scale amplification for positive phase shifts. For example, $\boldsymbol{\kappa}_r$ is amplified by more than a factor of 10^3 for

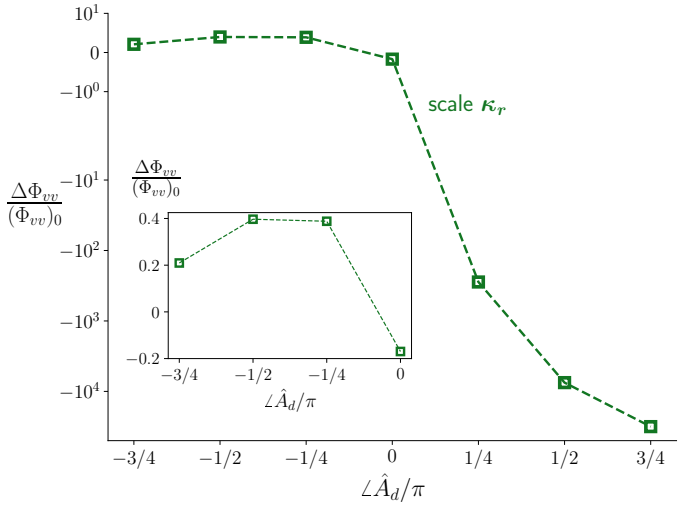

Figure 5.9: Suppression of scale κ_r for SS control with that same scale and sensors located at $y_d^+ = 15$ for various phase shifts $\angle\hat{A}_d$. Note that the ordinate of the main graph is in symmetric logarithmic scale (i.e. logarithmic in both the positive and negative directions from the origin, and linear around zero). The inset shows a magnification of the scale suppression for the range $-3\pi/4 \leq \angle\hat{A}_d \leq 0$ in linear scale.

$\angle\hat{A}_d = +\pi/2$, which again confirms that scale amplification can be significantly larger than the maximum scale suppression. Since the mean drag and scale amplification both increase significantly for positive phase shifts, it is reasonable to infer that the drag contribution of κ_r increases as well. In fact, the amplification is so strong that κ_r is likely the main driver of the drag increase, which is further supported by the spectrum in fig. 5.8c. Figure 5.9 further shows that control with $-3\pi/4 \leq \angle\hat{A}_d \leq -\pi/4$ suppresses the control scale. However, the missing imprint of κ_r in fig. 5.8b together with the scale suppression at this phase shift should not be taken as an indicator that control suppresses this scale completely. As can be seen from fig. 5.8a, the control scale is weak in the uncontrolled flow to start with and accounts for less than 0.02% of $\overline{v'v'}$ at the sensor location. Control in this phase shift regime does attenuate the scale, but it contains so little energy in the uncontrolled flow that the suppression does not translate into a mean drag reduction. In fact, all spanwise wave numbers at k_{xr} have a negligible energy content, which is why the single wave number controller did not lead to a mean flow response either. The last interesting observation is the slight amplification of the control scale for $\angle\hat{A}_d = 0$, but the flow response in this case is weak as well, so that no statistically significant drag change is observed.

5.4.3 Spanwise-Elongated Scales: DNS Flow Structure

The picture that emerges for $\boldsymbol{\kappa}_r$, and more generally for the spanwise-elongated family, is that of a mixed response to phase shifts. These scales are inactive for negative phase shifts, but can be amplified enormously for $\angle\hat{A}_d > 0$. The scale amplification goes hand in hand with an increase in drag, which can be as large as 80%, even if only a single spatial scale is controlled. The spectrum in fig. 5.8c further shows that the flow structure in the near-wall region is on average very different for drag-increased and uncontrolled flows. The spectral representation of the flow structure is quite abstract and challenging to translate into a physical picture. In order to get a better idea of what the structure of drag-increased flows looks like, we explore a representative instantaneous flow field for SS control with $\boldsymbol{\kappa}_r$ and $\angle\hat{A}_d = +\pi/2$.

The SS control input is periodic in x with wavelength $\lambda_{xr} = 2\pi/k_{xr}$, and constant in z. Instantaneous flow fields can thus be phase-averaged over λ_{xr} in the streamwise direction and averaged in the spanwise direction to remove local fluctuations. The phase average is defined in eq. (2.47) and quantities obtained from this averaging procedure in x and z are denoted by a subscript $\lambda_{xr,z}$. For example, $\langle u\rangle_{\lambda_{xr},z}$ is the phase and spanwise averaged streamwise velocity. A representative instantaneous flow structure that results from this averaging procedure is shown in fig. 5.10a as a function of the streamwise and wall-normal coordinate. The shading indicates the mean-subtracted spanwise vorticity, while the arrows outline the local mean-subtracted in-plane velocity field and the dashed line denotes the sensor location.

It is worth pointing out that the physical interpretation of the positive phase shift is very apparent in this figure. For example, compare the streamwise location of the largest negative sensor measurement ($x/\lambda_{xr} \approx 0.45$) and the largest positive control input ($x/\lambda_{xr} \approx 0.2$). The actuator input lags the sensor measurement by about a quarter of a wavelength, in agreement with the earlier interpretation of a $+\pi/2$ phase shift. Moving on to the features of the flow field, we observe a number of interesting properties. The control input generates a pair of counter-rotating spanwise rollers in immediate proximity of the wall ($y^+ \leq 5$). The imprint of these rollers can be seen in both the spanwise vorticity field and the velocity vectors. An additional pair of vortices with opposite sense of rotation is visible further away from the wall ($y^+ \approx 20$) and large streamwise velocity fluctuations are induced in the flow region between the two pairs. The flow also has two stagnation points in this region (indicated by the star symbols), which delimit ejection (above the yellow region

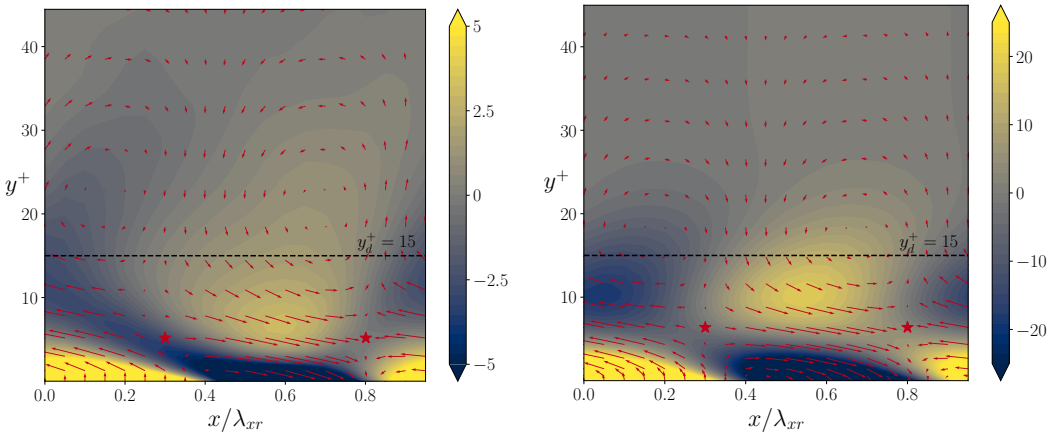

(a) DNS (b) Amplified eigenmode

Figure 5.10: Characteristic structure of the drag-increased flow for single scale control with $\boldsymbol{\kappa}_r$ and positive phase shift. Figure 5.10a shows a phase and spanwise averaged flow field of SS control, while fig. 5.10b shows the spatial structure of the amplified eigenmode as a function of the streamwise and wall-normal coordinate. The shading indicates the mean-subtracted spanwise vorticity, the arrows outline the mean-subtracted local in-plane velocity field and the star symbols denote stagnation points. In both cases, the sensors are located at $y_d^+ = 15$ (indicated by the dashed horizontal line) and the phase shift is $\angle \hat{A}_d = +\pi/2$. Note that the color scale is saturated at both ends to highlight features away from the wall. Reproduced from Toedtli, Yu, and McKeon (2020). © 2020 Elsevier Inc.

of positive $\langle \omega_z \rangle_{\lambda_{xr,z}}$ at the wall) and sweep-like events (above the blue region of negative $\langle \omega_z \rangle_{\lambda_{xr,z}}$ at the wall) in the flow. These sweep and ejection motions enhance momentum mixing in the wall-normal direction and lead to a fuller mean velocity profile close to the wall. It is therefore likely that the drag increase is tightly linked to the presence of the spanwise rollers. Actuators drawing high momentum fluid close to the wall have also been observed by Hammond, Bewley, and Moin (1998). They analyzed the flow structure of classical opposition control with sensors located above the center of the streamwise vortices, which also results in drag increase. The flow structure of fig. 5.10a bears some resemblance with their fig. 4a, even if the alignment of sensor measurement, actuator response, and stagnation point is different.

It is also interesting to note that the wall-normal location of the stagnation points ($y^+ \approx 5$) coincides with the location of the minimum in the v_{rms} profile in fig. 4.3. This observation suggests that the minima of v_{rms} are associated with local stagnation points, where the actuator input annihilates the motion detected at the sensor location. The presence of the stagnation point itself is not a guarantee for fluctuation

suppression or drag reduction, as this example demonstrates. The various degrees of drag reduction achieved with different phase shifts rather suggests that the streamwise arrangement of the sensor measurement, actuator response, and stagnation point is important.

5.4.4 Spanwise-Elongated Scales: Temporal Eigenspectrum

We now change our approach and use tools from modal analysis rather than DNS data to interrogate the behavior of the spanwise-elongated scales. Our goal is again to isolate the linear mechanisms that relate $\angle\hat{A}_d$ to the scale response, so that the observations from the previous sections can be linked directly to the change in boundary condition. The modal analyses follow the approach of the DNS study and consider the single scale controller with $\boldsymbol{\kappa}_r$ and sensors fixed at $y_d^+ = 15$. The current section analyzes the response of the spanwise-elongated family by means of the temporal eigenspectrum, while the following section focuses on resolvent analysis.

The main goal of this section is to understand how the temporal eigenvalues move in the complex plane as a function of the phase shift and whether there is a correlation between the observation of drag increase in the DNS and amplified eigenvalues in the eigenspectrum. Unless stated otherwise, we will use the eddy viscosity approximation of the uncontrolled mean profile as linearization point and incorporate the effect of control only through a change in boundary conditions (this corresponds to the first problem formulation of section 2.4).

An example temporal eigenspectrum for $\angle\hat{A}_d = +\pi/2$ is shown in fig. 5.11a in terms of wave speed. Recall that the real part c_r describes the phase speed of the mode, while the imaginary part c_i is the growth rate and $c_i > 0$ means amplification. The phase speed and growth rate are normalized with the centerline velocity of the uncontrolled mean flow $(U_c)_0$. The spectrum has a three-branch structure, similar to the ones in fig. 5.5, and following our earlier nomenclature, we term the left branch ($c_r \to 0$) wall modes. The wall modes come again in pairs of (almost) equal eigenvalues, which are indistinguishable from each other in fig. 5.11a, so that we can construct symmetric and anti-symmetric eigenvectors. For simplicity, we refer to these paired eigenvalues again as a single eigenvalue. It is interesting to note that the other branches do not have paired eigenvalues, analogous to section 5.3.3.

The location of the eigenvalues in the complex plane is in general a function of the phase shift. However, not all eigenvalues are equally sensitive to changes in

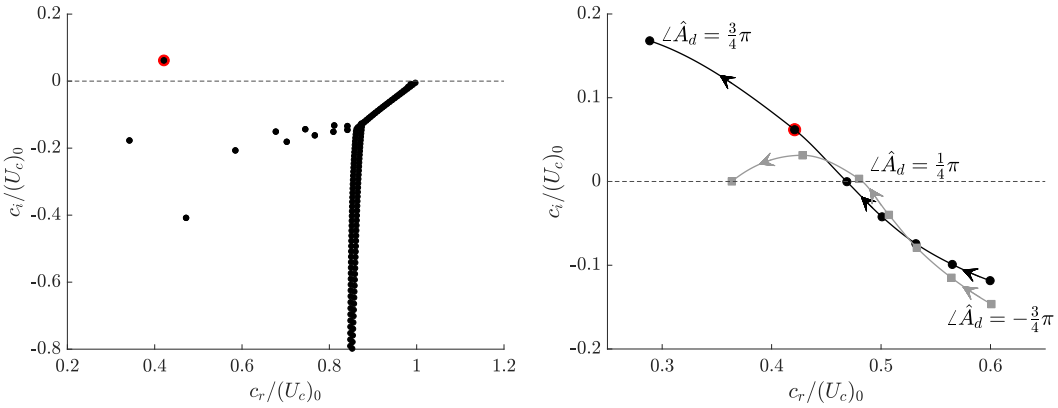

(a) Eigenspectrum for $y_d^+ = 15$, $\angle\hat{A}_d = +\pi/2$ (b) Root locus of amplified mode

Figure 5.11: Temporal eigenspectrum of single-scale control with $\boldsymbol{\kappa}_r$. Figure 5.11a shows the temporal eigenvalues for the controlled flow with $y_d^+ = 15$, $\angle\hat{A}_d = +\pi/2$, and fig. 5.11b shows the root locus of the amplified eigenvalue for various phase shifts. The red circle locates the amplified eigenvalue of $\angle\hat{A}_d = +\pi/2$ in the complex plane (fig. 5.11a) and in the root locus plot (fig. 5.11b). The eigenspectrum of fig. 5.11a and the black curve in fig. 5.11b are computed about an eddy viscosity approximation of the uncontrolled mean velocity profile, while the actual DNS mean is used to generate the gray curve in fig. 5.11b. The arrows in fig. 5.11b indicate the movement of the amplified eigenvalue for increasing $\angle\hat{A}_d$, and markers are placed at phase increases of $\pi/4$ along each curve. In both plots, the dashed horizontal delineates the amplified (above) and damped (below) half-plane. Reproduced from Toedtli, Yu, and McKeon (2020). © 2020 Elsevier Inc.

$\angle\hat{A}_d$, and only a subset of eigenvalues can be shifted significantly by adjusting the phase shift. Once again, only eigenmodes with substantial nonzero v at y_d can be detected by the sensors and acted upon by the actuators. The eigenvalues associated with such modes can be shifted in the complex plane by changing $\angle\hat{A}_d$. In contrast, eigenmodes with a zero (very small) wall-normal velocity at y_d are not (hardly) detected by the sensors and are therefore not (very little) affected by control. The eigenvalues associated with such modes do not change as SS control is applied and are not affected by changes in $\angle\hat{A}_d$. The most sensitive eigenvalues are two wall modes and while one of them stays in the damped lower half plane for all $\angle\hat{A}_d$, the other one approaches the real axis, and eventually becomes amplified. The remaining wall modes and the eigenvalues of the other branches do not change significantly under control.

Recall that the phase shift in Fig. 5.11a is $\angle\hat{A}_d = +\pi/2$, which resulted in substantial drag increase in the DNS of SS control. It is interesting to note that the eigenspectrum has a single amplified eigenvalue (highlighted with the red circle), while all others are

damped. This raises the question whether there is a correlation between the presence of amplified eigenvalues in the eigenspectrum and drag increase in the DNS. The calculation of the eigenspectrum can be repeated for different phase shifts and a scan through $\angle\hat{A}_d \in [-3\pi/4, +3\pi/4]$ reveals two recurring configurations: either one eigenvalue is amplified and all others are damped (as in Fig. 5.11a), or all the eigenvalues are damped. The amplified eigenvalue at any phase shift, if present, corresponds to one of the two sensitive wall modes mentioned earlier (the one that approaches and eventually crosses the real axis and is highlighted in red in Fig. 5.11a). It is therefore sufficient to track this one eigenvalue as a function of $\angle\hat{A}_d$, and we refer to this eigenvalue as the "amplified eigenvalue" hereafter, even if it does not have a positive imaginary part for all phase shifts.

Figure 5.11b shows the location of the amplified eigenvalue in the complex plane as a function of the phase shift $\angle\hat{A}_d$. We first focus on the black curve with circular markers, which shows the root locus of the amplified eigenvalue for eigenspectra computed about the uncontrolled mean (eddy viscosity approximation). The curve is traversed from the bottom right to the top left as the phase shift increases. In other words, the phase speed of the amplified eigenvalue decreases, while the growth rate increases with increasing $\angle\hat{A}_d$. The mode is damped for $\angle\hat{A}_d < +\pi/4$, approximately neutrally stable for $\angle\hat{A}_d = +\pi/4$ and amplified for $\angle\hat{A}_d > +\pi/4$. The dependence of amplification characteristic on phase shift agrees remarkably well with the DR behavior observed in the DNS (fig. 5.7): the drag remains unchanged for $\angle\hat{A}_d < +\pi/4$ (all eigenvalues damped), increases slightly for $\angle\hat{A}_d = +\pi/4$ (one neutrally stable eigenvalue), and increases substantially for $\angle\hat{A}_d > +\pi/4$ (one amplified eigenvalue).

Before looking at the spatial structure of the amplified eigenmode, it is worth examining the significance of the mean profile for the eigenspectrum calculation. The analysis so far has considered the eigenspectra about an uncontrolled mean, but the same procedure can be repeated with the actual DNS mean (this corresponds to the second problem formulation in section 2.4). The qualitative characteristics discussed earlier also apply to the spectra computed about the DNS mean: the spectra have a three-branch structure, and at most one amplified eigenvalue at any given $\angle\hat{A}_d$. The root locus of the amplified eigenvalue about the DNS mean as a function of phase shift is shown as gray curve with square markers in fig. 5.11b. The curve is traversed from bottom right to top left as the phase increases, that is, the phase speed decreases and amplification increases (except for the last data point) with increasing $\angle\hat{A}_d$. The

black and gray curve have the same amplification characteristics, which suggests that the uncontrolled mean is sufficient to approximate the qualitative behavior of the full nonlinear system, in agreement with the results in Chapter 3. It further indicates that the change in eigenvalue is a direct consequence of the change in boundary condition, and not a consequence of nonlinear mechanisms encoded in the mean. The only significant difference between the two root loci occurs at $\angle\hat{A}_d = +3\pi/4$. The uncontrolled mean produces the largest amplification at this phase shift, while the eigenvalue about the DNS mean is only slightly above neutrally stable. Recall that $\angle\hat{A}_d = +3\pi/4$ leads to the largest drag increase in the DNS and consequently the resulting mean profile is quite different from the uncontrolled one. The mismatch of the two eigenvalues is therefore not really surprising and confirms the intuition that the simplified model works better the closer the uncontrolled eddy viscosity mean is to the true controlled one. The attenuation of the most unstable mode about the controlled mean at $\angle\hat{A}_d = +3\pi/4$ suggests an eventual weakening of this amplification mechanism with increasing phase shift. Due to the periodicity of $\angle\hat{A}_d$, this is consistent with figs. 4.4a and 5.7 which show that the spanwise-elongated modes are not active at $\angle\hat{A}_d = -3\pi/4 = +5\pi/4$ and suggests that their amplification mechanism turns off somewhere between $\angle\hat{A}_d = +3\pi/4$ and $\angle\hat{A}_d = +5\pi/4$.

The correlation between drag increase observed in DNS and amplification of eigenvalues in the eigenspectrum suggests that the amplified eigenmode may play an important role in the dynamics of drag-increased flows. To further validate this hypothesis, we compare the spatial structure of the amplified eigenmode with the phase-averaged DNS flow field of fig. 5.10a. Figure 5.10b shows the spatial structure of the amplified eigenmode for $\angle\hat{A}_d = +\pi/2$ as a function of the streamwise and wall-normal coordinate. The shading indicates the spanwise vorticity ω_z, while the arrows outline the in-plane velocity components u and v. The flow structure shows two pairs of spanwise rollers, one pair at the wall and one centered around the sensor location y_d, which is indicated by the dashed horizontal line. The in-plane velocity field has two stagnation points (indicated by the star symbols) and illustrates ejection (above the yellow region of positive ω_z at the wall) and sweep (above the blue region of negative ω_z at the wall) motions in the near-wall region. The spatial structure of the eigenmode is strikingly similar to the phase-averaged DNS flow field shown in fig. 5.10a in terms of both the features and their localization in the wall-normal direction. It is worth pointing out that the magnitude of the spanwise vorticity is different in both plots. However, we have not attempted to weight the eigenmode to match the DNS data, i.e. the unweighted velocity and vorticity fields are plotted as

obtained from the eigenvalue problem. The good agreement between the two flow fields further supports the hypothesis that the amplified eigenmode is important for the dynamics of the full nonlinear system in the drag-increased regime.

5.4.5 Spanwise-Elongated Scales: Resolvent Analysis

The previous section showed a strong correlation between the presence of an amplified eigenvalue in the temporal eigenspectrum and drag increase in DNS of single-scale control with $\boldsymbol{\kappa}_r$. In addition, the phase-averaged DNS flow field very closely resembles the structure of the amplified eigenmode. These observations suggest that the response of $\boldsymbol{\kappa}_r$ to control with $\angle\hat{A}_d \geq +\pi/4$ is dominated by the amplified eigenvalue. Recall that $\boldsymbol{\kappa}_r$ is a representative for the spanwise-elongated family of scales. This region in spectral space is not energetic in the uncontrolled flow, but dominates the wall-normal velocity spectra in the near-wall region for large positive phase shifts. The strong amplification suggests that the response of the entire spanwise-elongated family to control with $\angle\hat{A}_d \geq +\pi/4$ is due to the presence of amplified eigenvalues in the temporal eigenspectrum, analogous to $\boldsymbol{\kappa}_r$.

On the other hand, all eigenvalues are damped for $\angle\hat{A}_d \leq 0$, which means that the eigenmodes decay exponentially and have no significance for the long-term control response of $\boldsymbol{\kappa}_r$. The linear response in this parameter range is therefore described by the resolvent. The goal of this section is to analyze whether the suppression of individual resolvent modes, as defined in eq. (5.7), is linked to changes in the phase shift. It is important to note that the resolvent is not meaningful if the temporal eigenspectrum has neutrally stable or amplified eigenvalues, so that the following analysis is restricted to $\angle\hat{A}_d \leq 0$. Based on the results of the previous section, which showed that the uncontrolled mean is sufficient to capture the qualitative behavior of the system, we formulate the resolvent operator about the uncontrolled mean velocity profile (eddy viscosity approximation). Recall that resolvent analysis operates in the temporal frequency domain and assumes neutrally stable modes that do not grow or decay in time. The temporal frequency and wave speed are therefore purely real, and analogous to section 5.3.4, we will use the terms wave speed and phase speed interchangeably in the context of resolvent modes.

Figure 5.12 shows various aspects of scale suppression as a function of wave speed and phase shift. The top panel shows the scale suppression $\Delta\Phi_{vv}/(\Phi_{vv})_0$ computed from DNS data for $-3\pi/4 \leq \angle\hat{A}_d \leq 0$ and corresponds to the small inset in fig. 5.9. The large panel on the bottom left shows $\Delta\sigma_1^2/\left(\sigma_1^2\right)_0$, which is the approximation

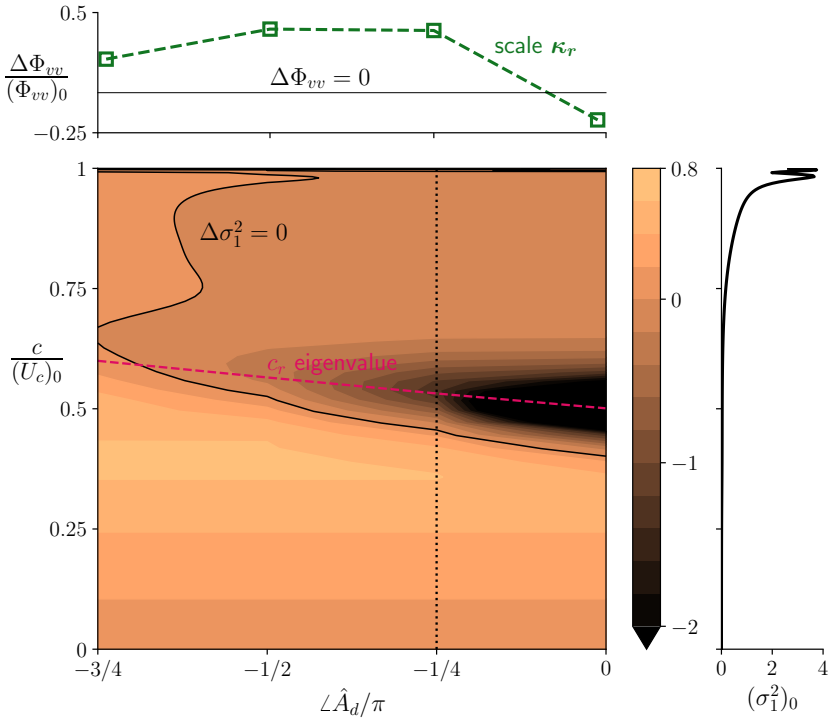

Figure 5.12: Suppression of scale κ_r as a function of the wave speed c and phase shift $\angle\hat{A}_d$. The top panel shows the DNS scale suppression over the range $-3\pi/4 \leq \angle\hat{A}_d \leq 0$ and corresponds to the inset of fig. 5.9. The panel on the bottom left displays the approximate resolvent mode suppression $\Delta\sigma_1/\left((\sigma_1)^2\right)_0$ as a function of c and $\angle\hat{A}_d$, while the bottom right panel shows the uncontrolled singular values $\left(\sigma_1^2\right)_0$ as a function of the wave speed. The solid black line in the top and bottom left panel delineate the regions of scale suppression and amplification, while the dashed red line indicates phase speed of the most amplified eigenvalue shown in fig. 5.11b. The dotted vertical line illustrates the suppression of resolvent modes for the example controller $\angle\hat{A}_d = -\pi/4$. Note that the color scale of the contour plot is saturated.

of resolvent mode suppression derived in eq. (5.11), as a function of c and $\angle\hat{A}_d$. Recall that the approximate metric is only based on the singular values and does not account for changes in the singular vectors due to control. The reason for presenting the approximation of the scale suppression will be given at the end of this section. Finally, the panel on the bottom right shows the uncontrolled singular values as a function of the wave speed. These three panels are related in the same way as for the streamwise-elongated scales, even if the approximation for the resolvent modes is reported. As a reminder for how to read this figure, consider the dotted vertical line in the bottom left panel of fig. 5.12. The product of the values along this line and the panel on the right equals the approximate resolvent mode suppression, $\Delta\sigma_1^2(c)$,

which is a function of wave speed. The integral of this product along the line (which is an integral in c) corresponds to the time-averaged resolvent scale suppression, which can be compared to the DNS metric in the panel above. Analogous to section 5.3.4, we look for quantitative agreement between resolvent and DNS scale suppression, which we interpret as evidence for a linear mechanism that relates scale suppression to the phase shift.

A first interesting aspect of fig. 5.12 is the magnitude of the singular values in the uncontrolled flow, shown in the bottom right panel. The singular values are almost zero for $c < 0.75\ (U_c)_0$, and even though they increase in magnitude with c, they are fairly small in comparison. For example, fig. 2.2 indicates that $(\sigma_1)_0$ of the mode $[\lambda_x^+ = 2262, \lambda_z^+ = 103, c^+ = 10]$ is more than a factor of three larger, and contributes almost an order of magnitude more energy than the most energetic mode at $\boldsymbol{\kappa}_r$ under the broadband forcing assumption. As explained earlier, the singular values alone do not describe the energy content of the real flow, but the small σ_1 are consistent with the DNS spectra, which showed that $\boldsymbol{\kappa}_r$ is not energetic in uncontrolled flows.

The panel on the bottom left shows that slow-moving resolvent modes ($c < 0.5\ (U_c)_0$) are suppressed by control with all phase shifts, while faster moving modes are mostly amplified. There is a region of strong local amplification, which becomes more pronounced as the phase shift approaches zero. Note that the color scale is saturated, which means that the amplification in this region is much stronger than indicated by the color. The comparison to DNS data is insofar challenging as the resolvent mode response is mixed across wave speeds. This makes it difficult to decide whether the resolvent would predict a net amplification or suppression. But despite this difficulty, we can detect qualitative similarities between the two panels. The DNS data indicates a scale amplification at $\angle \hat{A}_d = 0$, which is where the strong amplification occurs in the resolvent. For the other phase shifts, the resolvent scale suppression at a fixed c is fairly uniform, and similarly the DNS scale suppression is about constant in this parameter region. These matching trends provide evidence that the response of $\boldsymbol{\kappa}_r$ is linearly linked to changes in phase shift.

It is also interesting to note that the imprint of critical and attached modes, which was very pronounced in fig. 5.6, is not apparent here. Instead, the contour plot is dominated by the localized strong amplification around $\angle \hat{A}_d = 0$. In order to understand the origin of this large change in singular values, we have to connect the resolvent analysis to the eigenspectrum of the previous section. Recall that the temporal eigenspectrum of $\boldsymbol{\kappa}_r$ has one eigenmode that approaches the neutrally

stable axis, and eventually becomes amplified as $\angle\hat{A}_d$ increases. The phase speed of this eigenvalue at each $\angle\hat{A}_d$ was discussed in fig. 5.11b and is overlaid in this plot as red dashed line. The forcing frequencies of the resolvent along this line are the ones that have the smallest distance to the eigenvalue, and it is apparent that the amplification at those frequencies is largest. This phenomenon can be ascribed to the second mechanism that leads to large resolvent gains, termed resonance (Symon, Rosenberg, et al., 2018). It occurs if the eigenspectrum has one eigenvalue that is much closer to the neutral axis than all the others. These observations suggest that the behavior of the spanwise-elongated scales is fully determined by the eigenspectrum. The previous section showed that the amplified eigenvalue dominates the flow for $\angle\hat{A}_d \geq \pi/4$. And the current section shows that the resonance due to the proximity of the eigenvalue is the only significant amplification mechanism for the parameter range with damped eigenvalues. In particular, it is interesting to note that the transition from scale suppression to amplification occurs around $\angle\hat{A}_d = 0$, where the resonance mechanism is strongest.

Finally, we should also comment about the choice of resolvent scale suppression metric. As mentioned earlier, we reported the approximation $\Delta\sigma_1^2/\left(\sigma_1^2\right)_0$ in this section, which does not account for the changes in singular vectors due to control. We preferred this metric because the resonance mechanism uncovered in this section is a property of the singular values themselves, and can therefore be seen more cleanly if the influence of the singular vectors is omitted.

5.4.6 Spanwise-Elongated Scales: Summary

We close this section with a brief summary of the most important observations about the spanwise-elongated scales and their representative $\boldsymbol{\kappa}_r$. An analysis of the actuator spectra and drag reduction suggests that these scales are inactive for negative phase shifts and do not contribute to the behavior of varying-phase opposition control in this parameter regime. However, very strong amplification of spanwise-elongated scales and drag increase occur for positive phase shifts. The control response of $\boldsymbol{\kappa}_r$ is therefore not symmetric about $\angle\hat{A}_d = 0$. The eigenspectrum shows an amplified eigenvalue for all parameter combinations that lead to drag increase, and the DNS flow structure under single scale control with $\boldsymbol{\kappa}_r$ is very similar to the amplified eigenvalue. Furthermore, resolvent mode amplification occurs because of a resonance, which is observed when this one eigenvalue approaches the neutrally stable axis. The DNS and modal analyses provide strong evidence that the control response of $\boldsymbol{\kappa}_r$ is directly linked to its boundary condition by a linear mechanism.

This linear mechanism is fully driven by the eigenspectrum of the linearized Navier-Stokes operator.

5.5 Chapter Summary

The previous sections have explored and characterized the response of the streamwise-elongated and the spanwise-elongated scales to control with different phase shifts. In both cases, the changes in amplification and drag can be attributed to a linear response of each scale to the boundary condition. The response is linear in the sense that each scale reacts to the change in its own boundary condition, rather than to changes occurring at other scales. The mechanisms that underlie the response of each scale are encoded in the unforced or forced linearized Navier-Stokes operator, but they are different in nature for each family. The amplification of the spanwise-elongated scales is driven by the presence of an eigenvalue that approaches the neurally stable axis and eventually becomes amplified as the phase shift increases. On the other hand, the eigenvalues of the streamwise-elongated scales do not move in the complex plane as a function of the phase shift, and the response of this family is instead driven by a pseudoresonance mechanism. The goal of this section is to consider both families of scales together and use the previous insights to explain the topography of the drag reduction map in fig. 4.1. We will also compare the flow response under various control configurations to results in the literature to highlight the fundamental significance of these two families for flows with wall transpiration.

5.5.1 Topography of the Drag Reduction Map

We start the discussion by comparing the drag reduction obtained under varying-phase opposition control with all scales to the scale-restricted controllers. Following the approach of the previous sections, we focus on the effect of the phase shift and only consider the sensor location $y_d^+ = 15$. Figure 5.13 summarizes the drag reduction for various controllers as a function of $\angle \hat{A}_d$. The orange circles denote the drag reduction under varying-phase opposition control with all scales, which corresponds to the horizontal line in fig. 4.1. The green squares show the drag change under single scale control with the spanwise-elongated example scale $\boldsymbol{\kappa}_r$, which was shown earlier in fig. 5.7. The small inset displays a magnification of this curve for the parameter range $-3\pi/4 \leq \angle \hat{A}_d \leq \pi/4$, where the drag change is less pronounced. The blue diamonds finally show the drag change under single wave number control with the example streamwise-elongated scales $\{\boldsymbol{\kappa}\}_{k_{xs}}$, which was discussed in fig. 5.2. It is important to note that the figure has two ordinates. The

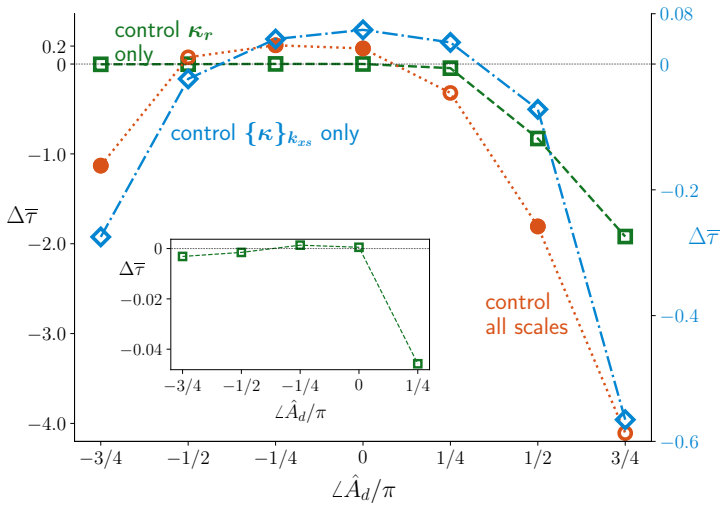

Figure 5.13: Drag reduction under varying-phase opposition control as a function of the phase shift $\angle\hat{A}_d$. The orange circles denote varying-phase opposition control with all scales and correspond to the orange horizontal line in fig. 4.1. The blue line shows the drag reduction for single wave number control with $\{\boldsymbol{\kappa}\}_{k_{xs}}$, while the green line denotes the drag change for single-scale control with $\boldsymbol{\kappa}_r$. The inset shows a magnification of the DR due to control with $\boldsymbol{\kappa}_r$ for the range $-3\pi/4 \leq \angle\hat{A}_d \leq +\pi/4$. Note that there are two ordinates on the main figure. The one on the left quantifies the drag reduction for the orange and green curve, while the ordinate on the right indicates the DR for the blue curve. In all cases, the sensors are located at $y_d^+ = 15$.

black ordinate on the left is the relevant one for varying-phase opposition control (orange line) and SS control with $\boldsymbol{\kappa}_r$ (green line). The drag reduction for SW control with $\{\boldsymbol{\kappa}\}_{k_{xs}}$ is quantified by the blue ordinate on the right. Recall from our previous discussions that positive values represent drag reduction, while negative values indicate drag increase.

We first compare the drag change magnitude of each curve, which allows identification of dominant scale families in different parts of the parameter space. The SS controller with $\boldsymbol{\kappa}_r$ does not lead to a statistically significant change in drag for $\angle\hat{A}_d \leq 0$, but control with this single scale can increase the drag by 82% ($\angle\hat{A}_d = +\pi/2$) or more for large positive phase shifts. Compared to this, the streamwise-elongated scales lead to much smaller drag changes. Recall from section 5.3.1 that control with the single scale $\boldsymbol{\kappa}_s$ did not lead to a statistically significant drag change for most phase shifts, and we had to increase the control input to all spanwise scales to obtain the blue curve in fig. 5.13. The single wave number controller acts on 169 Fourier modes instead of one, but only achieves drag reductions of the order of 8% and drag increases of a bit less than 60%. This shows that the amplification and ultimately

drag increase due to an amplified eigenvalue of the unforced linearized NSE ($\boldsymbol{\kappa}_r$) is much more pronounced than drag increase due to amplified singular values in the resolvent ($\{\boldsymbol{\kappa}\}_{k_{xs}}$). As a consequence, the flow response to control with all scales and $\angle\hat{A}_d > \pi/4$ is dominated by the spanwise-elongated family (i.e. by the amplified eigenvalues). The streamwise-elongated scales contribute to drag increase in this parameter regime as well, but their role is minor and their imprint is therefore not apparent in the spectrum of fig. 4.4d. On the other hand, the amplification changes of both families for $\angle\hat{A}_d \leq 0$ are determined by the singular values of the resolvent, so that their magnitude is comparable. The streamwise-elongated scales are much more energetic in the uncontrolled flow, so that that their singular value change has a more pronounced effect on the mean flow compared to the same change of the spanwise-elongated scales. The streamwise-elongated family therefore dominates the parameter range $\angle\hat{A}_d \leq 0$, and their imprint is most visible in the actuator spectra figs. 4.4a to 4.4c.

The drag reduction of varying-phase opposition control with all scales is now a superposition of the response of the two families, and each dominates in its phase shift range identified above. For $\angle\hat{A}_d \leq 0$, the streamwise-elongated family dominates, which results in drag increase for $\angle\hat{A}_d = -3\pi/4$, followed by a region of drag reduction for $-\pi/2 \leq \angle\hat{A}_d \leq 0$. The difference between the orange and the blue curve at $\angle\hat{A}_d = -\pi/2$ is likely because of the wave number dependent response of the streamwise-elongated scales at this phase shift, as explained in section 5.3. As the phase shift increases, the amplified eigenvalue of the spanwise-elongated family approaches the neutral axis and the scales become more energetic. They start dominating the flow response at $\angle\hat{A}_d = +\pi/4$ and drive the drag increase for larger phase shifts. The asymmetry of the drag reduction profile can also be explained by the two scale families. The response of the streamwise-elongated family is fairly symmetric about $\angle\hat{A}_d = 0$ and the symmetry only breaks for large $|\angle\hat{A}_d|$, because critical modes prefer negative phase shifts. On the other hand, the response of the spanwise-elongated family is not symmetric at all, because of the selective appearance of the amplified eigenvalue. The influence of the spanwise-elongated family therefore breaks the symmetry of the overall flow response, even at small phase shifts.

Finally, we consider the phase shift $\angle\hat{A}_d = 0$, which represents an interesting edge case. From the DR curve of the streamwise-elongated scales, one would expect that varying-phase opposition control should produce the largest drag reduction at this

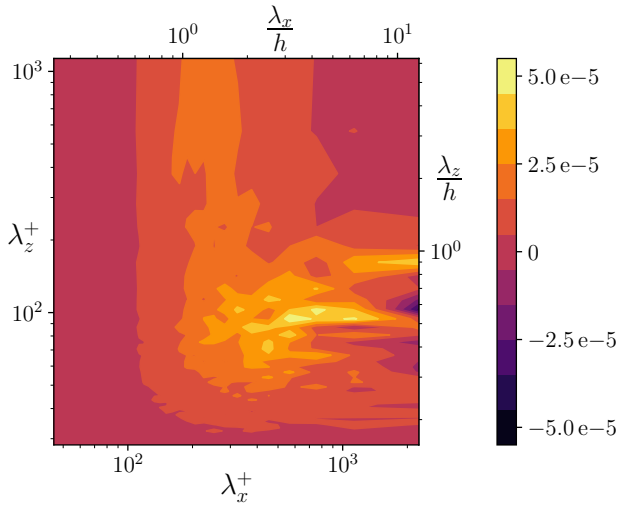

Figure 5.14: Difference of the time-averaged actuator spectra $\Phi_{vv}(y_w)$ at $\angle\hat{A}_d = 0$ (fig. 4.4c) and $\angle\hat{A}_d = -\pi/4$ (fig. 4.4b) as a function of the streamwise (λ_x) and spanwise wavelength (λ_z).

phase shift. But instead, the drag reduction is slightly lower than at $\angle\hat{A}_d = -\pi/4$. The SS controller with $\boldsymbol{\kappa}_r$ and the SW controller with $[k_x h = 6.5, k_z = 0]$ do both not produce a significant drag increase at $\angle\hat{A}_d = 0$, which raises the question what else could cause the deterioration. Possibly, the resonance mechanism identified for the spanwise-elongated scales around $\angle\hat{A}_d = 0$ still causes the deterioration, but at scales somewhat different than $\boldsymbol{\kappa}_r$. Recall that $\boldsymbol{\kappa}_r$ only accounts for 0.02% of the vv Reynolds stress at the sensor location, so that an amplification by a small factor does not result in a detectable mean change. However, if similar resonance mechanisms are present at more energetic scales of the spanwise-elongated family, they could conceivably cause the observed deterioration. If this reasoning applies, then the deterioration can be interpreted as an early warning for the catastrophic drag increase that takes place for slightly larger phase shifts when the eigenvalues cross over the neutral axis. Some evidence for this interpretation can be obtained by considering the difference of the actuation spectra at $\angle\hat{A}_d = 0$ and $\angle\hat{A}_d = -\pi/4$, which were discussed in fig. 4.4c and fig. 4.4b, respectively. Their difference is shown in fig. 5.14, now again as a function of wavelength in order to facilitate the comparison to the original actuator spectra. A positive value in fig. 5.14 indicates that the controller inputs more energy at $\angle\hat{A}_d = 0$ than at $\angle\hat{A}_d = -\pi/4$, and the opposite meaning applies for negative values. The interpretation of the figure is challenging, because a larger control input has different implications depending on which family a scale belongs to. It is also apparent that there is some overlap

between the families, so that the attribution is not always unique. Yet, one apparent feature is the more pronounced control input for spanwise-elongated scales centered around $\lambda_x^+ = 300$. These scales are expected to follow the trends of $\boldsymbol{\kappa}_r$, so that this additional control input will lead to further scale amplification due to the resonance mechanism shown in fig. 5.12. Provided that some of these scales are energetic enough, the scale amplification could translate into drag increase, and thus cause the overall deterioration of the controller performance. However, these conclusions are speculative and need further confirmation. It should be noted that the control input for the streamwise-elongated scales also changes between the two phase shifts. In particular, the actuator input for $\{\boldsymbol{\kappa}\}_{k_{xs}}$ decreases, which may also lead to a deterioration in control performance. In conclusion, the location of the maximum DR at $\angle\hat{A}_d = -\pi/4$ as well as the reason for the slight deterioration in control performance at $\angle\hat{A}_d = 0$ seem related to the interplay between the two scale families but the details of the deterioration still have to be clarified.

5.5.2 Comparison to Other Flows

The previous section suggests that the overall drag change of varying-phase opposition control results from the response of two different families of scales. For a fixed y_d, the phase shift $\angle\hat{A}_d$ controls which family of scales is dominant, and the spanwise-elongated family only becomes important for positive phase shifts. The goal of this section is to look for imprints of these scale families in flows with other forms of wall transpiration, which can help clarify their robustness and importance in such configurations.

The most comprehensive comparison can be made with the study of García-Mayoral and Jiménez (2011), who investigate the breakdown of the so-called viscous regime in a channel flow with rectangular riblets. For this flow geometry, the notion of wall transpiration applies to a wall-parallel plane located at the riblet tops, where the riblet grooves allow for a nonzero wall-normal velocity into or out of the plane. Beyond the viscous regime, the drag reduction due to riblets decreases with increasing riblet peak-to-peak distance and ultimately becomes a drag increase. The breakdown of the viscous regime and the following drag-increase coincides with the appearance of short and wide structures, characterized by $\lambda_x^+ \approx 150$ and $\lambda_z^+ \gtrsim 50$, above the riblet tops. These structures carry substantial Reynolds stresses and are therefore identified as the root-cause of the drag degradation. The scales that cause the viscous breakdown are similar to the energetic wavelengths of the spanwise-elongated family, which can be roughly characterized by $\lambda_x^+ \approx 170$ and $\lambda_z^+ \gtrsim 40$ (with a peak at

$\lambda_z^+ \to \infty$) from fig. 4.4d and table 4.1. In fact, the actuator input (v) of the controller with $\angle \hat{A}_d = +\pi/2$ and the wall-normal velocity above the riblet tops have a strikingly similar spectral content, as can be seen by comparing fig. 4.4d with fig. 8d of García-Mayoral and Jiménez (2011). The spanwise coherent structures above the riblets can be characterized as spanwise rollers centered around $y^+ \approx 10 - 15$, which is reminiscent of the flow structure shown in fig. 5.10a, even if the number of rollers is different. The similarities suggest that the structures causing the viscous breakdown are related to the spanwise-elongated scales that cause the drag increase in varying-phase opposition control.

Another qualitative analogy can be established between the streamwise-elongated scales and the flow response of near-wall cycle scales to riblets. A recent resolvent study by Chavarin and Luhar (2020) showed that the viscous regime and optimal spacing of rectangular riblets can be well approximated by considering the response of a near-wall resolvent mode $[\lambda_x^+ = 1000, \lambda_z^+ = 100, c^+ = 10]$ to various riblet spacings. In the viscous regime, the resolvent mode is increasingly suppressed with increasing riblet spacing, until the optimal spacing is reached. The singular value of the resolvent mode then starts increasing with riblet spacing and eventually leads to a drag increase. The resolvent calculations suggest that the near-wall cycle modes also contribute to the drag increase past the viscous breakdown, but their contribution is weaker compared to the spanwise rollers that dominate this regime. By our categorization of modes, the near-wall cycle mode would belong to the streamwise-elongated family of scales. Its response to various riblet spacings is reminiscent of the control response of the streamwise-elongated family to various phase shifts.

The behavior of varying-phase opposition control for positive phase shifts, where the spanwise rollers are dominant, can further be compared to a variety of other flows. Spanwise rollers have also been reported for flow over plant canopies (Finnigan, 2000), permeable (Breugem, Boersma, and Uittenbogaard, 2006; Efstathiou and Luhar, 2018; Gómez-de-Segura and García-Mayoral, 2019), and porous walls (Jiménez, Uhlmann, et al., 2001). In all cases, the appearance of the rollers is correlated with a significant change in flow structure and increase in drag, analogous to varying-phase opposition control with positive $\angle \hat{A}_d$. Spanwise coherent waves in combination with drag increase are also observed in turbulent flows over soft compliant walls. However, this case is somewhat different from the previous ones in that the drag increase and spanwise waves are attributed to a resonance of the

compliant wall under forcing of the flow (Kim and Choi, 2014). In other words, drag increase and formation of spanwise structures in this case do not only depend on the flow, but also on the material properties of the compliant wall.

The literature results mentioned above suggest that the mixed response of streamwise-elongated scales to control and the appearance of spanwise rollers are not a particularity of the present control scheme, but a robust feature of turbulent flows with some form of wall transpiration. In particular, the presence of spanwise rollers in drag-increased configurations seems to be a robust feature. There are quantitative differences, like the wavelength or wall-normal extent of the rollers, but it is intriguing that very different forms of wall-transpiration (active vs. passive, feedback vs. open-loop, etc.) all lead to essentially the same phenomenon. It is also interesting that modal analyses of all these flows provide insights into the formation of the rollers and the structure of the flow. For example, modal analyses of flow over riblets can predict the riblet peak-to-peak distance at which the viscous regime breaks down (García-Mayoral and Jiménez, 2011), or approximately reproduce the streamwise length scale and convection velocity of the spanwise rollers (Chavarin and Luhar, 2020).

At its core, the varying-phase opposition control scheme is a way to prescribe wall-transpiration based on templates that occur naturally in the flow, namely $\hat{v}(y_d)$, and to change the relative phase between transpiration and background flow at will by altering $\angle\hat{A}_d$. A range of phase shifts for transpiration with $\boldsymbol{\kappa}_r$ results in the same dynamical effect like a porous wall or a riblet past the viscous breakdown, at least phenomenologically. Another choice of phase shift with transpiration at $\boldsymbol{\kappa}_s$ damps the streamwise-elongated scales and leads to a similar flow response like a riblet in the viscous regime. In some sense, the phase shift $\angle\hat{A}_d$ is a knob that can be turned to reproduce, in isolation or superimposed, flow patterns that have been observed in other flows with wall transpiration. This suggests that the two families of scales together with the phase shift provide essential building blocks to study the physics of flows with wall-transpiration.

Compared to the other flow configurations, the varying-phase opposition control scheme has two advantages when it comes to studying the flow physics: first, the boundary condition can be changed on a scale-by-scale basis over a wide range of parameters. One can therefore tune the boundary condition to investigate a specific aspect of the problem. This gives the scheme more flexibility than say a porous or compliant wall, which are characterized by a few material parameters that act

uniformly on all spatial scales. Second, the flow phenomena of varying-phase opposition control are linear responses to boundary conditions at that same wave number. For example, the spanwise rollers induced by single scale control with κ_r occur because of boundary condition changes at that same κ_r. The direct link between boundary perturbation and scale response enables to analyze scales and phenomena in isolation. This is different for example from riblets, whose geometry offers similar design flexibility, but which interact with the flow in a complex way to trigger the observed responses. For instance, the riblets of García-Mayoral and Jiménez (2011) are streamwise constant and are characterized by their spanwise spacing and shape. It is not obvious what the link between this geometry and the suppression of near-wall cycle structures or the appearance of spanwise rollers is. This complicates even linear analyses of these flows, which have to include some nonlinear interactions to reproduce important flow phenomena (e.g. Chavarin and Luhar, 2020), or rely on simplifying assumptions about the flow in the riblet groves to produces a geometry-dependent boundary condition for all scales (e.g. linear stability analysis in García-Mayoral and Jiménez, 2011).

Chapter 6

PRESSURE CONSIDERATIONS

The results of the previous section show that the drag reduction characteristics of varying-phase opposition control and the presence of associated flow features are determined by phase relations at distinct spatial scales. For one set of scales, one can attenuate or amplify the near-wall cycle as a function of the phase shift, while for another set of scales, one can trigger the spanwise rollers for certain $\angle\hat{A}_d$. At least phenomenologically the interplay of near-wall cycle and spanwise rollers is a robust feature of flows with wall transpiration, and their correlation with phase shifts suggests that the latter may have a more fundamental meaning. If one thinks of varying-phase opposition control as simply providing a template for wall transpiration (i.e. the sensor measurement), then the phase shift changes the relation of the template relative to the background flow (in a relative phase or streamwise localization sense depending on the point of view). A natural question that arises from this line of thinking is whether one can elucidate the link between the shifted template and the background flow that underlies the observed phenomena. Of course there is no guarantee that a simple link exists, but if it did, it would raise hopes that all of the closed-loop wall transpiration configurations (to which we also count the passive control techniques with similar flow responses) can be reduced to a single problem. This chapter investigates whether the wall pressure is the link between wall transpiration and background flow.

6.1 Evidence for Velocity-Pressure Phase Relations in the Literature

Perhaps the most fundamental difference between flows with and without wall transpiration is the number of nonzero flow quantities at the wall. In the canonical case, the no-slip and no-through condition forces all velocity components to zero at the wall, so that the wall pressure is the only nonzero flow quantity. Of course the velocity gradients are nonzero as well, but this discussion focuses on the value of the primitive variables themselves, not their gradients. In contrast, a flow with wall transpiration has two non-zero wall quantities, the pressure and the vertical velocity. It is therefore quite intuitive that the relation between the wall pressure and the transpiration may be an important aspect of such flows. This was first appreciated by Xu, Rempfer, and Lumley (2003), who argued that a purely pressure-driven

compliant wall cannot reduce drag, because the induced velocity does not have the correct phase relative to the pressure field surrounding it. The reasoning behind this argument is that such compliant walls depress below high (i.e. positive) pressure regions, which results in a negative vertical velocity in the near-wall region and an out-of-phase relation between v and p. This is contrary to observations of drag-reducing active control schemes like opposition control, which likely induce positive vertical velocities in regions of high pressure (see the idealized sketch of fig. 1.3), so that v and p are in phase. In our terminology of the previous chapter, the suppression of quasi-streamwise vortices is associated with the streamwise-elongated scales, and the observations by Xu, Rempfer, and Lumley (2003) suggest that the velocity-pressure phase relation may be relevant for their control response.

The possible relevance of velocity-pressure phase relations is further supported by literature results on flow over porous and permeable walls (e.g. Jiménez, Uhlmann, et al., 2001; Efstathiou and Luhar, 2018; Gómez-de-Segura and García-Mayoral, 2019). These configurations typically relax the no-through condition and introduce a wall transpiration with a fixed velocity-pressure phase relation. For example, the transpiration boundary condition of a porous wall can be modeled as (Jiménez, Uhlmann, et al., 2001)

$$v(x, y, z, t) = -\beta\, p'(x, y, z, t) \tag{6.1}$$

where $\beta \geq 0$ is a material parameter and p' denotes the pressure fluctuations above the background pressure and mean gradients. By construction, these flows result in an out-of-phase relation between the wall transpiration and pressure, and result in drag increase for large enough β, thus supporting the argument of Xu, Rempfer, and Lumley (2003). The drag increase goes hand in hand with the appearance of spanwise rollers, which were associated with the spanwise-elongated scales in the previous chapter. The observations thus suggest that the velocity-pressure phase relation may be an important parameter for their behavior as well.

6.2 Validation of the Pressure Solver

The observations summarized in the previous section motivate an analysis of the control response of streamwise-elongated and spanwise-elongated scales from a pressure point of view. The DNS framework used in this study solves the Navier-Stokes equations in velocity-vorticity form (see section 2.2.1 for details), and does therefore not compute the pressure field as part of the solution. However, the pressure can be recovered in postprocessing, and to do so, we wrote a separate pressure

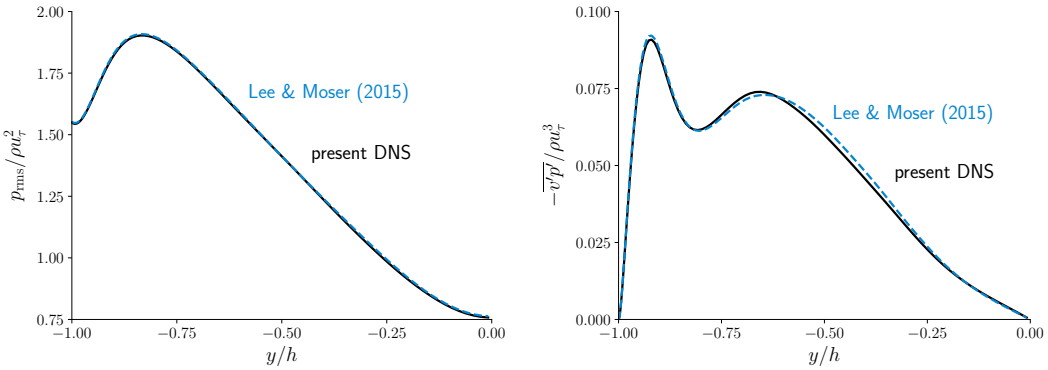

(a) Rms pressure profile

(b) Velocity pressure covariance

Figure 6.1: Validation of the pressure solver. Figure 6.1a compares the rms pressure profile and fig. 6.1b shows the velocity pressure covariance. The black line is data from the present solver, the dashed blue line is data from Lee and Moser (2015).

solver which is described in detail in section 2.2.2. Before analyzing controlled configurations, we validated the solver against literature data of canonical turbulent channel flows, and this section gives a brief summary of the results.

In analogy to the NSE solver, one would ideally validate the pressure solver for configurations with no-through walls and transpiration. The latter were not available for comparison, so that the validation is limited to the canonical flow. However, we note that the only change due to wall transpiration is an additional acceleration term in the Neumann boundary data (2.8) and one may therefore expect that even the canonical configuration provides an extensive test case for the solver. Figures 6.1a and 6.1b compare the rms pressure fluctuation profile and the $\overline{v'p'}$ covariance of a canonical channel flow at $\mathrm{Re}_\tau = 180$ with the data of Lee and Moser (2015). Excellent agreement is found for both quantities and throughout the channel domain, and gives confidence in the capabilities of the solver.

6.3 Evidence for Velocity-Pressure Phase Relations in Varying-Phase Opposition Control

We now turn our attention to the controlled configurations and consider a few select flows of particular interest.[1] Following the approach of Chapters 4 and 5, we consider varying-phase opposition control with sensors located at $y_d^+ = 15$ and focus on the effect of the phase shift. In particular, we are interested in the controller with $\angle \hat{A}_d = -\pi/4$ (maximum drag reduction, flow response dominated by streamwise-elongated

[1]The figures presented in this chapter are based on work done by D. Castillo during a Summer Undergraduate Research Fellowship (SURF) and subsequent senior thesis in our group.

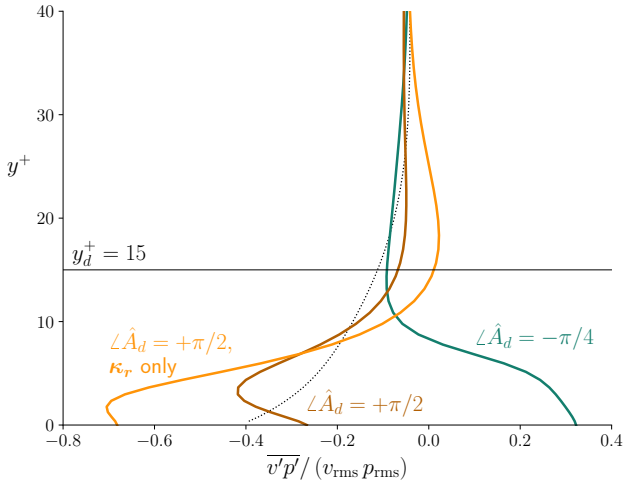

Figure 6.2: Velocity pressure correlation coefficient for various controlled flows. The phase shifts are specified in the plot, and the sensors are located at $y_d^+ = 15$ (indicated by the horizontal line) in all cases. Note that two control configurations are shown for $\angle\hat{A}_d = +\pi/2$: control with the single scale $\boldsymbol{\kappa}_r$ and control with all spatial scales. The dotted line denotes the correlation coefficient of the uncontrolled flow.

scales) and $\angle\hat{A}_d = +\pi/2$ (significant drag increase mainly driven by spanwise-elongated scales). The discussion of the drag-reducing configuration is based on control with all scales, while the drag-increasing configuration is explored by means of control with all scales and with the single scale $\boldsymbol{\kappa}_r$ defined in eq. (5.15). The SS control with $\boldsymbol{\kappa}_r$ at $\angle\hat{A}_d = +\pi/2$ is particularly insightful because the properties of its flow field have been explored in section 5.4.3.

We start the analysis with the correlation coefficient between the vertical velocity and pressure, which is shown in fig. 6.2 as a function of the wall-normal coordinate. In this specific case, the correlation coefficient is preferred over the covariance, because it eliminates differences in transpiration (see fig. 4.3) and pressure magnitude (data not shown) across the controlled flows, which simplifies the comparison. To aid the interpretation of the correlation coefficients, the figure further indicates the correlation in the uncontrolled flow (dotted line) and the sensor location (solid horizontal line). We note that an idealized out-of-phase control (e.g. porous wall) would result in a correlation coefficient of -1.0 at the wall, while an idealized in-phase control would correspond to a correlation coefficient of 1.0

A first observation is that all controllers change the phase relation in the near-wall region, and the modifications persist well past the sensor location up to $y^+ \approx 40$. Further away from the wall, the correlation in the controlled flows is no different

from the uncontrolled case (data not shown, but note the collapse of the profiles around $y^+ = 40$), so that the changes to the phase relation can be characterized as distinct, but local.

In order to connect fig. 6.2 with a physical picture, it is instructive to first consider the SS controller with $\angle \hat{A}_d = +\pi/2$. This configuration leads to a negative correlation between velocity and pressure in the near wall region and reaches a value of -0.68 at the wall. Since velocity and pressure are strongly correlated and out-of-phase, the transpiration resembles a porous wall on average. This can be seen physically from the phase-averaged flow field of fig. 5.10a: close to the wall, the spanwise rollers centered around $y^+ \approx 20$ induce a downwash (high pressure) region, which is roughly confined by the two stagnation points (i.e. $0.3 \leq x/\lambda_{xr} \leq 0.8$), and an upwash (low pressure) region further upstream and downstream. On average, the wall transpiration is negative below the high pressure region and positive below the low pressure region, which illustrates that SS control with $\boldsymbol{\kappa}_r$ and $\angle \hat{A}_d = +\pi/2$ has indeed a similar effect to a porous wall. However, note that transpiration and pressure are slightly offset in the streamwise direction, which likely reduces the correlation between the two quantities, which is consistent with fig. 6.2.

Control of all scales with $\angle \hat{A}_d = +\pi/2$ also leads to a negative correlation coefficient at the wall, even if the correlation reduces to -0.27. The decrease can likely be attributed to the activity of other scales (recall the many energetic scales in the actuation spectrum of fig. 4.4d), which will be explored subsequently. On the other hand, control with all scales and $\angle \hat{A}_d = -\pi/4$ leads to a positive correlation coefficient in the near wall region ($\overline{v'p'}/(v_{\mathrm{rms}}p_{\mathrm{rms}}) = 0.32$ at the wall). All these observations are consistent with the hypothesis that negative v-p phase relations correlate with drag increase, while positive v-p phase relations correlate with drag reduction.

Figure 6.2 further suggests that the phase relation varies across $\boldsymbol{\kappa}$, because the correlation of controller $\angle \hat{A}_d = +\pi/2$ decreases when more scales are controlled. To shed light on this aspect, we next consider the velocity pressure co-spectra Φ_{vp} shown in fig. 6.3a for $\angle \hat{A}_d = -\pi/4$ and fig. 6.3 for $\angle \hat{A}_d = +\pi/2$, which provide information about the sign and magnitude of the correlation at each scale. Note that both shown configurations control all spatial scales. The cospectrum for the single-scale controller is omitted, because it only has a single nonzero entry at $\boldsymbol{\kappa}_r$. For reference, the co-spectra also include contours of the corresponding actuator signal (15% and 30% of the maximum actuator input, respectively), to draw the

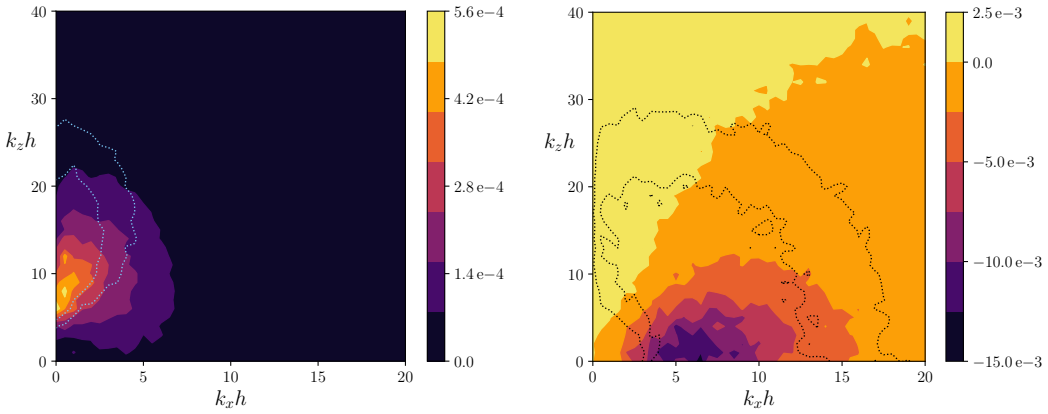

(a) $\angle \hat{A}_d = -\pi/4$ (b) $\angle \hat{A}_d = +\pi/2$

Figure 6.3: Velocity pressure cospectrum Φ_{vp} for two example controllers as a function of the streamwise and spanwise wave number. Control is applied to all spatial scales, and the dotted lines denote the contour levels of 15% and 30% of the maximum actuator input Φ_{vv} shown in figs. 4.4b and 4.4d, respectively. Note that the color scale is different in each figure.

attention to the most important control scales. The wave numbers $k_x h > 20$ and $k_z h > 40$ are omitted in these figures, since the actuator input is much smaller at these wave numbers.

We first consider the drag-reducing controller $\angle \hat{A}_d = -\pi/4$, whose cospectrum is shown in fig. 6.3a. In this case, the covariance is non-negative, and the largest contribution comes from the streamwise-elongated scales, which also dominate the actuator input. However, it is interesting to observe that the two contour maps are slightly offset. A range of long and wide scales, which do not have a significant imprint in the actuator spectrum, contribute to the covariance, and must therefore be associated with energetic wall pressure modes.

In comparison, the v-p cospectrum of the drag increasing controller $\angle \hat{A}_d = +\pi/2$ shown in fig. 6.3b is more complex (note the different color scale). The most active area in spectral space is centered around the spanwise-elongated scales, and their contributions are all negative, consistent with the observations for the SS controller. Similarly to the previous case, the contribution decreases away from the most active scales of the actuator, but interestingly, the sign of the covariance changes in parts of the wave number space (yellow region). The sign change occurs along an almost straight line (i.e. fixed aspect ratio of scales), but it is yet to be determined if this has a significance. In any case, the scales of the streamwise-elongated family are still positively correlated to the pressure, even at this phase shift. It remains unclear if this

correlation is due to the flow structure generated by the spanwise-elongated scales or if it is a characteristic of the streamwise-elongated family, and future single-scale control experiments are needed to clarify this aspect. The mixed v-p phase relation in spectral space certainly leads to a decrease of the overall correlation, which is consistent with the observations of fig. 6.2.

Despite these insights, it is important to point out the fundamental limitation of cospectra with regards to elucidating the v-p phase relations. In order to put our hypothesis about the correlation between velocity-pressure phase relation and drag reduction to test, we need to interrogate the time-averaged phase difference between v and p at each $\boldsymbol{\kappa}$. The sign information contained in the cospectrum encodes some of this information, but in a rather crude way. All one can infer from fig. 6.3 is whether the absolute value of the phase difference between v and p is larger or smaller than $\pi/2$ in an average sense, which is weighted by the time-dependent magnitude of the Fourier coefficients. The cospectrum can therefore not provide a measure for how strong a phase relation between $\hat{v}$ and $\hat{p}$ is at a specific $\boldsymbol{\kappa}$. To illustrate this point, assume that the entry in the cospectrum at a given $\boldsymbol{\kappa}$ is large. This large entry can have two possible origins: a strong phase relation (so that the cos function returns a value close to one), or large amplitudes of $\hat{v}$ and $\hat{p}$ at that scale. A different, purely phase based metric is needed to clarify the role of the velocity-pressure relations, and this is subject of ongoing work.

6.4 Energy Aspects

The velocity-pressure phase relations also have implications for the energy budget of the flow, which will be explored in this section. It will be shown that the kinetic energy equation includes expressions for the work done by the wall transpiration, so that this analysis also lends itself to analyze efficiency aspects of varying-phase opposition control.

The (nondimensional) kinetic energy of the flow at any instant in time is defined as

$$E_k(t) = \int_0^{L_x/h} \int_0^{L_z/h} \int_{-1}^{1} \frac{1}{2} \left(\boldsymbol{u} \cdot \boldsymbol{u}\right) \mathrm{d}\left(\frac{x}{h}\right) \mathrm{d}\left(\frac{z}{h}\right) \mathrm{d}\left(\frac{y}{h}\right), \tag{6.2}$$

and an evolution equation for E_k can be obtained from the integral of the dot product between the velocity vector and the NSE eq. (2.1). Often times, the kinetic energy equation of the mean flow and the fluctuations are considered separately, but for the purpose of this study, it will be advantageous to consider the energy of the full velocity field. Even so, it is advantageous to split the instantaneous velocity field

into a wall-parallel mean $\langle \boldsymbol{u} \rangle(y,t)$ and fluctuations $\boldsymbol{u}'(\boldsymbol{x},t)$ about that mean, and write the total kinetic energy equation in terms of these quantities. The resulting expression reads

$$\begin{aligned}\frac{\mathrm{d}E_k}{\mathrm{d}t} &= \frac{L_x}{h}\frac{L_z}{h}\Bigg[-2\Pi_x U_b + \left(\left.\frac{\langle (v')^3 \rangle}{2}\right|_{y/h=-1} + \langle v'p' \rangle|_{y/h=-1} \right) \\ &\quad - \left(\left.\frac{\langle (v')^3 \rangle}{2}\right|_{y/h=1} + \langle v'p' \rangle|_{y/h=1} \right) - \frac{1}{\mathrm{Re}} \int_{-1}^{1} \left(\frac{\partial \langle u \rangle}{\partial y}\frac{\partial \langle u \rangle}{\partial y} + \left\langle \frac{\partial u_i'}{\partial x_j}\frac{\partial u_i'}{\partial x_j} \right\rangle \right) \mathrm{d}\left(\frac{y}{h}\right) \Bigg] \end{aligned} \tag{6.3}$$

where the first term represents the work done by the pressure gradient to drive the bulk flow, the second and third terms are the work done by the wall transpiration, and the last term represents the viscous dissipation. The work done by the transpiration has two terms, one that quantifies kinetic energy input (first term) and one that quantifies pressure work (second term).

The average power input of the pressure gradient can be estimated from the time-average of the first term

$$W_{\mathrm{PG}} = -2\frac{L_x}{h}\frac{L_z}{h}\overline{\Pi}_x U_b. \tag{6.4}$$

Analogously, one can take the time-average of the second and third term to estimate the ideal power input of the actuation

$$W_{\mathrm{act}} = \frac{L_x}{h}\frac{L_z}{h}\left[\left(\left.\frac{\overline{(v')^3}}{2}\right|_{y/h=-1} + \left.\overline{v'p'}\right|_{y/h=-1} \right) - \left(\left.\frac{\overline{(v')^3}}{2}\right|_{y/h=1} + \left.\overline{v'p'}\right|_{y/h=1} \right) \right]. \tag{6.5}$$

It is important to note that each term is signed, which implies the assumption that the actuators can gain energy from the flow, for example when the terms at the bottom wall are negative. A more conservative estimate could preclude work done by the flow on the actuators and estimate the average power input based on the absolute value. There is an interesting connection between the kinetic energy equation and the velocity-pressure phase relations discussed earlier. The second term of the actuator input is proportional to the correlation coefficient of fig. 6.2, and also corresponds to the sum over the cospectra of fig. 6.3. From our discussion in the previous section, it is now apparent that this term corresponds to an energy sink of the flow in case of the drag-increasing controllers with $\angle \hat{A}_d = +\pi/2$, and an energy source of the flow for the drag-reducing controller with $\angle \hat{A}_d = -\pi/4$.

The work considerations further allow quantification of efficiency for a fixed mass flux flow. To this end, we first define the mean power saved as the difference between

the pressure gradient work in the uncontrolled and the controlled configuration

$$\Delta W_{\mathrm{PG}} = -2\frac{L_x}{h}\frac{L_z}{h}\left[\left(\overline{\Pi}_x\right)_0 - \left(\overline{\Pi}_x\right)_c\right]U_b. \tag{6.6}$$

We can then define a control efficiency η as power saved per control input

$$\eta = \frac{\Delta W_{\mathrm{PG}}}{W_{\mathrm{act}}}. \tag{6.7}$$

An evaluation of the balance between the pressure and kinetic energy term of the actuator work and the control efficiency for various control configurations is currently underway.

6.5 Chapter Summary

This chapter outlined an early analysis aimed at understanding whether the control response of streamwise-elongated and spanwise-elongated scales can be understood in terms of scale-by-scale phase relations between wall pressure and transpiration. This possible link was motivated by literature results on compliant and porous walls, which suggest that the attenuation of the near-wall cycle correlates with an in-phase relation of v and p (compliant wall), while the appearance of spanwise rollers is observed for out-of-phase relations (porous walls). To investigate this hypothesis, we developed and validated a solver to recover the pressure field, which is not required to march the Navier-Stokes equations in time and is therefore not computed, during postprocessing. The present results indicate that an out-of-phase relation between v and p correlates with drag increase, while an in-phase relation is associated with drag reduction. Further diagnostics and data from scale-restricted control configurations are needed to fully understand this aspect and both are subject of ongoing work. A confirmation of a robust relation between the velocity-pressure phase relation and drag reduction would further enable to control the two families of scales based on wall data only, which would be an important step towards the practical implementation of the control scheme. The pressure field also allows quantification of power savings and actuation efficiency, which is currently underway as well.

Chapter 7

CONCLUSIONS AND FUTURE WORK

Even after decades of active research, turbulent flow control for drag reduction remains an open problem of enormous practical relevance. Some of the challenges arise because we currently lack tools to analyze and design flow controllers at technologically relevant Reynolds numbers. Other challenges arise because the introduction of an actuator signal fundamentally changes the flow dynamics, and our understanding of these modified flows lags significantly behind the canonical configurations. In this context, the two open questions of particular interest for this thesis can be summarized as follows: what are suitable controller design tools for high Reynolds number flows? And how does actuation through closed-loop wall transpiration change the flow physics? The thesis contributed to those questions through direct numerical simulation and modal analyses of an example control scheme, dubbed varying-phase opposition control, which was applied to a turbulent channel flow at $\mathrm{Re}_\tau = 180$.

7.1 Summary

Varying-phase opposition control is a generalization of the well-known opposition control scheme (Choi, Moin, and Kim, 1994), and introduces a phase shift $\angle \hat{A}_d$ between the Fourier transformed sensor measurement $\hat{v}(y_d)$ and the actuation at the wall $\hat{v}(y_w)$. The DNS results of Chapter 3 showed that the drag reduction (DR) under varying-phase opposition control strongly depends on both the sensor location and the phase shift. The role of the sensor location has been clarified in a series of past publications (Choi, Moin, and Kim, 1994; Hammond, Bewley, and Moin, 1998; Chung and Talha, 2011; Luhar, Sharma, and McKeon, 2014b), and there is compelling evidence that the optimal sensor location roughly coincides with the center of the quasi-streamwise vortices, so that this aspect was not further considered. The DNS data also showed that varying-phase opposition control with a small negative $\angle \hat{A}_d$ leads to maximum DR, while a positive or large negative phase shift deteriorates the control performance and eventually leads to a drag increase.

Before exploring the role of the phase shift, we assessed in Chapter 3 whether a low-order model based on the resolvent framework is capable of approximating the DNS drag reduction trends. Even though the resolvent model was constructed with

the simplest assumptions possible (uncontrolled mean profile, rank-1 approximation, broadband forcing), it captured the DNS drag reduction trend over the entire parameter space considered. At $\mathrm{Re}_\tau = 180$, the resolvent model was about two orders of magnitude cheaper to evaluate than DNS. But more importantly, unlike DNS, the resolvent model is not limited to low Reynolds numbers, and we outlined a strategy based on sparse subsampling of the wave number space and analytical scalings of the resolvent modes (Moarref, Sharma, et al., 2013), which enabled a cheap model evaluation at technologically relevant Reynolds numbers. Chapter 3 therefore contributed to the first open question and demonstrated that the resolvent framework can be a suitable flow control design tool at large Re_τ.

The remainder of the thesis analyzed the role of the phase shift in varying-phase opposition control, which is closely related to the second open question. A comparison of DNS data for $\angle\hat{A}_d \in [-3\pi/4, 3\pi/4]$ showed that the structural and spectral features of controlled flows change as a function of the phase shift (Chapter 4). For negative $\angle\hat{A}_d$ (which can lead to drag reduction or increase), the flow structure was reminiscent of the canonical case and the controller signal was dominated by length scales that are typically associated with the near-wall cycle. In contrast, the flow structure at positive $\angle\hat{A}_d$ (which lead to drag increase) looked remarkably different and the controller was most active at spanwise-constant scales. These observations suggested that the physics of varying-phase opposition control can be understood by considering the flow response of two distinct families of scales, termed streamwise-elongated and spanwise-elongated scales. At the present $\mathrm{Re}_\tau = 180$, these families were localized in spectral space around the wave number pair $\boldsymbol{\kappa}_s = [k_{xs}h = 0.5, k_{zs}h = 11]$ (streamwise-elongated) and $\boldsymbol{\kappa}_r = [k_{xr}h = 6.5, k_{zr}h = 0]$ (spanwise-elongated), respectively.

We then conducted a series of direct numerical simulations to study the response of each scale family to control with various $\angle\hat{A}_d$ (chapter 5). In order to establish a clear link between phase shift and scale response, nonlinear effects were minimized as much as possible by controlling either a single Fourier mode in isolation (single scale control) or a subset of wave numbers (single wave number control), which cannot directly feed back on each other (i.e. they are not triadically consistent). The streamwise-elongated scales were active at all phase shifts, and the attainable drag reduction was found to be almost symmetric about $\angle\hat{A}_d = 0$. Control with small positive or negative phase shifts suppressed the streamwise-elongated scales and lead to drag reduction, while large positive or negative phase shifts further amplified

these scales, which resulted in a drag increase. These trends correlate with the ones of varying-phase opposition control, which suggested that the streamwise-elongated family shapes the drag reduction of the full scheme at least partially. A modal analysis further revealed that the temporal eigenvalues of the streamwise-elongated scales are damped for all phase shifts, and the amplification trends with $\angle \hat{A}_d$ could be well approximated by a resolvent analysis. In contrast, the spanwise-elongated scales were only energetic for positive $\angle \hat{A}_d$, and control in this parameter regime always lead to a strong scale amplification and drag increase. The trends for positive phase shifts correlated with ones of varying-phase opposition control, which suggested that the spanwise-elongated family contributes to the drag reduction in this parameter regime as well. The onset of the drag increase correlated well with the appearance of an amplified eigenvalue in the temporal eigenspectrum, and the phase averaged DNS flow field was indistinguishable from the associated eigenmode, which suggested that the control response of the spanwise-elongated scales was fully described by the eigenspectrum. The overall drag reduction behavior of varying-phase opposition control was then shown to correlate with the superposition of the control response of these two families. The spanwise-constant scales are inactive for negative phase shifts investigated here, so that this parameter regime is fully determined by the streamwise-elongated scales. On the other hand, both scale families contribute to the flow response at positive $\angle \hat{A}_d$, but the contribution of the spanwise-elongated scales is dominant. The resulting flow response to varying-phase opposition control is asymmetric about $\angle \hat{A}_d = 0$, mostly because of the spanwise-elongated scales. Chapter 5 therefore contributed to the second question and provided further evidence that flows with closed-loop wall transpiration exhibit different physics compared to the canonical case. The transpiration can interact with the near-wall cycle and either weaken or amplify it (streamwise-elongated scales). In addition, the transpiration can trigger spanwise rollers which are absent in the canonical flow (spanwise elongated scales). These rollers provide an additional (or alternative if the near-wall cycle is damped) mechanism for momentum mixing, and are therefore correlated with drag increase. An analysis of the wall pressure data further suggests that in-phase v-p configurations correlate with drag reduction, while out-of-phase velocity-pressure configurations are associated with drag increase. These findings are consistent with the conceptual model of Xu, Rempfer, and Lumley (2003) for compliant walls, and implications for the scale-by-scale control response are subject of ongoing investigations.

7.2 High-Level Perspective

The above results suggest a few high-level conclusions regarding the two open questions. With regards to modal analyses, a robust observation throughout this study was that the uncontrolled mean is sufficient to approximate the behavior of the nonlinear system to control. This is good news, because it implies that the eddy viscosity approximation of the uncontrolled mean provides a suitable flow state about which the low-order models can be formulated. In particular, the eddy viscosity approximation allows to extend these models to flow regimes for which no empirical data are available. There is likely a limit to the validity of this simplification, but it is currently not clear at what flow perturbation magnitude the uncontrolled mean ceases to be appropriate. The present study raises some hopes that the modal analyses are fairly robust, since the uncontrolled mean provided a good approximation even for control configurations which doubled Re_τ.

Another important conclusion for both questions can be drawn from the analysis of the temporal eigenspectrum. The mean profile of a canonical turbulent channel flow is thought to be linearly stable (Reynolds and Tiederman, 1967), but previous studies have shown that the relaxation of the no-through condition can destabilize the eigenvalues (Jiménez, Uhlmann, et al., 2001; García-Mayoral and Jiménez, 2011). The present study analyzed the relaxation of the no-through condition from the perspective of the temporal eigenspectrum, which does not include an eddy viscosity in the linearized operator and which describes the natural response of the system rather than the stability of the mean flow. The temporal eigenspectrum was shown to contain amplified eigenvalues for certain wave number combinations and phase shifts, very analogous to the aforementioned stability analyses. This comes with implications for the flow physics, which will be discussed later, and for resolvent-based low-order models for flow control. Since the resolvent operator characterizes the steady-state response of the system, it is only meaningful if the natural system response decays, i.e. if there are no amplified eigenvalues in the temporal eigenspectrum. A first step for resolvent-based control design should therefore be to analyze the temporal eigenspectrum under the control boundary conditions (e.g. wall transpiration). We were not yet aware of the large eigenvalue changes under wall transpiration with different phase shifts when we did the analysis of Chapter 3, and did therefore not do the preliminary eigenspectrum check. In light of Chapter 5, the integrated resolvent results for positive phase shifts (where amplified eigenvalues were shown to exist) should be considered with some caution. The resolvent model likely misses the influence of the spanwise-elongated family

for positive phase shifts, but still reproduces the correct trend, because it captures the drag increase due to the streamwise-elongated scales.

In terms of flow physics, there is growing evidence that closed-loop wall transpiration (or passive schemes that can be interpreted as such) lead to flow phenomena that are not observed in canonical flows. In particular, there seem to be two recurring scenarios: first, the transpiration attenuates or amplifies the near-wall cycle, and second, the transpiration can trigger spanwise-coherent rollers (among others Jiménez, Uhlmann, et al., 2001; Breugem, Boersma, and Uittenbogaard, 2006; García-Mayoral and Jiménez, 2011; Kim and Choi, 2014; Gómez-de-Segura and García-Mayoral, 2019; Chavarin and Luhar, 2020). In the passive control cases, the flow perturbation is set by the geometry or a few material parameters, and it is often difficult to track how the change in boundary condition affects individual scales. This is apparent in the linear analyses of these configurations, which often rely on assumptions about the flow close to the surface to arrive at a scale-dependent boundary condition (e.g. García-Mayoral and Jiménez, 2011), or need to account for a subset of nonlinear interactions (e.g. Chavarin and Luhar, 2020). The varying-phase opposition control scheme reproduces the same flow patterns, and offers a different, perhaps more fundamental perspective on their origin. In contrast to the passive methods, the flow response of varying-phase opposition control depends linearly on the phase shift, and the flow phenomena can be triggered by considering scales in isolation and choosing an appropriate $\angle \hat{A}_d$. In a more abstract interpretation, the varying-phase opposition control scheme provides a means to selecting a flow structure that naturally occurs in the flow (this is the sensor measurement $\hat{v}(y_d)$), and applying a shifted version of it at the wall (this is the actuator input $\hat{v}(y_w)$). It is these shifted templates that give rise to the additional physics of flows with closed-loop wall transpiration. This provides a possibly more fundamental description of such flows, in particular in conjunction with the wall pressure field. The pressure considerations of Chapter 6 suggest that the phase difference between wall pressure and transpiration is an important parameter of such flows, as conjectured earlier by Xu, Rempfer, and Lumley (2003).

With an eye towards practical applications, the results of the present thesis suggest that the spanwise-elongated scales do not reduce drag, but only increase it. These scales are best left uncontrolled (or measures should be put in place to ensure that they are not excited), since control can only make things worse. Exclusion of the deteriorating scales can help reduce the spatial resolution requirements of controllers

even in the drag-reducing regime, and especially with regards to small streamwise scales. For example, the scale κ_r, which can be left uncontrolled, is the smallest energetic scale over the considered parameter range. In this context, the temporal eigenspectrum can serve as a computationally cheap tool to identify scales to be excluded, which are the ones with amplified eigenvalues.

7.3 Future Work

More work is needed to conclusively answer the two questions formulated at the beginning of this chapter, and ideally different perspectives can provide complementary pieces to the puzzle. Below we outline a few future research directions that can further contribute to these open questions from the perspective taken in this thesis.

Chapter 3 showed that the broadband-forcing resolvent model is capable of approximating the DNS drag reduction trends at low Reynolds numbers. Moreover, the results confirmed that the known scaling laws of the uncontrolled resolvent operator also hold in the presence of wall transpiration, which enabled an efficient evaluation of the resolvent at high Re_τ. One aspect that the present study did not investigate is the performance of the broadband forcing assumption at higher Reynolds numbers, where the large scale influence on the near-wall region becomes more important. It is possible that the broadband forcing assumption is still adequate also in this flow regime, at least to first order. However, if the nonlinear amplitude modulation changes the relation between control input and flow response at leading order, then it has to be incorporated in the resolvent model, where it would enter the forcing term. Possible approaches to account for scale interactions have been reported in the literature and include addition of an eddy viscosity to the resolvent operator to model the Reynolds stresses (e.g. Morra, Semeraro, et al., 2019), or replacement of the broadband forcing with more sophisticated models (e.g. Moarref, Sharma, et al., 2013; McMullen, Rosenberg, and McKeon, 2020; Morra, Nogueira, et al., 2021). However, these studies focused on reconstruction of flow statistics, which is a more stringent requirement than needed for flow control purposes. An interesting future avenue would therefore be to explore what the simplest possible model of scale interactions is in a controls context, where one is mainly concerned about capturing the relation between control input and flow response.

In addition, it would be interesting to consider varying-phase opposition control from the perspective of the Orr-Sommerfeld and Squire decomposed resolvent (Rosenberg

and McKeon, 2019). In this framework, the control boundary condition, which was shown to drive the flow response, only enters the Orr-Sommerfeld operator. It is therefore likely that closed-loop wall transpiration has implications for the competition mechanism between Orr-Sommerfeld and Squire modes (Rosenberg and McKeon, 2019; McMullen, Rosenberg, and McKeon, 2020), and it would be interesting to investigate those in detail.

With regards to the flow physics of wall transpiration, it would further be important to understand if the spanwise-elongated scales remain important at higher Reynolds number. A recent experimental investigation of porous walls found evidence for their existence at $\mathrm{Re}_\tau \approx 1700$ (Efstathiou and Luhar, 2018), and it is possible that they persist well past that regime. To clarify this question, it may be sufficient to look at the temporal eigenspectrum, since the appearance of the spanwise rollers correlates with the presence of an amplified eigenvalue. However, the scaling of the rollers has to be investigated first in order to inform the wave number selection for the eigenspectrum. Finally, the correlation between drag reduction and the velocity pressure phase relation may be useful to devise future wall-based control schemes.

BIBLIOGRAPHY

Abbassi, M. et al. (2017). "Skin-friction drag reduction in a high-Reynolds-number turbulent boundary layer via real-time control of large-scale structures". In: *International Journal of Heat and Fluid Flow* 67. Symposium on Experiments and Simulations in Fluid Dynamics Research, pp. 30–41. DOI: 10.1016/j.ijheatfluidflow.2017.05.003.

Adrian, R. J., Meinhart, C. D., and Tomkins, C. D. (2000). "Vortex organization in the outer region of the turbulent boundary layer". In: *Journal of Fluid Mechanics* 422, pp. 1–54. DOI: 10.1017/S0022112000001580.

Batchelor, G. K. (2000). *An Introduction to Fluid Dynamics*. Cambridge Mathematical Library. Cambridge University Press. DOI: 10.1017/CBO9780511800955.

Bechert, D. W. et al. (1997). "Experiments on drag-reducing surfaces and their optimization with an adjustable geometry". In: *Journal of Fluid Mechanics* 338, pp. 59–87. DOI: 10.1017/S0022112096004673.

Bourguignon, J.-L. et al. (2014). "Compact representation of wall-bounded turbulence using compressive sampling". In: *Physics of Fluids* 26.1, p. 015109. DOI: 10.1063/1.4862303.

Breugem, W. P., Boersma, B. J., and Uittenbogaard, R. E. (2006). "The influence of wall permeability on turbulent channel flow". In: *Journal of Fluid Mechanics* 562, pp. 35–72. DOI: 10.1017/S0022112006000887.

Butler, K. M. and Farrell, B. F. (1992). "Three-dimensional optimal perturbations in viscous shear flow". In: *Physics of Fluids A: Fluid Dynamics* 4.8, pp. 1637–1650. DOI: 10.1063/1.858386.

Butler, K. M. and Farrell, B. F. (1993). "Optimal perturbations and streak spacing in wall-bounded turbulent shear flow". In: *Physics of Fluids A: Fluid Dynamics* 5.3, pp. 774–777. DOI: 10.1063/1.858663.

Canuto, C. et al. (1988). *Spectral Methods in Fluid Dynamics*. Springer Series in Computational Physics. Springer. DOI: 10.1007/978-3-642-84108-8.

Chang, Y., Collis, S. S., and Ramakrishnan, S. (2002). "Viscous effects in control of near-wall turbulence". In: *Physics of Fluids* 14.11, pp. 4069–4080. DOI: 10.1063/1.1509751.

Chavarin, A., Gómez-de-Segura, G., et al. (2021). "Resolvent-based predictions for turbulent flow over anisotropic permeable substrates". In: *Journal of Fluid Mechanics* 913, A24. DOI: 10.1017/jfm.2020.1169.

Chavarin, A. and Luhar, M. (2020). "Resolvent analysis for turbulent channel flow with riblets". In: *AIAA Journal* 58.2, pp. 589–599. DOI: 10.2514/1.J058205.

Chevalier, M. et al. (2006). "State estimation in wall-bounded flow systems. Part 2. Turbulent flows". In: *Journal of Fluid Mechanics* 552, pp. 167–187. DOI: 10.1017/S0022112005008578.

Choi, H., Moin, P., and Kim, J. (1993). "Direct numerical simulation of turbulent flow over riblets". In: *Journal of Fluid Mechanics* 255, pp. 503–539. DOI: 10.1017/S0022112093002575.

Choi, H., Moin, P., and Kim, J. (1994). "Active turbulence control for drag reduction in wall-bounded flows". In: *Journal of Fluid Mechanics* 262, pp. 75–110. DOI: 10.1017/S0022112094000431.

Chung, Y. M. and Sung, H. J. (2003). "Sensitivity study of turbulence control with wall blowing and suction". In: *Third Symposium on Turbulence and Shear Flow Phenomena*. Begel House Inc.

Chung, Y. M. and Talha, T. (2011). "Effectiveness of active flow control for turbulent skin friction drag reduction". In: *Physics of Fluids* 23.2, p. 025102. DOI: 10.1063/1.3553278.

Cottet, G.-H. and Koumoutsakos, P. D. (2000). *Vortex Methods: Theory and Practice*. Cambridge University Press. DOI: 10.1017/CBO9780511526442.

Del Álamo, J. C. et al. (2004). "Scaling of the energy spectra of turbulent channels". In: *Journal of Fluid Mechanics* 500, pp. 135–144. DOI: 10.1017/S002211200300733X.

Deng, B.-Q., Huang, W.-X., and Xu, C.-X. (2016). "Origin of effectiveness degradation in active drag reduction control of turbulent channel flow at Retau= 1000". In: *Journal of Turbulence* 17.8, pp. 758–786. DOI: 10.1080/14685248.2016.1181266.

Duque-Daza, C. A. et al. (2012). "Modelling turbulent skin-friction control using linearized Navier–Stokes equations". In: *Journal of Fluid Mechanics* 702, pp. 403–414. DOI: 10.1017/jfm.2012.189.

Efstathiou, C. and Luhar, M. (2018). "Mean turbulence statistics in boundary layers over high-porosity foams". In: *Journal of Fluid Mechanics* 841, pp. 351–379. DOI: 10.1017/jfm.2018.57.

Encinar, M. P. and Jiménez, J. (2019). "Logarithmic-layer turbulence: A view from the wall". In: *Physical Review Fluids* 4 (11), p. 114603. DOI: 10.1103/PhysRevFluids.4.114603.

Finnigan, J. (2000). "Turbulence in plant canopies". In: *Annual Review of Fluid Mechanics* 32.1, pp. 519–571. DOI: 10.1146/annurev.fluid.32.1.519.

Flores, O. and Jiménez, J. (2006). "Effect of wall-boundary disturbances on turbulent channel flows". In: *Journal of Fluid Mechanics* 566, pp. 357–376. DOI: 10.1017/S0022112006001534.

Fukagata, K., Iwamoto, K., and Kasagi, N. (2002). "Contribution of Reynolds stress distribution to the skin friction in wall-bounded flows". In: *Physics of Fluids* 14.11, pp. L73–L76. DOI: 10.1063/1.1516779.

Fukagata, K. and Kasagi, N. (2002). "Active control for drag reduction in turbulent pipe flow". In: *Engineering Turbulence Modelling and Experiments 5*. Ed. by W. Rodi and N. Fueyo. Oxford: Elsevier Science Ltd, pp. 607–616. DOI: 10.1016/B978-008044114-6/50058-2.

Fukagata, K., Kern, S., et al. (2008). "Evolutionary optimization of an anisotropic compliant surface for turbulent friction drag reduction". In: *Journal of Turbulence* 9, N35. DOI: 10.1080/14685240802441126.

García-Mayoral, R., Gómez-de-Segura, G., and Fairhall, C. T. (2019). "The control of near-wall turbulence through surface texturing". In: *Fluid Dynamics Research* 51.1, p. 011410. DOI: 10.1088/1873-7005/aadfcc.

García-Mayoral, R. and Jiménez, J. (2011). "Hydrodynamic stability and breakdown of the viscous regime over riblets". In: *Journal of Fluid Mechanics* 678, pp. 317–347. DOI: 10.1017/jfm.2011.114.

Gómez-de-Segura, G. and García-Mayoral, R. (2019). "Turbulent drag reduction by anisotropic permeable substrates – analysis and direct numerical simulations". In: *Journal of Fluid Mechanics* 875, pp. 124–172. DOI: 10.1017/jfm.2019.482.

Guala, M., Hommema, S. E., and Adrian, R. J. (2006). "Large-scale and very-large-scale motions in turbulent pipe flow". In: *Journal of Fluid Mechanics* 554, pp. 521–542. DOI: 10.1017/S0022112006008871.

Hammond, E. P., Bewley, T. R., and Moin, P. (1998). "Observed mechanisms for turbulence attenuation and enhancement in opposition-controlled wall-bounded flows". In: *Physics of Fluids* 10.9, pp. 2421–2423. DOI: 10.1063/1.869759.

Hoepffner, J. and Fukagata, K. (2009). "Pumping or drag reduction?" In: *Journal of Fluid Mechanics* 635, pp. 171–187. DOI: 10.1017/S0022112009007629.

Holmes, P., Lumley, J. L., and Berkooz, G. (1996). *Turbulence, Coherent Structures, Dynamical Systems and Symmetry*. Cambridge Monographs on Mechanics. Cambridge University Press. DOI: 10.1017/CBO9780511622700.

Hutchins, N. and Marusic, I. (2007a). "Evidence of very long meandering features in the logarithmic region of turbulent boundary layers". In: *Journal of Fluid Mechanics* 579, pp. 1–28. DOI: 10.1017/S0022112006003946.

Hutchins, N. and Marusic, I. (2007b). "Large-scale influences in near-wall turbulence". In: *Philosophical Transactions of the Royal Society A: Mathematical, Physical and Engineering Sciences* 365.1852, pp. 647–664. DOI: 10.1098/rsta.2006.1942.

Hwang, Y. and Cossu, C. (2010). "Linear non-normal energy amplification of harmonic and stochastic forcing in the turbulent channel flow". In: *Journal of Fluid Mechanics* 664, pp. 51–73. DOI: 10.1017/S0022112010003629.

Ibrahim, J. I., Guseva, A., and Garcia-Mayoral, R. (2020). "Selective opposition-like control of large-scale structures in wall-bounded turbulence". In: *Journal of Physics: Conference Series* 1522, p. 012015. DOI: 10.1088/1742-6596/1522/1/012015.

Jeong, J. and Hussain, F. (1995). "On the identification of a vortex". In: *Journal of Fluid Mechanics* 285, pp. 69–94. DOI: 10.1017/S0022112095000462.

Jiménez, J. and Pinelli, A. (1999). "The autonomous cycle of near-wall turbulence". In: *Journal of Fluid Mechanics* 389, pp. 335–359. DOI: 10.1017/S0022112099005066.

Jiménez, J., Uhlmann, M., et al. (2001). "Turbulent shear flow over active and passive porous surfaces". In: *Journal of Fluid Mechanics* 442, pp. 89–117. DOI: 10.1017/S0022112001004888.

Jovanović, M. R. (2021). "From bypass transition to flow control and data-driven turbulence modeling: An input–output viewpoint". In: *Annual Review of Fluid Mechanics* 53.1, pp. 311–345. DOI: 10.1146/annurev-fluid-010719-060244.

Jovanović, M. R. and Bamieh, B. (2005). "Componentwise energy amplification in channel flows". In: *Journal of Fluid Mechanics* 534, pp. 145–183. DOI: 10.1017/S0022112005004295.

Kang, S. and Choi, H. (2000). "Active wall motions for skin-friction drag reduction". In: *Physics of Fluids* 12.12, pp. 3301–3304. DOI: 10.1063/1.1320833.

Kawagoe, A. et al. (2019). "Proposal of control laws for turbulent skin friction reduction based on resolvent analysis". In: *Journal of Fluid Mechanics* 866, pp. 810–840. DOI: 10.1017/jfm.2019.157.

Kawahara, G., Uhlmann, M., and Veen, L. van (2012). "The significance of simple invariant solutions in turbulent flows". In: *Annual Review of Fluid Mechanics* 44.1, pp. 203–225. DOI: 10.1146/annurev-fluid-120710-101228.

Kim, E. and Choi, H. (2014). "Space–time characteristics of a compliant wall in a turbulent channel flow". In: *Journal of Fluid Mechanics* 756, pp. 30–53. DOI: 10.1017/jfm.2014.444.

Kim, E. and Choi, H. (2017). "Linear proportional–integral control for skin-friction reduction in a turbulent channel flow". In: *Journal of Fluid Mechanics* 814, pp. 430–451. DOI: 10.1017/jfm.2017.33.

Kim, J. (1989). "On the structure of pressure fluctuations in simulated turbulent channel flow". In: *Journal of Fluid Mechanics* 205, pp. 421–451. DOI: 10.1017/S0022112089002090.

Kim, J. and Bewley, T. R. (2007). "A linear systems approach to flow control". In: *Annual Review of Fluid Mechanics* 39.1, pp. 383–417. DOI: 10.1146/annurev.fluid.39.050905.110153.

Kim, J. and Lim, J. (2000). "A linear process in wall-bounded turbulent shear flows". In: *Physics of Fluids* 12.8, pp. 1885–1888. DOI: 10.1063/1.870437.

Kim, J., Moin, P., and Moser, R. (1987). "Turbulence statistics in fully developed channel flow at low Reynolds number". In: *Journal of Fluid Mechanics* 177, pp. 133–166. DOI: 10.1017/S0022112087000892.

Klewicki, J. et al. (2007). "A physical model of the turbulent boundary layer consonant with mean momentum balance structure". In: *Philosophical Transactions of the Royal Society A: Mathematical, Physical and Engineering Sciences* 365.1852, pp. 823–840. DOI: 10.1098/rsta.2006.1944.

Kline, S. J. et al. (1967). "The structure of turbulent boundary layers". In: *Journal of Fluid Mechanics* 30.4, pp. 741–773. DOI: 10.1017/S0022112067001740.

Koumoutsakos, P. (1999). "Vorticity flux control for a turbulent channel flow". In: *Physics of Fluids* 11.2, pp. 248–250. DOI: 10.1063/1.869874.

Laufer, J. (1948). "Investigation of turbulent flow in a two-dimensional channel". PhD thesis. California Institute of Technology. DOI: 10.7907/6ZYC-HJ88.

Leclercq, C. et al. (2019). "Linear iterative method for closed-loop control of quasiperiodic flows". In: *Journal of Fluid Mechanics* 868, pp. 26–65. DOI: 10.1017/jfm.2019.112.

Lee, C., Kim, J., Babcock, D., et al. (1997). "Application of neural networks to turbulence control for drag reduction". In: *Physics of Fluids* 9.6, pp. 1740–1747. DOI: 10.1063/1.869290.

Lee, C., Kim, J., and Choi, H. (1998). "Suboptimal control of turbulent channel flow for drag reduction". In: *Journal of Fluid Mechanics* 358, pp. 245–258. DOI: 10.1017/S002211209700815X.

Lee, J. (2015). "Opposition control of turbulent wall-bounded flow using upstream sensor". In: *Journal of Mechanical Science and Technology* 29.11, pp. 4729–4735. DOI: 10.1007/s12206-015-1020-2.

Lee, M. and Moser, R. D. (2015). "Direct numerical simulation of turbulent channel flow up to Retau = 5200". In: *Journal of Fluid Mechanics* 774, pp. 395–415. DOI: 10.1017/jfm.2015.268.

Lee, T., Fisher, M., and Schwarz, W. H. (1993). "Investigation of the stable interaction of a passive compliant surface with a turbulent boundary layer". In: *Journal of Fluid Mechanics* 257, pp. 373–401. DOI: 10.1017/S002211209300312X.

Lim, J. and Kim, J. (2004). "A singular value analysis of boundary layer control". In: *Physics of Fluids* 16.6, pp. 1980–1988. DOI: 10.1063/1.1710522.

Luhar, M., Sharma, A. S., and McKeon, B. J. (2014a). "On the structure and origin of pressure fluctuations in wall turbulence: Predictions based on the resolvent analysis". In: *Journal of Fluid Mechanics* 751, pp. 38–70. DOI: 10.1017/jfm.2014.283.

Luhar, M., Sharma, A. S., and McKeon, B. J. (2014b). "Opposition control within the resolvent analysis framework". In: *Journal of Fluid Mechanics* 749, pp. 597–626. DOI: 10.1017/jfm.2014.209.

Luhar, M., Sharma, A. S., and McKeon, B. J. (2015). "A framework for studying the effect of compliant surfaces on wall turbulence". In: *Journal of Fluid Mechanics* 768, pp. 415–441. DOI: 10.1017/jfm.2015.85.

Marusic, I., Mathis, R., and Hutchins, N. (2010). "Predictive model for wall-bounded turbulent flow". In: *Science* 329.5988, pp. 193–196. DOI: 10.1126/science.1188765.

Mathis, R., Hutchins, N., and Marusic, I. (2009). "Large-scale amplitude modulation of the small-scale structures in turbulent boundary layers". In: *Journal of Fluid Mechanics* 628, pp. 311–337. DOI: 10.1017/S0022112009006946.

McKeon, B. J. and Sharma, A. S. (2010). "A critical-layer framework for turbulent pipe flow". In: *Journal of Fluid Mechanics* 658, pp. 336–382. DOI: 10.1017/S002211201000176X.

McMullen, R. M., Rosenberg, K., and McKeon, B. J. (2020). "Interaction of forced Orr-Sommerfeld and Squire modes in a low-order representation of turbulent channel flow". In: *Physical Review Fluids* 5 (8), p. 084607. DOI: 10.1103/PhysRevFluids.5.084607.

Moarref, R., Jovanović, M. R., et al. (2014). "A low-order decomposition of turbulent channel flow via resolvent analysis and convex optimization". In: *Physics of Fluids* 26.5, p. 051701. DOI: 10.1063/1.4876195.

Moarref, R., Sharma, A. S., et al. (2013). "Model-based scaling of the streamwise energy density in high-Reynolds-number turbulent channels". In: *Journal of Fluid Mechanics* 734, pp. 275–316. DOI: 10.1017/jfm.2013.457.

Moin, P. and Kim, J. (1980). "On the numerical solution of time-dependent viscous incompressible fluid flows involving solid boundaries". In: *Journal of Computational Physics* 35.3, pp. 381–392. DOI: 10.1016/0021-9991(80)90076-5.

Monty, J. P. et al. (2009). "A comparison of turbulent pipe, channel and boundary layer flows". In: *Journal of Fluid Mechanics* 632, pp. 431–442. DOI: 10.1017/S0022112009007423.

Morra, P., Nogueira, P. A. S., et al. (2021). "The colour of forcing statistics in resolvent analyses of turbulent channel flows". In: *Journal of Fluid Mechanics* 907, A24. DOI: 10.1017/jfm.2020.802.

Morra, P., Semeraro, O., et al. (2019). "On the relevance of Reynolds stresses in resolvent analyses of turbulent wall-bounded flows". In: *Journal of Fluid Mechanics* 867, pp. 969–984. DOI: 10.1017/jfm.2019.196.

Nakashima, S., Fukagata, K., and Luhar, M. (2017). "Assessment of suboptimal control for turbulent skin friction reduction via resolvent analysis". In: *Journal of Fluid Mechanics* 828, pp. 496–526. DOI: 10.1017/jfm.2017.519.

Orszag, S. A. (1971). "Accurate solution of the Orr–Sommerfeld stability equation". In: *Journal of Fluid Mechanics* 50.4, pp. 689–703. DOI: 10.1017/S0022112071002842.

Padovan, A., Otto, S. E., and Rowley, C. W. (2020). "Analysis of amplification mechanisms and cross-frequency interactions in nonlinear flows via the harmonic resolvent". In: *Journal of Fluid Mechanics* 900, A14. DOI: 10.1017/jfm.2020.497.

Panton, R. L. (2001). "Overview of the self-sustaining mechanisms of wall turbulence". In: *Progress in Aerospace Sciences* 37.4, pp. 341–383. DOI: 10.1016/S0376-0421(01)00009-4.

Park, J. and Choi, H. (2020). "Machine-learning-based feedback control for drag reduction in a turbulent channel flow". In: *Journal of Fluid Mechanics* 904, A24. DOI: 10.1017/jfm.2020.690.

Pickering, E. et al. (2021). "Optimal eddy viscosity for resolvent-based models of coherent structures in turbulent jets". In: *Journal of Fluid Mechanics* 917, A29. DOI: 10.1017/jfm.2021.232.

Renard, N. and Deck, S. (2016). "A theoretical decomposition of mean skin friction generation into physical phenomena across the boundary layer". In: *Journal of Fluid Mechanics* 790, pp. 339–367. DOI: 10.1017/jfm.2016.12.

Reynolds, O. (1883). "XXIX. An experimental investigation of the circumstances which determine whether the motion of water shall be direct or sinuous, and of the law of resistance in parallel channels". In: *Philosophical Transactions of the Royal Society of London* 174, pp. 935–982. DOI: 10.1098/rstl.1883.0029.

Reynolds, W. C. and Tiederman, W. G. (1967). "Stability of turbulent channel flow, with application to Malkus theory". In: *Journal of Fluid Mechanics* 27.2, pp. 253–272. DOI: 10.1017/S0022112067000308.

Robinson, S. K. (1991). "Coherent motions in the turbulent boundary layer". In: *Annual Review of Fluid Mechanics* 23.1, pp. 601–639.

Rosenberg, K. and McKeon, B. J. (2019). "Efficient representation of exact coherent states of the Navier–Stokes equations using resolvent analysis". In: *Fluid Dynamics Research* 51.1, p. 011401. DOI: 10.1088/1873-7005/aab1ab.

Rowley, C. W. and Dawson, S. T. (2017). "Model reduction for flow analysis and control". In: *Annual Review of Fluid Mechanics* 49.1, pp. 387–417. DOI: 10.1146/annurev-fluid-010816-060042.

Samie, M. et al. (2020). "Near wall coherence in wall-bounded flows and implications for flow control". In: *International Journal of Heat and Fluid Flow* 86, p. 108683. DOI: 10.1016/j.ijheatfluidflow.2020.108683.

Schmid, P. J. (2007). "Nonmodal stability theory". In: *Annual Review of Fluid Mechanics* 39.1, pp. 129–162. DOI: 10.1146/annurev.fluid.38.050304.092139.

Schmid, P. J. and Brandt, L. (2014). "Analysis of fluid systems: Stability, receptivity, sensitivity: Lecture notes from the FLOW-NORDITA summer school on advanced instability methods for complex flows, Stockholm, Sweden, 2013". In: *Applied Mechanics Reviews* 66.2. 024803. DOI: 10.1115/1.4026375.

Schmid, P. J. and Henningson, D. S. (2001). *Stability and transition in shear flows*. Vol. 142. Applied Mathematical Sciences. Springer. DOI: 10.1007/978-1-4613-0185-1.

Schoppa, W. and Hussain, F. (2002). "Coherent structure generation in near-wall turbulence". In: *Journal of Fluid Mechanics* 453, pp. 57–108. DOI: 10.1017/S002211200100667X.

Schoppa, W. and Hussain, F. (1998). "A large-scale control strategy for drag reduction in turbulent boundary layers". In: *Physics of Fluids* 10.5, pp. 1049–1051. DOI: 10.1063/1.869789.

Schultz, M. P. and Flack, K. A. (2013). "Reynolds-number scaling of turbulent channel flow". In: *Physics of Fluids* 25.2, p. 025104. DOI: 10.1063/1.4791606.

Sharma, A. S. and McKeon, B. J. (2013). "On coherent structure in wall turbulence". In: *Journal of Fluid Mechanics* 728, pp. 196–238. DOI: 10.1017/jfm.2013.286.

Smits, A. J. and Marusic, I. (2013). "Wall-bounded turbulence". In: *Physics Today* 66.9, pp. 25–30. DOI: 10.1063/PT.3.2114.

Son, D., Jeon, S., and Choi, H. (2011). "A proportional-integral-differential control of flow over a circular cylinder". In: *Philosophical Transactions of the Royal Society A: Mathematical, Physical and Engineering Sciences* 369.1940, pp. 1540–1555. DOI: 10.1098/rsta.2010.0357.

Spalart, P. R. and McLean, J. D. (2011). "Drag reduction: Enticing turbulence, and then an industry". In: *Philosophical Transactions of the Royal Society A: Mathematical, Physical and Engineering Sciences* 369.1940, pp. 1556–1569. DOI: 10.1098/rsta.2010.0369.

Symon, S., Illingworth, S. J., and Marusic, I. (2021). "Energy transfer in turbulent channel flows and implications for resolvent modelling". In: *Journal of Fluid Mechanics* 911, A3. DOI: 10.1017/jfm.2020.929.

Symon, S., Rosenberg, K., et al. (2018). "Non-normality and classification of amplification mechanisms in stability and resolvent analysis". In: *Physical Review Fluids* 3 (5), p. 053902. DOI: 10.1103/PhysRevFluids.3.053902.

Tennekes, H. and Lumley, J. L. (1972). *A first course in turbulence*. Cambridge, Massachusetts, and London, England: MIT Press.

Toedtli, S., Yu, C., and McKeon, B. (2020). "On the origin of drag increase in varying-phase opposition control". In: *International Journal of Heat and Fluid Flow* 85, p. 108651. DOI: 10.1016/j.ijheatfluidflow.2020.108651.

Toedtli, S. S., Luhar, M., and McKeon, B. J. (2019). "Predicting the response of turbulent channel flow to varying-phase opposition control: Resolvent analysis as a tool for flow control design". In: *Physical Review Fluids* 4 (7), p. 073905. DOI: 10.1103/PhysRevFluids.4.073905.

Towne, A., Schmidt, O. T., and Colonius, T. (2018). "Spectral proper orthogonal decomposition and its relationship to dynamic mode decomposition and resolvent analysis". In: *Journal of Fluid Mechanics* 847, pp. 821–867. DOI: 10.1017/jfm.2018.283.

Townsend, A. A. (1956). *The Structure of Turbulent Shear Flow*. Cambridge: Cambridge University Press.

Trefethen, L. N. et al. (1993). "Hydrodynamic stability without eigenvalues". In: *Science* 261.5121, pp. 578–584. DOI: 10.1126/science.261.5121.578.

Waleffe, F. (1997). "On a self-sustaining process in shear flows". In: *Physics of Fluids* 9.4, pp. 883–900. DOI: 10.1063/1.869185.

Walsh, M. and Lindemann, A. (1984). "Optimization and application of riblets for turbulent drag reduction". In: *22 Aerospace Sciences Meeting*. DOI: 10.2514/6.1984-347.

Weideman, J. A. and Reddy, S. C. (2000). "A MATLAB differentiation matrix suite". In: *ACM Trans. Math. Softw.* 26.4, pp. 465–519. DOI: 10.1145/365723.365727.

Xu, S., Rempfer, D., and Lumley, J. (2003). "Turbulence over a compliant surface: Numerical simulation and analysis". In: *Journal of Fluid Mechanics* 478, pp. 11–34. DOI: 10.1017/S0022112002003324.

Yamamoto, Y. and Tsuji, Y. (2018). "Numerical evidence of logarithmic regions in channel flow at Ret = 8000". In: *Physical Review Fluids* 3 (1), p. 012602. DOI: 10.1103/PhysRevFluids.3.012602.

Yeh, C.-A. and Taira, K. (2019). "Resolvent-analysis-based design of airfoil separation control". In: *Journal of Fluid Mechanics* 867, pp. 572–610. DOI: 10.1017/jfm.2019.163.

Zare, A., Jovanović, M. R., and Georgiou, T. T. (2017). "Colour of turbulence". In: *Journal of Fluid Mechanics* 812, pp. 636–680. DOI: 10.1017/jfm.2016.682.

Appendix A

DERIVATION OF INTEGRAL DRAG REDUCTION MEASURES

This appendix outlines the derivation of the DNS and resolvent model integral drag reduction measure defined in eqs. (3.13) and (3.14), respectively. It will be important to distinguish between dimensional and dimensionless quantities in the derivation, and we therefore label the former with a tilde hereafter to make the distinction clear. We further follow the approach of Fukagata, Iwamoto, and Kasagi (2002) and nondimensionalize all length scales with the channel half-height $\tilde{h}$, and use twice the bulk velocity $\tilde{U}_b$ to make velocity scales dimensionless. For example, the vertical coordinate and streamwise velocity are nondimensionalized as follows

$$\begin{aligned} y &= \frac{\tilde{y}}{\tilde{h}} \\ u &= \frac{\tilde{u}}{2\tilde{U}_b}. \end{aligned} \tag{A.1}$$

This choice of reference velocity scale has the advantage that the nondimensional bulk velocity U_b simplifies to

$$U_b = \frac{1}{2}\int_{-1}^{1} \overline{u}(y)\,\mathrm{d}y = \frac{1}{2} \tag{A.2}$$

which follows from rescaling eq. (2.14).

The starting point of the derivation is the result of Fukagata, Iwamoto, and Kasagi (2002), which can be used to express the friction coefficient c_f in terms of a laminar and turbulent contribution

$$c_f = \frac{\tilde{\overline{\tau}}_w}{\frac{1}{2}\tilde{\rho}\tilde{U}_b} = \frac{12}{\mathrm{Re}_b} + 12\int_{-1}^{1} y\,(\overline{u'v'})\,\mathrm{d}y. \tag{A.3}$$

Note that we have adjusted the expression to the coordinate system used in this study. We now combine eqs. (3.12) and (A.3) to obtain

$$\Delta\tau = \frac{\int_{-1}^{1} y\left[(\overline{u'v'})_0^{\mathrm{DNS}} - (\overline{u'v'})_c^{\mathrm{DNS}}\right]\mathrm{d}y}{\frac{1}{\mathrm{Re}_b} + \int_{-1}^{1} y\,(\overline{u'v'})_0^{\mathrm{DNS}}\,\mathrm{d}y} \tag{A.4}$$

where the laminar contribution in the numerator drops out, because the mass flux is held constant when control is applied. To recover the DNS drag reduction measure

(3.13), we can rescale the velocities in eq. (A.4) with a desired reference velocity $\tilde{U}$ by multiplying the numerator and denominator by $(\mathrm{Re}_b/\mathrm{Re})^2$, where $\mathrm{Re} = \tilde{U}\tilde{h}/\tilde{\nu}$.

Next, we derive the drag reduction measure for the resolvent model, eq. (3.14). Note that we have introduced the superscript DNS in eq. (A.4) to label Reynolds stresses that satisfy the mean momentum equation. This is a given when working with DNS data, but Reynolds stresses obtained from the resolvent model may not satisfy the mean momentum equation. Model Reynolds stresses do therefore not have a superscript, to make the distinction clear. We next introduce a product of additional terms, whose numerator and denominator represent the model turbulent drag reduction, DNS turbulent drag contribution, and model turbulent drag contribution, respectively

$$\begin{aligned} 1 =& \frac{\int_{-1}^{1} y \left[(\overline{u'v'})_0 - (\overline{u'v'})_c\right] \mathrm{d}y}{\int_{-1}^{1} y \left[(\overline{u'v'})_0 - (\overline{u'v'})_c\right] \mathrm{d}y} \times \frac{\int_{-1}^{1} y \, (\overline{u'v'})_0^{\mathrm{DNS}} \, \mathrm{d}y}{\int_{-1}^{1} y \, (\overline{u'v'})_0^{\mathrm{DNS}} \, \mathrm{d}y} \\ & \times \frac{\int_{-1}^{1} y \, (\overline{u'v'})_0 \, \mathrm{d}y}{\int_{-1}^{1} y \, (\overline{u'v'})_0 \, \mathrm{d}y}. \end{aligned} \tag{A.5}$$

Note that the numerator and denominator of each fraction cancel. The product therefore evaluates to one and can be multiplied to the right-hand-side of eq. (A.4) without altering its value. After rearranging numerators and denominators, we obtain

$$\begin{aligned} \Delta\tau = & \underbrace{\frac{\int_{-1}^{1} y \left[(\overline{u'v'})_0 - (\overline{u'v'})_c\right] \mathrm{d}y}{\int_{-1}^{1} y \, (\overline{u'v'})_0 \, \mathrm{d}y}}_{=T_1(y_d, \angle\hat{A}_d)} \times \underbrace{\frac{\int_{-1}^{1} y \, (\overline{u'v'})_0^{\mathrm{DNS}} \, \mathrm{d}y}{\frac{1}{\mathrm{Re}_b} + \int_{-1}^{1} y \, (\overline{u'v'})_0^{\mathrm{DNS}} \, \mathrm{d}y}}_{=T_2} \\ & \times \underbrace{\frac{\int_{-1}^{1} y \left[(\overline{u'v'})_0^{\mathrm{DNS}} - (\overline{u'v'})_c^{\mathrm{DNS}}\right] \mathrm{d}y}{\int_{-1}^{1} y \left[(\overline{u'v'})_0 - (\overline{u'v'})_c\right] \mathrm{d}y}}_{=T_3(y_d, \angle\hat{A}_d)} \times \underbrace{\frac{\int_{-1}^{1} y \, (\overline{u'v'})_0 \, \mathrm{d}y}{\int_{-1}^{1} y \, (\overline{u'v'})_0^{\mathrm{DNS}} \, \mathrm{d}y}}_{=T_4} \end{aligned} \tag{A.6}$$

where we labeled the terms analogous to eq. (3.14). It is apparent that the terms T_1, T_3 and T_4 are already in their final form, and we only need to manipulate T_2 further.

The Reynolds stresses in the numerator and denominator of T_2 both satisfy the mean momentum equation, so that we can use eqs. (2.16) and (2.29) to rewrite them as

$$(\overline{u'v'})_0^{\mathrm{DNS}} = (u_\tau^2)_0 \, y + \frac{1}{\mathrm{Re}_b} \frac{\mathrm{d}\overline{u}}{\mathrm{d}y}. \tag{A.7}$$

We now define and evaluate the weighted wall-normal integral of eq. (A.7)

$$I = \int_{-1}^{1} y(\overline{u'v'})_0^{\mathrm{DNS}}\,\mathrm{d}y = \int_{-1}^{1} y\left[(u_\tau^2)_0\, y + \frac{1}{\mathrm{Re}_b}\frac{\mathrm{d}\overline{u}}{\mathrm{d}y}\right]\mathrm{d}y = \frac{2}{3}(u_\tau^2)_0 - \frac{1}{\mathrm{Re}_b} \tag{A.8}$$

where the last equality follows from eq. (A.2). We can use I to rewrite T_2 as

$$T_2 = \frac{I}{\frac{1}{\mathrm{Re}_b} + I} = 1 - \frac{3}{2}\frac{1}{\mathrm{Re}_b(u_\tau^2)_0} \tag{A.9}$$

which is already quite close to eq. (3.14). The final step is to bring this expression into a form that only depends on the friction Reynolds number of the uncontrolled flow and Re_b. The key for this final step is the definition of the Reynolds number and the normalization with twice the bulk velocity, which imply that

$$(\mathrm{Re}_\tau)_0 = \frac{(\tilde{u}_\tau)_0\,\tilde{h}}{\tilde{\nu}} = (u_\tau)_0\,\frac{2\tilde{U}_b\tilde{h}}{\tilde{\nu}} = (u_\tau)_0\,\mathrm{Re}_b. \tag{A.10}$$

With this expression, we can rewrite T_2 as

$$T_2 = 1 - \frac{3}{2}\frac{\mathrm{Re}_b}{(\mathrm{Re}_\tau^2)_0} \tag{A.11}$$

which together with eq. (A.6) leads to the resolvent model drag reduction definition of eq. (3.14).

It is important to point out that the normalization with the bulk velocity is only required to derive eq. (A.11). The Reynolds stresses in eq. (3.14) can be normalized by an arbitrary velocity scale once the above form of T_2 is found. The only constraint is that the same reference velocity is used in the numerator and denominator, so that the conversion factors cancel.

Appendix B

SIMPLIFICATION OF THE CONVOLUTION INTEGRAL FOR RESOLVENT MODES

This appendix derives the simplified convolution integral of eq. (3.17), which can be used to compute mean Reynolds stresses in the resolvent framework. The derivation relies on the additional symmetry of the resolvent modes in wavenumber space, eq. (3.2), and is therefore only valid under the broadband forcing assumption. In addition, the form given below only applies to the diagonal terms ($\overline{uu}, \overline{vv}, \overline{ww}$) and the $\overline{uv}$ entry of the Reynolds stress tensor. Quadratic quantities involving the first power of w have to be considered separately, because of the sign inversion implied in eq. (3.2). This aspect is not considered further below since $\overline{uw}$ and $\overline{vw}$ are not of interest in this study. We also note that the following derivation is valid for resolvent approximations at any rank, as long as the broadband forcing assumption is invoked.

The starting point for the derivation is Parseval's theorem (2.53), which we restate below in terms of the streamwise and wall-normal velocity

$$\overline{uv}(y) = \sum_{l=-\infty}^{\infty} \sum_{m=-\infty}^{\infty} \int_{-\infty}^{\infty} \hat{u}(\boldsymbol{k}, y)\, \hat{v}^*(\boldsymbol{k}, y)\, \mathrm{d}\omega. \tag{B.1}$$

Using Hermitian symmetry, we can rewrite eq. (B.1) as

$$\begin{aligned}
\overline{uv}(y) = &\sum_{l=1}^{\infty} \sum_{m=1}^{\infty} \int_{-\infty}^{\infty} 2 \left(\Re \left\{ \hat{u}(\boldsymbol{k}, y)\, \hat{v}^*(\boldsymbol{k}, y) \right\} + \Re \left\{ \hat{u}(\tilde{\boldsymbol{k}}, y)\, \hat{v}^*(\tilde{\boldsymbol{k}}, y) \right\} \right) \mathrm{d}\omega \\
&+ \sum_{l=1}^{\infty} \int_{-\infty}^{\infty} 2\Re \left\{ \hat{u}(l, m=0, \omega, y)\, \hat{v}^*(l, m=0, \omega, y) \right\} \mathrm{d}\omega \\
&+ \sum_{m=1}^{\infty} \int_{-\infty}^{\infty} 2\Re \left\{ \hat{u}(l=0, m, \omega, y)\, \hat{v}^*(l=0, m, \omega, y) \right\} \mathrm{d}\omega \\
&+ \int_{-\infty}^{\infty} \Re \left\{ \hat{u}(l=0, m=0, \omega, y)\, \hat{v}^*(l=0, m=0, \omega, y) \right\} \mathrm{d}\omega
\end{aligned} \tag{B.2}$$

where we used the identity $\Re\{\hat{u}\hat{v}^*\} = \Re\{\hat{u}^*\hat{v}\}$ to derive the last term in eq. (B.2). Now we use the additional wave number symmetry of the resolvent under broadband forcing, i.e. $\hat{u}(\tilde{\boldsymbol{k}}, y) = \hat{u}(\boldsymbol{k}, y)$ and $\hat{v}(\tilde{\boldsymbol{k}}, y) = \hat{v}(\boldsymbol{k}, y)$, to see that the two terms in the first integral of eq. (B.2) are equal. For convenience, we introduce the wave number

dependent coefficient

$$B_{lm} = \begin{cases} 1 & \text{if } l = m = 0 \\ 2 & \text{if either } l = 0 \text{ or } m = 0 \\ 4 & \text{else} \end{cases} \tag{B.3}$$

which can be used to rewrite eq. (B.2) compactly as

$$\overline{uv}(y) = \sum_{l=0}^{\infty} \sum_{m=0}^{\infty} \int_{-\infty}^{\infty} B_{lm}\, \Re\left\{\hat{u}(\boldsymbol{k}, y)\, \hat{v}^*(\boldsymbol{k}, y)\right\} \mathrm{d}\omega. \tag{B.4}$$

We note that expression (B.4) with B_{lm} according to eq. (B.3) is also valid if $u = v$. Furthermore, under a rank-1 approximation, we have $\hat{u} = \sigma_1 \hat{u}_1$ and $\hat{v} = \sigma_1 \hat{v}_1$, which recovers eq. (3.19).

Appendix C

RESOLVENT SCALE SUPPRESSION METRIC

This appendix outlines the derivation of the resolvent scale suppression metric (5.6) under a broadband forcing assumption. We first simplify the expression for the $\overline{vv}$ Reynolds stress, eq. (5.5), by using the result from appendix B

$$\overline{v'v'} = \sum_{l=0}^{\infty}\sum_{m=0}^{\infty}\int_{-\infty}^{\infty} B_{lm}\,|\hat{v}(\boldsymbol{k},y)|^2\,\mathrm{d}\omega. \tag{C.1}$$

We next show that a rank-1 approximation is sufficient for the scale suppression metric. To see this, first suppose that each Fourier coefficient in eq. (C.1) is represented by a rank-2 approximation with broadband forcing

$$\begin{aligned}|\hat{v}(\boldsymbol{k},y)|^2 = {}&\sigma_1^2(\boldsymbol{k})|\hat{v}_1(\boldsymbol{k},y)|^2 + \sigma_2^2(\boldsymbol{k})|\hat{v}_2(\boldsymbol{k},y)|^2 \\ &+ 2\sigma_1(\boldsymbol{k})\sigma_2(\boldsymbol{k})\Re\left\{\hat{v}_1(\boldsymbol{k},y)\hat{v}_2^*(\boldsymbol{k},y)\right\}.\end{aligned} \tag{C.2}$$

Recall from section 2.4.4 that almost all resolvent modes are paired ($\sigma_1 = \sigma_2$), and that the singular vectors of paired modes only differ in their wall-normal symmetry ($\hat{v}_1$ is an odd function of y, while $\hat{v}_2$ is even). For paired modes, the first two terms in eq. (C.2) are equal and even in y, while the last term is an odd function. Analogous to the DNS spectra, we average eq. (C.1) across symmetric planes in the bottom and top half of the channel, which results in the following expression for paired modes

$$\langle|\hat{v}(\boldsymbol{k},y)|^2\rangle_y = 2\sigma_1^2|\hat{v}_1(\boldsymbol{k},y)|^2. \tag{C.3}$$

Note that the last term of eq. (C.2) cancels because of the odd symmetry. As can be seen from eq. (C.3), the only difference between a rank-1 and rank-2 approximation for paired modes is a constant factor, which can be absorbed into B_{lm} and does therefore not enter the scale suppression metric. A rank-1 approximation is thus appropriate for paired modes, and since almost all modes are paired, it is sufficient to consider a rank-1 approximation of the resolvent as well (this is the same argument as in section 3.4.2).

The scale suppression metric (5.6) now follows from eqs. (5.1) and (C.1), and a rank-1 approximation

$$\begin{aligned}\Delta\overline{v'v'} &= \left(\overline{v'v'}\right)_0 (y_d) - \left(\overline{v'v'}\right)_c (y_d) \\ &= \sum_{l=0}^{\infty}\sum_{m=0}^{\infty}\int_{-\infty}^{\infty} B_{lm}\left(\sigma_1^2(\boldsymbol{k})|\hat{v}_1|^2(\boldsymbol{k}, y_d)\right)_0 - B_{lm}\left(\sigma_1^2(\boldsymbol{k})|\hat{v}_1|^2(\boldsymbol{k}, y_d)\right)_c \,\mathrm{d}\omega.\end{aligned} \tag{C.4}$$